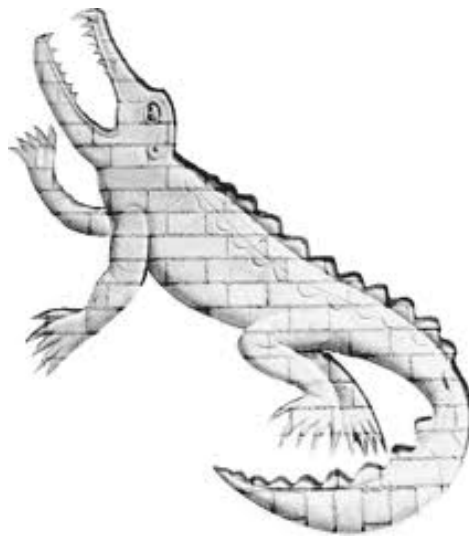


# Ferromagnetic dynamics in coupled systems



**James Powell Patchett**

Department of Physics  
University of Cambridge

This dissertation is submitted for the degree of

*Doctor of Philosophy*

Christ's College

October 2022



## **Declaration**

This thesis is the result of my own work and includes nothing which is the outcome of work done in collaboration except as declared text and acknowledgements. I further state that no substantial part of my thesis has already been submitted, or, is being concurrently submitted for any such degree, diploma or other qualification at the University of Cambridge or any other University or similar institution except as declared in the Preface and specified in the text. This dissertation contains less than 60,000 words, including abstract, tables, footnotes and appendices.

James Powell Patchett

October 2022



# Ferromagnetic dynamics in coupled systems

James Powell Patchett

In this work, ferromagnetic thin films coupled strongly to other physical subsystems (magnetic or otherwise) are studied, and the effect this coupling has on their static and dynamic properties is investigated in order to understand both the ferromagnets themselves, and the systems they are coupled to.

This work investigates recent claims that spin-triplet superconducting Cooper pairs can be generated at superconducting Nb-fullerene interfaces in thin-film heterostructures by looking for evidence of an increase in magnetic damping below the Nb transition temperature in an adjacent permalloy (Py) layer. From these measurements, it is proposed that the experimental evidence purported to show evidence of a spin-triplet population can instead be understood as a signal from the vortex population within a spin-singlet superconductor.

It is shown how it is possible to apply group theory to the dynamic modes of a ferromagnet, or multiple coupled ferromagnets, obeying the linearised Landau-Lifshitz-Gilbert (LLG) equation. From this, the effect of symmetry on the expected resonance spectrum of antiferromagnetically coupled magnetic moments is investigated. Features such as anticrossings and mode degeneracies are shown to be understandable from symmetry arguments, and this is demonstrated experimentally via measurements of the ferromagnetic resonance spectrum of two synthetic antiferromagnets: one bilayer with close to identical ferromagnetic layers, and another bilayer with layers with disparate properties.

Features of the magnetoresistance behaviour in CoFeB single-layers and synthetic antiferromagnetic CoFeB/Ru/CoFeB nanowires adjacent to heavy-metal Pt layers are reported. It is shown how symmetry arguments can be applied to understand features of the magnetoresistive signal and observe a current dependent uniaxial magnetoresistive signal at high current densities which is attributed to the onset of auto-oscillations within the exchange magnon population of the nanowires.



## Acknowledgements

I would first and foremost like to thank Dr Chiara Ciccarelli for her mentorship, guidance, and advice. Without her support and encouragement, this thesis would not have been possible. Many of the lessons I have learnt under her guidance will stay with me for the rest of my life.

I would also like to thank Dr James Haigh for his always pertinent help and advice and for all the time he has so generously donated; Dr Radoslav Chakalov for all his work keeping the lab running smoothly, and for all the knowledge and expertise he shared; Dr Andrew Ramsey and Dr Normann Mertig for their support and being so willing to open the door for me when no one else would; and Dr Tarun Vemulkar for his tireless help with the sputterer. I would also like to thank Tom Sharp for his help fabricating and fixing more things than I can remember, Dr Oscar Cespedes, Alistair Walton, and Dr Mathew Rodgers for providing materials, Dr Jung-Wei Liao for fabricating the synthetic antiferromagnets, Guillermo Nava-Antonio for performing SQUID magnetometry measurements, and Dr Pierre Roy for showing me his code for simulating ferromagnetic dynamics.

Without the above people and many more, the scientific content of this thesis would have taken twice as long and been half as good. However, for everything else, I am grateful to have met many amazing people during my time in Cambridge. I would like to thank Małgorzata Nguyen and Dionisius Hardjo Lukito for all the lunches, gelatos, and Halloween parties we've had the pleasure of sharing; Dr William Wood for generously sharing M113A with me, as well as his natural habitat, Clare MCR bar; Dr Remington Carey, the best DM anyone could ask for, and for finding me my favourite hat; Auriane Terki-Mignot for all her support,

encouragement, interest, and patient understanding (with the help of some friendly nocturnal animals); and finally everyone in the Microelectronics Research Centre and elsewhere whom I've had the pleasure of sharing the last four years with.

Last but not least, I would like to thank my parents and family for always supporting and encouraging me - even when they found themselves rather perplexed by my work. Thank you.

## **Publications**

J. Patchett, M. Drouhin, J. W. Liao, Z. Soban, D. Petit, J. Haigh, P. Roy, J. Wunderlich, R. P. Cowburn, C. Ciccarelli, "Symmetry effects on the static and dynamic properties of coupled magnetic oscillators," *Physical Review B*, vol 105, 10, p. 104436, 2022.



# Table of contents

<b>List of figures</b>	<b>xv</b>
<b>List of tables</b>	<b>xxxiii</b>
<b>Nomenclature</b>	<b>xxxvii</b>
<b>1 Introduction</b>	<b>1</b>
<b>2 Theoretical background</b>	<b>9</b>
2.1 Micromagnetics . . . . .	9
2.1.1 Exchange energy . . . . .	12
2.1.2 Zeeman energy . . . . .	14
2.1.3 Dipole interactions and magnetic anisotropy . . . . .	14
2.1.4 Non-local or indirect exchange fields . . . . .	18
2.2 Ferromagnetic resonance . . . . .	20
2.2.1 From the Landau Lifshitz Gilbert equation to ferromagnetic resonance	22
2.2.2 Magnetic damping and FMR . . . . .	27
2.2.3 Spin-orbit and spin-transfer torques . . . . .	31
2.2.4 Rashba and Dresselhaus torques . . . . .	36
2.2.5 Spin-Hall effect . . . . .	37
2.3 Synthetic antiferromagnets . . . . .	38

2.4	Auto-oscillations / self-oscillations . . . . .	41
2.4.1	Antiferromagnetic auto-oscillators . . . . .	44
2.5	Superspintronics . . . . .	45
2.5.1	Mechanisms of generating spin-triplet Cooper pairs . . . . .	48
2.5.2	Ferromagnetic resonance experiments on superconducting/ferromagnetic heterostructure . . . . .	52
2.5.3	Vortices in type-II superconductors . . . . .	56
2.6	Group theory . . . . .	58
2.6.1	Motivating the use of groups in physical problems . . . . .	58
2.6.2	Introduction to the mathematics of groups . . . . .	62
<b>3</b>	<b>Experimental methods</b>	<b>75</b>
3.1	Sample fabrication . . . . .	75
3.1.1	Substrate preparation . . . . .	76
3.1.2	Magnetron sputtering . . . . .	76
3.1.3	Thermal evaporation . . . . .	76
3.1.4	Photolithography . . . . .	76
3.1.5	E-beam lithography . . . . .	77
3.1.6	Ion milling . . . . .	78
3.2	Sample growth . . . . .	79
3.2.1	Superconducting/ $C_{60}$ /Permalloy spin-pumping devices . . . . .	79
3.2.2	Synthetic antiferromagnets for FMR and magnetoresistance measurements . . . . .	80
3.2.3	Narrow bars for magnetoresistance measurements . . . . .	81
3.3	FMR . . . . .	82
3.3.1	Stripline FMR . . . . .	85
3.3.2	Spin-torque FMR . . . . .	88

3.3.3	Microwave current calibration . . . . .	94
3.4	Magnetoresistance measurements . . . . .	97
3.5	Low-energy muon spin-rotation . . . . .	100
<b>4</b>	<b>In search of spin-triplets at metal-organic interfaces</b>	<b>105</b>
4.1	Introduction and scientific background . . . . .	106
4.2	Experimental design . . . . .	112
4.3	Results . . . . .	114
4.3.1	Initial sample characterisation . . . . .	114
4.3.2	Temperature and Magnetic field dependence of the linewidth . . . . .	115
4.3.3	Physical origin of the magnetic-superconductor interaction . . . . .	124
4.3.4	Alternative mechanisms of interaction between the superconducting and ferromagnetic order . . . . .	132
4.3.5	Flux-jumping/thermomagnetic avalanches . . . . .	135
4.4	Investigating the presence of a spin-triplet population . . . . .	140
4.4.1	Interpreting muon-rotation results in terms of vortices . . . . .	143
4.5	Future work . . . . .	145
4.6	Conclusion . . . . .	146
<b>5</b>	<b>Symmetry and the dynamics of magnetic oscillators</b>	<b>149</b>
5.1	Introduction and scientific background . . . . .	150
5.1.1	Motivating the use of groups for the LLG equation . . . . .	152
5.2	Introduction to using groups to analyse resonance phenomena . . . . .	154
5.3	Methods . . . . .	161
5.3.1	Computation methods used for the analysis of experimental data: . . . . .	161
5.3.2	Simulating the LLG for oscillating magnetic fields . . . . .	164
5.4	Results . . . . .	174

5.4.1	Group theory and the Landau-Lifshitz-Gilbert equation . . . . .	174
5.4.2	Analysing the ferromagnetic resonance modes of antiferromagnetically coupled oscillators using group theory . . . . .	179
5.4.3	Experimental realisation in synthetic antiferromagnets . . . . .	185
5.4.4	Comparison with other works . . . . .	190
5.5	Future work . . . . .	192
5.6	Conclusion . . . . .	193
<b>6</b>	<b>Magnetoresistance effects in synthetic antiferromagnets</b>	<b>195</b>
6.1	Introduction . . . . .	196
6.2	Symmetry and magnetoresistance . . . . .	197
6.3	Current dependent magnetoresistance asymmetry in SAFs . . . . .	202
6.3.1	Introduction . . . . .	202
6.3.2	Results . . . . .	203
6.4	Discussion . . . . .	211
6.5	Future work . . . . .	212
6.6	Conclusion . . . . .	214
<b>7</b>	<b>Conclusion</b>	<b>215</b>
	<b>References</b>	<b>217</b>
	<b>Appendix A Symmetry of Brown's equation for a uniaxial SAF</b>	<b>241</b>
A.1	Non-uniform magnetisation: . . . . .	243
	<b>Appendix B Characterising spin-orbit torques</b>	<b>245</b>
B.1	Rectified voltage as a function of external field angle . . . . .	246

# List of figures

- 1.1 The history of spintronics in terms of significant discoveries. Experimental discoveries are shown in red, theoretical concepts in blue, and commercial devices based on spintronic technology in black. Figure reproduced from [18]. 4
  
- 2.1 Diagram of a ferromagnet placed on a coplanar waveguide during an FMR measurement. A static external field,  $\mathbf{H}$ , is applied at an angle  $\phi_H$  in the x-y plane, with the magnetisation lying at angle  $\phi$  with respect to the x-axis and  $\theta$  with respect to the z-axis (in the most general case). A microwave current is applied down the stripline, which generates a microwave field  $\tilde{\mathbf{h}}(t)$  that excites the magnetisation to oscillate transverse to its static orientation, with the displacement vector given by  $\tilde{\mathbf{m}}(t)$ . The changes in intensity of transmitted microwave field are recorded as the output of the experiment. . 22
  
- 2.2 Dispersion of the magnon modes for two orientations of the external field in the thin-film limit. When the field is in-plane ( $\theta = 0$ ) there exist magnon modes degenerate with the uniform mode into which it can scatter into off impurities. This increases the magnetic damping. . . . . 29

- 
- 2.3 (a) The  $k$ -dependent spin-direction of the majority (blue-dashed line) and minority (red-dashed line) spin directions at the Fermi-energy for delocalised s-band electrons with a Rashba type spin-orbit coupling. (b) Under the application of an electric field, the electrons are shifted in  $k$ -space towards the electric field direction,  $\mathbf{E}$ , causing the electronic distribution acquires a net spin-polarisation due to the spin-orbit coupling (c)  $k$ -dependent direction of the majority spins in a free electron gas with Rashba-type spin-orbit coupling. (d)  $k$ -dependent direction of the majority spins due to Dresselhaus-type spin-orbit coupling. . . . . 31
- 2.4 Diagram of the FMR bar patterned by argon-ion milling in a ferromagnetic/heavy-metal heterostructure. The circular sections are bond pads which are electrically connected to the source and ground via wirebonds. These can include a bondpad made out of a Au/Cr heterostructure if it is felt that will aid bonding. 33
- 2.5 Frequency of the resonance modes versus field for (a) a SAF with an in-plane uniaxial magnetocrystalline anisotropy with external field along an in-plane easy axis, (b) the in-plane hard axis, (c) a uniaxial AF along an in-plane easy axis. . . . . 38
- 2.6 (a) Spin-Hall nano-gap oscillator. Current is concentrated in a small region where the damping native to the system is overcome via a spin-orbit torque due to the adjacent heavy metal layer (usually Pt). Figure reproduced from [37]. (b) Airy's model of the human vocal chords [137]. Air passes through a tube with an open end, one side of which is replaced with a flexible membrane. When subjected to the effect of the constant airflow, the membrane begins to oscillate with a well-defined frequency. . . . . 41

- 2.7 Andreev reflection allows for charge transfer across a superconductor / metallic ferromagnet interface despite the presence of a gap in the superconducting density of states through which particle transfer is forbidden. A free electron is transferred across the interface along with the retroreflection of a hole in the opposite spin band. The net result is a charge transfer of  $2e$ , with no associated spin-flux, carried into the superconductor by a Cooper pair. . . . 53
- 2.8 (a) Magnetisation of a type-I superconductor versus  $H$ . (b) Magnetisation of a type-II superconductor versus  $H$ . Blue curve represents a SC with no pinning and its reversible magnetisation curve. Defects can cause pinning of the vortices that result in a hysteresis in the magnetisation (red-curve). (c) Vortex core structure. Flux penetrates through a normal region of radius  $\xi$ . Supercurrents, rotating up to radius  $\lambda$ , shield the rest of the superconductor from this flux. . . . . 57
- 2.9 (a) Two modes who transform according to the same irreducible representation approach one another and form an anticrossing. (b) Two modes with differing irreducible representations are allowed to cross without interacting. 59
- 2.10 The electronic band structure of copper. Reproduced from [224]. . . . . 61
- 2.11 The product of two matrices in block diagonal form is also in block diagonal form, where the sub-matrices along the main diagonal are effectively multiplied independently. If the constituent elements of the combined block diagonal matrices are representations of the group, then so too is the combined matrix. If all the matrices in the representation (via a suitable similarity transformation if necessary) can be written in this form, then the representation is reducible. . . . . 66

2.12	Unit cell of a crystal structure with octahedral symmetry. Various rotation elements of this group are indicated on the diagram, where $C_n$ represents a rotation about an axis by $2\pi/n$ radians. Figure reproduced from [122]. . . .	70
3.1	Microscope image of a FMR bar patterned by argon-ion milling. The circular sections are bond pads for wirebonds. The current (MW or DC) is concentrated through the narrow central bar in order to excite and/or measure the desired magnetic effect. . . . .	80
3.2	. . . . .	84
3.2	(a) Block-diagram of the experimental set-up for stripline FMR. A magnetic field is applied across the sample during the experiment by an electromagnet internal to the cryostat. (b) Block-diagram of ST-FMR set-up. (c) Photograph of the electromagnet that the ferromagnet in Figure (b) sits between during the experiment. The ferromagnet is held at the end of the long-metallic pole in between the two poles of the electromagnet. (d) Photograph of the PCB board on which the sample is held during the experiment in (b). The sample is attached to the board and wirebonds are connected to it from the microwave input (SMP connector) and to ground. . . . .	85
3.3	(a) Ferromagnet on top of a microwave waveguide. The sample is held down by kapton tape to prevent movement during the measurement and minimise its distance to the waveguide. This box would be sealed and inserted into a cryostat, attached to microwave waveguides on either side via the protruding SMA connectors. (b) Cryostat used for stripline-FMR measurements. . . .	86
3.4	(a) Raw rectified voltages outputted from a stripline FMR experiment (blue line) and their associated fit to a combination of symmetric and antisymmetric Lorentzians (orange line). (b) Linewidth versus frequency from an FMR experiment. Straight line fit gives the Gilbert damping parameter. . . . .	87

---

3.5	FMR bar wire bonded to a microwave waveguide in a stripline FMR experiment.	88
3.6	Experimental setup used for ST-FMR measurements. The sample sits at the end of a holder in between the poles of an electromagnet that is used to apply a DC magnetic field across the sample. A MW current is based through the sample, and the resulting rectified DC current is detected at the DC port of a bias-Tee. . . . .	90
3.7	(a) Raw voltages produced by a ST-FMR experiment and the associated fit to symmetric and antisymmetric Lorentzians. (b) The angle dependence of the resonance field. From this the strength of in-plane magnetic anisotropies can be determined. . . . .	91
3.8	Example of the angular dependence of the strength of the symmetric (a) and antisymmetric (b) rectified DC voltages. From the fit of this data to (3.6), the strength of the current induce spin orbit torques can be determined from the $\sin \phi$ and $\cos \phi$ components of the angular dependence. . . . .	92
3.9	Linewidth versus DC current measured during an FMR experiment. The linewidth is affected by the DC current across the bar due to the antidamping torques, whose sign changes with the sign of the external field, as expected.	93
3.10	Block-diagram of the experimental set-up for ST-FMR with a DC bias current. The DC bias current generates an antidamping torque in the sample which can be used to modulate the magnetic damping. A modulation coil is used to filter out unwanted signal from bolometric effects. . . . .	94
3.11	Block diagram of the experimental set-up for calibrating the microwave current for a given microwave source power. . . . .	94

3.12	Ratio of the DC voltage across the sample versus the applied DC power and fit to equation (3.9). Joule heating causes a linear increase in the resistance, from which the parameter $\alpha$ in (3.9) can be determined. (b) Microwave current through the sample versus microwave power at the source. By measuring the change in the offset resistance, $R_0 + \alpha I^2/2$ , with microwave power, with knowledge of $\alpha$ from (a) the microwave current for a given power at the source can be determined. . . . .	96
3.13	Block diagram of the experimental setup used in measuring the magnetoresistance of devices . . . . .	97
3.14	(a) Implantation probability as a function of depth inside a thin film and average muon beam energy. Reproduced from [235]. (b) Typical muon beam detector setup. Muon beam is incident on the sample, and the resulting positron emissions are detected by detectors placed forwards and aft of the sample space. Reproduced from [236]. . . . .	100
3.15	(a) Number of muons' detected (count) at two detectors placed forwards and aft of the sample under study as a function of time after the initial muon beam pulse. (b) Asymmetry between the two detectors' counts over time. By spectrally analysing this signal, the Larmor frequency of the muons can be determined, and hence the local magnetic field they experience. Figure reproduced from [236]. . . . .	103

- 
- 4.1 (a) (top) The simulated local magnetic field for a London model with a penetration depth of 313 nm and 218 nm. (bottom) Fraction of muons implanted at a given depth for a range of muon beam energies. (b) Local magnetic field measured by muon spin-rotation and the associated fits to the London model. (c) (left) Fraction of muons implanted at a given depth for 9 keV and 20 keV muon beams in the sample without the  $I_{S-C}$ . (right) Calculated decay of the number density of Cooper pairs induced in the sample due to the proximity effect with distance from the Nb superconductor. (d) Local magnetic field variations with temperature (relative to the field measured in the normal state) inside the sample without the  $I_{S-C}$  for two muon-beam energies in an in-plane field of 30 mT. . . . . 111
- 4.1 (e) (left) Fraction of muons implanted at a given depth for 9 keV and 20 keV muon beams in the sample with the  $I_{S-C}$ . (right) Cartoon showing the proposed effect of the  $I_{S-C}$  on the relative proportion of spin-singlet ( $n_s$ ) and spin-triplet ( $n_t$ ) Cooper pairs. (f) Local magnetic field variations with temperature (relative to the field measured in the normal state) inside the sample with the  $I_{S-C}$  for two muon-beam energies in an in-plane field of 30 mT. The 9 keV beam shows a slight paramagnetic response, attributed to a significant spin-triplet Cooper pair condensate inside the sample. Figure reproduced from [235]. . . . . 112

- 
- 4.2 (a) Magnetisation versus field for sample  $I_{S-C}$  (orange dots) and sample  $C_{60}$  (blue dots) at 300 K. Insert: Magnetisation versus field at low fields for both samples. (b) Magnetisation versus field for sample C (no Py, magnetic moment is from the  $I_{S-C}$  only) at 300 K. (c) and (d) Magnetisation (due to the Meissner effect) versus temperature for samples  $C_{60}$  and  $I_{S-C}$  respectively, showing a transition temperature of around 8 – 8.5 K. All measurements were performed using SQUID magnetometry by Alistair Walton from the University of Leeds. . . . . 114
- 4.3 Linewidth versus frequency for (a) sample  $I_{S-C}$  and (b) sample  $C_{60}$  (data below  $T_C$  was collected after zero-field cooling below the transition temperature). An arbitrary offset has been added to each temperature to separate the curves clearly. Above and close to the transition temperature, ( $\sim 8.5$  K), the linewidth's frequency dependence is well described by a linear relationship as expected from the usual Gilbert damping expression for the linewidth (see linear lines of best fit). Beyond around 6 K for both samples, a shoulder develops in the frequency dependence. . . . . 115
- 4.4 Frequency dependence of the resonance field for (a) sample  $I_{S-C}$  at 5K in the ZFC (open blue circles) and FC (orange dots) case. Likewise for sample  $C_{60}$  (Nb/ $C_{60}$ /Py) (b). Dashed blue line shows a fit to the Kittel formula including only the thin-film demagnetisation term (as a free parameter), where  $M_s = 1.03$  T (a) and  $M_s = 0.98$  T (b), in excellent agreement with the room-temperature magnetometry measurements (Table 4.2). . . . . 118

- 4.5 Exemplary linewidth versus frequency curves for (a) sample  $C_{60}$  at 7 K, (b) sample  $C_{60}$  at 6 K, (c) sample  $I_{S-C}$  at 5 K, in the zero-field cooled case (orange circles) and field cooled (0.5 T saturating field applied prior to the measurement) case (blue circles) and (insert) fit of the (ZFC) linewidth to magnon-magnon scattering model. Below the transition temperature (8 K), field cooling increases the measured linewidth substantially at low frequencies, an effect that diminishes as the frequency/resonance field is increased until the two curves are indistinguishable. . . . . 119
- 4.6 Temperature dependence of the resonance field's ( $B_{res}$ ) frequency dependence above and below the transition temperature ( $\approx 8.5$  K) for sample  $I_{S-C}$  (a) and sample  $C_{60}$  (b). Neither sample shows a particularly strong temperature dependence, nor any signs of a particular dependence on the transition above/below  $T_C$ . . . . . 121
- 4.7 Measured rectified voltages above (a) and below (b) the transition temperature for a range of fields applied prior to the measurement (legend) for sample  $C_{60}$  (Nb/ $C_{60}$ /Py) at a 5 GHz. Above the transition temperature, applying a larger field prior to the measurement has no effect. Below the transition temperature, applying a saturating field has a significant effect on the measured linewidth, up until around 100 mT. Each resonance curve has been offset in the x-axis for clarity. . . . . 122
- 4.8 Normalised rectified voltage of the FMR signal at 5Ghz and 5K for sample  $C_{60}$  (Nb/ $C_{60}$ /Py) before and after a 250mT external field is applied. After the field is applied, the linewidth of the signal appears to increase, whilst the resonance frequency remains unaltered. . . . . 123

- 4.9 Frequency dependence of the lineshape of sample  $C_{60}$  (without  $I_{S-C}$ ) at 6 K in the ZFC (a) and FC (0.5 T field applied before the measurement) (b) case. Applying a saturating field results in a substantial distortion in the lineshape such that at sufficiently low frequencies, a whole new peak appears in the output voltage (labelled by a cross in (b)). . . . . 123
- 4.10 The difference in the magnetic moment of sample  $I_{S-C}$  (Nb/ $C_{60}$ /Cu/ $C_{60}$ /Py) at (a) and (d) 7 K, (b) and (e) 5 K, and (c) 3 K, and 10 K. At 7 K, the curve is characteristic of a type-II superconductor with a trapped vortex lattice. The data is left as the magnetic moment as the total volume over the superconducting region is uncertain due to a substantial proximity induced SC state in the  $C_{60}$ . Below this, the net magnetic moment displays unusual magnetic field dependence. (f) Raw magnetic moment at 7 K. The magnetic moment from the trapped flux dominates over the ferromagnetic contribution from the permalloy. Trapped flux at low fields at (g) 7 K, (h) 5 K, and (i) 3 K. The virgin ZFC and FC curves intersect at similar magnetic field values to where the ZFC and FC linewidth curves intersect. Measurements performed by Guillermo Nava-Antonio from the University of Cambridge. . . . . 126
- 4.11 Magneto-optical images of magnetic flux reentry in (a) 200 nm and (b) 100 nm thick Nb thin-films. In the 200 nm thick films, a population of in-plane vortices nucleated at the edge of the sample are unstable to TMAs, causing a highly chaotic dendritic pattern in the magnetic field. In the 100 nm sample, in-plane vortices are energetically forbidden at these fields, and so the magnetic flux reentry is smooth and uniform. Figures reproduced from [252]. . . . . 130

- 4.12 Magnetic moment of the superconductor in sample  $C_{60}$  (relative to 10 K) at: 7K (a), (d); 5 K (b), (e); 3 K (c), (f). Unlike sample  $I_{S-C}$  (Figure 4.10), this sample shows no sign of a significant vortex population below  $T_C$ . Subsequent FMR measurements showed that the hysteretic effect was no longer present, suggesting the sample had decayed as it is known to be sensitive to atmospheric/UV-light exposure. Measurements performed by Guillermo Nava-Antonio from the University of Cambridge. . . . . 132
- 4.13 (a)  $-M$  versus  $H$  curves observed by Evetts et al. [258]. Discontinuous jumps in  $M$  are observed due to the mutual annihilation of positive flux vortices with trapped negative flux vortices causing a macroscopic discontinuity in the magnetisation. Figure reproduced from [258].  $M$  versus  $H$  curves observed for Pb (200 nm, out-of-plane magnetic field) superconductors at a range of temperatures for a sample with large (b) and small (c) grain sizes. The sample with large grains exhibits similar behaviour to (a). As the grain size is reduced, the  $M$  versus  $H$  curve becomes symmetric about  $H = 0$ . Figures reproduced from [260]. . . . . 135
- 4.14 Gilbert damping coefficient,  $\alpha$ , versus temperature for sample  $I_{S-C}$  (a) and sample  $C_{60}$  (b). The transition temperature is indicated by the vertical blue line on each graph. Both samples show a decrease in  $\alpha$  below the transition temperature, indicating that the spin-singlet superconducting condensate is blocking the transmission of spin due to spin-pumping, and there is no evidence of a spin-triplet population in either system. . . . . 142

4.15	depolarization rate ( $\lambda_{TF}$ ) of 9 keV (a) and 20 keV (b) implanted muons in samples with and without the Cu ( $I_{S-C}$ ) layer. The 20 keV muons show a significant increase in the depolarization rate below $T_C$ , which may be attributable to the formation of flux-vortices in the superconductor. Figure reproduced from Rogers et al. supplementary information [235]. . . . .	143
5.1	The vibrational modes of H <sub>2</sub> O. Reproduced from [122]. . . . .	154
5.2	Vibrational modes of CO <sub>2</sub> . Modes 3 & 4 are both bending modes (where the O-C-O angle changes) with orthogonal displacements and are degenerate by symmetry. Figure reproduced from [122]. . . . .	156
5.3	The electronic band structure of Copper. Reproduced from [224]. . . . .	157
5.4	Power spectrum of the simulated magnetic oscillations of an elliptical magnet in response to a microwave driving field at different external field values. Dashed lines indicate the analytical resonance frequency; the two show excellent agreement. . . . .	165
5.5	Analytical expression for the two modes of a uniaxial antiferromagnet (dashed line) and the corresponding prediction by the simulation programme (dots). . . . .	173

- 5.6 Pictorial representation of the resonance modes (a) and some of the symmetry operations (b) of an antiferromagnet with a uniaxial anisotropy along the x-axis at zero magnetic field. The two arrows represent the magnetisations, and the cones the area they sweep out as they rotate.  $C_\infty(\phi)$  represents a rotation about the x-axis of angle  $\phi$ .  $\sigma_v(\delta)$  represents a reflection in a plane parallel to the x-axis and at angle  $\delta$  with respect to the z-axis.  $C'_2(\phi)$  represents a rotation of 180 degrees about an axis in the y-z plane at an angle  $\phi$  to the z-axis.  $\sigma_h$  represents a reflection in the y-z plane. Resonance modes (c) and symmetry operation  $C_2$ , a rotation of 180 degrees about the field direction, (d) for a system of thin-film antiferromagnetically coupled oscillators when the magnetic field,  $\mu_0 B$ , is applied along the hard-axis or is above the spin flop field. This figure has been reproduced from [268]. . . . . 179
- 5.7 Resonance frequencies versus field of an antiferromagnet with an in-plane magnetocrystalline uniaxial anisotropy (a), and a synthetic antiferromagnetic with an in-plane magnetocrystalline uniaxial anisotropy with symmetric (b) and asymmetric (c) magnetic layers calculated from the LLG equation. The external field,  $h_e$  is normalised relative to the field at which the two magnetisations align,  $h_{sat}$ . The external magnetic field is applied along the in-plane hard-axis. . . . . 181
- 5.8 (a) Resonance field ( $B_{res}$ ) versus frequency for the single ferromagnetic layer sample. From a fit to the Kittel mode (dashed blue line), a value of 211 mT is obtained for the effective magnetisation, suggesting that the lower layer in the SAF structures has sizeable out-of-plane anisotropy. (b)  $\phi_H$  dependence of the resonance field of the single layer sample. From a fit of  $B_{res}(\phi)$  from the Kittel formula, an estimate of the uniaxial in-plane anisotropy of 3.17 mT is obtained. . . . . 185

- 5.9 The net magnetic moment measured by VSM and the FMR spectrum for a field applied along the in-plane hard-axis for the single-sided, (a) & (c), and double-sided, (b) & (d), structures. In (a) and (b), the blue (red) data set represents the net magnetic moment when the external field is applied along the easy (hard) axis. Vertical dashed lines correspond to zero external field. VSM measurement was taken by Dr Z. Sorban of the Academy of Science of the Czech Republic. . . . . 187
- 6.1 A uniaxial SAF with an easy-axis/hard-axis (EA/HA) at  $45^\circ/135^\circ$  to the current direction.  $R$  is a reflection operator in the plane containing the hard-axis and the out-of-plane direction (translucent orange plane). By applying this reflection operator to the magnetisation and external field, one obtains a new solution to Brown's equation at the transformed external field. . . . . 197
- 6.2 Magnetoresistance data for the single-sided ((a) and (b)) and double-sided ((d) and (e)) structures when the magnetic field is swept from negative to positive values along different directions connected by symmetry (in-plane). The magnetoresistance is measured relative to the resistance at zero external field. Additionally, the magnetoresistance is measured along the hard and easy axes ((c) and (f)). Inserts: cartoons showing the magnetic field sweep directions (red and blue arrows) relative to the easy-axis (dotted line). . . . 200
- 6.3 (a) Asymmetry in the AMR of a Py/Pt nanowire at high current densities induced by the self-oscillation of exchange magnons at room temperature. (b) Magnitude of the asymmetry as a function of DC current at cryogenic temperatures (orange dots). Note that the magnitude of the resistance asymmetry is reduced compared to that at room temperature at comparable current densities. Also, the measured microwave power from the dipolar modes (blue triangles). Figures reproduced from [148]. . . . . 202

- 
- 6.4 (a) AMR of a single CoFeB layer taken at 3 different current densities (width 500 nm) at 55 mT (in-plane). As the current is increased, beyond a certain threshold the damping in the system is overcome and a burgeoning population of exchange magnons causes an asymmetry to develop in the magnetoresistance. This asymmetry is reversed when the current direction is reversed, confirming that it is related to the current-induced antidamping torque. (b) Size of the asymmetry as a function of DC current. Beyond around 2 mA, the natural damping in the system is overcome and an asymmetry in the magnetoresistance that increases with  $I_{DC}$  develops. . . . . 206
- 6.5 (a) Vibrating sample magnetometry data for the synthetic antiferromagnet nanowire sample before patterning at room temperature with an (in-plane) applied field. The SAF has relatively symmetric layer magnetisations, as shown by the small gap at zero field, and a saturating field of around 180 mT. (b) FMR linewidth versus DC current in the single-layer sample, showing a predicted onset of auto-oscillations at around 4 mA. . . . . 207

- 6.6 (a) Magnetoresistance as a function of  $\phi_H$  for the low-current regime (0.8 mA) and beyond the threshold current (3.1-3.2 mA). Beyond this current density, a large asymmetry in the magnetoresistance develops (22% of the AMR coefficient at 3.2 mA), indicative of an exchange magnon-induced asymmetry. The curves are offset to account for the change in the sample resistance with Joule heating. (b) At intermediate currents, a small asymmetry that reflects the symmetry of the exchange magnon magnetoresistance develops. (c) Sign and magnitude of the asymmetry as a function of current below the threshold current, showing a linear dependence on current. The origin of this small initial asymmetry is not well understood. (d) Comparison of magnetoresistance dependence at low and high currents, showing that the high current case does not also have a decrease in resistance at  $90^\circ$ , ruling out magnetoresistive effects with a  $\sin \phi_H$  dependence. . . . . 208
- B.1 Fit of the symmetric (a) and antisymmetric (b) components of the rectified voltage to the theoretically predicted curves (green dashed line) and the predicted curves plus a  $\sin \phi$  term (orange solid line). The expected curve plus a sin term produce good fits to the data. The sin term is attributed to the anomalous Nernst effect. From these plots, the strength of the SOT-induced effective fields can be determined. . . . . 248
- B.2 Device resistance versus microwave power at the source. The resistance depends linearly on the applied DC power except for a diverging term at low current that occurs because the instrument measures a non-zero voltage at zero current,  $V_{off}$ . Orange points are the raw data, and the blue line is a fit to B.3 with an additional  $V_{off}/I_{DC}$  term to account for the low current divergence. . . . . 249

---

B.3 Microwave (MW) current in the device  $5\mu\text{m} \times 10\mu\text{m}$ ) as a function of microwave power applied by the source at 5GHz. MW current is calculated by looking at the increase in DC resistance compared to a reference data set with no applied MW power. . . . . 249



# List of tables

2.1	Character table for the octahedral group, $O$ . $C_n$ represents an n-fold rotation (of $2\pi/n$ radians) about a given axis; $E$ is the identity element. The symmetry operations are grouped by class, with the number of elements in each class indicated by the number before the $C_n$ symbol. This is the usual presentation of character tables, as symmetry elements in the same class always have the same character [122]. . . . .	71
2.2	Character table for the first 4 irreducible representations of the full symmetry group labeled by their angular momentum $l$ , focusing only on the elements that are also in the octahedral group [122]. . . . .	72
3.1	Structures of the samples measured in Chapter 4. The thickness of the metallic layers was measured by x-ray reflectometry, and the thickness of the $C_{60}$ layer by a quartz microbalance during deposition. . . . .	79
3.2	(All thicknesses in nm) Structures of the synthetic antiferromagnet and ferromagnet samples measured in Chapter 5. The thickness of each layer is determined by the sputtering time multiplied by the measured deposition rate of the sputterer under the same deposition conditions. . . . .	81
3.3	Milling parameters used during the ion milling of the narrow bar samples. . . . .	82

3.4	(All thicknesses in nm) Structures of the synthetic antiferromagnet and ferromagnet samples measured in Chapter 6. The thickness of each layer is determined by the sputtering time multiplied by the measured deposition rate of the sputterer under the same deposition conditions. . . . .	82
4.1	Structures of the proposed spin-converter interface samples. The thickness of the metallic layers was measured by x-ray reflectometry, and the thickness of the $C_{60}$ layer by a quartz microbalance during deposition. . . . .	113
4.2	Sample properties measured by SQUID magnetometry. *The measurement of the saturation magnetisation of Py in this sample assumes the magnetic moment from the $I_{S-C}$ is negligible in comparison with the moment from Py.	115
5.1	The irreducible representations of the symmetry group of $H_2O$ and which of its vibrational modes correspond to which representation. Here $E$ is the identity, $C_2$ a 180-degree rotation about the axis down the centre of the molecule, and $\sigma_v$ and $\sigma'_v$ are reflections in the plane and perpendicular to the plane of the molecule respectively. . . . .	155
5.2	The irreducible representations of the symmetry group of $CO_2$ and which of its vibrational modes correspond to which representation. Here $E$ is the identity, $C_\infty$ a set of rotations by an angle $\phi$ about the axis of the molecule, $\infty\sigma_v$ are a set of reflections in a plane of the molecule at an angle $\phi$ , $i$ is an inversion, $2S_\infty$ are improper rotations about an angle $\phi$ about the molecule axis, and $\infty C'_2$ are rotations by 180 degrees about axes perpendicular to the molecular axis. . . . .	157
5.3	Resonance frequencies of an AF with the external field applied perpendicular to its easy axis. . . . .	172

---

5.4	Representations of a selection symmetry operations engendered by the degenerate eigenmodes of a uniaxial antiferromagnet at zero fields. Note the effect the pseudo-vector nature of the magnetisation has on the representations of the reflection operator $\sigma_h$ . Were the magnetisation a vector, its modes would engender the representation $E_{1u}$ . . . . .	181
5.5	Numerical parameters calculated from FMR and VSM fitting. . . . .	186
6.1	(All thicknesses in nm) Structures of the synthetic antiferromagnet and ferromagnet samples measured in Chapter 6. The thickness of each layer is determined by the sputtering time multiplied by the measured deposition rate of the sputterer under the same deposition conditions. . . . .	204
B.1	Summary of the MW torques divided by the bar width, $w = 5 \mu\text{m}$ , per unit MW current. For a 1 mA current passing through a 5 $\mu\text{m}$ bar, this corresponds to an antidamping torque of about 3 mT. . . . .	250



# Nomenclature

## Roman Symbols

$D$  Diffusion coefficient

## Greek Symbols

$\alpha$  Gilbert damping parameter

$\chi$  Magnetic susceptibility

$\lambda$  Superconducting penetration depth

$\mu$  Chemical potential

$\Theta$  Curie temperature

$\xi$  Superconducting coherence length

## Physical constants

$\hbar$  Reduced Planck's constant

$k_B$  Boltzmann's constant

## Subscripts

$\Delta H_0$  Inhomogeneous broadening

$H_{C1}$  Lower-critical field (type-II superconductor)

$H_{C2}$  Upper-critical field (type-II superconductor)

$T_C$  Superconducting critical temperature

### **Acronyms / Abbreviations**

AF Antiferromagnet

AFM Atomic-force microscope

AMR Anisotropic magnetoresistance

FC Field cooling

FM Ferromagnet

FMR Microwave

GMR Giant magnetoresistance

HOMO Highest occupied molecular orbital

LLG Landau-Lifshitz-Gilbert (equation)

MW Microwave

NMR Nuclear magnetic resonance

PMA Perpendicular magnetic anisotropy

Py Permalloy

RKKY Ruderman-Kittel-Kasuya-Yosida (interaction)

SAF Synthetic antiferromagnet

SC Superconductor

SHE Spin-Hall effect

SOT Spin-orbit torque

ST-FMR Spin-torque ferromagnetic resonance

STT Spin-transfer torque

TMA Thermomagnetic avalanche

TMR Tunneling magnetoresistance

USHMR Undirectional spin-Hall magnetoresistance

YIG Yttrium iron garnet

ZFC Zero-field cooling



# Chapter 1

## Introduction

Global energy consumption is projected to increase by around 50% in the next three decades [1]. Of this, the IT sector will account for 21% by 2030 [2], contributing to a doubling of the demand for electricity from the commercial sector [1]. It is clear that scientists will need to continue to explore different ways of generating new devices based on novel physics if these demands are to be met, as well as improving the speed and performance of electronic devices.

Spintronics, at a basic level, is about the electronic manipulation and detection of the spin-state inside a material or device. In doing so, it opens up electronic devices to use not just the charge of an electron as an information carrier but its spin as well. Spintronics has already produced giant-magnetoresistive and tunneling magnetoresistive magnetic memory hard-drives [3] which led to a revolution in the density of information that could be stored in a commercial hard-drive, also offers the potential of improved energy performance compared with charge-only based counterparts due to the low dissipation nature of spin-currents, and promises new device capabilities based on novel magnetic physics.

## Magnetoresistive effects

Spintronics is based upon the ability to both read and manipulate the spin-state inside a material or device electronically. In order to read the state of a magnetic material electronically, it is necessary for there to be some kind of coupling between the electronic transport and the magnetisation resulting in a dependence of the device's resistance on its magnetic configuration or orientation. This is known as magnetoresistance.

The earliest known form of magnetoresistance was anisotropic magnetoresistance, or AMR. AMR has a  $\cos^2$  dependence in its resistance on the angle between the magnetisation and the current, with a coefficient of a few percent in commonly used materials such as Permalloy [4]. The modern field of spintronics began with the discovery of new magnetoresistive effects, most notably tunneling magnetoresistance (TMR) and giant magnetoresistance (GMR), during the 1970s to late 80s [5–12]. A variety of other spin-based magnetoresistances, such as the spin-Hall magnetoresistance [13], and unidirectional spin-Hall magnetoresistance [14], have also been observed and utilised in spintronic devices.

GMR and TMR are based on the spin-dependent transport properties of magnetic heterostructures. In GMR, antiferromagnetically coupled ferromagnetic layers in a synthetic antiferromagnet have differing resistances depending on the relative orientation of their magnetic moments, leading to a low resistance state when they are parallel, and high resistance state when they are antiparallel [15]. TMR is based on a similar principle but includes a tunneling barrier in between the ferromagnetic layers to enhance this effect.

These magnetoresistive effects are much stronger than AMR, with coefficients ranging up to 82% in GMR [16], to over 100% for TMR [17] at room temperature. This allows for differing orientations of the magnetisation, each one representing either a 1 or a 0, to be detected easily and incorporated inside existing computer technologies, leading to the first generation of magnetic GMR-based memories, whose technological impact was recognised by the 2007 Nobel prize [3], and were the first to achieve widespread commercial adoption.

## Spin-currents and spin-torques

Electrical manipulation of magnetic moments is achieved via spin-torques such as the spin-transfer torque (STT) and spin-orbit torque (SOT). From the perspective of magnetic memories, they allow the magnetic state (and hence the information contained) to be flipped between states without the need for an external magnetic field. Improving miniaturisation, efficiency, and power consumption [18]. They also form the basis of a range of proposed future spintronic devices, as related effects like the antidamping torque allow practitioners to generate dynamics that could not be achieved with magnetic fields alone [19].

The first theoretical and experimental realisation of this was the STT, which is based on the generation of a spin-current by passing a pure-charge current through a first ferromagnetic layer that acts as a ‘spin-filter,’ generating a spin-current polarised along the orientation of its moment that is then incident on a second layer [20, 21]. A spin-current can be thought of as a flux of oppositely spin-polarised electrons traveling in opposite directions, resulting in a net transfer of spin (and angular momentum) — but no charge. Because there is no charge transport, they do not dissipate energy via Joule heating, meaning that devices based on spin could potentially have much lower power consumption than their charge-based counterparts [18]. These spin-currents are used to manipulate the magnetic moment as when their net spin is absorbed by the magnet onto which they are incident, conservation of angular momentum torques its magnetisation towards the spin-current polarisation direction.

Developing new means of generating spin-torques remains central to progress in spintronics. The spin-transfer torque has been followed by SOTs, where spin-orbit coupling is used to generate a net spin-polarisation that torques the magnetisation when a current passes through a device. This can include utilising the spin-Hall effect in heavy metal (Pt, Ta, etc.) layers [22], the Rashba effect at heterostructure interfaces [23, 24], the Dresselhaus torque from spin-orbit coupling resulting from non-centrosymmetric crystal structures [25] (e.g. GaAs [26]), topological materials, and the spin-Hall effect in antiferromagnets [27]. New materials

that are capable of supporting long distance and low loss spin transport are being explored all the time, including spin-triplet supercurrents in ferromagnet/superconductor heterostructures [28], organic polymers [29], graphene [30], and carbon nanotubes [31] to name but a few.

## Spintronic devices

Spintronics is a branch of device physics and aims to use the ability to both manipulate and detect the state of an electron's spin electronically described above to improve and create new devices. Figure 1.1 shows a timeline of the development of spintronic devices, experimental discoveries, and theoretical concepts, including devices based on spintronics that have been successfully commercialised.

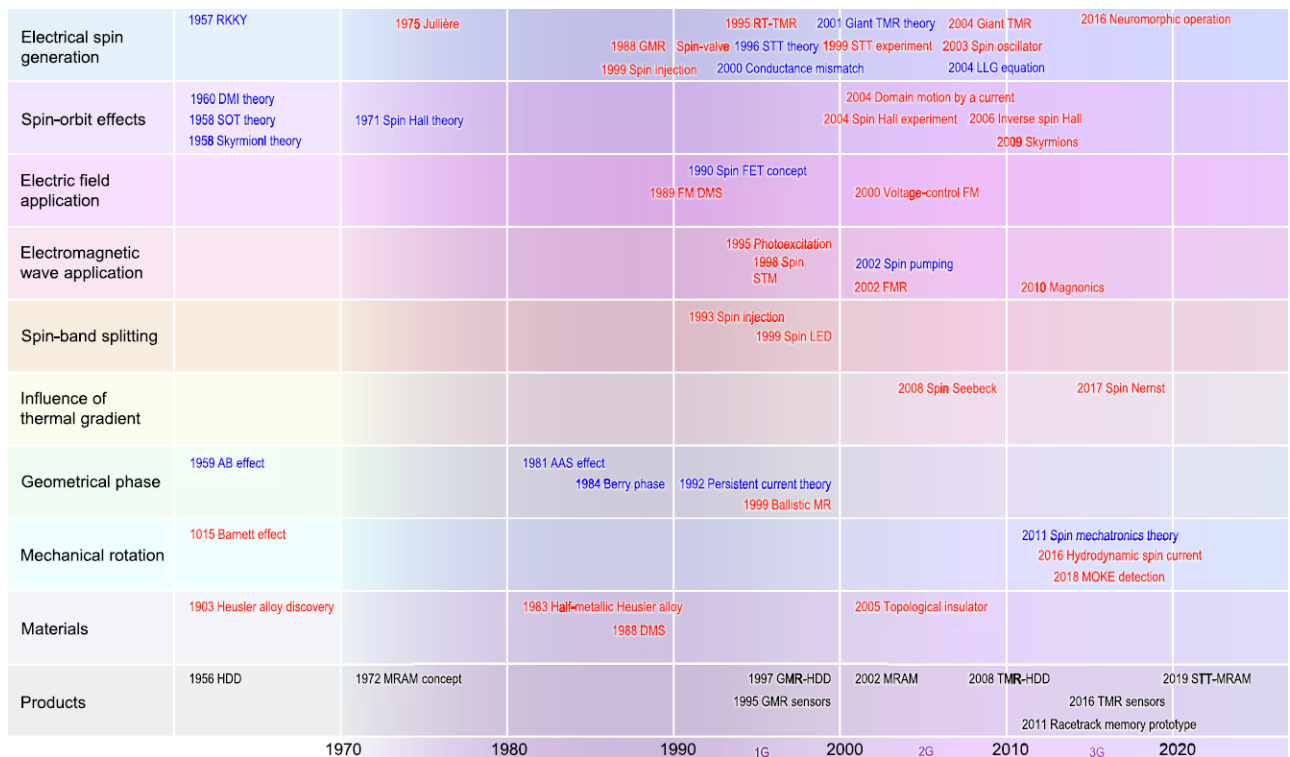


Fig. 1.1 The history of spintronics in terms of significant discoveries. Experimental discoveries are shown in red, theoretical concepts in blue, and commercial devices based on spintronic technology in black. Figure reproduced from [18].

Magnetic memories have already been described above, and other spin-based replacements for traditional electronic components have been proposed, from spin-transistors [32, 33] to spin-LEDs [34]. The contemporary field has also branched out into a number of active areas based on the unique interactions between spin and charge that spintronics enables, covering applications as diverse as neuromorphic computing [35] to race-track memories [36].

Figure 1.1 shows some of the key areas current practitioners are focusing on. Two potential devices that are important to this work are spin-oscillators and frequency interconverters in hybrid quantum systems. Spin-oscillators are based on the antidamping torque, generated by a spin-orbit torque or spin-current, that allows a magnet to act as an effectively dissipationless oscillator. Consequently, the magnetisation can be induced to oscillate indefinitely at microwave to terahertz frequencies. By using a magnetoresistive effect to generate an oscillating voltage, miniaturised, on-chip, microwave power generators could be created [37–39].

Devices that are capable of efficient frequency interconversion are desirable because they allow for the interconversion between the high and low frequency part of the electromagnetic spectrum, allowing future quantum computers to be built out of different quantum systems operating in different frequency ranges all in constant communication with one another. A number of schemes for such devices have been proposed [40, 41]. Recently, it has been suggested that the coupling between magnon modes in an antiferromagnet oscillator could form the basis of such a device [42, 43].

In order to realise some of these novel devices, and improve existing ones, researchers are always looking to branch out into new areas to find new effects and physics. This work will focus on phenomena related to superspintronics, where superconductivity is coupled with ferromagnetism to enhance spintronic devices, and spintronics in antiferromagnetically

coupled devices, which offer a number of advantages over their more traditional ferromagnet based counterparts.

### **Spintronics and superconductivity: superspintronics**

Generating new means of manipulating magnetic elements using spin-currents is of vital importance to the continued progress of spintronics. In recent years there have been a range of novel superconducting heterostructures that have shown a significant spin-triplet, as opposed to the regular spin-singlet, Cooper pair population. A range of means of generating these spin-triplet Cooper pairs have been demonstrated, including in bulk p-wave superconductor [44–46], interfacing with non-homogeneous ferromagnets [47–50], and non-collinear spin-orbit coupling and exchange fields [51]. Fundamentally, they rely on using two non-collinear fields (often an exchange field or spin-orbit coupling) acting on the Cooper pairs' spin. The first rotates the spin state from the  $|0, 0\rangle$  spin state to the  $|1, 0\rangle$  state, and the second to the final  $|1, 1\rangle$  spin-triplet state.

These spin-triplet populations are significant for spintronics as they carry a net spin, meaning that they can potentially be combined into existing spintronic devices as a means of carrying spin-currents. These spin-currents could be generated effectively dissipationlessly inside the superconductor, greatly reducing the energy consumption of many spintronic devices. New materials and architectures capable of generating these spin-triplets populations are of great interest to this nascent field.

### **Antiferromagnet and synthetic antiferromagnet spintronics**

Researchers have been looking towards replacing the ferromagnetic elements in traditional ferromagnetic devices with antiferromagnetic and ferrimagnetic materials, whose coupled magnetic sublattices lead to improved magnetisation dynamics for applications such as magnetic memories and microwave signal generation [52–54].

SAFs, with their peculiar blend of ferromagnetic and antiferromagnetic like behaviour, have long been a cornerstone of spintronics [55]. In contrast, antiferromagnets (AFs) have only recently emerged as a viable material on which to base spintronic devices [52, 53]. In principle, antiferromagnets have the capability to overcome many of the problems facing regular ferromagnetic spintronics. Because of their net-zero magnetic moment, they are both impermeable to external magnetic fields — and produce none of their own. Consequently, magnetic memories based on antiferromagnets could potentially be miniaturised well beyond what is achievable with simple ferromagnet based designs, as at sufficiently small scales ferromagnetic memory cells are liable to erroneous switching events caused by their interaction with the stray fields of adjacent magnetic memory elements — or current induced magnetic fields from the device’s general operation. Indeed, they are resistant to external fields of all kinds. Furthermore, because of the extremely strong couplings between the magnetic sublattices, the dynamics of these antiferromagnets occur on extremely fast time scales. This has been suggested as a route towards producing faster magnetic memories [53], and on-chip terahertz radiation generators [54].

The benefits of AFs also present the greatest challenge to their utilisation. Their lack of a magnetic moment means that their dynamics and state are both hard to manipulate, hard to detect, and owing to their relative lack of investigation, not as fully understood as in ferromagnets. Researchers are gradually overcoming these challenges (with recent discoveries including AMR [56], spin-Hall magnetoresistance [57], and the anomalous Hall effect [58] in AFs) and AFs and other coupled ferromagnetic structures remain one of the field’s most promising candidates heading into the future. Developing new understanding of the dynamics of these coupled ferromagnetic materials/structures, and how their properties feed into improving spintronic devices, will be an important part of realising their potential.

## Outlook

In order to progress the field, it is necessary to search for new device architectures capable of new and improved performances, and look for novel behaviour in existing ones. This work studies spintronic devices by probing their behaviour, typically via ferromagnetic resonance experiments, in order to study their properties and elucidate the underlying physical mechanisms. Of particular interest to me are devices based on coupled ferromagnetic elements.

Chapter 4 looks at a proposed new heterostructure based on  $C_{60}/\text{Nb}$  layers that previous experimental work has suggested might be capable of supporting spin-triplet Cooper pairs. From FMR measurements of the linewidth, and VSM of the net moment, it was found that the heterostructure supports an unexpectedly strong vortex population, which may explain the previous experimental results instead of a spin-triplet population.

Next, the dynamical behaviour of antiferromagnetically coupled magnetisations is studied. In Chapter 5, the FMR modes of two SAFs are studied, one with identical, and one with disparate, layers. An anticrossing between the modes was found in the asymmetric sample, but not in the symmetric one, which is explained as being due to a loss of symmetry via a new theoretical understanding of this phenomenon by showing how group theory applies to the Landau-Lifshitz-Gilbert equation that governs their dynamics.

Lastly, Chapter 6 looks at the effect of symmetry on the static behaviour of a SAF, as measured by its magnetoresistance. A large DC current was applied across a SAF in an attempt to overcome the native damping in the system via the antidamping torque and evidence was found for the generation of exchange magnons by this effect.

# Chapter 2

## Theoretical background

### 2.1 Micromagnetics

At a fundamental level, magnetism is unequivocally a quantum mechanical phenomenon. The source of the magnetic moments in most materials, the electronic spin, is quantum mechanical in nature, and the exchange force that causes them to align spontaneously in ferromagnets (FMs), first described by Heisenberg in 1928 [59], can only be understood by considering the particle exchange symmetry of the wavefunction in both space and spin coordinates.

Classical notions of an exchange field did exist. The idea of an exchange-type field was first proposed by Weiss, who suggested that the local magnetic moments experienced a mysterious “molecular” field which promoted the mutual alignment of adjacent magnetic moments via an effective magnetic field proportional to the local magnetic moment. That is, in an external field  $\mathbf{B}$ , the magnetisation of a paramagnet should be given by  $\mathbf{M} = \chi(\mathbf{B} + \lambda\mathbf{M})$ , where  $\chi$  is the paramagnetic susceptibility, and  $\lambda$  the Weiss molecular field constant that promotes the magnetisations to align with one another, which can be solved self-consistently for  $\mathbf{M}$ . The idea that there should be localised magnetic moments at all was first proposed by Langevin, who derived from this the temperature dependence of the Curie law for

paramagnetic susceptibility,  $\chi \propto 1/(T - T_C)$ , meaning at  $T_C$   $\chi$  diverges in a phase transition to ferromagnetic order [60].

However, any attempt to form a fundamental theory of magnetism from a classical picture is doomed to failure, as shown by Bohr and Van Leeuwen (independently) [61], whose eponymously named Bohr-Van Leeuwen theorem shows that if one only considers classical energy terms, the net-magnetisation of a material should not only be zero at zero field, but zero at all fields: not just ferromagnetism, but also paramagnetism and diamagnetism, are forbidden. Even if one were to introduce an intrinsic magnetic moment to the electrons as an *ad-hoc* addition to the classical theory, the classical dipole-dipole interactions are only capable of producing aligning forces on an energy scale of a few Kelvin in magnitude — massively inferior to the greater than 1000 K Curie temperatures [62] observed in the most powerful ferromagnets.

Keeping track of the magnetic state of a material using quantum mechanics would be untenably cumbersome. Luckily, one is generally only concerned with magnetic variations on a length scale much greater than the unit cell and consequently can adopt a coarse-grained approach, analogous to the manner in which the electric and magnetic field are treated when considering Maxwell's equations in solid-state materials. Here, the microscopic variations in the magnetic moments are neglected in favour of considering only some appropriately volume-averaged macroscopic field. This continuum approximation approach, known as micromagnetics, was first developed in the 1930s and 40s [60, 63, 64] when early practitioners attempted to derive phenomenological models that could explain the hysteresis curves of standard ferromagnets (for a review of this early history, see Brown 1963 [60], Chapter 2 and Brown 1959 [65]). In this work, micromagnetics will be employed to model the static and dynamic behaviour of the magnetic samples.

The general approach is as follows. First the system must be furnished with an appropriate number of energy terms of various physical origins, total energy  $E$ , the most important/-

common of which are detailed in the sections below. Each term is expressed as an integral in terms of the magnetisation density,  $\mathbf{M}(\mathbf{r})$ , which is a vector field computed from the sum of all the magnetic moments in some appropriately size volume on the atomic scale. This work is typically concerned with changes in the magnetisation that happen on a time scale much shorter than the time for thermal equilibrium to be re-established. Consequently, the oscillations can be considered adiabatic, and the appropriate free energy is simply the energy [60]. By computing derivatives of the energy in terms of the magnetic components,  $\mathbf{M} = M_s(m_x, m_y, m_z) = M_s \hat{\mathbf{m}}$  ( $M_s$  is the saturation magnetisation), in some coordinate basis, the  $i^{th}$  component of the effective field that the magnetisation experiences can be derived [60]:

$$(\mathbf{H}_{eff})_i = \frac{1}{\mu_0 M_s} \left( \frac{\partial^2 E}{\partial m_i \partial V} \right)_{m_j \neq i} = \frac{1}{\mu_0 M_s} \left( \frac{\partial \epsilon}{\partial m_i} \right)_{m_j \neq i} \quad (2.1)$$

where  $\partial/\partial V$  is the differential operator with respect to volume, and  $\epsilon$  is the energy density:  $E = \int dV \epsilon$ . From the energy and corresponding effective field, the static and dynamic behaviour can be modelled via Brown's equation [60, 65]:

$$\mathbf{M} \times \mathbf{H}_{eff} = \mathbf{0} \quad (2.2)$$

and the Landau-Lifshitz-Gilbert (LLG) equation [63, 66, 67]:

$$\frac{\partial \mathbf{M}}{\partial t} = -\gamma \mu_0 \mathbf{M} \times \mathbf{H}_{eff} + \frac{\alpha}{M_s} \mathbf{M} \times \frac{\partial \mathbf{M}}{\partial t} \quad (2.3)$$

respectively, where  $\gamma$  is the gyromagnetic ratio (taken to be the value for a free electron unless stated otherwise,  $\gamma/2\pi = 28$  GHz/T),  $\mu_0$  is the permeability of free space, and  $\alpha$  is a measure of the damping in the system. Note that (5.17) conserves the magnitude of  $\mathbf{M}$  ( $\partial_t |\mathbf{M}|^2 = 2\mathbf{M} \cdot \partial_t \mathbf{M} = 0$ ), as in a ferromagnet sufficiently far below its Curie temperature,

$\Theta$ , any excitation that changes the magnitude of the magnetisation is likely to be rapidly damped by the strong exchange forces.

Brown's equation, (2.2), which determines the equilibrium orientation of the magnetisation, is equivalent to finding a local minimum of the total energy [60]. Its solutions are not unique, and this can result in a hysteresis in the magnetic orientation depending on past experimental conditions.

The LLG equation (5.17) models how an out-of-equilibrium magnetisation varies with time. The first term is a gyroscopic term that describes how the magnetisation follows the local energy contours whilst maintaining a constant magnitude. The second is a phenomenological damping term, first described by Gilbert [67] as a modification to the original equation proposed by Landau and Lifshitz [63] to correct for the unphysical rapid suppression of the magnetic motion that the original Landau-Lifshitz equation predicted in the limit of large damping, and which describes the rate at which the non-equilibrium magnetisation returns to equilibrium. The strength of the damping, which typically includes contributions from a variety of physical sources [68], is described by the phenomenological (scalar) constant,  $\alpha \geq 0$ , the Gilbert damping parameter. Under certain conditions, it may be appropriate to model the Gilbert damping as a direction-dependent tensor [69, 70].

In the following section, the common energy terms that determine/dictate the behaviour of ferromagnets will be examined.

### 2.1.1 Exchange energy

Ferromagnetism is characterised by the existence of long-range parallel spin alignment in a material below its Curie temperature, often up to  $\geq 1000$  K. Such a strong alignment requires an equally strong 'force' that makes this arrangement sufficiently energetically favourable that it can survive even up to such high temperatures. Broadly speaking, there are two competing physical origins of such a force: the Heisenberg picture, which applies to

localised moments, and the Stoner-Bloch picture, which applies to itinerant moments (e.g. delocalised electrons in spin-polarised bands). The Heisenberg picture describes the energy (via a Hamiltonian,  $\hat{H}$ ) of a lattice of localised spins,  $\sigma_i$  being the  $i^{\text{th}}$  spin, coupled to one another via an exchange interaction characterised by an exchange strength  $J$ :

$$\hat{H} = -\frac{J}{2} \sum_i^N \sum_j \sigma_i \sigma_j - h \sum_i^N \sigma_i \quad (2.4)$$

where  $h$  is an external magnetic field, the sum over  $j$  runs over the nearest neighbours of  $i$ , and the sum over  $i$  runs over all the spins in the lattice. When  $J$  is positive, there is an energy benefit to the spins aligning in the same direction leading to a ferromagnetic order that aligns with the external field.

As with all such dichotomies, nature is rarely so neat. This work is principally interested in transition metal 3d ferromagnets and their alloys, in which the precise form of the origin of magnetism is still somewhat contentious. This is despite the fact that these are some of the oldest known ferromagnetic materials (Fe, Co, Ni etc.), and that they have been extensively studied since the earliest days of the modern scientific method [71–73]. For the purposes of this work, it is sufficient to know that there are magnetic moments that experience a ferromagnetic exchange force with a corresponding energy term:

$$E_{ex} = A \int dV (\nabla \mathbf{M})^2 \quad (2.5)$$

in the continuum limit, where  $A$  is the exchange constant (which, in quasi-isotropic polycrystalline materials, can be taken to be a scalar). (2.5) has a clear physical interpretation, for  $A \geq 0$ , it promotes uniform magnetic alignment by imposing an energy penalty on any spatial fluctuations in the magnetisation.

Throughout much of this work, an additional approximation known as the *macrospin* approximation will be employed, where it is assumed that the magnetisation is perfectly

aligned throughout the sample by the strong exchange forces (minimising  $E_{ex}$ ). This is typically justified by the spatial profile and energy scale of the driving forces employed in exciting the magnetic moments in a background static external field well in excess of their saturating field,  $H_{sat}$ . Once this approximation is made, the exchange energy can be neglected in all further calculations and the relevant physical quantities replaced with their volume average.

### 2.1.2 Zeeman energy

Named after Dutch physicist Pieter Zeeman, who, in 1896, discovered that spectral lines in sodium could be broadened by the application of a magnetic field [74] and, following Lorentz's theoretical prediction, observed a splitting of the lines in 1897 under the application of a more powerful magnetic field [75], the Zeeman energy is the energy of a spin in a magnetic field. After integrating over all the spins in the volume to obtain an expression for the energy density in terms of the magnetisation density, one obtains the following expression:

$$E_Z = -\mu_0 \int dV \mathbf{M} \cdot \mathbf{H} \quad (2.6)$$

where  $\mathbf{H}$  is the external magnetic field strength. Consequently, the magnetisation tends to align with the external field.

### 2.1.3 Dipole interactions and magnetic anisotropy

*Dipole-dipole interaction (demagnetisation energy):* The magnetic field produced by a collection of classical dipoles, where the  $i^{th}$  dipole has a dipole vector  $\boldsymbol{\mu}_i$ , has the form [76]:

$$\mathbf{H}(\mathbf{r}) = \frac{1}{4\pi} \sum_i 3\mathbf{R}_i \frac{\boldsymbol{\mu}_i \cdot \mathbf{R}_i}{R_i^5} - \frac{\boldsymbol{\mu}_i}{R_i^3} \quad (2.7)$$

where  $\mathbf{r}$  is the point at which the field is being evaluated, and  $|\mathbf{R}_i| = R_i$  is the vector connecting the location of the  $i^{\text{th}}$  dipole to  $\mathbf{r}$ . Using the continuum approximation, one can obtain the following convenient forms for the energy of the dipole-dipole interactions,  $E_{dipole}$ , and the strength of the local field,  $\mathbf{H}_{demag}(\mathbf{r})$  [77]:

$$\begin{aligned} \mathbf{H}_{demag}(\mathbf{r}) &= -\nabla\phi(\mathbf{r}) \\ \phi(\mathbf{r}) &= \frac{-1}{4\pi} \int_V d^3\mathbf{r}' \frac{\nabla' \cdot \mathbf{M}(\mathbf{r}')}{|\mathbf{r} - \mathbf{r}'|} + \frac{1}{4\pi} \int_S d\mathbf{S}' \cdot \frac{\mathbf{M}(\mathbf{r}')}{|\mathbf{r} - \mathbf{r}'|} \end{aligned} \quad (2.8)$$

$$E_{demag} = \frac{\mu_0}{2} \int_V dV |\mathbf{H}_{demag}(\mathbf{r})|^2 \quad (2.9)$$

where  $\phi(\mathbf{r})$  is the magnetic scalar potential, defined by the first equation of 2.8 when there are no free currents. The integral (and corresponding surface integral), runs over all space, not just the ferromagnet's body. In the case of a uniform magnetisation, only terms on the surface of the magnet in the integral in (2.8) survive). This allows the *average* demagnetisation field experienced by the whole magnetic volume to be expressed as a simple matrix product [78, 77]:

$$\mathbf{H}_{demag} = -\mathbf{N}\mathbf{M} \quad (2.10)$$

where  $\mathbf{N}$  is a 3x3 tensor known as the demagnetisation tensor. The precise mathematical form of this tensor is generally complicated (see [78] for the case of uniformly magnetised cuboids), and often much simpler to evaluate numerically than analytically. However, for an infinitely thin film (i.e. the thickness of the film is significantly less than either of its two lateral dimensions — known as the *thin-film approximation*),  $\mathbf{N}$  simplifies to a diagonal tensor with components  $\text{diag}(0, 0, 1)$ , where the z-axis is the out-of-plane direction.

From (2.7) it is clear that in a one-dimensional chain the lowest energy state occurs when all the dipoles are aligned in parallel along the chain direction. In two dimensions and above, however, the energy can always be lowered by flipping some of the spins from the perfectly aligned case. Consequently, the demagnetisation field tends to promote an alignment of the

dipoles with zero overall moment. For  $R$  on the order of the atomic distance, the strength of the demagnetisation field is negligible compared to the exchange interaction. However, unlike the exchange interaction, which decays to almost zero after a few atomic spacings, the demagnetisation field decays relatively modestly with a  $1/R^3$  power-law dependence, meaning it has a significant effect on the long-range magnetic order.

The significance of the dipole-dipole interactions in dictating the long-ranged order of ferromagnets was first appreciated by Frenkel and Dorfman [79], who realised that its tendency to promote the anti-parallel alignment of spins would result in the long-ranged magnetic order breaking up into domains of differing magnetic orientations. Domains are small regions of the magnet where the spins are well-aligned by the exchange field, with transition regions between these domains, known as domain walls, where the spins reorientate themselves into the adjacent domain's magnetic direction. In this sense, the demagnetisation field is the antagonist of the exchange field, which prefers a perfectly aligned magnetisation everywhere, the exact magnetic microstructure determined by the balance of the competing energy terms.

The demagnetisation field has another important effect in thin films. Equation (2.9) vanishes if the magnetisation lies entirely in-plane in thin-films (where the lateral extent of the film is so large compared with its thickness it can be taken to be infinitely wide in the in-plane directions). Consequently, the demagnetisation field tends to align the magnetisation in-plane with significant strength, up to the value of the saturation magnetisation itself ( $\approx 1500$  mT in bulk CoFeB for instance). The tendency for the magnetisation to align along a particular axis of a body is sometimes known as *shape anisotropy*.

*Spin-orbit interaction (magnetocrystalline anisotropy)*: The existence of a spin-orbit interaction was first postulated by Goudsmit and Uhlenbeck [80], who anticipated that an electron moving in orbits in a crystal lattice should experience a magnetic field due to the relativistic transformation of the crystal lattice electric field into its own rest-frame. Because

of the nature of the relativistic transformation, the strength of the field is typically around a factor of  $(v/c)^2$  smaller than the exchange field [77], where  $v$  is the electron's velocity and  $c$  is the speed of light. As  $v/c \ll 1$  in typical soft ferromagnetic materials (e.g. CoFeB, Py), this means the field strength is usually on the order of a few mT: in hard ferromagnets, it can be substantially in excess of this.

Despite this, its importance in understanding the static and dynamic properties of the magnetic moments often outweighs its size due to its typically anisotropic nature: i.e. it depends on the direction of the magnetic moments relative to the electric field of the crystal lattice, giving the equilibrium magnetisation a preferred direction even in zero field for an otherwise isotropic body. Within the continuum approximation, the magnetic anisotropy energy can be written as a power series in the magnetisation that respects the symmetry of the crystal lattice and the underlying physical symmetries of the system. In particular, as time-reversal symmetry ( $t \rightarrow -t$ ) is a symmetry element which changes the sign of  $\mathbf{M}$ , this expansion can only include even powers of  $\mathbf{M}$ .

This work will generally be dealing with thin-film ferromagnets grown by magnetron sputtering and thermal evaporation. If a magnetic field is applied during growth, they can develop a preferred direction that results in a uniaxial magnetisation with an energy density:

$$\epsilon_{ani} = -K(\hat{\mathbf{m}} \cdot \hat{\mathbf{n}})^2 \quad (2.11)$$

where  $\hat{\mathbf{m}}$  is the unit vector in the direction of the magnetisation,  $\mathbf{M} = M_s \hat{\mathbf{m}}$ ,  $\hat{\mathbf{n}}$  is a unit vector in the direction of the easy axis, i.e. the lowest energy direction (for positive  $K$ , negative  $K$  results in an *easy-plane* type anisotropy), and  $K$  is a constant known as the anisotropy constant with units J/m<sup>3</sup>. This is often expressed in terms of the directional cosines/sines. In this form it appears as:

$$\epsilon_{ani} = -K \sin^2 \theta \quad (2.12)$$

where  $\theta$  is defined as in Figure 2.1. The uniaxial anisotropy induced during growth is typically in the plane of the film. However, thin films, particularly when grown adjacent to materials that either have intrinsic, or can induce at the interface, strong-spin orbit coupling such as heavy metal films [81] or metal oxides [82, 83], can also exhibit another important kind of magnetocrystalline anisotropy: perpendicular magnetic anisotropy (PMA). PMA, which was first theoretically predicted by Néel on the basis of the lowered symmetry at the interface [84] and first experimentally observed in 1968 in ultrathin NiFe films [85], tends to counteract the natural tendency of thin-films to have an easy-plane in-plane due to the shape anisotropy by adding an additional uniaxial surface anisotropy term to the overall energy of the ferromagnet with an out-of-plane easy axis. Consequently, in thin films around  $\leq 1$  nm, the surface anisotropy term can be appreciable, and it is possible for the PMA to overcome the shape anisotropy. This causes the equilibrium direction of the thin-film magnetisation to lie out of the plane.

#### 2.1.4 Non-local or indirect exchange fields

The exchange field is based on the indirect coupling of the space and spin degrees of freedom via Coulombic repulsion and the Pauli-exclusion principle, as first proposed by Heisenberg [59], and acts only between adjacent atoms in a crystal lattice: it is atypical to see appreciable coupling beyond one or two degrees of atomic separation. However, there exist additional methods of indirect exchange coupling between localised spins that are mediated by delocalised particles capable of travelling and interacting over long distances, usually the conduction electrons. Such mechanisms lead to highly non-local exchange coupling between spins that decays only relatively weakly (polynomially) with distance.

*RKKY interaction:* Perhaps the best-known form of indirect exchange coupling observed in material systems is the Ruderman-Kittel-Kasuya-Yosida (or RKKY) interaction [86–88],

which couples distant, localised spins, via their spin-dependent scattering of the conduction electrons.

A mechanism of this type was first proposed by Ruderman and Kittel in 1954 [86], who attempted to explain experimentally observed linewidth broadening in nuclear magnetic resonance (NMR) experiments via an indirect coupling of the nuclear spins due to the hyperfine interaction with the conduction band electrons. In doing so, they derived an effective exchange interaction between the nuclear spins,  $i$ , and,  $j$ , with spin-direction,  $\mathbf{I}_i$ , and,  $\mathbf{I}_j$ , respectively, whose energy,  $E_{RKKY}$  varied with the distance between the spins,  $R$ , as:

$$E_{RKKY} \propto \frac{\mathbf{I}_i \cdot \mathbf{I}_j}{R^4} \times [2k_f R \cos(2k_f R) - \sin(2k_f R)] \quad (2.13)$$

where  $k_f$  is the Fermi-wavevector in the material. (2.13) shows that the interaction oscillates between antiferromagnetic and ferromagnetic with a period of  $\pi/k_f$ , decaying polynomially with distance as  $1/R^3$ .

Kasuya [87] and Yosida [88] expanded on Ruderman and Kittel's work by considering a similar interaction between localised (and spin-polarised) d-band orbitals and conduction s-band electrons based on Zenner's model of rare-earth and transition metal ferromagnets. The RKKY interaction is responsible for the coupling between adjacent ferromagnetic layers,  $A$  and  $B$ , with magnetisations  $\mathbf{M}_A$  and  $\mathbf{M}_B$ , in synthetic antiferromagnets (SAFs), whereby adjacent spins on the surface of the ferromagnets, separated by a non-magnetic metallic spacer layer, are coupled via this interaction modelled phenomenologically as a surface energy term:

$$E_A = - \int_{S_A} dS J \mathbf{M}_A \cdot \mathbf{M}_B \quad (2.14)$$

where  $E_A$  is the contribution of the RKKY interaction to the energy of layer  $A$ , and  $J$  is the coupling constant. The integration runs over the surface of each layer,  $S_i$  for layer  $i$ .

If the distance between the two layers is tuned correctly, one can achieve maximal antiferromagnetic coupling between the two ferromagnetic layers, leading to an antiparallel arrangement at zero field.

*Biquadratic exchange interaction:* In addition to the usual bilinear Heisenberg type coupling between adjacent ferromagnetic layers,  $\propto \mathbf{M}_A \cdot \mathbf{M}_B$ , they may also have an additional energy term that is biquadratic in the two magnetisations, i.e.  $\propto (\mathbf{M}_A \cdot \mathbf{M}_B)^2$ . The strength of this term varies from system to system, but can in fact be quite substantial, and indeed dominate the bilinear term, promoting a  $90^\circ$  alignment of the two magnetisations at zero field [89].

Although the physical origin of such a coupling is a little more contentious, it is generally believed to be the result of coupling between the two layers and impurity spins in the metallic spacer layer (either present during fabrication, or from ions that diffuse from the ferromagnetic layer into the spacer-layer). The coupling between the layer and impurity spins is mediated via some (e.g. the RKKY interaction itself) indirect exchange field, which couples the two layers together as a second-order effect [90, 91]. The contribution of this term to the energy of layer  $A$ ,  $E_A$ , is modelled as another surface energy term:

$$E_A = \int_{S_A} dS J_2 (\mathbf{M}_A \cdot \mathbf{M}_B)^2 \quad (2.15)$$

where  $J_2$  is the exchange constant with the usual sign convention. Unlike the RKKY interaction, where the sign of  $J$  can oscillate,  $J_2$  has been found experimentally to be always positive [89–92].

## 2.2 Ferromagnetic resonance

Ferromagnetic resonance (FMR) was first observed experimentally by Griffiths in 1946 [93]. He observed an anomalous increase in the frequency magnetic susceptibility of transition

metal ferromagnets (Fe, Ni, and Co) at microwave frequencies by applying a microwave current to a sample and measuring the resistance. The susceptibility exhibited a dependence on the external magnetic field that could not be explained by the usual formula for the Larmor precession (at frequency  $\omega_L = \gamma\mu_0 H$ ) of spins in an external field,  $H$ . The origin of this increase was first explained by Kittel in 1947 [94, 95], who predicted that the susceptibility,  $\chi$ , of a dissipationless thin-film ferromagnetic, saturation magnetisation  $M_s$ , in an in-plane external field,  $H$ , should have the angular frequency,  $\omega$ , dependence:

$$\chi = \frac{\chi_0}{1 - (\omega/\omega_0)^2} \quad (2.16)$$

where  $\omega_0 = \gamma\mu_0\sqrt{(H + M_s)H}$  and  $\chi_0$  is a frequency independent numerator. (2.16) shows that the susceptibility diverges as the applied microwave (MW) frequency approaches the ferromagnetic resonance frequency,  $\omega_0$ , which is modified from the usual Larmor precession frequency by the thin-film demagnetisation field,  $M_s\hat{z}$  ( $\hat{z}$  being the out of plane direction).

Ferromagnetic resonance, where a microwave driving field (spin current, Oersted field) is applied to a ferromagnet and the subsequent magnetic oscillations detected, will be the principal experimental technique employed in this work to investigate the magnetic and electric properties of ferromagnetic samples. In the following section, the theoretical background and basics of interpreting ferromagnetic resonance experiments will be elucidated. For details of the experimental procedure, please refer to Section 3.3.

### 2.2.1 From the Landau Lifshitz Gilbert equation to ferromagnetic resonance

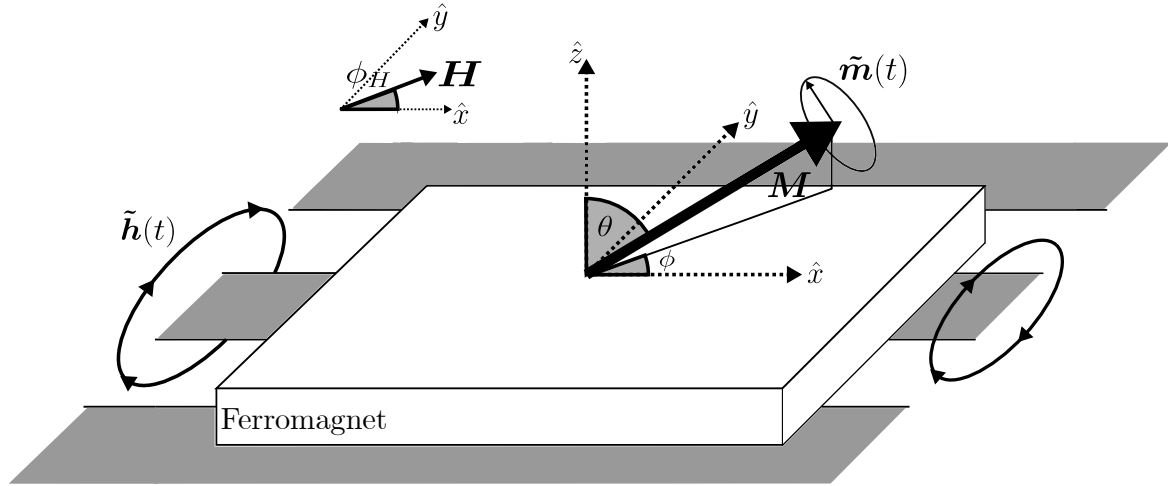


Fig. 2.1 Diagram of a ferromagnet placed on a coplanar waveguide during an FMR measurement. A static external field,  $\mathbf{H}$ , is applied at an angle  $\phi_H$  in the  $x$ - $y$  plane, with the magnetisation lying at angle  $\phi$  with respect to the  $x$ -axis and  $\theta$  with respect to the  $z$ -axis (in the most general case). A microwave current is applied down the stripline, which generates a microwave field  $\tilde{\mathbf{h}}(t)$  that excites the magnetisation to oscillate transverse to its static orientation, with the displacement vector given by  $\tilde{\mathbf{m}}(t)$ . The changes in intensity of transmitted microwave field are recorded as the output of the experiment.

In Section 2.1, it is shown how the Landau Lifshitz Gilbert equation, combined with an appropriate expression for the magnetisation dependence of the energy, can describe the dynamics of an out-of-equilibrium magnetisation. The resulting set of equations for the time evolution of each component is generally insoluble analytically. However, under typical FMR conditions, the microwave driving field is much smaller than the static fields, and hence the size of the transverse oscillations can be taken to be small. By linearising the LLG equations with respect to these small oscillations, one can obtain an eigenvalue equation that can be solved for the transverse components of the magnetisation and the frequency of their oscillations. Hereafter, unless explicitly stated otherwise, this work will be working within the *macrospin approximation*; i.e. all spatial variations in the magnetisation, both in and out of equilibrium, will be neglected. This is typically the experimentally relevant condition

encountered in this work. It should be noted that in this case, the effective relevant field is the *average* effective field felt over the whole sample, as can be seen by taking the volume average of (5.17):

$$\begin{aligned} \frac{\partial \mathbf{M}}{\partial t} &= -\gamma \mu_0 \mathbf{M} \times \frac{1}{V} \int_{\text{ferromagnet}} dV \mathbf{H}_{\text{eff}}(\mathbf{r}) + \frac{\alpha}{M_s} \mathbf{M} \times \frac{\partial \mathbf{M}}{\partial t} \\ \frac{\partial \mathbf{M}}{\partial t} &= -\gamma \mu_0 \mathbf{M} \times \mathbf{H}_{\text{eff}} + \frac{\alpha}{M_s} \mathbf{M} \times \frac{\partial \mathbf{M}}{\partial t} \end{aligned} \quad (2.17)$$

From here on,  $\mathbf{H}_{\text{eff}} = -(1/\mu_0 M_s) \frac{\partial^2 E}{\partial V \partial \mathbf{m}}$  will be used interchangeably with  $\mathbf{H}_{\text{eff}} = -(1/\mu_0 M_s V) \frac{\partial E}{\partial \mathbf{m}}$  in the macrospin approximation.

This procedure explicitly can be illustrated with the simple case first considered by Kittel [94] to explain Griffiths' observations [93]. Kittel modelled the thin-film ferromagnet (out of plane direction  $\hat{\mathbf{z}}$ ) as having two energy terms: one, the Zeeman energy (2.1.2), and two, the demagnetisation energy (2.1.3) in the thin-film limit. This gives a total energy and effective field:

$$\begin{aligned} E &= -\mu_0 V \mathbf{H} \cdot \mathbf{M} + \frac{\mu_0 V}{2} (\mathbf{M} \cdot \hat{\mathbf{z}})^2 \\ \mathbf{H}_{\text{eff}} &= \mathbf{H} - (\mathbf{M} \cdot \hat{\mathbf{z}}) \hat{\mathbf{z}} \end{aligned} \quad (2.18)$$

where  $\mathbf{H} = H \hat{\mathbf{x}}$  and the equilibrium value of  $\mathbf{M}$  lies aligned with the external field. Plugging (2.18) into (5.17), assuming a solution of the form  $\mathbf{M} = M_s \hat{\mathbf{x}} + M_s (m_x, m_y, m_z) e^{i\omega t} = M_s \hat{\mathbf{x}} + M_s \hat{\mathbf{m}} e^{i\omega t}$  and linearising in terms of the small components, the following eigenvalue equation in the limit  $\alpha = 0$  is obtained:

$$\begin{aligned} \begin{pmatrix} i\omega/\gamma_0 & H + M_s \\ -H & i\omega/\gamma_0 \end{pmatrix} \begin{pmatrix} m_y \\ m_z \end{pmatrix} &= \begin{pmatrix} 0 \\ 0 \end{pmatrix} \\ A(\omega) \tilde{\mathbf{m}} &= \mathbf{0} \end{aligned} \quad (2.19)$$

where  $\gamma_0 = \mu_0\gamma$ , and  $\tilde{\mathbf{m}}$  has been defined as the oscillating transverse components of the magnetisation ( $m_x = 0$  to first order in small quantities). (2.19) can be solved for the eigenfrequency,  $\omega_0$ , via the usual condition  $\det\{A(\omega_0)\} = 0$ , giving:

$$\omega_0 = \gamma_0 \sqrt{H(H + M)} \quad (2.20)$$

Consequently, the ferromagnetic resonance frequency is the Lamour frequency, modified by the effect of the demagnetisation field due to the shape anisotropy, as expected. By including a MW driving field  $\tilde{\mathbf{h}}e^{i\omega t}$  and allowing  $\alpha \neq 0$ , an expression for the transverse microwave susceptibility,  $\chi$ ,  $\tilde{\mathbf{m}} = (m_y, m_z) = \chi\tilde{\mathbf{h}}$ , can be obtained as:

$$\chi = \frac{1}{(H + i\Delta H)(H + M_s + i\Delta H) - (\omega/\gamma_0)^2} \begin{pmatrix} H + M_s + i\Delta H & i\omega/\gamma_0 \\ -i\omega/\gamma_0 & H + i\Delta H \end{pmatrix} \quad (2.21)$$

where  $i\Delta H$  is defined as  $i\Delta H = i\omega\alpha/\gamma_0$ , which reflects the fact that this is the measured linewidth of the resonance during FMR experiments.

(2.21) shows that: 1) in the limit of zero damping ( $\alpha = 0$ ), the susceptibility diverges at the ferromagnetic resonance frequency,  $\omega_0$ , and 2) the effect of non-zero damping is to make finite the susceptibility at resonance and to broaden this resonance by  $\omega\alpha/\gamma_0$  during field sweeps under fixed frequency conditions. The Gilbert damping also modifies the resonance frequency by a factor of  $\sim 1 + \alpha^2$ . In typical ferromagnets,  $\alpha$  is on the order of 0.01 – 0.1. Consequently, this correction is usually neglected.

Even this simple example illustrates the power of FMR as an experimental technique for probing the magnetic properties of a ferromagnet. From a simple measurement of the susceptibility's frequency dependence, it is possible to infer values for the saturation magnetisation and the Gilbert damping. The more complex the model, the more information that can be obtained, although additional measurements may be required to uniquely identify the contributions from each term (e.g. angle-dependent measurements to extract the anisotropy).

The procedure outlined above is technically always valid. However, it quickly becomes cumbersome for more than a few simple terms. Instead, for more complex cases, the method of Smit and Beljers [96] will be used, which is often computationally more straightforward and reveals an important mathematical structure contained within the linearised LLG equation that a straightforward expansion in small oscillating components obscures. First writing the energy as a Taylor expansion in the magnetisation components about the equilibrium value:

$$E = E_{eq}(\mathbf{M}) + \frac{1}{2} \tilde{\mathbf{m}}^\dagger \cdot \mathcal{H} \cdot \tilde{\mathbf{m}} \quad (2.22)$$

where  $\mathcal{H}$  is the Hessian of the energy,  $\tilde{\mathbf{m}}$  is the (unnormalised) transverse displacement in the magnetisation, and higher order terms have been neglected. It is convenient to work in spherical polar co-ordinates, where the equilibrium magnetisation becomes  $\mathbf{M} = M_s(1, 0, 0)$  at some  $\theta$ , the polar angle, and  $\phi$ , the azimuthal angle (see Figure 2.1), and the transverse oscillations become  $\tilde{\mathbf{m}} = m_\theta \mathbf{e}_\theta + \mathbf{e}_\phi m_\phi$  ( $\mathbf{e}_\theta$  is the unit vector in the polar direction,  $\mathbf{e}_\phi$  is the unit vector in the azimuthal direction and  $m_\theta$  and  $m_\phi$  are the components of  $\tilde{\mathbf{m}}$  in those directions). The effective field, to first order in  $\tilde{\mathbf{m}}$ , is then straightforwardly:

$$\mathbf{H}_{eff} = \frac{-1}{\mu_0 M_s V} \mathcal{H} \tilde{\mathbf{m}} \quad (2.23)$$

$$\mathbf{H}_{eff} = \frac{-1}{\mu_0 M_s V} \begin{pmatrix} \frac{\partial^2 E}{\partial \theta^2} & \frac{1}{\sin \theta} \frac{\partial^2 E}{\partial \theta \partial \phi} \\ \frac{1}{\sin \theta} \frac{\partial^2 E}{\partial \theta \partial \phi} & \frac{1}{\sin^2 \theta} \frac{\partial^2 E}{\partial \phi^2} \end{pmatrix} \begin{pmatrix} m_\theta \\ m_\phi \end{pmatrix}$$

Substituting (2.23) into the LLG equation (5.17) with  $\alpha = 0$ , and noting that the cross product with the equilibrium magnetisation can be replaced by a matrix product, the following eigenvalue equation is obtained:

$$\omega/\gamma_0 \begin{pmatrix} 0 & i \\ -i & 0 \end{pmatrix} \tilde{\mathbf{m}} = \frac{1}{\mu_0 M_s V} \begin{pmatrix} \frac{\partial^2 E}{\partial \theta^2} & \frac{1}{\sin \theta} \frac{\partial^2 E}{\partial \theta \partial \phi} \\ \frac{1}{\sin \theta} \frac{\partial^2 E}{\partial \theta \partial \phi} & \frac{1}{\sin^2 \theta} \frac{\partial^2 E}{\partial \phi^2} \end{pmatrix} \tilde{\mathbf{m}} \quad (2.24)$$

where the matrix on the left-hand side originates from the cross product  $\mathbf{M} \times \mathbf{H}_{eff}$ , and has been taken to the left-hand side to emphasise that, in the dissipationless limit, the LLG equation is a *generalised Hermitian eigenvalue problem*. ‘Generalised’ in this context meaning that it has the form  $A\mathbf{u} = \lambda B\mathbf{u}$ , where  $B$  is now allowed to be any matrix, not just the identity, so long as both  $A$  and  $B$  are both Hermitian. This important, and hitherto largely under-appreciated, property of the LLG equation is central to understanding the behaviour of coupled oscillators in Chapter 5.

Completing the matrix product to convert (2.24) into the usual eigenvalue problem form (which has no particular symmetry in its matrix elements) and solving for  $\omega$  in the usual way, a useful formula for the resonance frequency of a single ferromagnet can be obtained:

$$2\pi f/\gamma_0 = \frac{1}{\mu_0 V M_s \sin \theta} \left( \frac{\partial^2 E}{\partial \theta^2} \frac{\partial^2 E}{\partial \phi^2} - \left( \frac{\partial^2 E}{\partial \theta \partial \phi} \right)^2 \right)^{1/2} \quad (2.25)$$

where  $f$  is the frequency, related to the angular frequency by  $2\pi f = \omega$ . This work will be dealing with thin-film ferromagnets with uniaxial anisotropies both in and out of the plane of the film. Higher-order terms, such as cubic anisotropies, are generally not expected in these sputtered or evaporated thin films. Consequently, the typical form for the energy of a single-layer magnetic film is given by:

$$E = -\mu_0 V \mathbf{H} \cdot \mathbf{M} + \frac{\mu_0 V}{2} \mathbf{M} \cdot \mathbf{N} \cdot \mathbf{M} + \frac{V K_{\parallel}}{M_s^2} (\mathbf{M} \cdot \hat{\mathbf{e}}_{\parallel})^2 + \frac{A K_{\perp}}{M_s^2} (\mathbf{M} \cdot \mathbf{z})^2 \quad (2.26)$$

where the in-plane uniaxial anisotropy is characterised by the anisotropy constant  $K_{\parallel} < 0$  and the normalised vector along its easy axis  $\hat{\mathbf{e}}_{\parallel}$ , and the out of plane anisotropy is characterised by  $K_{\perp} < 0$  and  $\hat{\mathbf{z}}$ , the out of plane direction, whose distinct physical origins were discussed in Section 2.1.3. The out-of-plane anisotropy is multiplied by the film area,  $A$ , rather than volume,  $V$ , to reflect the fact that typically this is a term that originates from the surface physics [84], and gives an effective field that varies as  $1/t$ , which has been verified

experimentally for many thin-film compositions (see, for instance, [97–100]). In the thin-film limit, and with an in-plane external field,  $\theta = \pi/2$ , equation (2.25) gives the resonance frequency:

$$\begin{aligned} f(\phi, H) &= \frac{\gamma_0}{2\pi} \sqrt{(H + M_s - H_\perp + H_\parallel \cos^2(\phi + \psi))(H + H_\parallel \cos 2(\phi + \psi))} \\ &= \frac{\gamma_0}{2\pi} \sqrt{(H + H_1)(H + H_2)} \end{aligned} \quad (2.27)$$

where the effective fields  $H_\parallel = 2K_\parallel/M_s$  and  $H_\perp = 2K_\perp/M_s t$  have been introduced ( $t$  being the thickness of the film,  $V = At$ ), which characterise the strengths of the anisotropy, and the angle of the in-plane easy-axis with respect to the x-axis,  $\psi$ . The quantities  $H_1$  and  $H_2$  are a notational convenience for future rearrangements that reflect the typical form of the result as the square root of a quadratic. A resonance frequency of this form was first reported by Kittel [95].

Equation (2.27) shows that from a measurement of the angular dependence of the FMR frequency, values of the strength and direction of the in-plane uniaxial anisotropy can be obtained, and from the frequency dependence on the external field,  $H$ , the effective magnetisation,  $M_{eff} = M_s - H_\perp$ .

### 2.2.2 Magnetic damping and FMR

In Section 2.2.1 it was shown how measurements of the ferromagnetic resonance frequency as a function of external field and angle can be used to determine information about the physical properties of the ferromagnet, such as the effective magnetisation and the anisotropy.

Increasingly, FMR is being used for detailed measurements of the magnetic damping, characterised by the Gilbert damping parameter  $\alpha$  in (5.17). These measurements are of great physical interest, less so because of the raw values of  $\alpha$  they produce, but rather because of the insight one can obtain into the physical processes that contribute to the magnetic damping. By measuring the influence of temperature, design, composition, magnetic field strength,

angle etc. on the magnetic damping, through careful analysis it may be possible to identify the presence and strength of important physical processes in the system. In the following section, the physical origin of many of the most important processes that contribute to the magnetic damping will be described. Understanding each contribution, and how they can be isolated via careful experimentation and analysis is key to a successful FMR damping experiment.

*Fundamentals:* Equation (2.21) shows that the measured linewidth in an FMR experiment,  $\Delta H$ , should vary linearly with the angular frequency,  $\omega$ , with a gradient proportional to Gilbert damping parameter [101]. In practice, there are additional contributions to the linewidth outside of the Gilbert damping that result in the frequency-dependent linewidth having the following form:

$$\Delta H = \Delta H_0 + \alpha\omega/\gamma_0 \quad (2.28)$$

The zero-frequency offset,  $\Delta H_0$ , is often known as the *extrinsic* contribution to the damping (in contrast to the *intrinsic* Gilbert damping) or the *inhomogeneous broadening*, as the physical mechanisms responsible for it are often related to inhomogeneities in the sample or magnetic fields. Below some of the common sources of magnetic damping outside of the intrinsic Gilbert damping are listed.

*Two magnon scattering:*

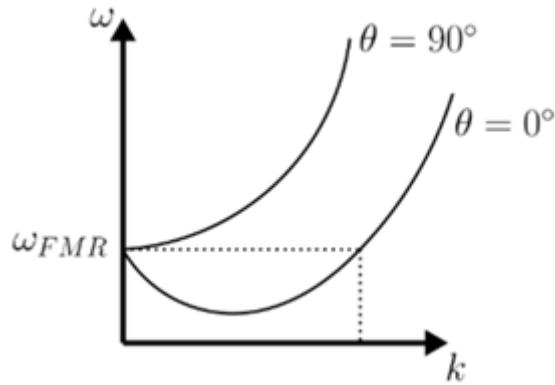


Fig. 2.2 Dispersion of the magnon modes for two orientations of the external field in the thin-film limit. When the field is in-plane ( $\theta = 0$ ) there exist magnon modes degenerate with the uniform mode into which it can scatter into off impurities. This increases the magnetic damping.

Because of the approximately uniform driving field used in most FMR set-ups, one is typically exciting, and detecting, a uniform, or  $\mathbf{k} = \mathbf{0}$ , precessional mode. Like all systems of coupled oscillators with translational symmetry, there exists a spectrum of oscillatory modes, characterised by their  $\mathbf{k}$ -vector,  $\mathbf{k}$ , or pseudo-momentum, and some associated frequency/energy. These qualities are related by the dispersion relationship,  $\omega(\mathbf{k})$ , which is determined by the characteristics of the magnetic material and the external conditions. In thin-films, for certain orientations of the external field  $\partial\omega/\partial k < 0$  at  $\mathbf{k} = \mathbf{0}$ , and so there exist modes (magnons in the quasi-particle picture) with  $\mathbf{k} \neq \mathbf{0}$  that are degenerate with the uniform mode [102–105] (Figure 2.2).

In a completely translationally invariant system, (pseudo-)momentum is conserved, and there is no way for these modes to interact with the uniform mode. However, if there exist inhomogeneities in the system, then in the quantum mechanical magnon picture it is said that the uniform mode can ‘scatter’ off these inhomogeneities into the degenerate  $\mathbf{k} \neq \mathbf{0}$  modes [106]. This results in a frequency-independent source of damping, and it is often the dominant contribution to  $\Delta H_0$ , and perhaps even the damping itself, at low frequencies and in low intrinsic damping systems (for example YIG (yttrium iron garnet) [107]). Whilst possible

in any magnetic system with a degenerate mode spectrum, the effect can be particularly pronounced in thin films due to the increased strength of surface effects (e.g. scattering of surface defects) and the demagnetisation field producing a ready-made set of degenerate modes for certain magnetic field orientations with respect to the film surface.

This applies so long as the inhomogeneities are not so large that they can be treated by this perturbative picture of magnon-magnon interactions. In the case of strong inhomogeneities, the oscillations can become localised, oscillating at their own local frequency around their own local effective field. This leads to an enhancement in the linewidth via the broadening effect of multiple overlapping resonances at slightly offset frequencies [101, 108–110].

*Spin-pumping:* When a DC spin-current is incident on a ferromagnet with a spin-polarisation non-colinear with its ferromagnetic moment, this spin is absorbed by the ferromagnet, torquing it in the direction of the spin-current polarisation by conservation of angular momentum. This is the basics of the spin-transfer torque [19, 111], a phenomenon that is discussed in more detail in Section 2.2.3. The reciprocal of this phenomenon is known as spin-pumping, where a precessing magnetisation produces a DC spin-current. If this spin current is incident on the surface of the sample it can penetrate into the adjacent material and, via spin non-conserving processes such as spin-orbit coupling, lose its angular momentum before it can backflow into the ferromagnet, resulting in a net loss of angular momentum that shows up as an enhancement in the Gilbert damping [112–115]. Although the loss of angular momentum occurs outside of the ferromagnet, it is still considered an intrinsic process as all the sub-processes are intrinsic to the heterostructure (i.e. not reliant on defects or external influences).

*Additional mechanisms:* Inhomogeneities of many kinds allow the uniform mode to couple to some kind of sink of energy, resulting in an extrinsic contribution to the damping. Some of the mechanisms that have been considered include: coupling to the lattice vibrations/phonons [116], intrinsic 4-magnon scattering processes [117], coupling between dopant

energy levels and magnons [118, 119] etc. For a review of these mechanisms, and the ones mentioned above, see Azzawi et al. 2017 [120] and the references therein.

### 2.2.3 Spin-orbit and spin-transfer torques

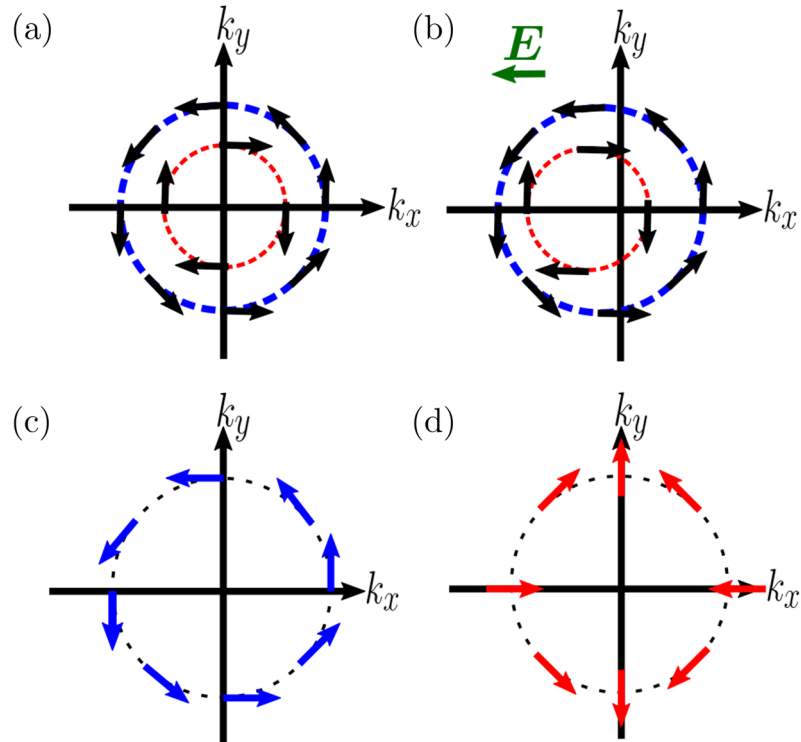


Fig. 2.3 (a) The  $k$ -dependent spin-direction of the majority (blue-dashed line) and minority (red-dashed line) spin directions at the Fermi-energy for delocalised s-band electrons with a Rashba type spin-orbit coupling. (b) Under the application of an electric field, the electrons are shifted in  $k$ -space towards the electric field direction,  $E$ , causing the electronic distribution acquires a net spin-polarisation due to the spin-orbit coupling (c)  $k$ -dependent direction of the majority spins in a free electron gas with Rashba-type spin-orbit coupling. (d)  $k$ -dependent direction of the majority spins due to Dresselhaus-type spin-orbit coupling.

The basic phenomenology of the spin-orbit and spin-transfer torques (SOTs and STTs respectively) is as follows: first, generate a non-equilibrium spin-distribution via the application of a voltage/electric field, then secondly, transfer the accumulated angular momentum to the ordered spin-structure, torquing their net momentum in the direction of the non-equilibrium spin-polarisation. Where they differ is in how this non-equilibrium spin distribution is gen-

erated. The spin-transfer torque [19, 111, 121] generates a spin-current via an additional ‘pinned’ ferromagnet layer that acts as a spin-filter, spin-polarising a charge current that is then incident on a separate ferromagnetic ‘free’ layer and torquing its moment towards the direction of the pinned layer’s orientation via the conservation of angular momentum.

The spin-orbit torque relies on the spin-splitting of the band structure itself to generate a non-equilibrium spin polarisation. The basic phenomenology is most easily understood by considering a simple s-d model of a ferromagnetic metal, where the s-band electrons form a highly delocalised conduction band, and the d-electrons are localised, but strongly spin-polarised, forming the bulk of the detectable magnetic moment. In a material/device with inversion symmetry the band structure of the delocalised electrons is forced to be spin-degenerate:  $E_{\sigma}(\mathbf{k}) = E_{\bar{\sigma}}(\mathbf{k})$  (where  $\mathbf{k}$  is the wavevector and  $\sigma/\bar{\sigma}$  are antiparallel spin polarisations). If this inversion symmetry is broken, either via the intrinsic symmetry of the crystal structure itself or close to an interface in a heterostructure, then the weaker condition  $E_{\sigma}(\mathbf{k}) = E_{\bar{\sigma}}(-\mathbf{k})$  applies [25, 122].

This is not sufficient to spin-polarise the conduction electrons at equilibrium (Figure 2.3a). However, under the application of an electric field the Fermi-surface of the delocalised s-band electrons ‘shifts’ in the direction of the applied field, causing them to develop a net polarisation (Figure 2.3b). This net polarization is in general misaligned with the localised d-electron’s polarisation, and so, via a coupling of the s and d-spins, the s-electrons torque the spin of the d-electrons towards the direction of their net polarization.

A model of this kind was first proposed by Manchon and Zang [123], and offers a simple illustration of how the band structure and its symmetry-enforced properties can induce a net-torque on the ferromagnetic order under the application of an electric field/voltage. For a more detailed discussion of the mechanistic origin of current induced SOTs see [26, 124].

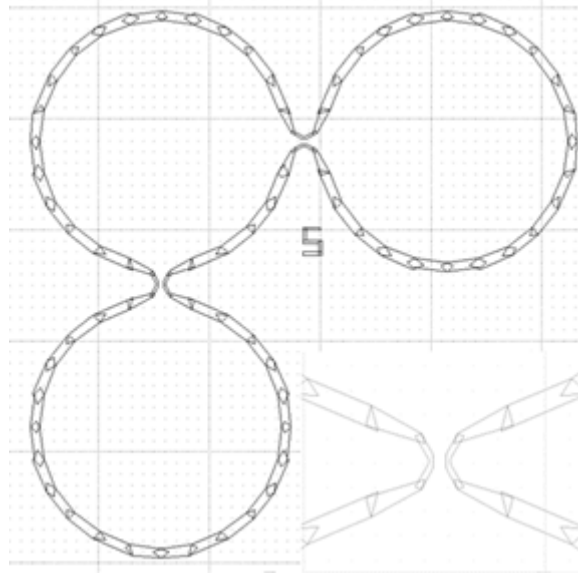


Fig. 2.4 Diagram of the FMR bar patterned by argon-ion milling in a ferromagnetic/heavy-metal heterostructure. The circular sections are bond pads which are electrically connected to the source and ground via wirebonds. These can include a bondpad made out of a Au/Cr heterostructure if it is felt that will aid bonding.

The net effect of the presence of such a torque is the modification of the LLG equation to include two new terms [26]:

$$\frac{\partial \mathbf{M}}{\partial t} = -\gamma \mu_0 \mathbf{M} \times (\mathbf{H}_{eff} + \mathbf{H}_{FL}) + \frac{\alpha}{M_s} \mathbf{M} \times \frac{\partial \mathbf{M}}{\partial t} + \frac{1}{M_s} \mathbf{M} \times (\mathbf{H}_{AD} \times \mathbf{M}) \quad (2.29)$$

where  $\mathbf{H}_{FL}$  is the effective field corresponding to a *field-like* torque, and  $\mathbf{H}_{AD}$  is the effective field of the *antidamping torque*. The field-like torque is so called because it appears in the LLG equation with the same functional dependence as the original effective field, and the antidamping torque is a dissipative term that has the same functional form as the original formulation of the phenomenological magnetic damping by Landau and Lifshitz [63]. Magnetic damping is, in essence, the rate of loss of angular momentum to the lattice and other reservoirs. Hence, the physical origin of this antidamping torque can be understood as the replacement of this angular momentum via the current-generated spin accumulation.

In order to accurately characterise the strength and nature of these torques (field-like, antidamping, angular dependencies etc.), one can perform spin-torque ferromagnetic resonance (ST-FMR) experiments on patterned FMR bars (Figure 2.4). ST-FMR is similar to traditional FMR experiments in that a microwave frequency torque is used to induce resonance oscillations in the magnetisation, but rather than using a waveguide or cavity to apply the oscillating magnetic field, an AC current is passed through a bar-geometry device and the resulting AC spin-orbit torques (and the current's Oersted field) are used to torque the magnetisation instead. The resulting magnetic oscillations couple to the AC current via magnetoresistive effects (usually polycrystalline AMR), resulting in an AC component of the resistance at the resonance frequency,  $R(\omega)$ . Multiplying this resistance by the AC current,  $I(\omega)$ , a rectified DC voltage is generated,  $V_{DC} = 1/2R(\omega)I(\omega)$  (the factor of 1/2 resulting from time averaging) that is detected as the experiment's output. The generation of a DC voltage from an AC input in this way is known as the spin-diode effect [125].

The details of the experimental procedure can be found in Section 3.3. For now, it will be sufficient to know that the resulting rectified DC voltage,  $V_{SD}$ , has a magnetic field dependence (at fixed frequency) that can be fit by a combination of symmetric and antisymmetric Lorentzians centred on the resonance field,  $H_{res}$ , with a linewidth given by  $\Delta H$  (2.28):

$$V_{SD} = V_{sym} \frac{\Delta H^2}{(H - H_{res})^2 + \Delta H^2} + V_{asym} \frac{(H - H_{res})\Delta H}{(H - H_{res})^2 + \Delta H^2} \quad (2.30)$$

where  $V_{sym}$  and  $V_{asym}$  are the magnitude of the symmetric and antisymmetric components of the voltage signal. They have the following dependence on the physical quantities and

experimental parameters:

$$\begin{aligned}
V_{sym} &= \frac{I\Delta R}{2} \frac{\omega}{\gamma_0 \Delta H (2H_{res} + H_1 + H_2)} h_z \sin 2\phi \\
&= \frac{I\Delta R}{2} A_{sym} h_z \sin 2\phi \\
V_{asym} &= \frac{I\Delta R}{2} \frac{H_{res} + H_1}{\Delta H (2H_{res} + H_1 + H_2)} (-h_x \sin \phi + h_y \cos \phi) \sin 2\phi \\
&= \frac{I\Delta R}{2} A_{asym} (-h_x \sin \phi + h_y \cos \phi) \sin 2\phi
\end{aligned} \tag{2.31}$$

where  $I = I(\omega)$ ,  $H_1$  and  $H_2$  are defined in (2.27) and can be substituted for the equivalent quantity from the resonance frequency equation if additional terms (higher order anisotropies etc.) are required, and  $\mathbf{h}_{MW}$  is the effective oscillating field from the SOTs, given by:

$$\mathbf{h}_{MW} e^{i\omega t} = (h_x, h_y, h_z) e^{i\omega t} = \mathbf{H}_{FL} + (1/M_s) \mathbf{H}_{AD} \times \mathbf{M} \tag{2.32}$$

Hence, the contribution of the microwave fields to the LLG equation can be written as  $\partial_t \mathbf{M} = -\gamma_0 \mathbf{M} \times \mathbf{h}_{MW} e^{i\omega t}$ .  $A_{sym}$  and  $A_{asym}$  are angle-independent terms (beyond the slight angular dependence of the resonance field and associated quantities, which may often be neglected in this context) that have been introduced for notational convenience.

(2.31) shows that, by measuring the magnitudes of the symmetric and antisymmetric components of the rectified voltage as a function of  $\phi$ , the strength and nature of the SOTs can be characterised. Below, the most common sources of SOTs and their associated symmetries that dictate which of the three components of  $\mathbf{h}_{MW}$  they contribute to are enumerated. It should be noted that, independent of its physical origin, the fields  $\mathbf{H}_{AD}$  and  $\mathbf{H}_{FL}$  are typically in-plane, so the antisymmetric component of  $V_{SD}$  is associated with the field-like torques, and the symmetric component,  $V_{sym}$ , with the antidamping torque.

### 2.2.4 Rashba and Dresselhaus torques

SOTs can be broadly classified into those originating from the band structure into two categories based on their symmetry properties: Rashba and Dresselhaus. Both torques originate from the intrinsic broken inversion symmetry in the crystal lattice, which results in additional momentum direction-dependent spin- $\mathbf{k}$  coupling terms in the Hamiltonian that split the Fermi-level of the spin-band into majority/minority spin directions (Figure 2.3a). A spin-orbit torque can then be generated via current-driven spin accumulation as in Section 2.2.3. The angular dependence/symmetry of this spin-orbit torque will reflect the underlying symmetry of the spin-splitting term in the resultant Hamiltonian, allowing them to be distinguished via angle-dependent ST-FMR measurements.

Dresselhaus-type Hamiltonians include spin splitting-momentum coupling terms where the majority spin direction is parallel/anti-parallel to the  $\mathbf{k}$  vector direction (Figure 2.3d). For example, in strained GaAs, the spin-orbit coupling term in the Hamiltonian has the functional form  $H_D \propto \sigma_x p_x - \sigma_y p_y$  (up to linear order in  $\mathbf{k}$ ) [25, 26], where  $\sigma_i$  is the usual Pauli matrix for the  $i^{\text{th}}$  direction, and  $p_i$  is the corresponding momentum operator.

Rashba-type spin-orbit coupling results in a momentum-dependent spin-splitting that is perpendicular to the wavevector direction [23] (Figure 2.3c), and in heterostructures is most usually associated with the inversion symmetry breaking at the layer interfaces (though such terms can result from the symmetry of the crystal lattice [23]). For example, for an electron gas at the interface of a heterostructure with surface normal in the  $\hat{z}$  direction, one obtains a term with the form  $H_R \propto (\mathbf{p} \times \boldsymbol{\sigma}) \cdot \hat{z}$ . The precise term one obtains depends on the exact nature of the symmetry lowering effect of the crystal/heterostructure, although all structures that lack inversion symmetry should have some form of  $\mathbf{k}$  dependent spin splitting due to the spin-orbit coupling (there are 21 such point groups which lack inversion symmetry [126], each which give rise to their own particular combination of terms). [68, 127].

The distinct symmetry characteristics of the two torques allow them to be distinguished in FMR measurements as the  $k$ -dependence of their spin-accumulation means the (field-like) Rashba torque contributes to  $h_y$  and the Dresselhaus term to  $h_x$ . In sputtered thin-film heterostructures the Rashba term dominates. Although, it is indistinguishable from the Oersted field, which also adds constructively to  $h_x$ . Both terms are capable of producing field-like [124, 128] and antidamping torques [26].

### 2.2.5 Spin-Hall effect

The spin-Hall effect (SHE) was first theoretically predicted in 1971, by Dyakonov and Perel [129, 130], and observed experimentally by Bakun et al. [131] in 1984. It is the spin analogue to the Hall effect, where a transverse voltage develops due to a longitudinal current in a magnetic field, the three vectors forming a right-handed set. In the spin-Hall effect, a spin current is induced transverse to a longitudinal charge current, with spin polarisation orthogonal to both. The strength of this effect is characterised by the spin-Hall angle,  $\theta_{SH}$ , which acts as the constant of proportionality between the spin current  $\mathbf{J}_s$ , and the charge current density,  $\mathbf{J}_c$ , which are related by the formula:

$$\mathbf{J}_s = \theta_{SH} \boldsymbol{\sigma} \times \mathbf{J}_c \quad (2.33)$$

where  $\boldsymbol{\sigma}$  is the spin polarisations.

The effect has two distinct physical origins: intrinsic, that is, induced by the characteristics of the electronic band transport [132–135], and extrinsic, induced by spin-dependent electron scattering [130]. The latter is analogous to the spin-dependent Mott scattering of a beam of free electrons [12, 129, 130], and is observable in condensed matter systems, even at thermal velocities due to the greatly enhanced spin-orbit interaction compared with that experienced by free electrons [131].

By creating heterostructures with one ferromagnetic layer, and another made out of a material with large spin-orbit coupling, such as the heavy metals Pt, Ta, W etc., spin-current-induced antidamping torques are created that contributes to the z-component of  $\mathbf{h}_{MW}$ . Because the spin-orbit coupling originates from the relativistic transformation of the electric field into a magnetic field in the electron's rest frame, the spin-orbit coupling strength scales with  $Z$ , the atomic number, due to the large velocities of the valence shell electrons in the stronger electric fields of heavier atoms [136].

### 2.3 Synthetic antiferromagnets

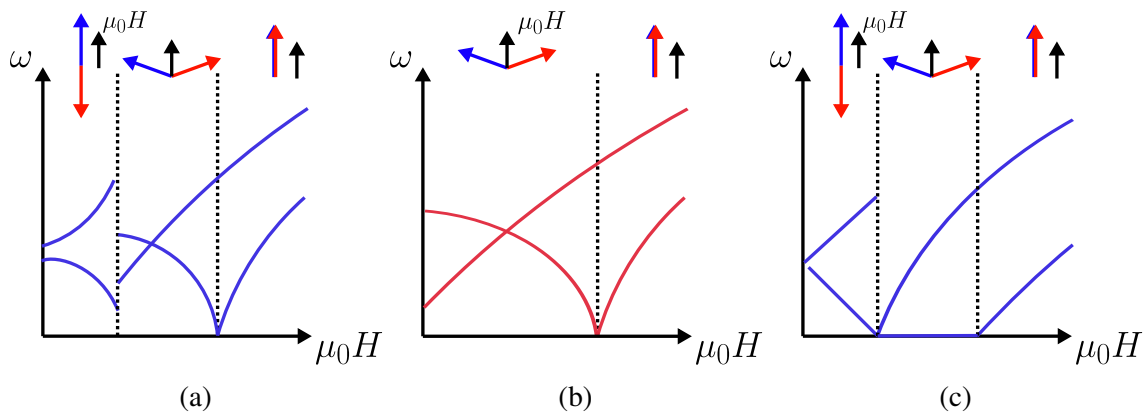


Fig. 2.5 Frequency of the resonance modes versus field for (a) a SAF with an in-plane uniaxial magnetocrystalline anisotropy with external field along an in-plane easy axis, (b) the in-plane hard axis, (c) a uniaxial AF along an in-plane easy axis.

This work will investigate the static and dynamic properties of synthetic antiferromagnets (SAFs) extensively. In the following section, the basics of their behaviour, both static and dynamic — which are themselves strongly coupled — will be described.

SAFs are formed from two ferromagnetic layers coupled via an indirect exchange interaction (the RKKY interaction) that couples them antiferromagnetically. Consequently, their behaviour is somewhere between a true antiferromagnet (AF) and a ferromagnet, inheriting aspects of both. On the one hand, the exchange interaction between the two layers, which

dominates the behaviour of most antiferromagnets, is crucial to understanding their properties. However, unlike in an antiferromagnet, the demagnetisation field of the two sub-lattices, physically separated in space, does not cancel, and indeed can outweigh the exchange field by an order of magnitude or more. Consequently, many aspects of their behaviour resemble that of a thin-film ferromagnet.

Within the macrospin approximation, a SAF can be modelled with two layers,  $A$  (bottom, closest to the substrate) and  $B$  (top), as having the following functional form for its energy:

$$\begin{aligned}
E/\mu_0V = & -\mathbf{H} \cdot (\mathbf{M}_A + \mathbf{M}_B) + \frac{1}{2}\mathbf{M}_A \cdot \mathbf{N}_{AA} \cdot \mathbf{M}_A + \frac{1}{2}\mathbf{M}_B \cdot \mathbf{N}_{BB} \cdot \mathbf{M}_B \\
& + \mathbf{M}_A \cdot \mathbf{N}_{AB} \cdot \mathbf{M}_B + \frac{K_{\parallel}}{\mu_0 M_s^2} ((\mathbf{M}_A \cdot \hat{\mathbf{e}}_{\parallel})^2 + (\mathbf{M}_B \cdot \hat{\mathbf{e}}_{\parallel})^2) + \frac{K_{\perp}^A}{\mu_0 t M_s^2} (\mathbf{M}_A \cdot \mathbf{z})^2 \\
& + \frac{K_{\perp}^B}{\mu_0 t M_s^2} (\mathbf{M}_B \cdot \mathbf{z})^2 - \frac{J}{\mu_0 t} \mathbf{M}_A \cdot \mathbf{M}_B + \frac{J_2}{\mu_0 t} (\mathbf{M}_A \cdot \mathbf{M}_B)^2
\end{aligned} \tag{2.34}$$

where  $N_{ij}$  is the demagnetisation tensor defined by the demagnetisation field in layer  $i$  due to the magnetisation in layer  $j$  [78]:  $\mathbf{H}_i = -N_{ij}\mathbf{M}_j$ ,  $\mathbf{e}_{\parallel}$  and  $K_{\parallel/\perp}$  are the directions and strength constant of the in-plane/out-of-plane magnetocrystalline uniaxial anisotropy field,  $J$  is the exchange constant of the RKKY exchange field, and  $J_2$  the exchange constant of the biquadratic exchange field between the layers. In this expression, it has been assumed that the volume (and thickness,  $t$ ), magnetisation, and in-plane anisotropy of each layer are identical, only allowing the perpendicular anisotropy constant  $K_{\perp}^i$  to vary between the layers. However, it is straightforward to modify (2.34) to allow for differences between the layers. The remaining symbols have their usual definitions (Section 2.1). Note that there are two sources of anisotropy in the SAFs that will be investigated in this work: an out of plane anisotropy with an easy plane in plane, and an in-plane anisotropy with an easy axis in plane. Because of this, the easy axis in plane will be referred to as the easy axis, and in the hard axis *in plane* as the hard axis. In some works on thin-film SAFs, the out of plane

direction is referred to as the hard axis. The exact hard-axis under consideration will be denoted explicitly when there is the potential for ambiguity.

From (2.34) and the corresponding effective field, it is possible to solve Brown's equation for a magnetic field orientated along and perpendicular to the easy axis. Then plugging the values for the orientation of the layer magnetisations into the LLG equation, it is possible to plot the predicted resonance frequencies for a perfectly symmetric SAF (i.e. layers  $A$  and  $B$  are identical) (Figure 2.5a and 2.5b).

*External field along the easy axis:* The static behaviour of a SAF when the external field is applied along the easy axis can be divided into three distinct regions (Figure 2.5a). The first is below what is known as the 'spin-flop' field where the magnetisation remains along the easy axis. Here, the two modes diverge in frequency, as the mode that primarily involves the oscillation of the magnetisation antiparallel to the field is lowered in energy (frequency) and vice versa. Above the spin flop field, the magnetisation undergoes a discontinuous change to a still antiparallel but now perpendicular to the external field/easy axis alignment. From here, the magnetisations cant ever closer to the external field direction as its strength is increased until, at last, at the saturation field, they are aligned with it. The two modes now follow a Kittel-mode-like dependence on the external field, their frequencies offset by the raising/lowering of their energy by the antiferromagnetic coupling.

*External field along the hard axis:* The behaviour when the field is applied along the hard axis is much the same as along the easy axis, except that the magnetisations now begin to cant towards the external field direction from any non-zero field (Figure 2.5b).

For comparison purposes, Figure 2.5c shows the equivalent plot for an antiferromagnet. The frequency dependence of the modes shows a similar dependence to a SAF. The main qualitative difference is that at zero field the two modes are degenerate. This relates to the symmetry properties of a SAF, a feature which will be explored further in Chapter 5.

## 2.4 Auto-oscillations / self-oscillations

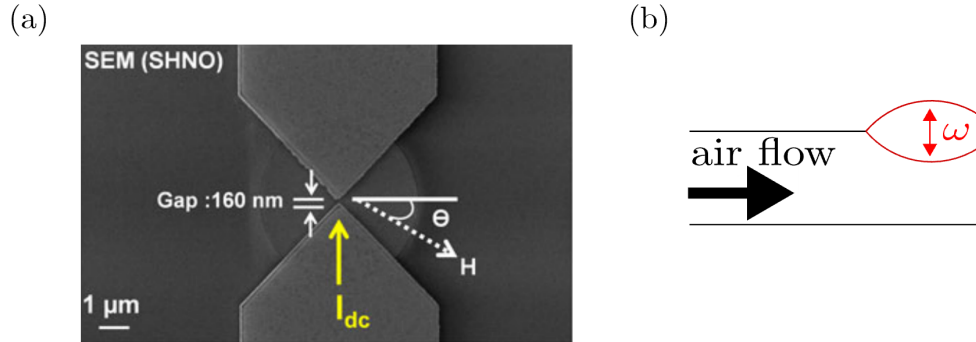


Fig. 2.6 (a) Spin-Hall nano-gap oscillator. Current is concentrated in a small region where the damping native to the system is overcome via a spin-orbit torque due to the adjacent heavy metal layer (usually Pt). Figure reproduced from [37]. (b) Airy's model of the human vocal chords [137]. Air passes through a tube with an open end, one side of which is replaced with a flexible membrane. When subjected to the effect of the constant airflow, the membrane begins to oscillate with a well-defined frequency.

Auto-oscillations, also known as self-oscillations, are a category of oscillatory phenomena whereby a non-periodic (almost always DC) source of power is capable of inducing periodic oscillations in a physical system. Such phenomena can exist because of a feedback mechanism that exists between the oscillations themselves and the external source of power. This feedback mechanism modulates the absorption of power by the system in such a way that, over a single period of oscillation, a non-zero amount of energy is absorbed by the system [138].

A simple, but edifying, physical scenario to consider is why a membrane diaphragm begins to develop periodic oscillations when attached to a tube through which air is passed at a fixed rate (Figure 2.6b). This was first proposed as a simplified model of the human vocal chord by Airy [137] in 1830. Airy developed the following mathematical model for how such a setup could lead to self-sustaining oscillations in the vertical displacement of the membrane,  $q$ :

$$\ddot{q}(t) = -\omega^2 q(t) - \delta q(t - \Delta t) \quad (2.35)$$

The first term,  $-\omega^2 q(t)$  represents the restoring force provided by the passing air, and  $-\delta q(t - \Delta t)$  is another restoring term ( $\delta \ll \omega^2$ ) that depends on the position membrane at some earlier time,  $t - \Delta t$ . Physically this represents the time taken for the airflow to react to the change in the position of the membrane. Taylor expanding (2.35) for small time  $t$ , the following equation of motion is obtained:

$$\ddot{q}(t) - \delta \dot{q}(t) + (\omega^2 + \delta)q(t) = 0 \quad (2.36)$$

which should be immediately recognisable as the equation of motion of a linear oscillator with negative damping. Solving 2.36 for  $q(t)$ , one can see that the oscillations grows exponentially with time. Consequently, auto-oscillations can also be thought of as resulting from an external power source inducing an effective negative damping term in the equation of motion. The corresponding physical picture is simple and appealing: negative damping cancels out the natural sources of damping present in the system, resulting in an effective dissipationless system that will be unstable to the formation of periodic oscillations. In practice, once the oscillations reach a certain amplitude, the linear equation of motion will break down, and non-linear effects must be accounted for. This tends to act as a natural limiting factor to the amplitude of the oscillations. The interested reader may wish to refer to Jenkins 2013 [138] for further examples and a more in-depth explanation of the basic principles.

Antidamping torques (Section 2.2.3) provide a natural source of negative damping. Hence, it might expect that by simply applying a large enough DC current to a HM/FM bilayer, similar to the one used in ST-FMR measurements, that it will be possible to induce self-oscillations in the magnetisation. Such devices are often referred to as *spin-Hall nano-oscillators*[37–39].

Experiments of this kind were attempted in early in the field's history [139–141]. However, it was soon appreciated that as well as increasing the population of the desired mode, the background population of thermal magnon was likewise increased, resulting in an enhanced

contribution to the damping via magnon-magnon interactions that cancelled out the negative damping of the antidamping torque [139, 142, 143]. Consequently, the necessary current densities required to induce self-oscillations in the magnetisation were prohibitively high and lead to the destruction of the device via Joule heating or electromigration. Electromigration tends to set in in metallic contacts at current densities of around  $10^9 - 10^{10}$  A/cm<sup>2</sup> [144]. Current densities required to excite self-oscillations are typically on the order of  $10^8 - 10^9$  A/cm<sup>2</sup> [145]. In order to overcome the magnon-induced non-linear damping and observe auto-oscillations, novel device geometries have been developed that limit the ability of the linear magnon spectrum to interact with the auto-oscillating mode.

The first of these new geometries was the nano-gap geometry (Figure 2.6a), in which a pair of highly conductive Au electrodes is patterned above a HM/FM bilayer with a separation on the order of 100 nm (Figure 2.6a) [146]. These are typically Pt/Py bilayers owing to Pt's large spin-Hall coefficient, and Py's low intrinsic damping and relatively high AMR coefficient; typical AMR coefficients in Py are around five times those found in CoFeB [37]. The current is shunted almost entirely through the Au electrodes until the tip of the triangle where it enters the bilayer with a highly concentrated spatial distribution. The resulting high current density at the tip excites a localised 'bullet' mode, which exists outside of the linear spectrum of modes. Any magnonic modes that are excited by the current distribution quickly propagate away from the central area, keeping their population sufficiently low that their parasitic effect does not impede the self-oscillation of the bullet mode.

This work will explore the potential of inducing self-oscillations in synthetic antiferromagnets using a nanowire geometry. This geometry resembles an FMR bar, where the width of the bar is sufficiently thin such that the energy of the exchange-magnon modes are raised by confinement effects. Consequently, there no longer exists a set of exchange-magnon modes degenerate with the uniform mode [147, 148], which limits their ability to inhibit its

amplitude via effects such as magnon-magnon scattering. These devices benefit from their relative ease of fabrication compared to other geometries.

The technological promise for such devices is that the oscillating magnetisation will have a corresponding oscillating resistance,  $R(\omega)$ , due to coupling between the resistance and magnetisation direction (e.g. AMR). Consequently, when the microwave resistance couples to the DC current, a coherent microwave voltage can be generated. This would be useful for on-chip microwave generation, e.g. for microwave frequency communications. The principal limitation of such devices is that the total volume of magnetic material that oscillates in these localised modes is typically very small, on the order of the gap size in diameter and a few nanometres thick. Consequently, the generated output power is far too small to be of any practical use (less than 1 nW [37, 149, 150]). A great deal of effort has gone into generating geometries in which multiple localised modes are able to coherently phase lock to one another, increasing the total output power and reducing the linewidth substantially [151]. However, at present, there are limitations as to how far this scheme can be pushed, with geometries involving larger and larger numbers of oscillators losing their phase coherence [151]. This is one of the major technological challenges facing the field.

### 2.4.1 Antiferromagnetic auto-oscillators

Ferromagnetic resonance occurs on a timescale of a few to tens of gigahertz for typical ferromagnetic metals. Auto-oscillations observed in these systems have a similar frequency range [146–148]. In order to produce higher frequency outputs, there has been significant interest in generating similar auto-oscillatory modes in antiferromagnets. Antiferromagnets, due to the strength of the antiparallel exchange coupling between adjacent sublattices, have modes whose frequencies extend into the terahertz range [152]. Novel means of generating terahertz radiation, particularly in the highly spatially compact form promised by magnetic auto-oscillators, is an area of device physics attracting increasing attention [153].

Terahertz radiation is non-ionizing, allows for the minimisation of component size compared to microwave radiation employed in mobile communications [154], and allows for safe and effective biomedical imaging [155].

Despite a by-now considerable body of theoretical proposals for antiferromagnet self-oscillators (see [145] and the references therein), experimental realisation of such schemes has not been forthcoming. Nevertheless, there has been some progress with regards to manipulating the order parameter (the Néel vector, the difference in the sublattice magnetisations:  $N = M_A - M_B$ ), with recent works reporting spin-orbit torque induced switching of AFs [52, 156–158]. Consequently, the first experimental realisation of auto-oscillations in AFs may not be so far away.

## 2.5 Superspintronics

It is something of a cliché within the field of super-spintronics to begin any article by stating that ferromagnetism and superconductivity are antagonistic states of matter. But if it is so, it is only because it neatly encapsulates the fact that some 60 years after interactions between superconductors and ferromagnets began to be studied seriously [159], these two states of matter, which from the outset seem determined to destroy one another, should continue to surprise with the rich range of phenomena of physical and technological interest they are able to support. Indeed, one could argue that this antagonism is what allows such a rich range of phenomena to exist. Depending on which way the scales tip between the forces driving ferromagnetic or superconducting order, quite distinct phenomena are likely to manifest. Ferromagnetism is characterised by long-range order in the (parallel) alignment of particle spin inside a material, such that the material acquires an overall non-zero magnetic moment. The alignment of spins in close proximity to one another is promoted by means of a quantum mechanical exchange interaction [59, 160], which lowers the energy of the parallel spin configuration. Superconductivity, by contrast, is a state of matter characterised

by having zero electrical resistance and by the expelling of all external magnetic fields via the Meissner effect [161–163]. Electronic currents are carried by spin anti-aligned (spin-singlet) Cooper pairs, which form from the Fermi-gas when the material passes through its critical temperature,  $T_C$ , and are able to move through a material without dissipation owing to the lack of available states they can scatter into due to the formation of a gap in the density of states [164–166].

The presence of an exchange interaction should inhibit the formation of Cooper pairs by raising the energy of their antiparallel spin configuration. If the exchange interaction were sufficiently strong, then it would no longer be energetically favourable for the Fermi-gas to transition to a superfluid of Cooper pairs and superconductivity would be entirely suppressed. This mechanism of pair-breaking was first suggested by Matthias et. al [159] who, in 1958, attempted to explain the variation in  $T_C$  of lanthanum with rare earth impurities. They found it to vary with the net spin of the impurity via an exchange mechanism between the impurity spins mediated by the conduction electrons (the RKKY interaction). This mechanism of pair breaking is commonly referred to as the exchange mechanism, and the phenomenon is known as the paramagnetic effect. Magnetic fields can also suppress superconductivity due to the interaction of the electronic charge with the vector potential of the magnetic field, raising the kinetic energy of the condensate. This is the so-called electromagnetic mechanism of pair suppression, which was first suggested by Ginzburg in 1956 whilst formulating a theory of ferromagnetic superconductors [167].

Consequently, ferromagnetism has the tendency to suppress superconductivity in a traditional superconductor. For example, the  $T_C$  of a superconductor can be decreased by doping the superconductor with an increasing impurity of paramagnetic ions [168, 169]. The inverse effect is also observed. Superconductivity has been shown to suppress ferromagnetism to produce a ‘cryptoferromagnetic’ state, where an inhomogeneous ferromagnetic state coexists with a superconducting condensate — a phenomenon which has been widely

experimentally observed in a range of systems [170–174], and studied theoretically [49, 50, 175].

If, instead of forming a spin-singlet, the Cooper pairs were instead generated in a parallel spin spin-triplet configuration, then they would be impermeable to the pair-breaking effect of the exchange field. In a ferromagnet in the diffusive transport limit with exchange splitting  $J$  and a diffusion coefficient  $D$ , the amplitude of the spin singlet, and spin-triplet with  $S_z = 0$ , Cooper pair condensate decays exponentially with a length scale given by  $\zeta_J = \sqrt{\hbar D/J}$ . In contrast, spin-triplet Cooper pairs with  $S_z = \pm 1$  decay with the thermal coherence length scale  $\zeta_T = \sqrt{\hbar D/(2\pi k_B T + 2\hbar/\tau_s)}$ , where  $\tau_s$  is the spin-flip scattering rate: i.e. unless an electron's spin is flipped in a scattering event, they behave like spin-singlet Cooper pairs in a normal metal [176].

Aside from the physical interest in such systems, spin-triplets have been extensively explored due to the prospects of utilising their dissipationless and phase-coherent properties to improve the performance of spintronic devices [177, 178]. Spintronics promises a new way of designing computer architectures with significantly improved power consumption, either through the dissipationless nature of spin-currents themselves, or through overthrowing the traditional paradigm of Von-Neuman computer architectures [35, 179]. Whilst spin-currents are, in theory, dissipationless, in practice, their generation is always associated with some kind of charge current and hence suffers from the usual issue of Ohmic dissipation. Consequently, there is great interest in discovering new materials/material systems that are capable of increasing the spin-polarisation of these charge currents to improve their efficiency. In this respect, spin-triplet supercurrents are a natural candidate: dissipationless and phase coherent by design, so long as one is willing to pay the price of maintaining the device below  $T_C$ .

There have also been proposals to utilise spin-polarised quasiparticles states that lie above the valence band in superconductors for spin-transport. These have the advantage of much

longer coherence lengths, up to the micron-scale [180, 181] (by comparison, spin-triplets have a coherence length on the order of the superconducting coherence length, typically 10s to 100s of nanometres). However, they are neither dissipationless nor phase coherent [177].

### 2.5.1 Mechanisms of generating spin-triplet Cooper pairs

There are a few known bulk materials that are able to exhibit a coexistence of traditional spin-singlet superconductivity with ferromagnetism [44–46], but typically most superconductors are unable to support spin-triplets, and many that do are p-wave type superconductors, whose Cooper pairs are sensitive to the pair breaking effect of impurity scattering. Consequently, the main area of interest for generating spin-triplet condensates is at superconductor/ferromagnetic (SC/FM) interfaces, where the presence of an interface naturally breaks the translation symmetry of the system, allowing Cooper pairs to form with unconventional symmetries.

The first indication that the superconducting condensate could extend over significant distances into ferromagnets came from transport studies on thin-films with SC/FM interfaces [171] such as In/Ni and Pb/Ni [172], Sn/Ni [182], Al/Co [173], and Al/Ni [174], and Josephson junctions with a ferromagnetic spacer-layer (SC/FM/SC structures). These transport studies indicated that ferromagnets could support phase coherence lengths significantly larger than expected from the usual superconducting proximity effect, and exhibited proximity-induced conductances in the ferromagnetic layers that could only be explained by long-range proximity effects. In Josephson junctions, the amplitude of the spin-triplet condensate both decreases and oscillates in the ferromagnetic layer [183, 184], leading to oscillations in the critical superconducting temperature [185] and critical Josephson current [186, 187]. It was found that even the half metal  $\text{CrO}_2$ , which has entirely spin-polarised conduction electrons, could support a supercurrent when placed between superconducting NbTiN electrodes [47, 188]. These results were attributed to an inhomogeneous magnetic texture at the SC/FM interface [189, 190], which could allow for the generation of odd spin-triplet Cooper pairs.

The phenomenology of this mechanism is as follows. In a device with a SC/FM interface, the presence of a homogeneous exchange field  $h_{ex}$  in the ferromagnet causes electrons entering the ferromagnetic material from the superconducting side to acquire a spin-dependent phase as they penetrate into, and then are reflected from, the interface due to the energy difference between up and down spins inside the ferromagnet. This results in spin-zero Cooper pairs being converted to spin-triplets with  $S_z = 0$  [47, 48] (where the quantisation axis is taken to be aligned with  $h_{ex}$ , and is still a conserved quantity as the system maintains rotational symmetry around this preferred axis). Mathematically this transformation can be represented as follows:  $|0, 0\rangle \rightarrow |\uparrow\rangle |\downarrow\rangle e^{i\theta} - |\downarrow\rangle |\uparrow\rangle e^{-i\theta} = \cos(\theta) |0, 0\rangle + i \sin \theta |1, 0\rangle$  [176], where  $\theta$  is the relative phase difference between the up and down spins. In order to convert these Cooper pairs into spin-triplets with  $S_z = \pm 1$ , it is necessary to realise some field which leaves the system without a preferred axis so that  $S_z$  is no longer conserved and the  $|1, 0\rangle$  component of the Cooper pair wavefunction can be rotated to a  $|1, 1\rangle$  component. This is the role of the inhomogeneous magnetisation (and the associated inhomogeneous exchange field).

Superconductivity-induced non-uniform magnetic textures were first considered by Suhl and Anderson [49], who studied theoretically a dispersion of ion-core spins embedded inside a superconductor coupled by a long-ranged RKKY interaction. In SC/FM heterojunctions (where the ferromagnetic layer is metallic, insulating ferromagnets do not suppress the superconducting condensate at the interface, and consequently the phenomenology is different [191]) the phenomenon of cryptoferromagnetic textures is most straightforwardly illustrated by the theory of Buzdin and Bulaevskii [50], who consider, in their words, “a patently greatly simplified model,” which nevertheless has a clear phenomenology that highlights the important tension between the energy of the superconducting condensate and the magnetic texture.

When a spin-singlet condensate is incident on a ferromagnet, the condensate will be suppressed near the interface via the pair-breaking mechanism considered above. This results in a raising of the condensate energy as the electrons are no longer able to form energetically favourable Cooper pairs. However, if the magnetisation can be broken up into a non-uniform texture that varies on a length scale comparable with the superconducting coherence length (the average size of Cooper pairs),  $\xi$ , then the Cooper pairs will feel the ‘average’ exchange field over this length scale, which may be greatly reduced. If the Curie temperature,  $\Theta$ , is greater than the critical temperature (i.e. the exchange energy is much larger than the energy gain of forming Cooper pairs versus a Fermi gas of unpaired electrons), then the magnetisation will be encouraged to form a domain structure, so long as the energy of the domain walls is lower than the energy decrease in the condensate (i.e. the Curie temperature should not be so large as to suppress the effect). This is analogous to the formation of domain walls at remanence in traditional ferromagnetic structures in order to reduce the stray field energy. This effect is therefore expected to be favoured in devices with weak exchange fields, long superconducting coherence lengths, and high density of states in the superconductor. The transition from the homogeneous state to the domain state, consisting of domains which are uniform in the thickness of the thin film, occurs as a first-order phase transition below  $T_C$  if the following criteria can be satisfied:

$$\frac{\Theta h d}{T_C^2 l} \left( \frac{d}{\xi} \right)^{1/2} \leq 1 \quad (2.37)$$

where  $\Theta$  is the Curie temperature of the ferromagnet,  $d$  is the ferromagnetic film thickness, and  $l$  is the electron mean free path, which is assumed to be  $\ll \xi$ .

In practice, this criteria is far too prohibitive to fit with experimental observations, where cryptoferromagnetic states have been observed in thick ( $d \gg 1$  nm) ferromagnets with  $\Theta > 1000$  K that are far from satisfying (2.37) [192, 193]. Consequently, some energy has been put into generating more complex theories which should allow for more gentle

cryptoferromagnetic states with correspondingly softer energy requirements [175]. It should be noted, however, that even these theories generally fail to produce energy conditions close to the right order of magnitude to explain the formation of these states. However, the experimental evidence of their existence is overwhelming (backed up by fits to theoretical predictions of their behaviour predicated on the assumption that such states *do* exist) and there are a number of physically reasonable arguments as to why the energy requirements should not be so strict in practice. Despite its incongruence with experimental reality, (2.37) has the advantage of showing the general dependencies one might expect such a state to exhibit on relevant physical quantities.

It is not straightforward to predict which devices will form non-uniform magnetic textures, leading to a large number of seemingly conflicting results early on in the field's development [194]. It is possible to overcome this difficulty by engineering materials with complex exchange fields [195]. However, this severely limits the range of usable materials. Recently, there has been a great deal of attention paid to devices with homogeneous magnetisations. These devices require an additional field other than the homogeneous exchange field to generate spin-triplet Cooper pairs but allow for greater control and predictability in device design. One possible mechanism is a device with a strong spin-orbit coupling that has a component orthogonal to  $h_{ex}$ . In such a system, the  $S_z$  component of the Cooper pair is no longer conserved, and can then be rotated into a spin-state with a component of the spin of the in the  $S_z$  direction. The overall conversion efficiency scales with the strength of both the exchange field and the spin-orbit coupling [28, 196, 197].

An analogous mechanism exists if the system contains two homogeneous magnetisations (and hence exchange fields) aligned at a non-zero angle to one another. The phenomenology is similar to the previous case of an exchange field in the presence of non-aligned spin-orbit coupling. The first exchange field rotates some of the spin-singlet Cooper pairs to spin-triplet  $S_z = 0$  Cooper pairs. The second, non-collinear magnetisation then rotates the spin of the

Cooper pairs so they have a component in the  $S_z$  direction [198, 199], so long as the two ferromagnets are separated by a distance less than the distance over which Cooper pairs can propagate without scattering. This was first demonstrated in Josephson junctions with a SC/FM/NM/SAF/NM/FM'/SC structure, where NM is a normal metal layer, FM and FM' are non-collinear ferromagnetic layers, and SAF is a synthetic antiferromagnet [200].

### **2.5.2 Ferromagnetic resonance experiments on superconducting/ferromagnet heterostructure**

The earliest experimental evidence for spin-triplet Cooper pairs came from transport measurements in structures with a SC/FM interface, and from measurements of Josephson junctions with ferromagnetic spacer layers. Increasingly, ferromagnetic resonance studies are providing important insights into spin-transport across ferromagnetic/superconducting interfaces [51, 201, 202], which is strongly affected by the presence of spin-triplets.

Spin-pumping, the generation of a spin-current by an oscillating ferromagnet (see Section 2.2.2), shows up in FMR experiments as an enhancement of the Gilbert damping [113, 114, 203]. By measuring the change in the linewidth of ferromagnetic resonance as the temperature passes through and below the superconducting transition, the physical changes that occur at the SC/FM interface as the superconducting gap opens lead to a modification in the spin-transport properties of the interface, resulting in considerable changes in the damping with temperature. Consequently, by measuring the Gilbert damping as a function of temperature, it is possible to probe for the existence of spin-triplet Cooper pairs in a superconductor.

The physical basis of the measurement is as follows. The electrons have energies well below the superconducting gap (1.5 meV at  $T = 0$  K [204] in Nb) and hence cannot pass into the superconductor as quasiparticles. In the absence of spin-triplets, when the superconductor

is cooled through its transition temperature, the only way for electrons to pass from the ferromagnetic metal to the superconductor is through Andreev reflection.

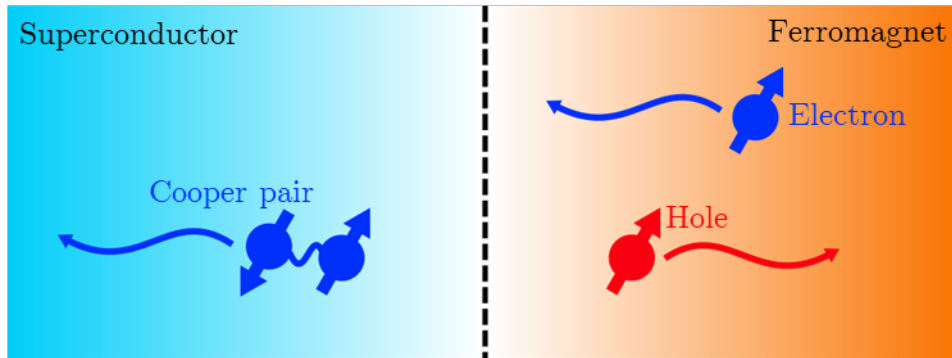


Fig. 2.7 Andreev reflection allows for charge transfer across a superconductor / metallic ferromagnet interface despite the presence of a gap in the superconducting density of states through which particle transfer is forbidden. A free electron is transferred across the interface along with the retroreflection of a hole in the opposite spin band. The net result is a charge transfer of  $2e$ , with no associated spin-flux, carried into the superconductor by a Cooper pair.

In Andreev reflection (Figure 2.7), an incident electron from the metallic side, with energy  $\mu + \epsilon$ , where  $\mu$  is the chemical potential of the superconducting condensate, and spin  $|\uparrow\rangle$ , must pair with an electron of energy  $\mu - \epsilon$  and spin  $|\downarrow\rangle$  to form a spin-singlet Cooper pair with energy  $2\mu$  in order to pass into the superconducting side of the junction. The loss of this additional electron is accompanied by the coherent retro-reflection of the hole it leaves behind, carrying with it spin  $|\uparrow\rangle$  [205–207]. Consequently, there is no net loss of spin from the ferromagnet and spin-pumping mediated damping is suppressed below  $T_C$ .

If, however, a spin-triplet condensate is present in the superconductor, a pathway is opened for the angular momentum of the spin-pumping generated spin-current to be transferred into a current of spin-triplet Cooper pairs, restoring, and indeed enhancing if paired with an efficient spin sink such as Pt or W, the contribution to the Gilbert damping from spin-pumping [51].

In principle, it should be possible to identify the presence of spin-triplet Cooper pairs from a measurement of  $\alpha$  against  $T$ , observing an increase in  $\alpha$  below  $T_C$  if they are present,

and a decreasing  $\alpha$  if they are not. Whilst this may be the case for certain experimental architectures, in practice the nature of the damping dependence on temperature can vary considerably, and has attracted a range of physical explanations for each case, illustrating the complex nature of the physics involved at SC/FM interfaces.

The first spin-pumping experiment on SC/FM devices was performed in 2008 by Bell et al. [204, 208], who measured the temperature-dependent linewidth of Nb/Py samples and found a decrease in the linewidth below the transition temperature. They interpreted this result as being due to a reduction in the interface contribution to the damping, owing to the inability of spin-currents produced by the oscillating magnetisations to penetrate into the superconductor.

In general, this behaviour is typical of interfaces where s-wave superconductors are in contact with ferromagnetic metals. If, instead, the ferromagnetic metal is replaced with an insulating layer, the superconducting gap can survive right up until the SC/FM interface because electrons cannot penetrate through the interface and hence are not subject to the pair-breaking effect. This causes a significant difference in the observed behaviour. Inoue et al. , who, in 2017, studied this case theoretically, [201] found an initial increase in the Gilbert damping below  $T_C$  that then tails off into a slight decrease by  $T = 0$  K.

The picture considered by Inoue et al. was of a homogeneous ferromagnet and superconductor. However, recent experimental [209], and subsequent theoretical work [210], point towards inhomogeneities at the interface playing an important role. Yao et al. [209] observed an enhancement in Gilbert damping below  $T_C$  in NbN/GdN/NbN thin-films that cannot be adequately described by the homogeneous theory of Inoue et al. [201]. Instead, Silaev [210] has suggested that localised inhomogeneity-induced quasi-particle states lead to an enhancement of the density of states below the superconducting gap. These states are known as Andreev bound states [211–213]. They form at inhomogeneities that suppress the superconducting order parameter at the interfacial normal layer due to the inverse proximity

effect. They are able to absorb magnons incident from the ferromagnet and contribute to an enhanced Gilbert damping below  $T_C$ .

These are only a small selection of the various physical effects that have been proposed to have a significant effect on spin-current transport at SC/FM interfaces. Whilst many of these mechanisms are active only for insulators, and although this work will exclusively consider ferrometallic metals, they serve to illustrate a general point of caution about interpreting spin-pumping measurements. The physics of ferromagnetic-superconducting can be highly complex, and great care needs to be taken to uniquely identify the correct mechanistic explanation. In particular, aside from the range of spin-triplet mechanisms, the Meissner screening that emerges in the superconductor below  $T_C$  can have a substantial impact on the measured ferromagnetic resonance properties. Jeon et al. have observed changes in the ferromagnetic linewidth below  $T_C$  which they attribute, not to spin-triplets or some other exotic mechanism, but rather to the influence of the Meissner screening on ferromagnetic oscillations near the SC/FM interface [214]. The difficulties in disentangling the contributions of the Meissner screening from spin-triplet-related mechanisms are perhaps most neatly encapsulated by the ongoing debate about the origin of a substantial shift in the resonance frequency/field below  $T_C$  in SC/FM/SC stack structures [178, 215–217]. Shifts of up to  $\sim 0.3$  T in the resonance field have been reported experimentally [216], and have been attributed to both Meissner screening and spin-triplet-related mechanisms.

In short, SC/FM interfaces are complex and display a wide range of physical effects, many of which can be probed by spin-pumping FMR experiments. However, great care must be taken in analysing the results of such an experiment to uniquely identify which of the plethora of possible physical effects are operative, both above and below the transition temperature.

### 2.5.3 Vortices in type-II superconductors

Superconductors can be divided into two categories: types I and II. The principal difference is in their behaviour in an externally applied magnetic field. Type-I superconductors expel all external magnetic fields beyond their penetration depth,  $\lambda$ , up to some critical field,  $H_C$ , where the magnetic superconducting state is destroyed, the field decaying exponentially with depth into the sample. The resulting magnetisation,  $M$  (defined as  $M = B/\mu_0 - H$  averaged over the whole sample), of the sample as a function of applied field,  $H$ , is shown in Figure 2.8a.

Type-II superconductors, which form a major component of the devices in Section 4, have a more complex magnetic field dependence. For low fields, below a lower critical field  $H_{C1}$ , they behave much the same as type-I superconductors, expelling all external magnetic fields except for those in a thin region around their surface of depth  $\lambda$ . This regime is sometimes referred to as the ‘Meissner state’ [218]. Above this field, as first observed by Shubnikov et al. [219] in 1937, a new phase emerges. Type-II superconductors are characterised by having a penetration depth larger than their coherence length,  $\xi$ : the distance over which the superconducting condensate restores itself when perturbed by imperfections and defects. This implies that the interface between a superconducting and normal phase regions should have a negative surface energy [220, 221], and hence results in the spontaneous formation of normal phase regions inside the superconductor at sufficiently large magnetic fields (above  $H_{C1}$ ) due to the energy decrease of the increased magnetic-flux penetration out-weighting the energy gain from the suppression of the superconducting order [222].

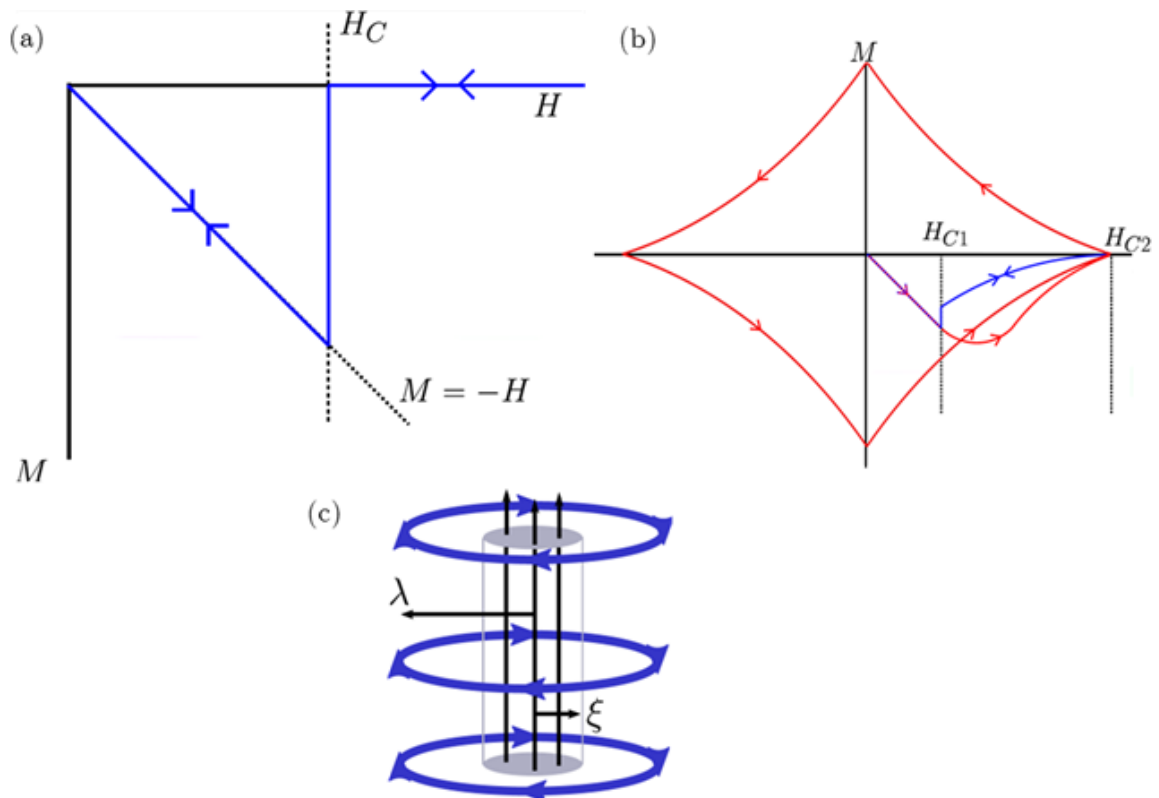


Fig. 2.8 (a) Magnetisation of a type-I superconductor versus  $H$ . (b) Magnetisation of a type-II superconductor versus  $H$ . Blue curve represents a SC with no pinning and its reversible magnetisation curve. Defects can cause pinning of the vortices that result in a hysteresis in the magnetisation (red-curve). (c) Vortex core structure. Flux penetrates through a normal region of radius  $\xi$ . Supercurrents, rotating up to radius  $\lambda$ , shield the rest of the superconductor from this flux.

The nature of this normal phase is non-trivial. Upon an application of a field larger than  $H_{C1}$ , vortices, consisting of a normal core with radius  $\xi$  surrounded by a superconducting vortex current that screens the penetrating magnetic field (Figure 2.8c) over the penetration depth, begin to nucleate within the sample. Figure 2.8b shows the magnetisation curve for a defect-free type-II superconductor. At  $H_{C1}$  the first core is nucleated, and as the cores can only interact over a distance on the order of  $\lambda$ , they nucleate rapidly until their density is such that the separation becomes similar to the penetration depth. From here on, the nucleation is much slower, gradually filling the superconductor with cores until their separation is less

than the coherence length. At this point, the normal cores overlap, and the superconducting order is destroyed (the field strength at which this occurs is the upper critical field:  $H_{C2}$ ).

In the case of defect-free type-II superconductors, the magnetisation curve is reversible. However, in the presence of defects, the vortices can become pinned to the defect sites. Consequently, when the magnetic field is reduced, the vortices and their associated magnetic flux become trapped at their defect site, resulting in a hysteresis in the sample magnetisation and a positive magnetic moment on the return stroke (Figure 2.8b). The vortex phase is often known as the Shubnikov phase [223].

## 2.6 Group theory

### 2.6.1 Motivating the use of groups in physical problems

A group is a mathematical structure that consists of a collection of elements, combined with an operator,  $\circ$ , that takes two elements as its input and produces a third element as its output. In order for this combination of a set of elements and an operator to be considered a group, they must obey the following criteria:

1. The set of elements must be closed under  $\circ$ . That is, if  $R$  and  $M$  are in the group, and  $R \circ M = G$ , then  $G$  must also be in the group for all combinations of  $R$ ,  $M$ , and  $G$ .
2. Associativity under  $\circ$ , i.e.  $R \circ (M \circ G) = (R \circ M) \circ G$ .
3. The identity element,  $E$ , is a member of the group.
4. For every element in the group,  $R$ , its inverse,  $R^{-1}$ , is also in the group, where  $R \circ R^{-1} = R^{-1} \circ R = E$ .

The definition of a group does nothing to dispel the notion that they are a rather abstract mathematical construction, disconnected from the typical physical problems encountered by

the working physicist during their day-to-day work. However, the potential utility of groups becomes obvious when considering what it is that a physicist is doing they write down an equation to describe the physical system they are studying. *Physicists use mathematical representations of real-world objects to understand and predict their behaviour. Many of these mathematical representations form a group. Group theory studies these structures. It should be no surprise therefore that it can be used to determine a great deal about the behaviour of these representations and the objects they represent.*

If the mathematical objects under study do form a group, then group theory is typically used to study these objects largely for two purposes: to simplify complex calculations and to offer insight into the behaviour of the objects under study.

Despite their frequency application across a range of physical phenomena, group theory has not previously been applied to the solutions of the LLG equation before. Chapter 5 will explore applying group theory to the LLG equation, demonstrating how they can be used to simply calculations and aid understanding of physical effects, as well as provide an alternative view on some recently reported effects relating to the symmetry of coupled magnetic oscillators.

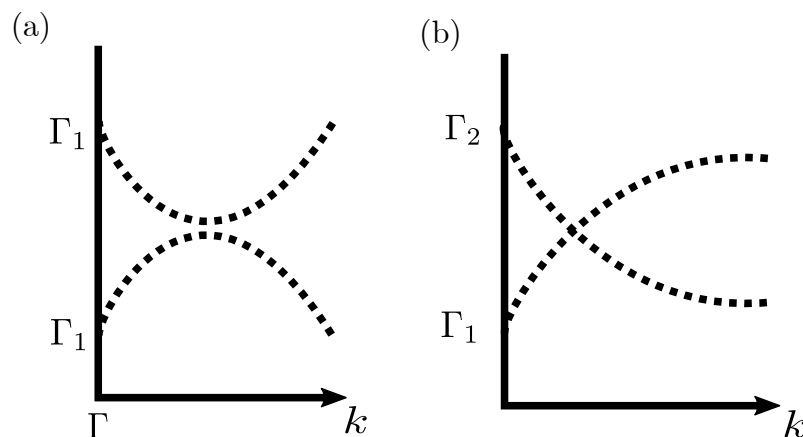


Fig. 2.9 (a) Two modes who transform according to the same irreducible representation approach one another and form an anticrossing. (b) Two modes with differing irreducible representations are allowed to cross without interacting.

As a simple illustration of the practical utility of using groups, Figure 2.9 shows two diagrams of two band structures. Band structures are of course, a graphical representation of the eigenvalues of the eigenmodes of the Hamiltonian/eigenvalue equation of a particular physical system. As it will be demonstrated in the next Section, collections of eigenvectors can be studied by examining their behaviour under the application of an important group: the collection of symmetry operations in a system. This allows the analysis of the behaviour of the modes, and their associated bands structures, from the perspective of symmetry.

Figure 2.9(a) shows two modes, both labeled with the irreducible representations  $\Gamma_1$ , that repel one another to form an anticrossing; Figure 2.9(b) shows two modes, labeled  $\Gamma_1$  and  $\Gamma_2$ , that are allowed to cross. The difference in behaviour is due to the difference in the irreducible representations of each mode, a concept from Group theory that will be explained in greater depth in the next section, which describes ‘how’ a mode transforms under the symmetry operations of a physical system. Looking to a real-world example, similar crossings/anticrossings can be seen in Figure 2.10 that shows the band structure of Copper, where each band is likewise labeled by its irreducible representation using similar notation. The difference in behaviour of the two sets of modes comes down exclusively to the difference/similarity in their irreducible representations. From knowledge of their irreducible representation alone, one is able to infer that the modes in Figure A will repel one another to form an anticrossing, and in Figure B they will not interact and cross. No knowledge of the underlying equations is required, and the principle is equally as valid in the simple example in Figure 2.9, as it is in the complex band structure in Figure 2.10.

Groups can also be used to understand mode degeneracy. Observe the modes close to the gamma point in Figure 2.10. The  $\Gamma_{25}$  modes come together at the gamma point and then split apart as they move away from it inside the Brillouin zone. The mode  $\Gamma_{12}$  splits apart along to X, but remain degenerate along to L, only losing its degeneracy along the path from L to W. The difference in behaviour is because of the difference in the symmetry of the Brillouin

zone at the X point versus L and W. The previous examples illustrate two important uses of

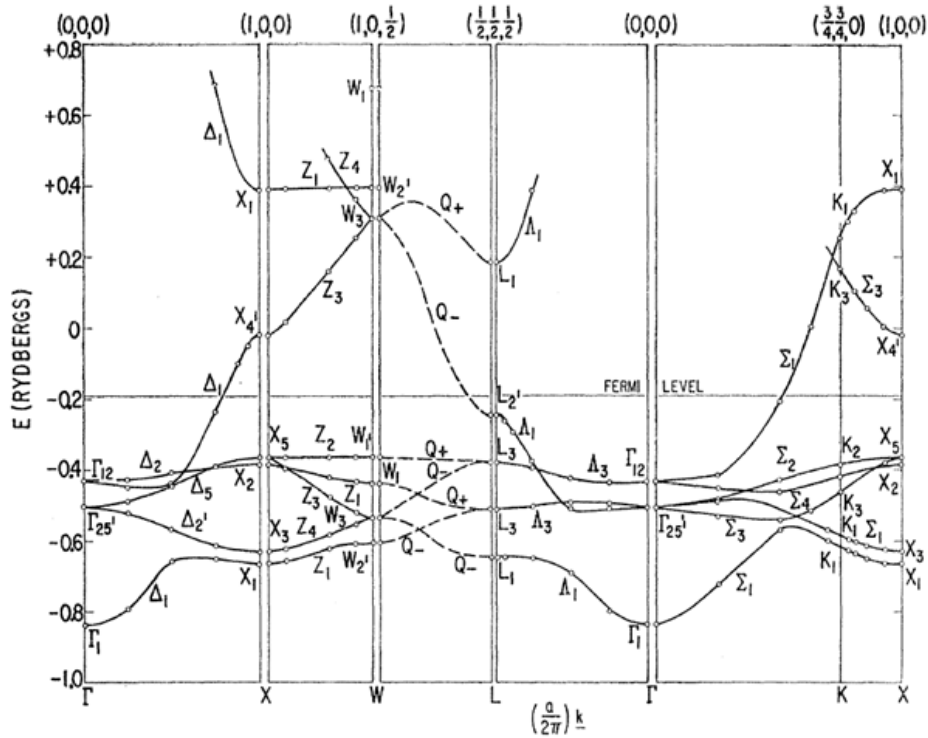


Fig. 2.10 The electronic band structure of copper. Reproduced from [224].

groups that will be employed in Chapter 5: analysing degeneracy, and analysing anticrossings. Groups arise in the study of magnetic oscillations because the magnetic oscillators have symmetry, and their modes are described by the eigenvectors of an eigenvalue equations (with some minor modifications that will be discussed in Chapter 5 from the case typically encountered in physics). In order to perform a similar analysis of these magnetic modes as was done for the electronic band structure modes above, it is necessary to first understand some of the underlying mathematics that underpins group theory. An introduction to the mathematics behind group theory is presented in the next section.

## 2.6.2 Introduction to the mathematics of groups

### Fundamentals and axioms

Group theory is a powerful mathematical tool that is widely applied across the physical sciences. The following section serves as an introduction to the basic principles and intends to illustrate how group theory can be used to obtain insights into the behaviour of physical systems [122].

To the physicist, group theory is associated with the study of the symmetries of physical systems, where the physical system of interest can typically be modeled by a linear eigenvalue equation with the usual form:

$$A\mathbf{x}_i = \lambda_i\mathbf{x}_i \quad (2.38)$$

where  $A$  is some linear operator,  $\lambda_i$  is a scalar, and  $\mathbf{x}_i$  is a vector that represents the dynamics of the system under study. It is important that  $A$  is Hermitian so that the collection of eigenvectors inherit the following properties:

1. They form a complete basis.
2. They are orthogonal under the “standard” inner product.

A symmetry transformation is straightforwardly defined as any physical transformation that leaves the system under consideration unchanged (accounting for any indistinguishability that may be present). If the symmetry transformation for the system modeled by (2.38) is represented by the matrix  $R$ , then, as the system is unchanged, it must be that  $R$  commutes with  $A$ :  $RAR^{-1} = A \implies [A, R] = 0$ . The criteria that  $R$  commutes with  $A$  is both a necessary and sufficient condition for  $R$  to be a symmetry operation.

### The representation formed by the eigenvectors

It is first necessary to establish that a collection of symmetry operations of a physical system form a group. In order to do so, they must obey all the four axioms described in Section 2.6.

Axiom 1 follows from the definition of a symmetry element. If successive symmetry operations,  $A$  and  $B$ , are applied one after the other, the combined operation,  $C = AB$ , must also be a symmetry operation, and hence satisfy axiom 1. Likewise leaving the system unchanged must be a symmetry operation, so the identity is in the collection, satisfying axiom 3. It also follows from the commutation criteria established above that if  $R$  is a symmetry element, then so must  $R^{-1}$ , satisfying axiom 4.

Perhaps the simplest way to see that a collection of symmetry elements obeys the final axiom is to consider the behaviour of the standard matrices that are commonly used to represent symmetry operations in physical problems. For instance, a rotation about an angle  $\phi$  in 2-dimensions is commonly represented by the matrix:

$$\begin{bmatrix} \cos \phi & -\sin \phi \\ \sin \phi & \cos \phi \end{bmatrix} \quad (2.39)$$

Other standard matrix representations of common symmetry operations are well known. The standard matrix representations (e.g. (2.39)) are said to ‘faithfully represent’ (the notion of a matrix ‘representing’ a symmetry operation will become important later) these symmetry operations, as it is very familiar that applying one symmetry operation after the other is equivalent to matrix multiplying their two matrix forms to get the combined element’s matrix representation. That is if  $C = AB$ , then its matrix representations obey,  $R(C) = R(A) \circ R(B)$ , where  $R(x)$  is the matrix representation of some symmetry operation  $x$ , and  $\circ$  is the standard matrix multiplication operation.

Because the symmetry operations are faithfully represented by the matrices, it is possible to consider them in lieu of the symmetry elements themselves. Their repeated application must be associative because of the associativity of matrix multiplication, and hence axiom 2 is satisfied. Consequently, a collection of symmetry elements of a physical system forms a group.

Having established that the collection of symmetry elements forms a group, one must now consider how these elements interact with the eigenvectors. By definition, a symmetry operation,  $R$ , leaves the system unchanged. Hence, for an eigenvalue problem:

$$A\mathbf{x}_i = \lambda\mathbf{x}_i \quad (2.40)$$

then because  $R^{-1}AR = A$ :

$$RR^{-1}AR\mathbf{x}_i = AR\mathbf{x}_i = R\lambda\mathbf{x}_i \quad (2.41)$$

Consequently,  $R\mathbf{x}_i$  is an eigenvector of the same equation with a *degenerate eigenvalue*. This is the first step towards using group theory to analyse degeneracy, which will be important in Chapter 5.

If the eigenvector has a unique eigenvalue, then every symmetry operation must transform it back into itself, i.e.  $R\mathbf{x}_i = \mathbf{x}_i$  (acting under the assumption that all symmetry elements are norm-conserving). However, if there are repeated eigenvalues, then a symmetry operation may transform the eigenvectors into a linear combination of one another. For example, if two solutions,  $\mathbf{u}$  and  $\mathbf{v}$ , have degenerate eigenvalue  $\lambda$ , then presume the symmetry operations,  $R$  and  $M$ , have the effect:

$$\begin{aligned} R\mathbf{u} &= a\mathbf{u} + b\mathbf{v}, & R\mathbf{v} &= c\mathbf{u} + d\mathbf{v} \\ M\mathbf{u} &= e\mathbf{u} + f\mathbf{v}, & M\mathbf{v} &= g\mathbf{u} + h\mathbf{v} \end{aligned} \quad (2.42)$$

Using the coefficients  $a, b, \dots$  etc. it is possible to form what is known as a representation of the operations  $R$  or  $M$  by equating  $R$  and  $M$  with the matrices:

$$\begin{aligned} R &\rightarrow \begin{pmatrix} a & b \\ c & d \end{pmatrix} \\ M &\rightarrow \begin{pmatrix} e & f \\ g & h \end{pmatrix} \end{aligned} \tag{2.43}$$

These coefficients can be easily extracted by taking the inner product with the left-hand side of the equations in (2.42), e.g.  $v^\dagger R u = b$ , using the orthogonality and completeness of the set of eigenvectors demanded from the eigenvalue equation.

What does it mean for this set of matrices to form a ‘representation’ of the group? It means for each operation there is exactly one matrix associated with it (although the same matrix may represent multiple elements), and the matrices are chosen such that for any three elements  $A, B$  and  $C$  from the group that obey  $AB = C$ , then  $R(A)R(B) = R(C)$  under matrix multiplication, like in the example above. One can confirm that a set of matrices constructed like this forms a representation of the group.

This matrix representation:

1. Need not be the same as the ‘standard’ matrix representation of the symmetry operation.
2. Is not required to ‘faithfully’ represent all the symmetry operations in the group. That is, two or more symmetry operations may end up with the same matrix representing them.

The representations of the symmetry operations engendered by the eigenvectors of an eigenvector equation are one of the most important objects in using groups to study eigenvector equations. By carefully analysing the representations the eigenvectors generate,

$$\begin{bmatrix} \overline{a} & \overline{b} & \overline{0} \\ \overline{c} & \overline{d} & \overline{0} \\ \overline{0} & \overline{0} & \overline{x} \end{bmatrix} \begin{bmatrix} \overline{e} & \overline{f} & \overline{0} \\ \overline{g} & \overline{h} & \overline{0} \\ \overline{0} & \overline{0} & \overline{y} \end{bmatrix} = \begin{bmatrix} \overline{ae+bg} & \overline{af+bh} & \overline{0} \\ \overline{ce+dg} & \overline{cf+dh} & \overline{0} \\ \overline{0} & \overline{0} & \overline{xy} \end{bmatrix}$$

Fig. 2.11 The product of two matrices in block diagonal form is also in block diagonal form, where the sub-matrices along the main diagonal are effectively multiplied independently. If the constituent elements of the combined block diagonal matrices are representations of the group, then so too is the combined matrix. If all the matrices in the representation (via a suitable similarity transformation if necessary) can be written in this form, then the representation is reducible.

it is possible to infer their degeneracies, operator matrix elements in quantum mechanics, and how they interact with one another under perturbations.

### Reducible and irreducible representations:

Two ways of representing the symmetry operations of a physical system have already been presented: the ‘standard’ matrix representations most physicists are familiar with, and the representation(s) generated by degenerate sets of eigenvectors. These are far from the only matrix representations one can construct for a group. The most straightforward additional representation to construct is to have each element represented by the scalar 1. That is, every symmetry element is mapped to the number one:

$$R \rightarrow 1 \tag{2.44}$$

Clearly, this representation is not faithful. One should note that this representation is so general that it forms a representation of any group and consequently has its own name, the “trivial representation.” Indeed, from this it is possible to immediately produce as many representations as desired by constructing representations out of higher and higher-order identity matrices, creating an infinite number of possible, seemingly trivial, representations of the symmetry group.

To tame this ‘zoo’ of representations, it is necessary to partition them into two categories, those that are in some sense ‘unique’ (which will be called irreducible) and those that are not (that will be called reducible). The identity matrix-based representations are simply the representation formed by each element being mapped onto the number 1 repeated along the matrix diagonal. Likewise, if there is, for example, a 1-dimensional representation and a 2-dimensional one, it is always possible to form a new 3-dimensional representation by creating a matrix in block diagonal form with the aforementioned representations along the main diagonal. Matrix multiplying these new matrices in the 3-dimensional representation is equivalent to multiplying the 1-dimensional and 2-dimensional matrices independently (Figure 2.11). Consequently, a representation formed in this way contains no new information that is not already present within its constituent parts, and so is not considered ‘unique.’ If every matrix in the representation is in block diagonal form as above, then one can say that it is ‘reducible.’

It may not be immediately obvious whether a representation is reducible or not. As well as stacking representations on top of one another in block diagonal form, one can always generate a new representation from an old one by means of a similarity transformation,  $R \rightarrow XRX^{-1}$  for every  $R$  in the group (the new set of matrices can be verified to satisfy the 4 axioms and structure-preserving requirements). This new representation is merely the old one expressed in a new basis and does not qualify as ‘unique’ either. Like the block diagonal case above, two representations that are connected by such a similarity transformation are also considered to be identical. These two tests for uniqueness can be combined into one: *if a representation can be transformed by means of a similarity transformation into block diagonal form, then it is also considered a reducible representation.* Representations for which there exists no similarity transform that can convert it into block diagonal form are then called ‘irreducible,’ and there are restrictions on the number and dimensionality of these representations for every group.

The irreducible representations that remain after all the reducible representations have been thrown out form a set of ‘building blocks’ for the others, that is *every reducible representation can be constructed out of the finite number of irreducible ones arranged in block diagonal form*. Irreducible representations therefore form the most fundamental representations of the group and the most important objects of study within group theory.

When constructing the representations of the group formed by the eigenvectors, the resulting representation may or may not be irreducible depending on the choice of eigenvectors. By decomposing the reducible representations into their irreducible components (if necessary) it is possible to begin to use groups to study the physical problem in earnest.

### **Using the representation engendered by the eigenvectors to analyse physical problems**

The representation obtained from the procedure described in (2.42)-(2.43) may be reducible. If it is reducible, some similarity transformation can always be found that casts it into a block diagonal form of irreducible representations, and by applying this same transformation to the eigenvectors, a new set of eigenvectors can be obtained formed of linear combinations of the old ones. By grouping these new eigenvectors together into the sets that transform into one another under the symmetry operations, sets of eigenvectors that all transform as the same irreducible representation of the group can be generated.

The sets of eigenvectors obtained are important because eigenvectors that transform as part of the same irreducible representation are symmetry bound to be degenerate. This is because modes that are part of the same irreducible representation can be transformed, at least in part, into one another by at least one symmetry operation  $R$ . Hence, from (2.41) it is known that this means they must have the same eigenvector/be degenerate.

Note that there may be multiple sets of eigenvectors transforming as the same kind of irreducible representation independently of one another. These eigenvectors are *not* symmetry bound to be degenerate, as although they transform in similar ways under the

symmetry operations, they do so amongst themselves as a closed set, and so (2.41) does not apply. However, as will be shown, the fact they transform as the same kind of irreducible representation has important implications for their interactions. As shown later, modes that transform according to different versions of the same irreducible representation are not allowed to be degenerate under certain conditions.

At this stage, it is possible to say that given one requires an initial set of eigenvectors and eigenvalues in order to calculate the irreducible representations, one must already know if they were degenerate a priori – so how does understanding the irreducible representations of the eigenvectors help one analyse the physical problem at hand?

The power of group theory is that, having established an initial set of eigenvectors that transform as a known irreducible representation of the group, it is possible to predict and understand their evolution under the application of perturbations on symmetry grounds alone. By applying a perturbation the symmetry of the system was typically be lowered: that is, the new symmetry group will consist of the old one minus some elements. Such a group is a sub-group of the original group. The irreducible representations of the old, larger group must still be a representation of the new, smaller group. However, they may not in general be irreducible. To see this, imagine finding a similarity transformation,  $X$ , that casts all the matrices in the representation into block diagonal form except for one, which will be called  $T$ . If a new group is formed by removing  $T$  as an element, then the impediment to  $X$  block-diagonalising the representation has been removed, and the representation is now reducible.

If a representation is made reducible by a symmetry-lowering perturbation, then it can be written in block diagonal form composed of multiple irreducible representations of the new group. By calculating this decomposition, it is possible to predict how the degeneracies of the eigenvectors will be affected by the perturbation. For example, if in a given system there are 3 degenerate eigenvectors whose irreducible representation becomes a reducible

representation after a perturbation is applied consisting of a 2-dimensional and 1-dimensional irreducible representation of the new group, then one of the eigenvectors will become split off from the other two whose eigenvalues will remain degenerate. Note that this is entirely a consequence of the symmetry of the system and can be calculated from knowledge of the group alone, entirely independently of any physical context or equation (beyond the prerequisites already described).

### Decomposing reducible representations into their irreducible components

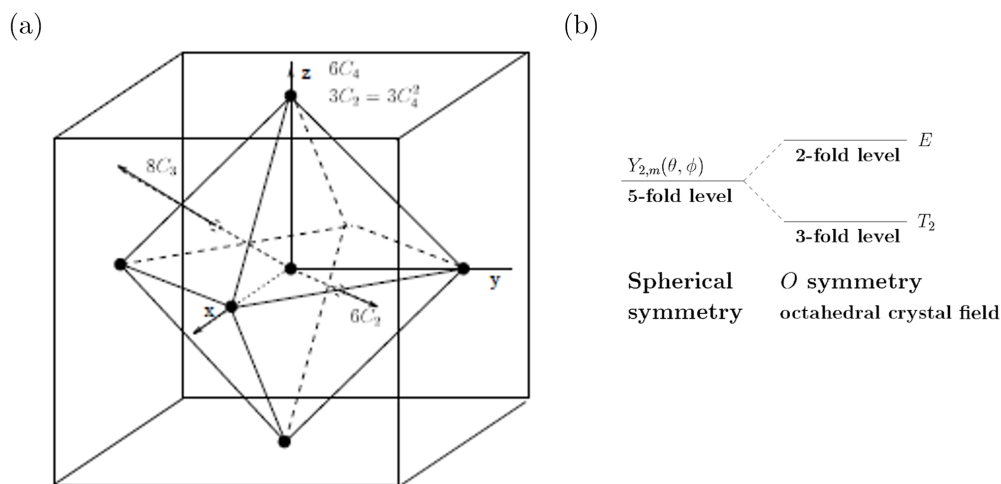


Fig. 2.12 Unit cell of a crystal structure with octahedral symmetry. Various rotation elements of this group are indicated on the diagram, where  $C_n$  represents a rotation about an axis by  $2\pi/n$  radians. Figure reproduced from [122].

An important procedure to understand is how to decompose a reducible representation into its irreducible components. This is similar in procedure to decomposing a vector into its constituent basis parts. This is the process used when analysing how symmetry lowering affects the degeneracies in the system, as described in the section above.

The formula is as follows. Given some reducible representation of the symmetry elements on a group, it is possible to write down what is known as the *character* table of the representation. This is the trace of the matrices of each element. For instance, using the usual matrix

representation of the rotation matrix given in (2.39), the character of the representation is  $2 \cos \phi$ . Given a reducible representation with characters,  $\chi_{red.}(C_k)$ , for all the symmetry elements  $C_k$  in a symmetry group, the irreducible representations it contains can be found using the formula:

$$a_j = \frac{1}{h} \sum_k \chi^j(C_k) \chi_{red.}(C_k) \quad (2.45)$$

where  $a_j$  says how many times a given irreducible representation, labeled by  $j$ , occurs in a given reducible representation,  $h$  is the order of the reducible representation, or the number of dimensions of the matrices it contains, and the sum over  $k$  is the sum over all the symmetry elements in the group [122].

This can be illustrated explicitly by a simple example, reproduced from [122]. Consider a crystal with octahedral symmetry; Figure 2.12a shows a unit cell of the crystal with all the symmetry operations of the octahedral symmetry group labeled. Table 2.1 shows all of its irreducible representations and the characters of the representation of each element.

$O$	$E$	$8C_3$	$3C_2$	$6C_2$	$6C_4$
$A_1$	1	1	1	1	1
$A_2$	1	1	1	-1	-1
$E$	2	-1	2	0	0
$T_1$	3	0	-1	-1	1
$T_2$	3	0	-1	1	-1

Table 2.1 Character table for the octahedral group,  $O$ .  $C_n$  represents an  $n$ -fold rotation (of  $2\pi/n$  radians) about a given axis;  $E$  is the identity element. The symmetry operations are grouped by class, with the number of elements in each class indicated by the number before the  $C_n$  symbol. This is the usual presentation of character tables, as symmetry elements in the same class always have the same character [122].

Imagine that there is a paramagnetic impurity with angular momentum  $l = 2$  that is placed at a lattice site inside the octahedral crystal. It has the usual energy degeneracy of

$2l + 1$ . That is, it is a fivefold degenerate energy level. What is the effect of the crystal's electric field on the degeneracy of the energy levels of the impurity? Much like moving away from the  $\Gamma$  point in Figure 2.10, the electric field of the crystal acts as a symmetry lowering perturbation, and the decomposition formula (2.45) can be used to establish its effect.

A Magnetic impurity with angular momentum  $l = 2$  is known to transform as the  $\Gamma_{l=2}$  representation of the full rotational symmetry group: that is the symmetry group of a point or a sphere. The character table of the irreducible representations of the full rotational symmetry group for the symmetry elements in  $O$  are given in Table 2.2.

$O$	$E$	$8C_3$	$3C_2$	$6C_2$	$6C_4$
$\Gamma_{l=0}$	1	1	1	1	1
$\Gamma_{l=1}$	3	0	-1	1	-1
$\Gamma_{l=2}$	5	-1	1	1	-1
$\Gamma_{l=3}$	7	0	1	1	1

Table 2.2 Character table for the first 4 irreducible representations of the full symmetry group labeled by their angular momentum  $l$ , focusing only on the elements that are also in the octahedral group [122].

This representation is an irreducible one of the full rotation symmetry group but is reducible for the octahedral symmetry group, and so the formula (2.45) can be used in conjunction with the character tables 2.1 and 2.2, to decompose it into the irreducible representations of the octahedral group.

For instance, take the irreducible representation  $A_1$ . The above procedure gives us:

$$a_{A_1} = \frac{1}{24}(5 - 8 + 3 + 6 - 6) = 0 \quad (2.46)$$

whereas for  $E$ , one has:

$$a_E = \frac{1}{24}(10 + 8 + 6 + 0 + 0) = 1 \quad (2.47)$$

In fact, all the other irreducible representations are not contained within  $\Gamma_{l=2}$ , except for  $T_2$ , where (2.45) gives:

$$a_{T_2} = \frac{1}{24}(15 + 0 - 3 + 6 + 6) = 1 \quad (2.48)$$

So one can write:

$$\Gamma_{l=2} = E + T_2 \quad (2.49)$$

Because  $T_2$  is a 3-dimensional representation, and  $E$  is a 2-dimensional representation, the 5-fold degenerate  $l = 2$  energy level is split into a 3-fold degenerate set of levels and a 2-fold degenerate set of levels by the crystal splitting (Figure 2.12b).

### Avoided crossings and the Wigner-Von Neuman avoided crossing theorem

Once the irreducible representation associated with each mode has been determined, it is straightforward to determine whether or not they are allowed to cross. According to the Wigner-Von Neumann avoided crossing theorem [225], *two modes can cross only if they transform according to different irreducible representations.*

To see intuitively why this must be so, consider a hermitian eigenvalue problem parameterised by some value  $x$  (e.g. the external magnetic field, wave-vector, etc.):

$$H(x) |i\rangle = \lambda_i |i\rangle \quad (2.50)$$

where  $|i\rangle$  is the  $i^{\text{th}}$  eigenvector with eigenvalue  $\lambda_i$ . Now consider the eigenvalue problem:

$$H(x + \delta x) |i'\rangle = \lambda_{i'} |i'\rangle = (H(x) + \delta H) |i'\rangle = (\lambda_i + \delta \lambda_i) |i'\rangle \quad (2.51)$$

where  $\delta x$  is some small perturbation, resulting in a small perturbative matrix  $\delta H$  that changes the eigenvector to  $|i'\rangle$  with eigenvalue  $\lambda_i + \delta \lambda_i$ , where  $\delta \lambda_i \ll \lambda_i$ . For small perturbations  $\delta H$ , the new eigenvalues can be approximated in terms of the old ones by a Taylor expansion

of the form:

$$\lambda'_i \approx \lambda_i + \langle i | \delta H | i \rangle + \sum_{j \neq i} \frac{|\langle j | \delta H | i \rangle|^2}{\lambda_i - \lambda_j} \quad (2.52)$$

up to second order in  $\delta H$ . Hence if  $\lambda_i > \lambda_j$ , as they approach one another as  $x$  increases, if  $\langle j | \delta H | i \rangle$  does not vanish, then  $\lambda'_i$  will be increasingly pushed upwards by the diverging  $\frac{|\langle j | \delta H | i \rangle|^2}{\lambda_i - \lambda_j} > 0$  term, and  $\lambda'_j$  downwards by the  $\frac{|\langle i | \delta H | j \rangle|^2}{\lambda_j - \lambda_i} < 0$  term in their perturbation expansion. It is only when  $\langle j | \delta H | i \rangle$  vanishes that they may cross, which group theory shows *only* occurs when the two modes transform according to different irreducible representations of the group [122].

This proof is not rigorous, as as  $\lambda_i$  approaches  $\lambda_j$ , perturbation theory must necessarily break down before the  $\lambda_i - \lambda_j$  denominator diverges, but it gives a straightforward explanation of why the Wigner Von-Neuman avoided crossing theorem works.

# Chapter 3

## Experimental methods

### 3.1 Sample fabrication

The samples under study in this work are all thin, predominantly metallic, films deposited on an underlying insulating substrate. The basic procedure is as follows: 1) perform lithography on the sample to define the geometry of the device if required, and then 2) mill away areas of the device or deposit subsequent layers as defined by the previous lithography step. This process is then repeated until the desired device architecture is achieved. Sections 3.1.2 and 3.1.3 describe the two techniques used for sample deposition in this work: sputtering, and thermal evaporation. Sections 3.1.4 and 3.1.5 describe the procedure behind photolithography and e-beam lithography for lithographic patterning of the materials respectively, and Section 3.1.6 explains the process of ion-milling for removing the areas of the sample defined by the overlying layer of resist.

### 3.1.1 Substrate preparation

In order to prepare a clean substrate for growth, each substrate is sonicated in acetone and then subsequently IPA for 30 seconds each, before being plasma ashed in oxygen plasma for up to 10 minutes.

### 3.1.2 Magnetron sputtering

Sputtering is a means of physical vapour deposition that generates a vapour of the desired target material that deposits itself on a nearby target substrate, forming a thin film of material at a controllable rate [226]. The vapour is generated by accelerating argon ions in a plasma towards a target of the desired material composition held at a large negative potential at the cathode. This physical bombardment ejects atoms from the target, forming a gas that deposits itself on the substrate positioned at the anode. The gas itself is confined by a magnetic field within the chamber. This improves the deposition rate and gives the ‘magnetron’ part of magnetron sputtering its name.

### 3.1.3 Thermal evaporation

Thermal evaporation is used for depositing metal films with sufficiently low melting/sublimation temperatures that can be achieved via resistive heating. The sample is placed in a vacuum chamber ( $\sim 10^{-6}$  mbar) along with the desired material held in a tungsten boat. A large current is then passed through the boat, heating it, and causing the metal to evaporate and deposit as a thin film on the sample surface.

### 3.1.4 Photolithography

Photolithography is a technique for patterning a polymer layer deposited on top of the sample in order to lithographically define patterns that can be used for the creation of device

architectures in subsequent fabrication steps (ion-milling, physical vapour deposition). Prior to photolithography, the sample is successively sonicated in acetone and IPA, before being plasma ashed for up to 10 minutes. This plasma-ashing step is important in order to remove any hydrophobic layers from the sample surface, which will prevent the resist from adhering well, if at all, to the sample's surface.

Microposit S1813 (positive) photoresist is spin-coated onto the substrate at 5000 rpm for 60s and annealed on a hot-plate at 120 degrees for a further 60s. This produces a layer of resist around 1.2  $\mu\text{m}$  thick. The sample is then exposed to UV light using a Karl Suss MJB3 mask aligner in conjunction with a photomask placed between the sample and the UV source in order to change the chemical properties of the resist in the exposed areas defined by the photomask. The exposure time varies depending on the substrate. For Si/SiO<sub>2</sub> substrates, 12s is sufficient, for Al<sub>2</sub>O<sub>3</sub> substrates, which are transparent, and hence reflect less of the incident UV light back into the resist, a slightly longer exposure time of 30s was found to ensure complete development of the exposed resist in the subsequent development stage.

Following exposure, the photoresist is developed for 20s in Microposit MF-321 developer. The development process is then quenched in de-ionised water (DI-water) for a further 20s. The developer dissolves away the exposed sections of the resist, leaving behind the desired pattern. The sample can then be plasma ashed for a further 2 minutes to remove any residual resist from the exposed area if required.

### **3.1.5 E-beam lithography**

The resolution of photolithography is limited to a few micrometres by the wavelength of UV light [227]. Consequently, to achieve finer structures, it is necessary to look for alternative means of exposing the resist using smaller wavelengths. E-beam lithography uses a beam of electrons to expose the resist and can achieve features on a length scale of just a few nanometres [228].

The procedure is similar to photolithography (3.1.4). The sample is sonicated in acetone, then IPA, for 30s each, before being plasma-ashed for up to 10 minutes. 495K A5 PMMA is spin-coated onto the sample at 3000 rpm (this creates a layer of resist around 400 nm thick) and annealed on a hot plate at 170 degrees for 60s. If the substrate is sufficiently conductive (e.g. Si/SiO<sub>2</sub> with a sufficiently thin layer of oxide) then the sample can proceed to development. For insulating substrates (e.g. Al<sub>2</sub>O<sub>3</sub>), a 30 nm layer of Au is then sputtered on top to act as a conduction layer. This conduction layer prevents the detrimental build-up of charge during the exposure process.

The sample is then exposed to a beam of electrons in a predefined pattern at a dosage calibrated (  $760 \mu\text{C}/\text{cm}^2$ ) for the desired resolution and structure. Following exposure, if the sample has a conducting Au layer on top, this is first removed by submersing the sample in gold etchant (30s), followed by rinsing the sample in DI-water for a further 30s. The sample is then developed in 1:3 MIBK:IPA for 60s, followed by quenching in IPA for a further 20s. If required, the sample can then be plasma ashed for a short time (20s) to remove any residual resist still remaining in the exposed regions.

### 3.1.6 Ion milling

The physical basis behind ion milling is essentially the same as sputtering (3.1.2), except that instead of a target of the desired material composition at the cathode, the sample becomes the target. The accelerated ions strike the sample, etching away any exposed areas at a rate typically on the order of a few Angstrom to nanometres per second depending on the experimental conditions and sample structure. If the sample has a patterned resist layer on top, the resist will protect the underlying sample where it hasn't been developed away, allowing sophisticated patterns to be etched into the sample.

The milling rate was calibrated by milling a series of test samples over a range of milling durations and then measuring the depth of the milled area with a Dektak profilometer. The

samples are then milled for a time corresponding to a predicted milling depth of at least twice the depth of the sample to ensure that they are milled all the way through. Although the sample chamber is water-cooled, milling still heats the chamber and the sample, causing the resist to sometimes become ‘baked’ to the sample. To remove the resist following milling, the sample is soaked in acetone overnight, sonicated in acetone, and then plasma ashed for 5 to 10 minutes to remove any residual resist still on the device.

## 3.2 Sample growth

### 3.2.1 Superconducting/ $C_{60}$ /Permalloy spin-pumping devices

In Chapter 4, superconducting/organic-molecular/ferromagnetic heterostructures are measured via FMR at cryogenic temperatures in search of evidence of spin-triplet Cooper pairs. These samples were fabricated by A. Walton from the University of Leeds. Table 3.1 shows each measured sample’s structure. The metallic films were grown by DC magnetron sputtering on top of a Si/SiO<sub>2</sub> substrate with a base pressure of  $2.9 \times 10^{-8}$  mbar, and at a partial pressure in argon of 2.5 mbar. The  $C_{60}$  layers were grown (without breaking vacuum) via thermal evaporation in the same chamber in Al<sub>2</sub>O<sub>3</sub> boats from a 99.9% pure source. The Al<sub>2</sub>O<sub>3</sub> layer acts as a capping layer to protect the sample from oxidation.

Sample A	(Si/SiO <sub>2</sub> )Nb[49] $C_{60}$ [10]Cu[2.7] $C_{60}$ [10]Py[7.7] Al[10] $C_{60}$ [20]Al <sub>2</sub> O <sub>3</sub> [2]
Sample B	(Si/SiO <sub>2</sub> )Nb[49] $C_{60}$ [20]Py[7.7] Al[10] $C_{60}$ [20]Al <sub>2</sub> O <sub>3</sub> [2]
Sample C	(Si/SiO <sub>2</sub> )Nb[49] $C_{60}$ [10]Cu[2.7] $C_{60}$ [10] Al[10] $C_{60}$ [20]Al <sub>2</sub> O <sub>3</sub> [2]

Table 3.1 Structures of the samples measured in Chapter 4. The thickness of the metallic layers was measured by x-ray reflectometry, and the thickness of the  $C_{60}$  layer by a quartz microbalance during deposition.

Similar structures have been fabricated in the same group. Low-angle X-ray measurements on these samples demonstrated that there is negligible diffusion of the molecular film

into the metallic layers, and transmission electron microscopy also showed “that the metallic layers are continuous and the  $C_{60}$  layers are polycrystalline” [229].

### 3.2.2 Synthetic antiferromagnets for FMR and magnetoresistance measurements

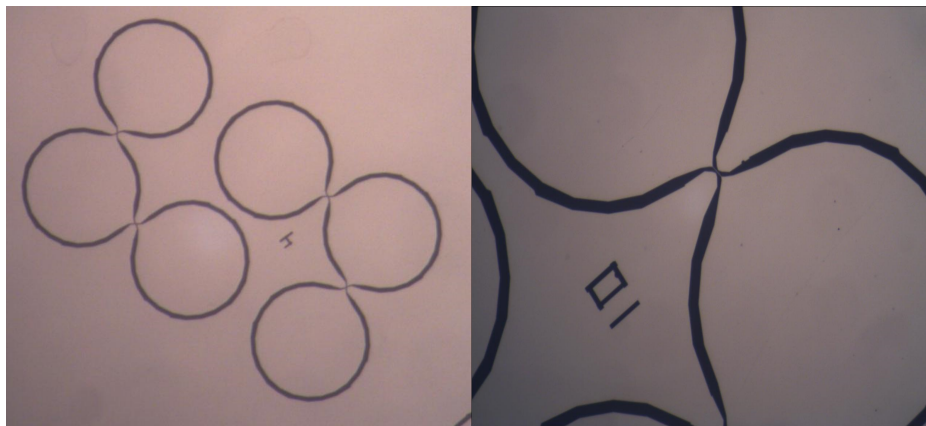


Fig. 3.1 Microscope image of a FMR bar patterned by argon-ion milling. The circular sections are bond pads for wirebonds. The current (MW or DC) is concentrated through the narrow central bar in order to excite and/or measure the desired magnetic effect.

The synthetic antiferromagnet (SAF) samples and the single ferromagnetic layer sample measured in Chapter 5 were grown and prepared by Dr J-W. Liao in the group of Prof. R. P. Cowburn at the University of Cambridge. The samples were grown via DC magnetron sputtering on Si/SiO<sub>2</sub> substrates at a base pressure of  $1 \times 10^{-7}$  mbar and a partial pressure of  $9 \times 10^{-3}$  mbar in argon gas. During sputtering, a DC magnetic field was applied in-plane in order to induce a crystalline uniaxial anisotropy in the ferromagnetic thin films. Subsequently, the films were spin-coated with a layer of PMMA e-beam resist and patterned by e-beam lithography into FMR bars of varying dimensions and orientations with respect to the easy-axis. Following the development of the exposed resist, the samples were etched via argon-ion milling by Dr Z. Sorban of the Academy of Science of the Czech Republic in

order to produce the final bar-structure (Figure 3.1). Table 3.2 gives the layered structure of each sample.

‘Single-sided’ SAF	(Si/SiO <sub>2</sub> )Ta[2]Pt[3]CoFeB[1.4]Ru[0.9]CoFeB[1.4]Pt[1]Ta[2]
‘Double-sided’ SAF	(Si/SiO <sub>2</sub> )Ta[2]Pt[3]CoFeB[1.4]Ru[0.9]CoFeB[1.4]Pt[6]Ta[2]
‘Single-layer’	(Si/SiO <sub>2</sub> )Ta[2]Pt[3]CoFeB[1.4]Ru[0.9]Ta[2]

Table 3.2 (All thicknesses in nm) Structures of the synthetic antiferromagnet and ferromagnet samples measured in Chapter 5. The thickness of each layer is determined by the sputtering time multiplied by the measured deposition rate of the sputterer under the same deposition conditions.

Each device is grown on top of a 2 nm seed layer of Ta and capped with another 2 nm Ta layer. The seed layer reduces the sample roughness and is necessary for the multilayer structure to exhibit (antiferromagnetic-)coupling between the CoFeB layers. It also encourages the formation of a crystalline orientation of Pt that enhances the spin-orbit coupling induced PMA at the interface [230–232]. The capping layer protects the device from oxidation, and will itself oxidise to tantalum oxide under atmospheric conditions: an inert insulator. The thickness of Ru was chosen to maximise the RKKY antiferromagnetic interlayer coupling. A Ru layer was also included in the single-layer sample in order to replicate the interfacial conditions of the lower ferromagnetic layer in the SAF stacks.

### 3.2.3 Narrow bars for magnetoresistance measurements

In Chapter 6, current-induced asymmetry in the magnetoresistance properties of a synthetic antiferromagnet and signal ferromagnetic layer are measured. These samples were grown first with DC magnetron sputtering on sapphire substrates at a base pressure of  $1 \times 10^{-7}$  mbar and a partial pressure of  $9 \times 10^{-3}$  mbar in argon gas with the structures described in Table 3.4. Subsequently, the films were spin-coated with PMMA e-beam resist (3000rpm, producing a layer of resist 400 nm thick) and patterned into narrow FMR bars of width 500 nm and

various lengths from 4  $\mu\text{m}$  to 10  $\mu\text{m}$  in steps of 2  $\mu\text{m}$ . The samples were then etched via argon-ion milling and the resist layer removed. The parameters used during the ion milling step are summarised in Table 3.3. Finally, a capping layer of 50 nm of  $\text{Al}_2\text{O}_x$  was sputtered using RF sputtering in order to protect the device and aid in dissipating the heat generated by the high current densities used in the experiments.

Cathode V (V)	Cathode I (A)	Discharge I (A)	Pressure (mbar)	Time (s)
5.4	6.1	0.4	$7.2 \times 10^{-2}$	180

Table 3.3 Milling parameters used during the ion milling of the narrow bar samples.

Synthetic antiferromagnet	$(\text{Al}_2\text{O}_x)\text{Ta}[2]\text{Pt}[3]\text{CoFeB}[2]\text{Ru}[0.9]\text{CoFeB}[2]\text{Pt}[6]\text{Ta}[2]\text{Al}_2\text{O}_x[50]$
Single-layer	$(\text{Al}_2\text{O}_x)\text{Ta}[2]\text{Pt}[3]\text{CoFeB}[4]\text{Ru}[0.9]\text{Ta}[2]\text{Al}_2\text{O}_x[50]$

Table 3.4 (All thicknesses in nm) Structures of the synthetic antiferromagnet and ferromagnet samples measured in Chapter 6. The thickness of each layer is determined by the sputtering time multiplied by the measured deposition rate of the sputterer under the same deposition conditions.

The thickness of the single layer was chosen to replicate the device structure measured in [148], but with a CoFeB ferromagnetic layer rather than Py, to match the SAF. Sapphire was chosen as a substrate because of its superior thermal conductivity to  $\text{SiO}_2$ , which aids in reducing the damage caused by Joule heating at high current densities.

### 3.3 FMR

The theoretical background behind ferromagnetic resonance was explained in Section 2.2. In practice, there are a number of different ways of implementing a ferromagnetic resonance measurement. What they all have in common is the application of an oscillating microwave magnetic field (effective or real) to induce oscillations in the magnetisation of a sample.

These oscillations produce a signal detected at the output of the experiment proportional to the amplitude (and potentially phase) of the oscillations.

This work employs two primary means of exciting and detecting ferromagnetic resonance: stripline FMR and spin-torque FMR (ST-FMR), which differ in both their means of exciting the magnetisation, and in how they detect the resultant resonant oscillations. The experimental details of each are given in the next two sections.

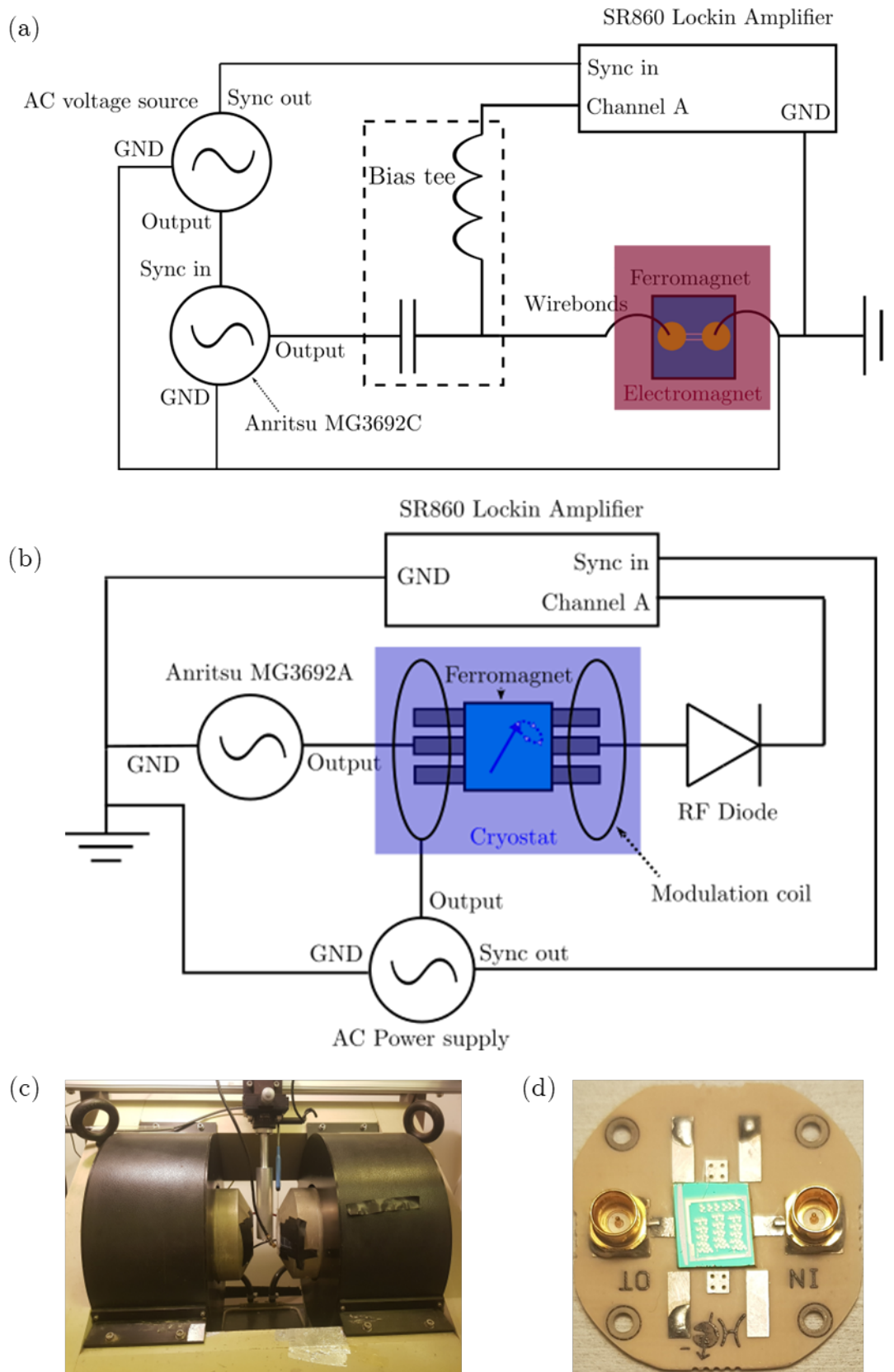


Fig. 3.2

---

Fig. 3.2 (*previous page*) (a) Block-diagram of the experimental set-up for stripline FMR. A magnetic field is applied across the sample during the experiment by an electromagnet internal to the cryostat. (b) Block-diagram of ST-FMR set-up. (c) Photograph of the electromagnet that the ferromagnet in Figure (b) sits between during the experiment. The ferromagnet is held at the end of the long-metallic pole in between the two poles of the electromagnet. (d) Photograph of the PCB board on which the sample is held during the experiment in (b). The sample is attached to the board and wirebonds are connected to it from the microwave input (SMP connector) and to ground.

### 3.3.1 Stripline FMR

Figure 3.2a shows a block diagram of the typical set-up employed in a stripline FMR measurement. A microwave magnetic field from a signal generator (Anritsu MG3692A) is passed down a waveguide on top of which the ferromagnetic sample is positioned (usually a microstrip or coplanar stripline, see Figure 3.3a) inside a liquid helium cryostat (Figure 3.3b) that allows the temperature of the sample to be controlled down to around 2 K, and contains an inbuilt superconducting electromagnet that allows for a DC magnetic field to be applied up to several Tesla in strength. The waveguide couples to the ferromagnetic sample inductively, causing a significant drop in the transmitted power at the output port when the ferromagnetic resonance condition is fulfilled [233]. This drop in transmitted power is detected by a microwave diode, which is attached to the output of the waveguide (outside the cryostat) and converts the microwave output signal into a DC signal proportional to the amplitude of the incoming microwaves. The principal advantage of this technique is that it can be used over a broadband range of frequencies (versus cavity-based techniques), does not require the fabrication of devices (versus ST-FMR), and produces straightforward output curves with good signal-noise ratios that require minimal post-processing (versus VNA based techniques) [233].

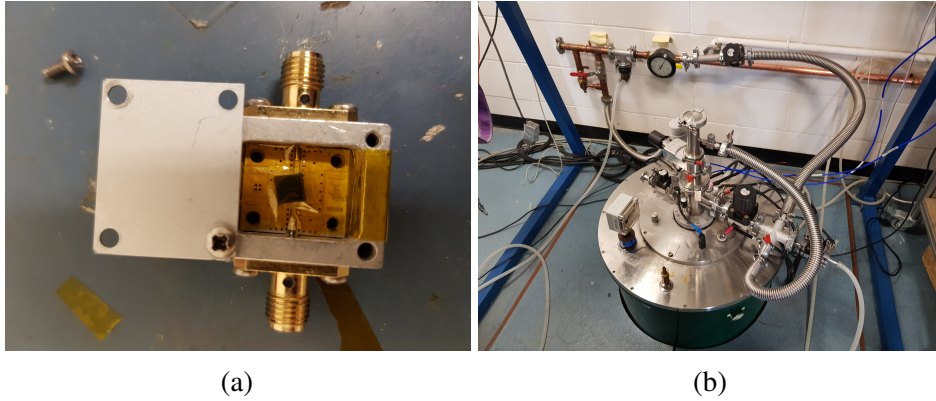


Fig. 3.3 (a) Ferromagnet on top of a microwave waveguide. The sample is held down by kapton tape to prevent movement during the measurement and minimise its distance to the waveguide. This box would be sealed and inserted into a cryostat, attached to microwave waveguides on either side via the protruding SMA connectors. (b) Cryostat used for stripline-FMR measurements.

In order to obtain a measurement of the susceptibility, a fixed microwave frequency is chosen and a DC magnetic field is swept across an appropriate range of field values. The resulting output from the diode is proportional to the susceptibility of the ferromagnet,  $\chi(H, \omega)$ , and hence by fitting the output voltage to a theoretical formula proportional to  $\chi$  derived from the LLG equation (Section 2.2.1), important physical parameters of the ferromagnet can be derived, such as the linewidth and resonance frequency. Figure 3.4a shows a typical plot of the detected voltage versus the magnetic field, and the theoretical fit to the formula:

$$V_{diode} = V_s \frac{\Delta H^2}{(H - H_{res})^2 + \Delta H^2} + V_a \frac{(H - H_{res})\Delta H}{(H - H_{res})^2 + \Delta H^2} \quad (3.1)$$

The exact formula for the resonance field,  $H_{res}$ , comes from the model adopted in the LLG equation. This fitting is performed numerically using least-squares regression, and provides estimates and errors for all of the experimental quantities that appear in the expression for the resonance field and the linewidth.

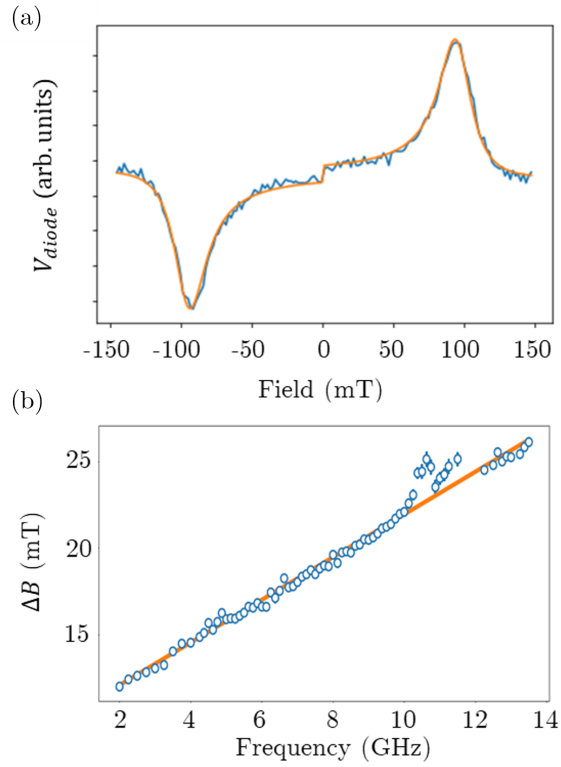


Fig. 3.4 (a) Raw rectified voltages outputted from a stripline FMR experiment (blue line) and their associated fit to a combination of symmetric and antisymmetric Lorentzians (orange line). (b) Linewidth versus frequency from an FMR experiment. Straight line fit gives the Gilbert damping parameter.

Additionally, another useful measurement is the dependence of the linewidth against frequency. From the LLG equation, it is possible to show that the linewidth has a frequency dependence given by:

$$\mu_0 \Delta H = \mu_0 \Delta H_0 + \alpha f / \gamma \quad (3.2)$$

where  $\Delta H_0$  is the zero frequency offset known as the inhomogeneous broadening [65]. Figure 3.4b shows a plot of the linewidth's linear dependence on frequency, from which the Gilbert damping parameter can be easily determined.

In order to improve the sensitivity of the set-up, an oscillating (but quasi-DC on the timescale of ferromagnetic resonance) magnetic field, known as the modulation field, is applied by an inductive coil attached to a signal generator (HP Universal Source 3245A) that

surrounds the sample. Consequently, the detected signal is proportional to the oscillating part of:

$$\chi(H + he^{i\omega_{mod}t}) \approx \chi(H) + he^{i\omega_{mod}t} d\chi/dH \quad (3.3)$$

giving a predicted output voltage:

$$V_{diode} = -V_s \frac{\Delta H^2 (H - H_{res})}{((H - H_{res})^2 + \Delta H^2)^2} - V_a \frac{(H - H_{res})^2 \Delta H}{((H - H_{res})^2 + \Delta H^2)^2} + V_a \frac{\Delta H}{(H - H_{res})^2 + \Delta H^2} \quad (3.4)$$

By detecting this signal with a lock-in amplifier (SRS SR830) tuned to the modulation frequency,  $\omega_{mod}$ , one can significantly improve the signal-to-noise ratio of the output signal.

### 3.3.2 Spin-torque FMR

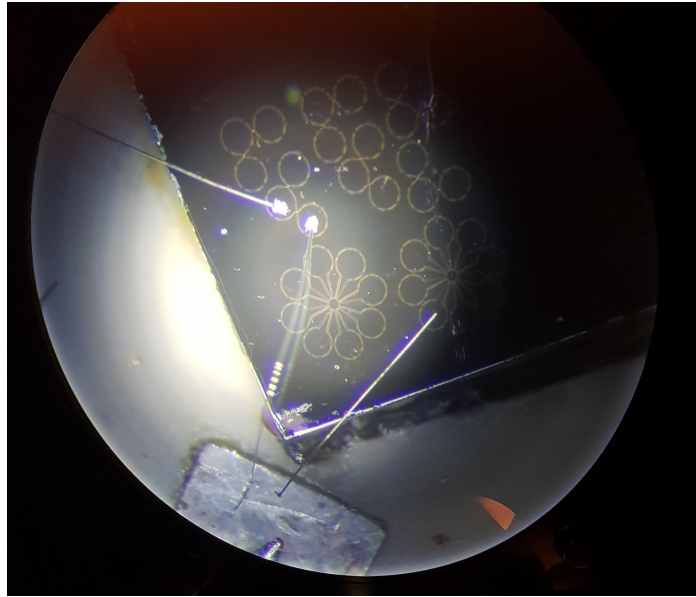


Fig. 3.5 FMR bar wire bonded to a microwave waveguide in a stripline FMR experiment.

Rather than using the magnetic field of a passing electromagnetic wave as in stripline FMR, Spin-torque FMR (ST-FMR) (Figure 3.2b) relies on the spin-torques generated by a MW current passing through the sample itself to excite and detect the magnetisation dynamics.

Although it requires additional fabrication steps over stripline FMR, through analysis of the detected signal, the strength and nature of the spin-orbit torques in the device can be determined from this measurement.

First, the sample is fabricated into a bar shape in order to direct and collimate the current (see Section 3.2.2 for details of the fabrication procedure). The sample is then mounted on a PCB board (Figure 3.2d), which is then connected to the microwave source and earth via wirebonds at either end (Figure 3.5). The sample is placed between two ends of an electromagnet (Figure 3.6) which applies an external field that it can be rotated with respect to. The microwave current passing through the device generates an AC signal at the frequency of the modulation of the microwave source by an external function generator, as described in Section 2.2.3. This is detected by a lock-in amplifier connected to the DC-port of a bias tee.

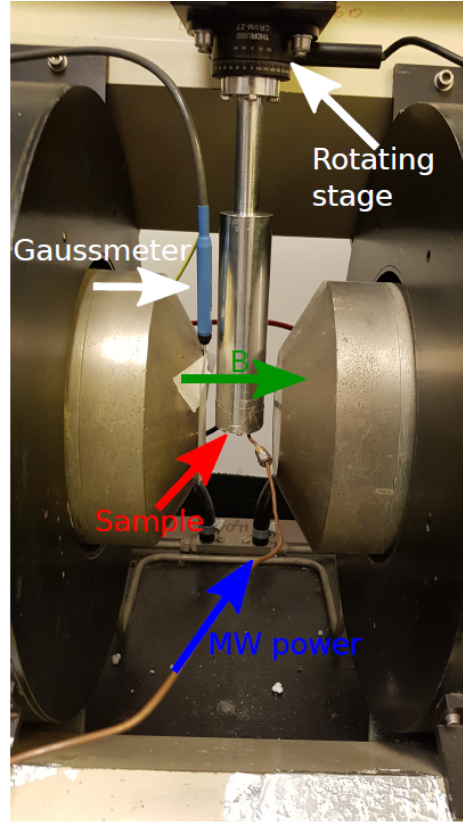


Fig. 3.6 Experimental setup used for ST-FMR measurements. The sample sits at the end of a holder in between the poles of an electromagnet that is used to apply a DC magnetic field across the sample. A MW current is biased through the sample, and the resulting rectified DC current is detected at the DC port of a bias-Tee.

The analysis of this signal is similar to in stripline-FMR; the experimental data is fit to a formula (using numerical least squares regression) derived from the LLG equation (see Figure 3.7a). The formula for the predicted rectified voltage produced at resonance during a ST-FMR experiment is given by (2.30)-(2.31), reproduced here:

$$\begin{aligned}
 V_{SD} &= V_s \frac{\Delta H^2}{(H - H_{res})^2 + \Delta H^2} + V_a \frac{(H - H_{res})\Delta H}{(H - H_{res})^2 + \Delta H^2} \\
 V_s &= \frac{I\Delta R}{2} \frac{\omega}{\gamma_0 \Delta H (2H_{res} + H_1 + H_2)} h_z \sin 2\phi \\
 V_a &= \frac{I\Delta R}{2} \frac{H_{res} + H_1}{\Delta H (2H_{res} + H_1 + H_2)} (-h_x \sin \phi + h_y \cos \phi) \sin 2\phi
 \end{aligned} \tag{3.5}$$

where  $\mu_0 H_{res}$  is field strength of the resonance, usually substituted for a theoretical formula depending on the magnetic quantities appearing the LLG equation (see Figure 3.7b for a plot and fit of the resonance fields experimental and theoretical dependence on angle respectively),  $\mu_0 \Delta H = \Delta B$  is the linewidth,  $I$  is the MW current through the bar,  $\Delta R$  is the AMR coefficient,  $h_i$  the strength of the spin-orbit torques in the  $i^{th}$  direction,  $\phi$  the angle between the current direction and the magnetisation/external field, and  $V_s$  and  $V_a$  describe the strength of the symmetric and antisymmetric Lorentzian components of the resonance respectively.

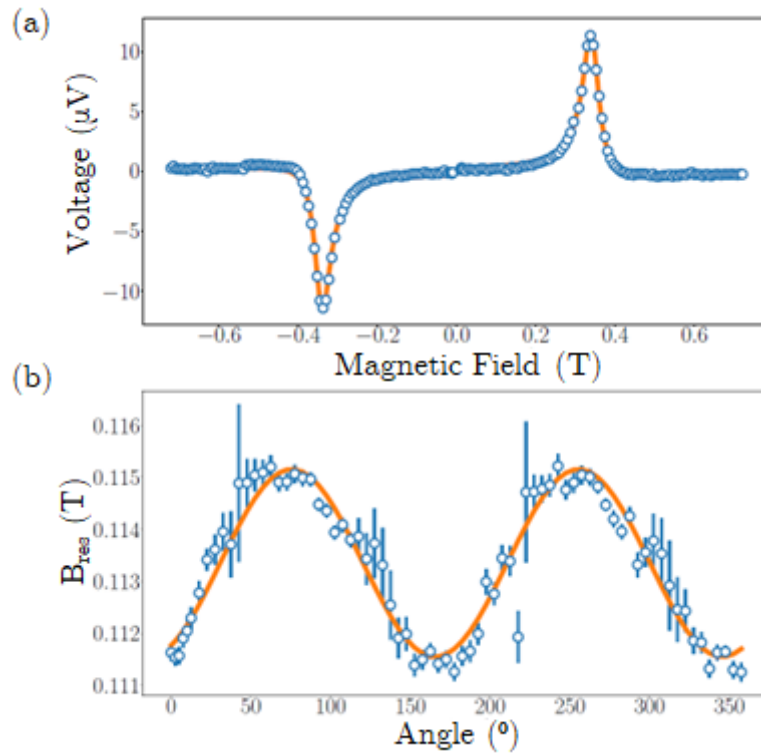


Fig. 3.7 (a) Raw voltages produced by a ST-FMR experiment and the associated fit to symmetric and antisymmetric Lorentzians. (b) The angle dependence of the resonance field. From this the strength of in-plane magnetic anisotropies can be determined.

As in stripline-FMR, these fits can be used to determine important magnetic parameters in the same way. Additionally, it is often interesting to analyse the magnitude of the signal, as this gives the strength of the current induced torques — so long as the MW current is already known (the experimental procedure for determining the MW current in the bar is given in

Section 3.3.3). Figure 3.8 shows a typical experimental output. From the signal strength's (broken down into the symmetric,  $V_s$ , and antisymmetric,  $V_a$ , Lorentzian components) dependence on the angle between the current and the magnetisation (external field) direction,  $\phi$ , one can determine the strength of the spin-orbit torques in each direction from the formula:

$$V_{SD} = V_{sym} \frac{\Delta H^2}{(H - H_{res})^2 + \Delta H^2} + V_{asym} \frac{(H - H_{res})\Delta H}{(H - H_{res})^2 + \Delta H^2}$$

$$V_{sym} = \frac{I\Delta R}{2} \frac{\omega}{\gamma_0 \Delta H (2H_{res} + H_1 + H_2)} h_z \sin 2\phi \quad (3.6)$$

$$V_{asym} = \frac{I\Delta R}{2} \frac{H_{res} + H_1}{\Delta H (2H_{res} + H_1 + H_2)} (-h_x \sin \phi + h_y \cos \phi) \sin 2\phi$$

by looking at the  $\sin \phi$  and  $\cos \phi$  components of the angular dependence.

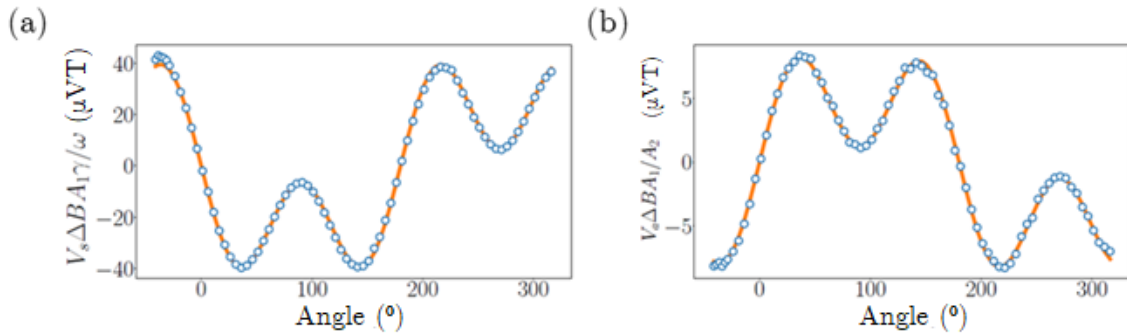


Fig. 3.8 Example of the angular dependence of the strength of the symmetric (a) and antisymmetric (b) rectified DC voltages. From the fit of this data to (3.6), the strength of the current induce spin orbit torques can be determined from the  $\sin \phi$  and  $\cos \phi$  components of the angular dependence.

### DC current damping modulation in FMR

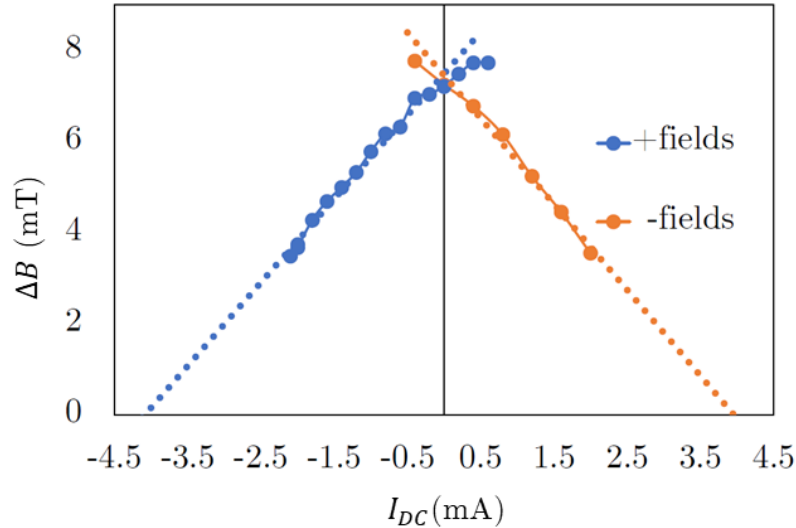


Fig. 3.9 Linewidth versus DC current measured during an FMR experiment. The linewidth is affected by the DC current across the bar due to the antidamping torques, whose sign changes with the sign of the external field, as expected.

If a DC current is passed through the device, via the antidamping torque, the damping in the system can be reduced or enhanced. This appears in the detected signal as a reduction/enhancement of the linewidth, in theory linearly with the applied current (Figure 3.9). The principal experimental difficulty when performing this measurement is that the large DC currents required to obtain an observable effect will also induce significant thermal voltages via bolometric effects [234]. The resulting voltages can be orders of magnitude larger than the desired signal.

Consequently, something of a hybrid set-up between the stripline FMR and ST-FMR setups is used (Figure 3.10). The set-up is superficially similar to that used in ST-FMR, except, instead of modulating the MW current directly, a modulation coil is used to modulate the output signal from the device. This is because the thermal voltages should have minimal external magnetic field dependence, and should be effectively filtered out by the lock-in tuned to the modulation current frequency.

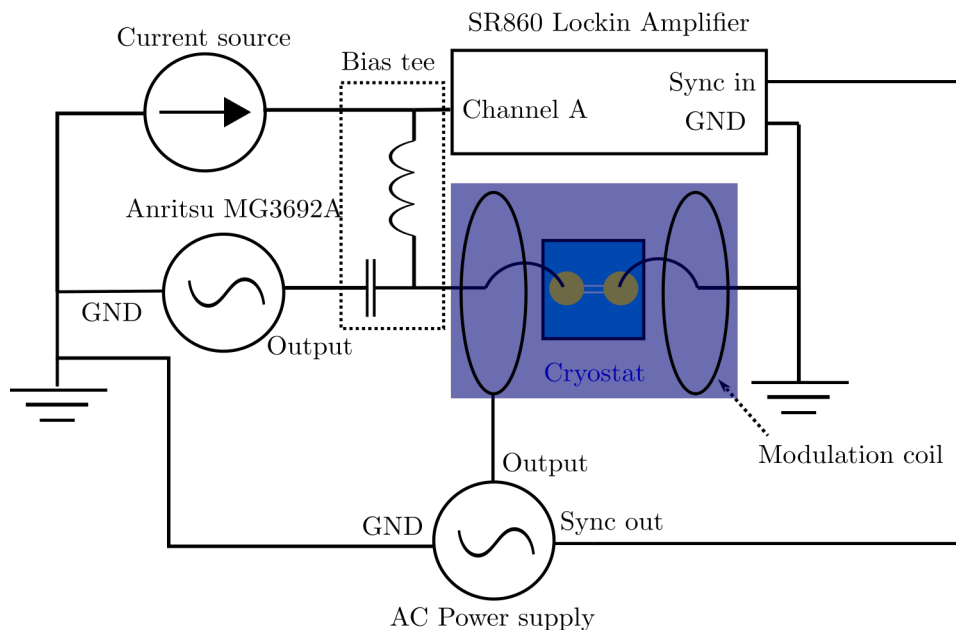


Fig. 3.10 Block-diagram of the experimental set-up for ST-FMR with a DC bias current. The DC bias current generates an antidamping torque in the sample which can be used to modulate the magnetic damping. A modulation coil is used to filter out unwanted signal from bolometric effects.

### 3.3.3 Microwave current calibration

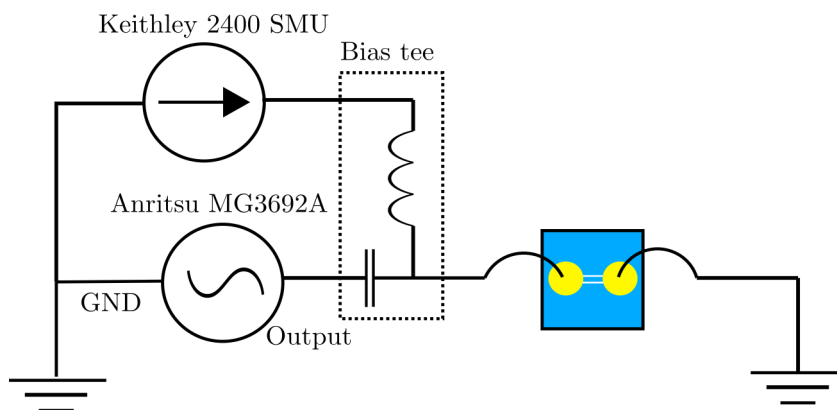


Fig. 3.11 Block diagram of the experimental set-up for calibrating the microwave current for a given microwave source power.

The formula for the predicted rectified voltage produced at resonance during a ST-FMR experiment is given by (2.30)-(2.31), reproduced here [26]:

$$\begin{aligned}
 V_{SD} &= V_{sym} \frac{\Delta H^2}{(H - H_{res})^2 + \Delta H^2} + V_{asym} \frac{(H - H_{res})\Delta H}{(H - H_{res})^2 + \Delta H^2} \\
 V_{sym} &= \frac{I\Delta R}{2} \frac{\omega}{\gamma_0 \Delta H (2H_{res} + H_1 + H_2)} h_z \sin 2\phi \\
 V_{asym} &= \frac{I\Delta R}{2} \frac{H_{res} + H_1}{\Delta H (2H_{res} + H_1 + H_2)} (-h_x \sin \phi + h_y \cos \phi) \sin 2\phi
 \end{aligned} \tag{3.7}$$

In order to accurately determine the strength of the spin-orbit torque fields ( $h_{x/y/z}$ ), it is necessary to obtain accurate measurements of the physical parameters/variables appearing in 3.7. The AMR co-efficient  $\Delta R$ , where the resistance of the ferromagnet is given by  $R = R_{\perp} + \Delta R \cos^2 \phi$ , where  $\phi$  is the angle between the current and the magnetisation direction, is straightforwardly determined from a simple DC-resistance measurement.

The MW current,  $I$ , passing through the device is less straightforward to determine, as reflections, absorption from the line etc. cause the amount of power actually applied to the sample to vary from what is applied at the source. Consequently, an independent measurement is required to determine the actual current.

This is achieved by means of a bolometric measurement, exploiting the fact that the power dissipated in the sample is proportional to the square of the current independently of its frequency. This raises the sample's temperature, and hence resistance, linearly with the applied power. By measuring the resistance of the sample versus the applied DC-current,  $I_{DC}$ , it is possible to calibrate how the resistance of the sample varies with the current in the device. In order to determine the MW current, the measurement is repeated at a fixed MW frequency and power. The applied MW current should give an offset in the y-axis intercept of the  $R$  versus  $I_{DC}^2$  curve (a straight-line), which can be used to determine the value of the microwave current:

$$R = \left( R_0 + \alpha \frac{I^2}{2} \right) + \alpha I_{DC}^2 \tag{3.8}$$

where the factor of  $1/2$  comes from time-averaging the square of the microwave current. This measurement must be repeated for every frequency, applied power, or new device used. Once the microwave current has been determined, the remaining free parameters in 3.7 are straightforwardly determined from the standard FMR measurement.

In order to measure the resistance as a function of DC current, a 2-wire resistance measurement was employed using a Keithley 2400 SMU connected to the DC port of a bias-Tee (see Figure 3.11). A microwave source (Anritsu MG3692A) is connected to the RF port of the bias-Tee and applies a constant power of microwave current to the device. The resistance is then measured as a function of the DC current for each microwave power where the current needs to be determined.

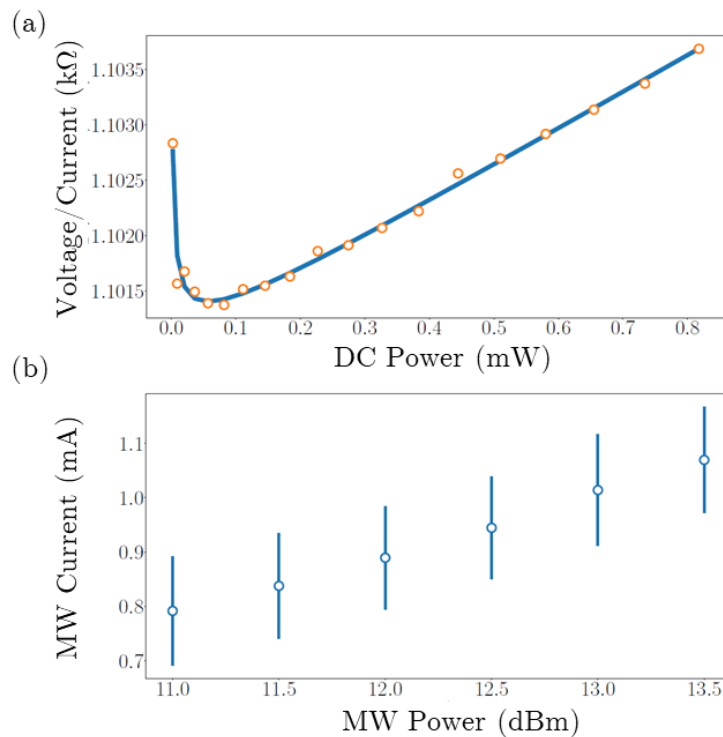


Fig. 3.12 Ratio of the DC voltage across the sample versus the applied DC power and fit to equation (3.9). Joule heating causes a linear increase in the resistance, from which the parameter  $\alpha$  in (3.9) can be determined. (b) Microwave current through the sample versus microwave power at the source. By measuring the change in the offset resistance,  $R_0 + \alpha I^2/2$ , with microwave power, with knowledge of  $\alpha$  from (a) the microwave current for a given power at the source can be determined.

Because of small offset voltages (thermal effects etc.) the voltage across the sample does not go to zero at zero source current, causing an apparent divergence in the ‘resistance’ at low DC-current. This is purely a measurement artifact, and the data from this region can either be excluded, or corrected for by modifying (3.8) to:

$$R = \left( R_0 + \alpha \frac{I^2}{2} \right) + \alpha I_{DC}^2 + V_0 / I_{DC} \quad (3.9)$$

where  $V_0$  is the DC voltage across the sample at zero DC current. Figure 3.12a shows a plot of the DC resistance versus the DC power and a fit to (3.9). From these plots,  $\alpha$  can be determined. From repeated measurements at different MW currents,  $I$ , the microwave current in the bar, for a given microwave power can be determined from the offset resistance term in (3.9):  $R_0 + \alpha I^2 / 2$  (see Figure 3.12b).

### 3.4 Magnetoresistance measurements

In order to measure the variation in the sample resistance with respect to the orientation of the external magnetic field, the experiment setup shown in Figure 3.13 is used.

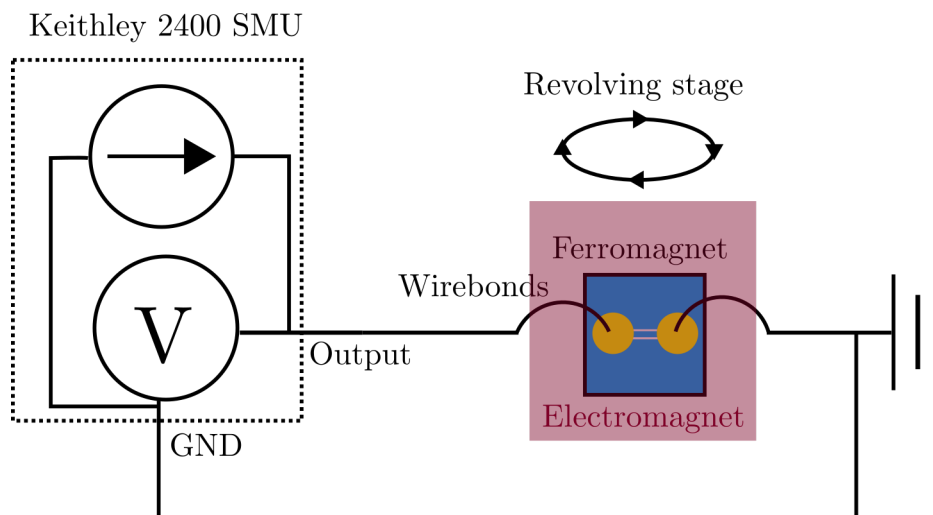


Fig. 3.13 Block diagram of the experimental setup used in measuring the magnetoresistance of devices

Here, the resistance is measured by applying a current across the sample and measuring the resultant voltage using a Keithley 2400 SMU. By mounting the sample on a revolving stage inside the poles of the static electromagnet (Figure 3.6, the sample can be rotated with respect to the external field and it is possible to measure the magnetoresistance of the device.

This setup uses as a two-probe measurement of the resistance. A two-probe measurement is used because it can be performed on the same bar devices used for ST-FMR measurements (Figure 3.5), which becomes important when looking for changes in the linewidth of the FMR signal with DC current across the sample. A two-probe measurement has the disadvantage of there being no way to decouple the resistance of the device from the resistance of the leads. This is acceptable in this case because here one is only interested in the relative variation of the resistance with the orientation of the magnetic field. Of the leads, only the wire bonds move with the rotation of the stage, the remainder of the leads being attached to the sample via SMP connections that are free to rotate. The wire bonds both have a much smaller resistance ( $< 1\Omega$ ) than the sample ( $\sim 1000\Omega$ ), and as they are not expected to exhibit any significant magnetoresistance, their total contribution to the magnetoresistance will be negligible.

When measuring small variations in the magnetoresistance, it is important to take into account both the resolution of the instrumentation, and any bolometric effects that may drown out, or be confused for, the desired signal. The accuracy of a Keithley 2400 SMU is quoted by the manufacturer as 0.012% (or 6 and a half significant figures). Using a sourced current value of 3 mA – representative of the higher end of currents used in the magnetoresistive measurements – for a sample with a resistance of 1 k $\Omega$ , one must use the 10 V range on the Keithley's input. Combined with the Keithley's measurement accuracy of 0.012%, this gives a minimum resolvable resistance change of 3.6  $\mu\Omega$  — or 1.2 mV. In practice, both the signal and noise levels are far in excess of this limit, so it is not expected that the resolution of the instrumentation to be a significant limitation in resolving the desired signal.

When performing measurements at high current densities, the sample will heat up and increase its resistance until it reaches a new stable temperature. This can have a significant effect on the resistance of the sample. For this reason 1) only relative changes in the magnetoresistance are meaningful to report, and 2) the sample must be allowed to come into thermal equilibrium before the measurement can proceed. This second point was achieved by applying the desired current to the device and waiting for the absolute resistance of the sample to stabilise before proceeding to the full measurement. Each magnetoresistance sweep was then performed multiple times. If there was any significant change in the sample resistance over time due to temperature changes, which usually manifests themselves as a gradient in the resistance over time and differences between the different sets of data, then the measurement was discarded and repeated until a repeatable set of data could be obtained.

This final point also enables the detection of changes to the sample's microscopic structure caused by the high current densities and heat produced during the experiment: for example, electromigration. As a final check against this possibility, each sample was measured at a low current density after the final measurement, and the magnetoresistance was recorded compared with its resistance at that same current density before the current sweep to ensure that its behaviour had not changed.

### 3.5 Low-energy muon spin-rotation

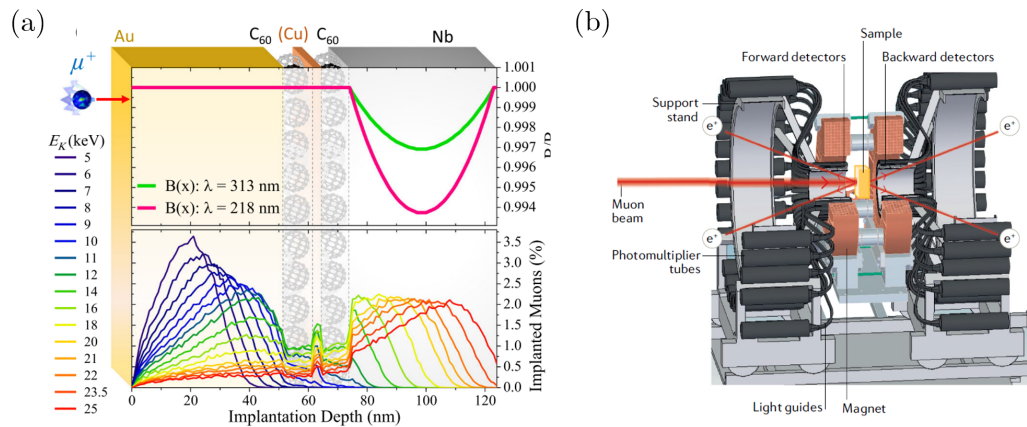


Fig. 3.14 (a) Implantation probability as a function of depth inside a thin film and average muon beam energy. Reproduced from [235]. (b) Typical muon beam detector setup. Muon beam is incident on the sample, and the resulting positron emissions are detected by detectors placed forwards and aft of the sample space. Reproduced from [236].

Low-energy muon spin-rotation is a technique for locally probing the magnetic field within a thin film as a function of depth into the sample. Included here is a short description of the basic workings of this measurement technique, as not all readers will be familiar with it and, although not employed here explicitly, it forms an important part of the claimed evidence for the observation of spin-triplet Cooper pairs in Nb/C<sub>60</sub>/Cu/C<sub>60</sub> heterostructures. These heterostructures are investigated in Chapter 4.

The basic principles are as follows. First, a beam of spin-polarised muons is fired at a thin-film sample. These muons typically have a few keV in energy in the low-energy variant used in thin films. The energy of the muons determines the depth at which they ‘implant’ in the sample, where they rapidly thermalise (Figure 3.14a). There, their magnetic moments then oscillate at the Larmor frequency,  $\omega_L = \gamma\mu_0 H$ , around the local magnetic field,  $\mu_0 H$ , until they decay, with a lifetime of around  $2\mu\text{s}$ . Once they decay, they emit positrons preferentially in the direction of their magnetic moment. By detecting these positron emissions, the magnetic moment of the cloud of muons as a function of time can be

determined, and from their precessional frequency, the strength of the magnetic field [237]. Consequently, the local magnetic field can be calculated by measuring the Larmor frequency of the muons from the time-varying frequency of the detection of their positron emissions at different positions relative to the sample. By tuning the energy of the beam, the implantation depth can be tuned, and the magnetic field inside a thin-film sample measured locally with a resolution determined by the stopping profile of the muon beam.

The time evolution of the number of positrons detected per unit time,  $N_i(t)$ , at a detector positioned parallel to a given axis,  $i$ , can be described by the expression:

$$N_i(t) = N_0 \exp\left(-\frac{t}{\tau_\mu}\right) (1 + a_0 P_i(t)) \quad (3.10)$$

where  $N_0$  is a measure of the number of muons in each muon packet,  $\tau_\mu$  is the muon lifetime,  $P_i(t)$  is the muon spin polarization along a given direction; the direction between the sample and the position of the detector, and  $a_0$  is an empirical constant that depends on the experimental setup [236]. If one can determine  $P_i(t)$  with sufficient accuracy, it should be possible to determine the magnetic moment experienced by the muons at a given spatial location and time. This is typically achieved by measuring the asymmetry in the number of muons recorded over time (the count) and two oppositely position detectors, forwards and backward of the sample space (Figure 3.14b). This gives a good measure of the polarisation as the positrons are emitted preferentially in the direction of the muon spin polarisation, leading to an asymmetry in the count.

For a given muon source-detector configuration, experiments are broadly classified based on the direction of the external field applied across the sample space during the measurement. No field, a field longitudinal to the incoming muon polarisation, a field transverse to the incoming muon polarisation, or a field that cancels out any field inside the sample space to produce a net zero field, can all be applied during the experiment. In Chapter 4, the experiment performed that forms the basis of this work utilised a transverse external field

during the measurement, as is often employed in measurements on superconducting samples [236]. Hence, it is this case that will be focused on here, although the principles are similar across all variants.

In the case of a transverse external magnetic field,  $P_i(t)$  is related to the asymmetry,  $A_\mu$ , in detection between the number of counts measured by two detectors placed on opposite sides of the sample space by the formula:

$$P_i(t) = A_\mu(t) \cos(\gamma_\mu B_T t + \psi) \exp(-\lambda t) \quad (3.11)$$

where  $\gamma_\mu$  is the muon's gyromagnetic ration,  $B_T$  is the external transverse magnetic field,  $\psi$  is a phase constant, and  $\lambda$  is the depolarisation rate [235]. The oscillatory term in (3.11) represents the muons' precession about the external field, and the depolarisation term relates to the loss of coherency in the muon beam over time — typically due to interactions with nuclear magnetic moments. In order to determine  $P_i(t)$  with any accuracy, it is necessary to capture millions of muon decay events with a sufficient time accuracy to resolve the rotation of their magnetic moments (Figure 3.15a). From this, it is possible to determine the asymmetry in the probability of a given positron being detected in either the forward or the backwards detector, and from this the polarisation along that axis. The asymmetry in the detection rate between the two detectors in a typical experiment is plotted in Figure 3.15a.

Figure 3.15b shows a damped oscillating dependence of the asymmetry on time. By spectrally analysing this signal (typically using either Fourier transform or maximum entropy methods), the Larmor frequency of the decaying muons can be determined, and hence recover the strength and direction of the local magnetic field.

In practice, analysing muon spin rotation data is often much more challenging than the basic picture presented above. For instance, the notion that this measurement is 'local' is clearly somewhat problematic given the relatively broad (relative to the extent of the sample) distribution of stopping distances for a given muon energy (see Figure 3.14a). Reconstructing

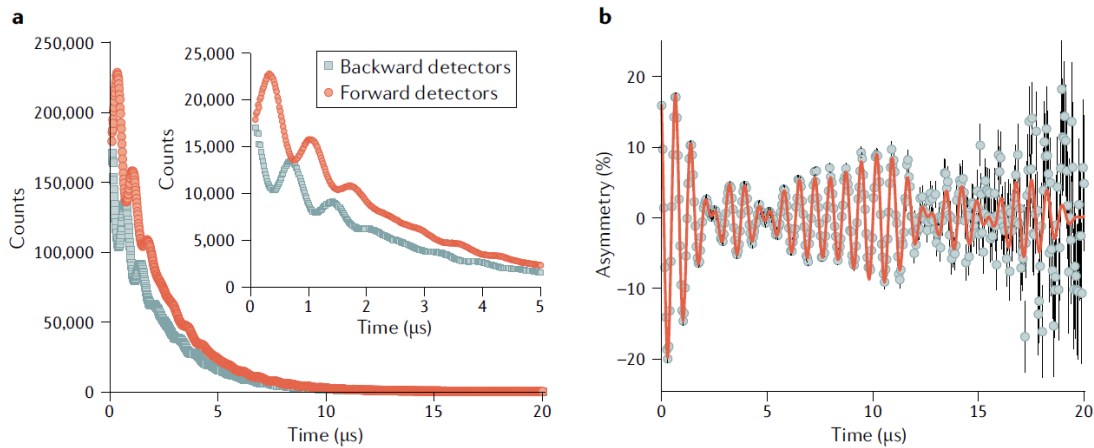


Fig. 3.15 (a) Number of muons' detected (count) at two detectors placed forwards and aft of the sample under study as a function of time after the initial muon beam pulse. (b) Asymmetry between the two detectors' counts over time. By spectrally analysing this signal, the Larmor frequency of the muons can be determined, and hence the local magnetic field they experience. Figure reproduced from [236].

a local magnetic field distribution from this measurement with any given accuracy can therefore be challenging. The simple picture of independent muons rotating around a local magnetic field can also be violated. A common complication is that muons may not only exist within the material as an isolated, and effectively independent, muon but may also combine with electrons inside the material to form a bound, hydrogen-like, atom known as muonium. They may also form chemical bonds with the material under certain conditions. These new states of the muons inside the material can influence the interpretation of the data collected and must be carefully considered when analysing each data set. The interested reader can consult references such as [236] for additional details.



## Chapter 4

# In search of spin-triplets at metal-organic interfaces

*In recent years there has been some interest in the properties of metallic-molecular interfaces for spintronic applications. It has been shown that a  $C_{60}$  (fullerene) thin-film can induce ferromagnetic order at the interface with the bulk-paramagnet Cu (and Mn), and that the spin-orbit coupling at Pt/ $C_{60}$  and Ta/ $C_{60}$  interfaces can be sizeably enhanced, increasing the spin-Hall magnetoresistance and the spin-Hall angle. Recently, it has been reported that a  $C_{60}/Cu/C_{60}$  layer may be able to act as a 'spin-converter interface' when placed adjacent to a superconducting thin-film, acting to rotate the spin-singlet Cooper pairs native to the conventional superconductor into spin-triplet Cooper pairs. Chapter searches for evidence of the presence of a spin-triplet Cooper pair condensate in a Nb/ $C_{60}/Cu/C_{60}$ /Permalloy heterostructure via spin-pumping FMR measurements.*

*Instead of finding evidence of a spin-triplet Cooper pair condensate, however, it is found that the ferromagnetic moments in the permalloy become strongly coupled to the superconducting condensate below the transition temperature, resulting in strong hysteretic behaviour in its FMR response, both with respect to temperature and magnetic field. This coupling is revealed result from the formation of a vortex state in the adjacent superconducting layer.*

*More specifically, it is caused by an instability of the vortex population to the formation of thermomagnetic avalanches, or flux jumping, a phenomenon that should be energetically forbidden in thin-film Nb under these experimental conditions. The existence of this anomalous vortex state suggests some kind of modification of the superconducting properties by the  $C_{60}$ , and that the low-energy muon spin-rotation measurements, purported to show evidence of spin-triplet Cooper pairs, may in fact have been measuring the magnetic moment of the superconducting vortices forming in this anomalous vortex state.*

## 4.1 Introduction and scientific background

Molecular interfaces first attracted the interest of the spintronics community after it was demonstrated that molecular-ferromagnetic structures could be used as effective spin-tunnel junctions in a FM/M(molecular)/FM heterojunction. It was discovered that these devices could exhibit large local magnetoresistance [238]: the dependence of the device's resistance on the relative orientation of the ferromagnetic terminals. The local magnetoresistance was measured over areas tens of nm<sup>2</sup> large using an atomic-force microscope (AFM) tip. In some cases, it was possible to achieve local magnetoresistances of around 300%, comparable with the best performing inorganic devices.

This was explained as resulting from the hybridisation of the local molecules' HOMO (highest-occupied molecular orbital) with the conduction band of the ferromagnetic terminals. This hybridisation is expected to vary, not only with the molecular composition, but also with the local orientation and arrangement of said molecules. These results were of great interest to the spintronic community, not so much because of the overall performance of the device, but because of the physical mechanism behind it and the potential freedom it offered experimentalists for device design and optimisation [238, 239]. By carefully selecting the molecules used for the molecular interface out of the effectively limitless number available, and perhaps even their orientation, stacking or arrangement, it may be possible to tune the

properties of ferromagnetic-molecular interfaces in order to deliver devices displaying novel phenomena and exciting performances.

That was the basic promise, and whilst exploiting ‘spinterface’ science’s potential is still an ongoing project, there have been a number of interesting discoveries from a fundamental physics and device perspective [229, 235, 238–243]. For a review of the field’s progress and fundamentals, see [240] and the references therein.

This chapter will be investigating the behaviour of metallic-molecular interfaces using  $C_{60}$  (fullerene) molecular films.  $C_{60}$  is a natural choice of molecule for spintronic applications as it has good energy matching of its molecular  $\pi$ -bonded  $p$  electrons with the  $3d_z$  electrons of common transition metal ferromagnets [229] (Fe, Co, etc.). The result of this interaction is the transfer of charge between the metallic layer and the molecular layer [229, 240]. This modifies the Fermi occupancy at the interface because of the difference in the work function of the molecular HOMO and the conduction band electrons, an effect that is quickly quenched in the metal as you enter into the bulk. Additionally, the molecular states hybridise with the metallic states, resulting in the formation of new hybrid states localised to the interface that may come to dominate the properties of the device [240]. Consequently, the properties of the resulting hybrid thin-film structure may differ substantially from what one would expect naïvely from the properties of the bulk materials in isolation, and there is a growing body of work showing how  $C_{60}$  thin-films can be used to modify and improve spintronic devices [229, 235, 243, 244].

Of particular relevance to this work is the observation that the interaction between  $C_{60}$  and the transition metals Cu and Mn is capable of inducing ferromagnetism in the previously bulk-paramagnetic materials [229, 244]. The evidence for this interaction follows from magnetometry and low-energy muon spin rotation measurements in heterostructures composed of thin ( $\leq 3$  nm) Cu (or Mn) layers, sandwiched in between two 15 nm  $C_{60}$  films. Magnetometry measurements detected the presence of a ferromagnetic moment that

disappears when the Cu layers are separated from the  $C_{60}$  by a 3nm layer of Al on either side. Low-energy muon spin-rotation measurements (see Section 3.5) reveal that this moment is localised inside the Cu layer, and that it is rapidly quenched with increasing Cu layer thickness, vanishing when the Cu layer is just 4 nm thick after a peak at 2.5 nm. Consequently, the detected moment can be unambiguously attributed to a ferromagnetic order inside the Cu itself.

This observation is still not well understood theoretically. Density functional theory simulations based on an itinerant electron model of ferromagnetism predict an increase in the density of states at the Fermi level due to the aforementioned charge transfer. However, the calculated change in the density of states was insufficient to overcome the Stoner criteria. Nevertheless, the experimental evidence is compelling, suggesting that some kind of charge transfer mechanism is causing magnetic ordering/hardening localised at the  $C_{60}/Cu$  interface.

It was these ferromagnetic  $C_{60}/Cu/C_{60}$  layers that were proposed as a spin-converter interface ( $I_{S-C}$ ) in a recent work claiming to have detected evidence of spin-triplets in Nb[50]/ $C_{60}$ [10]/Cu[3]/ $C_{60}$ [10] heterostructures (the numbers in brackets are the layer thicknesses in nm). In the presence of a spin-triplet condensate, the sign of the Meissner effect may change from diamagnetic to paramagnetic. By measuring the local magnetic field using low-energy muon spin rotation measurements, Rogers et al. [235] were able to detect a local paramagnetic Meissner screening signal, which they attribute to the presence of a spin-triplet Cooper pair condensate inside the heterostructure.

They began with transport measurements on Nb/ $C_{60}$ /Metal heterostructures, which showed that, below the transition temperature of Nb, the adjacent  $C_{60}$  layer becomes superconducting via the proximity effect. The condensate extends into the  $C_{60}$  over a characteristic length scale of  $30 \pm 9$  nm. This was measured via the suppression of  $T_C$  with decreasing  $C_{60}$  thickness in Nb/ $C_{60}$ /Metal heterostructures [235].

Low-energy muon spin rotation experiments were performed in two device architectures: Nb[50]/C<sub>60</sub>[10]/Cu[3]/C<sub>60</sub>[10]/Au[50]/C(apping)L(ayer) and Nb[50]/C<sub>60</sub>[20]/Au[50]/CL. The Au layers act as a target for the muons to implant in, and by using different muon beam energies the implantation depth can be varied (Figure 4.1a). The local field, measured at a variety of implantation depths (energies) is shown in Figure 4.1b, and is consistent with a London model with a London penetration depth of 313 nm and 218 nm in the samples with and without Cu respectively. This shows that there is a substantial modification of the superconducting parameters between the two samples that cannot be explained by suppression of the superconductivity due to the ferromagnetism in the Cu layer; as this would suppress the transition temperature when it is in fact found to be slightly larger for the sample with Cu.

The low-energy muon rotation experiments were repeated on Nb[50]/C<sub>60</sub>[30]/Au[10]/C<sub>60</sub>[20]/Au[10]/C<sub>60</sub>[20]/Au[10] (the control) and Nb[50]/C<sub>60</sub>[15]/Cu[4]/C<sub>60</sub>[15]/Au[10]/C<sub>60</sub>[20]/Au[10]/C<sub>60</sub>[20]/Au[10] structures using two beam energies: 9 keV, which implants primarily in the layer of Au above the C<sub>60</sub>[30] /  $I_{S-C}$  layer, and 20 keV, which implants in the Nb superconductor itself (Figures 4.1c and 4.1e). In both samples, the 20 keV beam measures a decrease in the local magnetic field compared to the normal state due to the Meissner screening in the type-II superconducting Nb (Figures 4.1d and 4.1f). However, this reduction is decreased by a factor of two in the sample with the  $I_{S-C}$  compared to the control. In the control, the 9 keV beam measures a local field that either stays the same as in the normal state, or slightly decreases (Figure 4.1d). As the propagation length of the Cooper pairs in the C<sub>60</sub> layer is about the same length as the layer thickness, any screening effect is much reduced compared to the 20 keV beam. In contrast, the 9 keV beam in the sample containing the spin-converter interface shows an *enhanced* local magnetic field compared with the normal state (Figure 4.1f).

An enhanced local field is indicative of a *paramagnetic*-Meissner effect, a signature of a Cooper pair condensate containing a greater density of spin-triplet Cooper pairs,  $n_T$ , than

spin-singlets,  $n_S$  [245–247]: i.e.  $n_T/n_S > 1$ . It is this evidence that forms the basis of the claim that the spin-converter interface can produce a spin-triplet condensate, though it is not presently well understood how the  $I_{S-C}$  could act to rotate the native spin-singlet Cooper pairs in the Nb into spin-triplets. The mechanism may involve a non-uniform magnetic texture in the ferromagnetic Cu, or a misalignment of the spin-orbit coupling field in the  $C_{60}$  and the exchange field in the Cu.

In the following Chapter, FMR measurements will be used to search for evidence of these spin-triplets on samples with and without the  $I_{S-C}$ , above and below the transition temperature. Instead of finding evidence for spin-triplets however, a substantial and anomalous population of magnetic vortices in the superconducting condensate is found. These vortices have a strong influence on the magnetic resonance behaviour of the devices, and may prompt a reinterpretation of the low-energy muon spin-rotation measurements.

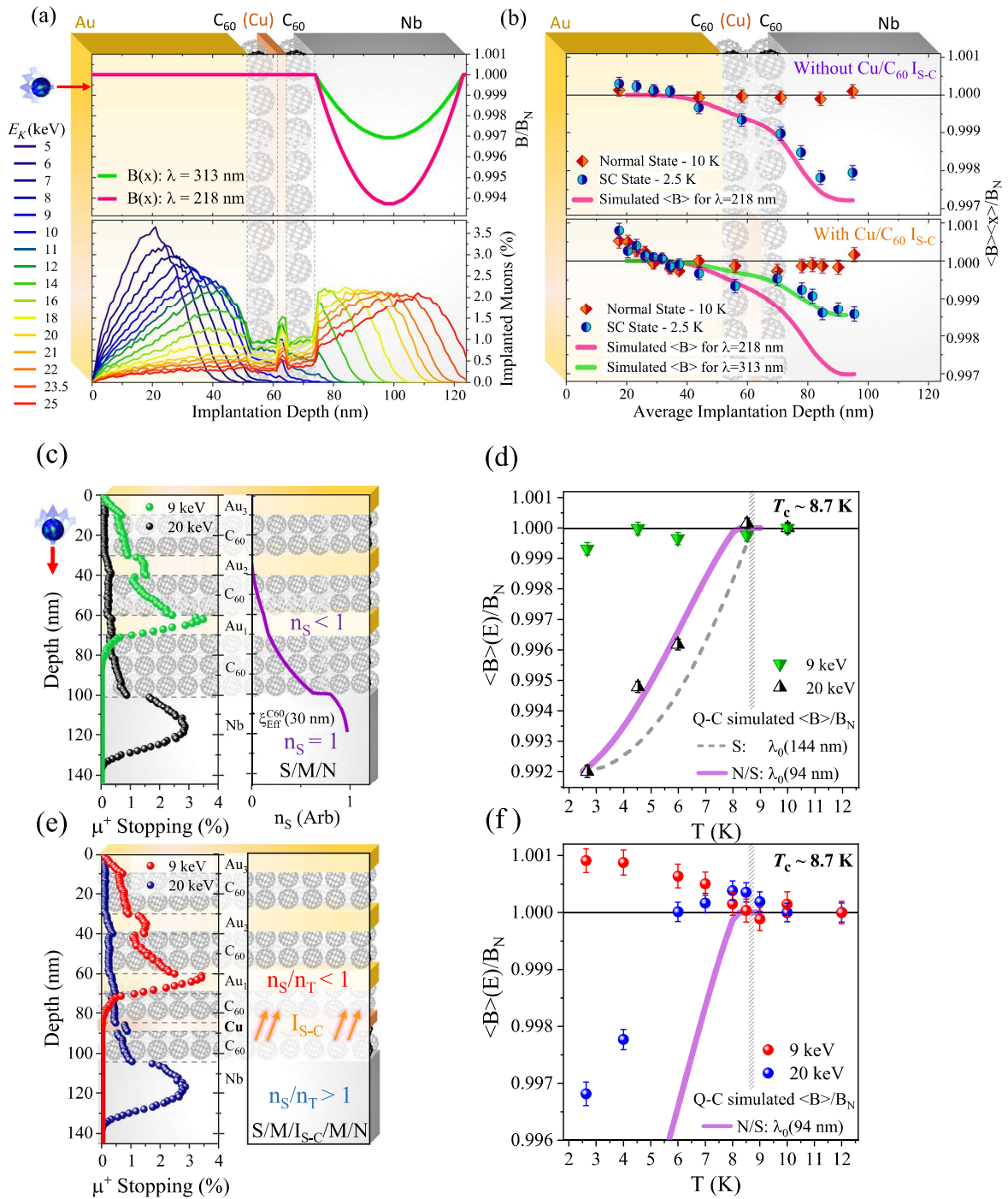


Fig. 4.1 (a) (top) The simulated local magnetic field for a London model with a penetration depth of 313 nm and 218 nm. (bottom) Fraction of muons implanted at a given depth for a range of muon beam energies. (b) Local magnetic field measured by muon spin-rotation and the associated fits to the London model. (c) (left) Fraction of muons implanted at a given depth for 9 keV and 20 keV muon beams in the sample without the  $I_{S-C}$ . (right) Calculated decay of the number density of Cooper pairs induced in the sample due to the proximity effect with distance from the Nb superconductor. (d) Local magnetic field variations with temperature (relative to the field measured in the normal state) inside the sample without the  $I_{S-C}$  for two muon-beam energies in an in-plane field of 30 mT.

Fig. 4.1 (*previous page*) (e) (left) Fraction of muons implanted at a given depth for 9 keV and 20 keV muon beams in the sample with the  $I_{S-C}$ . (right) Cartoon showing the proposed effect of the  $I_{S-C}$  on the relative proportion of spin-singlet ( $n_s$ ) and spin-triplet ( $n_t$ ) Cooper pairs. (f) Local magnetic field variations with temperature (relative to the field measured in the normal state) inside the sample with the  $I_{S-C}$  for two muon-beam energies in an in-plane field of 30 mT. The 9 keV beam shows a slight paramagnetic response, attributed to a significant spin-triplet Cooper pair condensate inside the sample. Figure reproduced from [235].

## 4.2 Experimental design

Section 2.5.2 contains an in-depth explanation of the effect the presence of spin-triplets has on the measured FMR linewidth as a function of temperature above and below the superconducting transition. To summarise, in a well-behaved metallic-ferromagnet/superconductor heterostructure containing a significant spin-triplet condensate, one would expect the linewidth of the ferromagnetic resonance to exhibit a reasonably sharp increase below the transition temperature due to the ability of the spin-triplets to carry spin-angular momentum produced via spin-pumping from the precessing ferromagnet away from the ferromagnet/superconductor interface. In contrast, should the superconductor only contain spin-singlet Cooper pairs, it would be expected instead to see a decrease in the linewidth below the transition temperature as Andreev reflection does not allow for the transmission of angular momentum across the interface, quenching the influence of spin-pumping on the frequency-dependent damping.

The ferromagnetic resonance linewidth of two samples will be measured, sample  $I_{S-C}$  and sample  $C_{60}$ , fabricated by Alistair Walton from the University of Leeds. Their structures are shown in Table 4.1:

Sample $I_{S-C}$	(Si/SiO <sub>2</sub> )Nb[49] C <sub>60</sub> [10]Cu[2.7]C <sub>60</sub> [10]Py[7.7] Al[10]C <sub>60</sub> [20]Al <sub>2</sub> O <sub>3</sub> [2]
Sample C <sub>60</sub>	(Si/SiO <sub>2</sub> )Nb[49] C <sub>60</sub> [20]Py[7.7] Al[10]C <sub>60</sub> [20]Al <sub>2</sub> O <sub>3</sub> [2]
Sample C	(Si/SiO <sub>2</sub> )Nb[49] C <sub>60</sub> [10]Cu[2.7]C <sub>60</sub> [10] Al[10]C <sub>60</sub> [20]Al <sub>2</sub> O <sub>3</sub> [2]

Table 4.1 Structures of the proposed spin-converter interface samples. The thickness of the metallic layers was measured by x-ray reflectometry, and the thickness of the C<sub>60</sub> layer by a quartz microbalance during deposition.

Precise details of the fabrication procedure can be found in Section 3.2.1. Samples  $I_{S-C}$  and C<sub>60</sub> both contain a 50 nm layer of the type-II superconductor Nb and an 8 nm layer of ferromagnetic permalloy (Py), separated from one another by either an  $I_{S-C}$  structure (sample  $I_{S-C}$ ), or 20 nm of C<sub>60</sub> (sample C<sub>60</sub>). Sample C is a reference sample, used to characterise the ferromagnetic properties of the  $I_{S-C}$  structure without interference from the Py layer.

FMR measurements will be performed on the two samples, samples  $I_{S-C}$  and samples C<sub>60</sub> (Table 4.1), using a stripline FMR set-up (see Section 3.3.1). The sample is contained within a liquid-Helium cryostat equipped with a superconducting magnet that allows the external magnetic field in-plane to be varied in one direction, and whose temperature is controlled using a heater connected to a PID controller.

## 4.3 Results

### 4.3.1 Initial sample characterisation

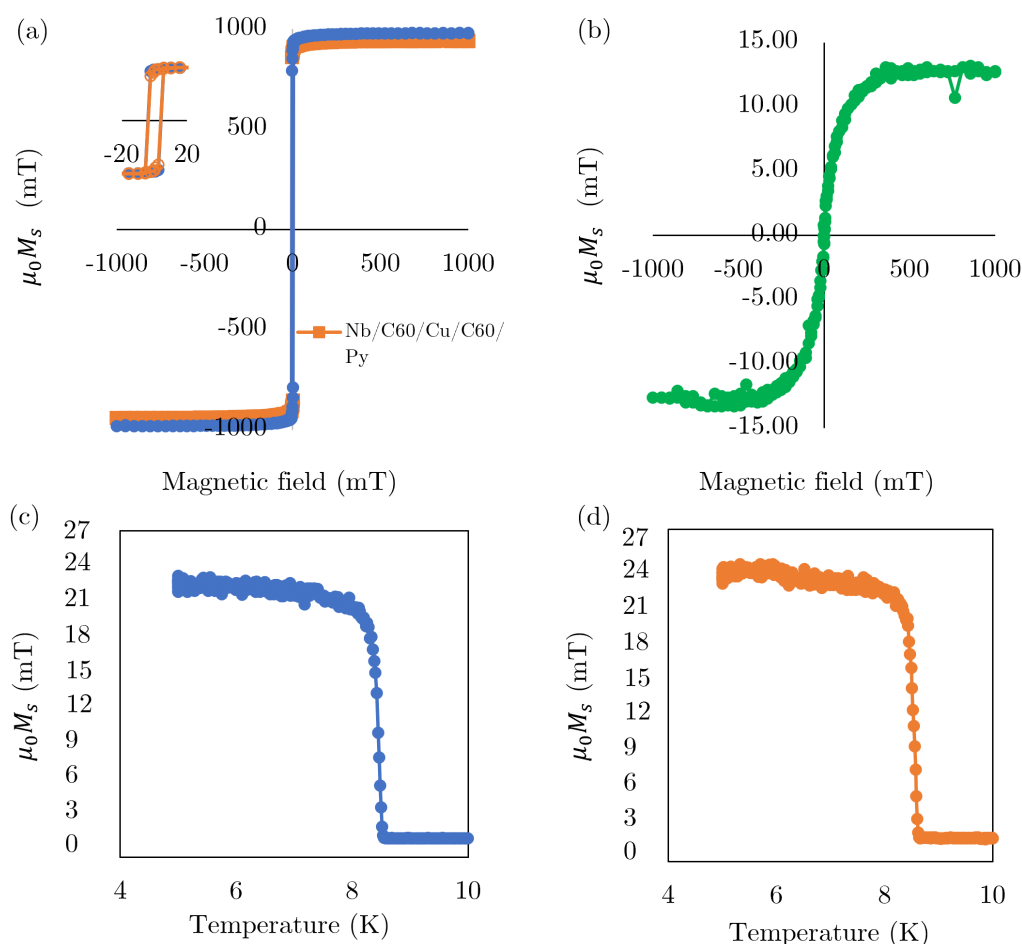


Fig. 4.2 (a) Magnetisation versus field for sample  $I_{S-C}$  (orange dots) and sample  $C_{60}$  (blue dots) at 300 K. Insert: Magnetisation versus field at low fields for both samples. (b) Magnetisation versus field for sample C (no Py, magnetic moment is from the  $I_{S-C}$  only) at 300 K. (c) and (d) Magnetisation (due to the Meissner effect) versus temperature for samples  $C_{60}$  and  $I_{S-C}$  respectively, showing a transition temperature of around 8 – 8.5 K. All measurements were performed using SQUID magnetometry by Alistair Walton from the University of Leeds.

Post fabrication, the critical temperature and magnetic moments ( $M_s$ ) of the samples in Table 4.1 were measured by SQUID magnetometry by Alistair Walton from the University

of Leeds (Figure 4.2). The critical temperatures and magnetic moments extracted from these measurements are shown in Table 4.2.

Both samples exhibit a superconducting transition around 8.5 K, and similar magnetic properties of their Py layers.

Sample	$T_C$ / K	$\mu_0 M_s(\text{Py})$ / mT	$\mu_0 M_s(\text{Cu/C}_{60}\text{/Cu})$ / mT
Sample $I_{S-C}$ *	$8.25 \pm 0.05$	$940 \pm 25$	N/A
Sample $C_{60}$	$8.55 \pm 0.05$	$980 \pm 25$	N/A
Sample C	$8.25 \pm 0.05$	N/A	$12.7 \pm 0.5$

Table 4.2 Sample properties measured by SQUID magnetometry. \*The measurement of the saturation magnetisation of Py in this sample assumes the magnetic moment from the  $I_{S-C}$  is negligible in comparison with the moment from Py.

### 4.3.2 Temperature and Magnetic field dependence of the linewidth

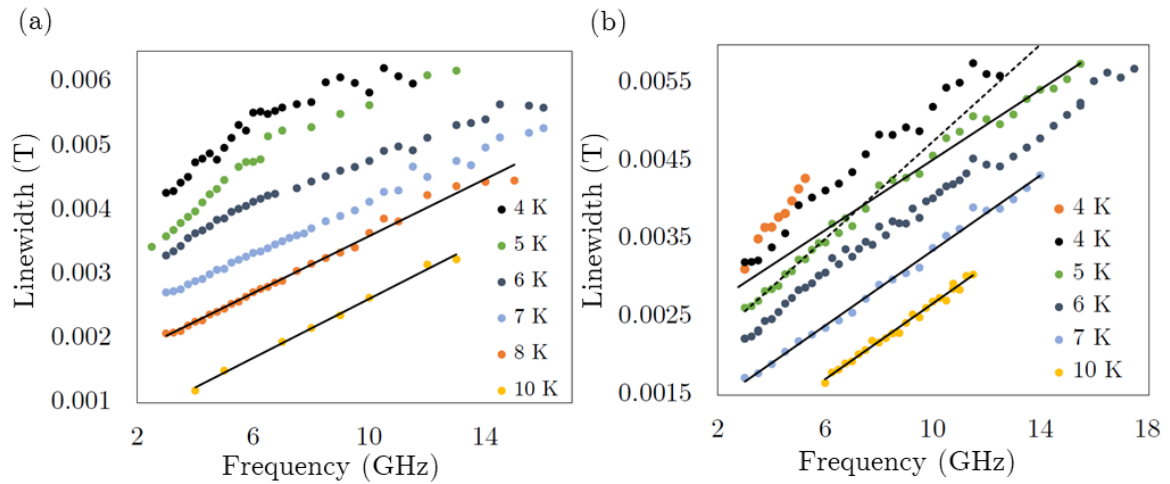


Fig. 4.3 Linewidth versus frequency for (a) sample  $I_{S-C}$  and (b) sample  $C_{60}$  (data below  $T_C$  was collected after zero-field cooling below the transition temperature). An arbitrary offset has been added to each temperature to separate the curves clearly. Above and close to the transition temperature, ( $\sim 8.5$  K), the linewidth's frequency dependence is well described by a linear relationship as expected from the usual Gilbert damping expression for the linewidth (see linear lines of best fit). Beyond around 6 K for both samples, a shoulder develops in the frequency dependence.

In order to detect evidence of a spin-triplet condensate, the Gilbert damping was measured above and below the transition temperature via spin-pumping FMR experiments. Figures 4.3a and 4.3b show the (in-plane) frequency dependence of the linewidth for a range of temperatures above and below the transition temperature for samples  $I_{S-C}$  and  $C_{60}$  respectively. Above the transition temperature, the samples behave as expected, showing a linear dependence of the linewidth on the frequency from which it is possible to extract the Gilbert damping and inhomogeneous broadening (see lines of best fit to high T data in Figure 4.3). Below the transition temperature, however, a sizeable divergence from the expected linear frequency dependence is seen. At low frequencies, the linewidth depends linearly on frequency, before a shoulder appears and the frequency dependence switches to a new, linear, dependence with a lower gradient.

### **Low-frequency gradient in the linewidth**

This nature and position of this shoulder depended on both the strength of the magnetic field applied and the temperature. Figure 4.3 clearly shows that in the field-cooling case, the shoulder becomes more pronounced as one goes further below the transition temperature. Because of the two distinctly linear regions, it is worth considering if meaningful information can be obtained from the gradient of the low-frequency region. However, the gradient of the linewidth and position of the shoulder were found to be strongly dependent on the experimental conditions used to measure the data in such a way that the gradient of the linewidth in this regime cannot be accurately interpreted in terms of the presence (or otherwise) of spin-triplets.

In particular, when conducting an FMR measurement at constant frequency, it is necessary to sweep the field from below to above the resonance over a certain range. It was found that in the low frequency region, the recorded linewidth strongly depended on how far past the resonance the magnetic field was swept when recording the data. As the data was

collected from low to high frequency successively, this means that the recorded linewidth was dependent on the highest previously applied magnetic field. This suggests that there is a magnetic origin to this phenomena, and also meant that the gradient in the linewidth could not be used to extract the Gilbert damping in this regime.

### **Non-linear linewidth dependence below $T_C$**

In order to find evidence of spin-triplet Cooper pairs from the temperature dependence of the linewidth, it will be necessary to understand and model the physical mechanism behind this unusual frequency dependence. A model of interaction between the superconducting condensate and the magnetic moments in the Py based on the formation of stray vortexes within the superconducting layer will be proposed, ruled out as energetically impossible in previous analysis [235]. From this, it is propose that the purported evidence for spin-triplet Cooper pairs, is in fact signal resulting from the formation of these vortices instead.

Non-linear frequency dependencies are usually the result of magnon-magnon scattering induced damping caused by sample inhomogeneities. The phenomenology of this mechanism is described in Section 2.2.2. The precise frequency dependence of the magnon-magnon scattering linewidth contribution ( $\Delta H_{M-M}$ ) depends on the model of inhomogeneity one adopts [248], and is in general non-trivial to calculate. A commonly adopted model is to assume the inhomogeneity is a result of pits and troughs in the magnetic interface due to non-zero surface roughness [103, 109]. It is expected that for these samples the surface roughness will be around 1 nm for a film thickness of 8 nm [229, 244, 249], which is a considerable fraction of the total film thickness. Consequently, one might expect a similar mechanism to be in operation here. Adopting this model results in the following frequency dependence of the linewidth [103, 248]:

$$\Delta H_{M-M} = \Gamma \arcsin \left( \frac{\sqrt{\omega^2 - \omega_0^2} - \omega_0}{\sqrt{\omega^2 + \omega_0^2} + \omega_0} \right) \quad (4.1)$$

where  $\Gamma$  relates to the strength of the magnon-magnon scattering and is treated as a free parameter, and  $\omega_0 = \gamma_0(K_{\perp} - M_s/2) \approx \gamma_0 M_s/2$ , which follows as it is not expected to see significant PMA in these samples. This is confirmed by the excellent agreement of the effective magnetisation,  $M_{eff} = M_s - H_{\perp}$ , in the Kittel formula fit to FMR measurements of the resonance frequency of the samples (see Figure 4.4) and the room temperature magnetometry measurements (Table 4.2).

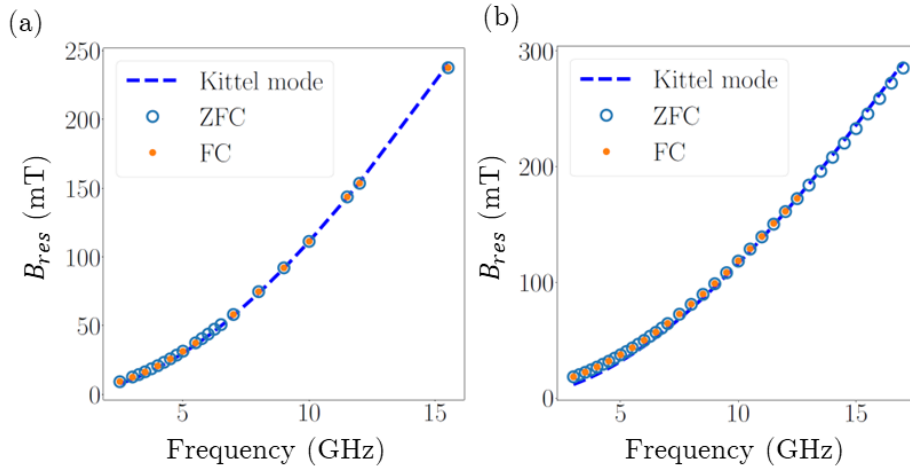


Fig. 4.4 Frequency dependence of the resonance field for (a) sample  $I_{S-C}$  at 5K in the ZFC (open blue circles) and FC (orange dots) case. Likewise for sample  $C_{60}$  (Nb/ $C_{60}$ /Py) (b). Dashed blue line shows a fit to the Kittel formula including only the thin-film demagnetisation term (as a free parameter), where  $M_s = 1.03$  T (a) and  $M_s = 0.98$  T (b), in excellent agreement with the room-temperature magnetometry measurements (Table 4.2).

Figure 4.5c (insert) shows an exemplary fit of the linewidth data using a model of inhomogeneous broadening + Gilbert damping + magnon-magnon scattering:

$$\Delta H = \Delta H_0 + \frac{\alpha}{2\pi\gamma_0}\omega + \Gamma \arcsin \left( \frac{\sqrt{\omega^2 + \omega_0^2} - \omega_0}{\sqrt{\omega^2 + \omega_0^2} + \omega_0} \right) \quad (4.2)$$

The fit fails to reproduce the experimentally measured linewidth frequency dependence. Additionally, if magnon-magnon scattering were the dominant cause of the non-linear linewidth dependence, it should be expected to show up in the linewidth dependence above

$T_C$  as well, which is well fitted by the usual Gilbert damping expression for  $\Delta H$  (although this does not necessarily rule out some ferromagnet-superconducting condensate interaction enhancing this effect below  $T_C$ ).

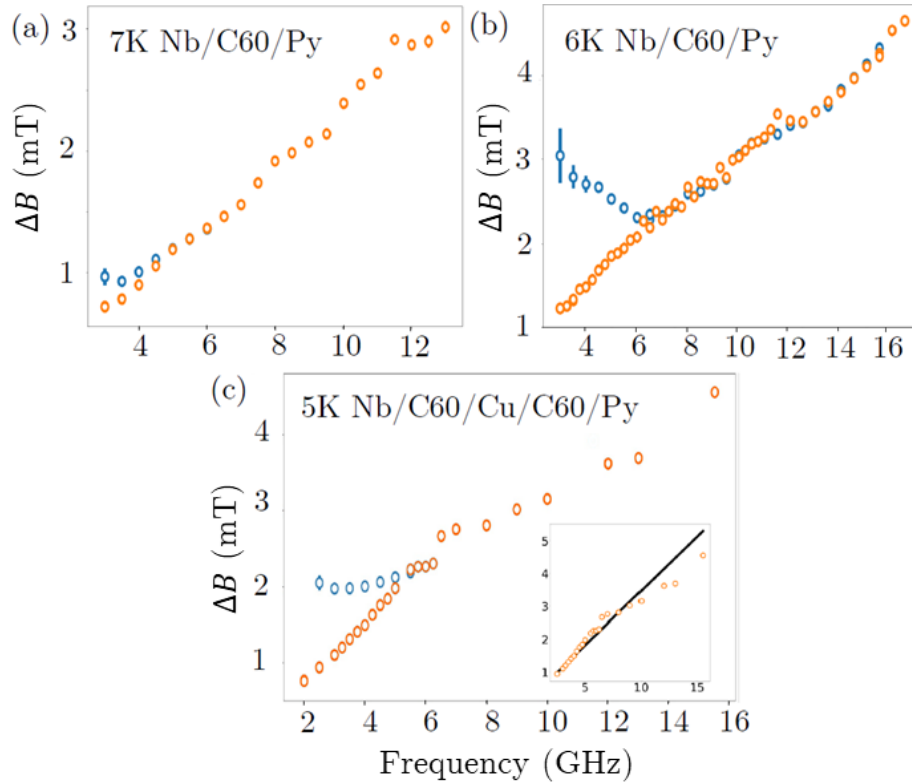


Fig. 4.5 Exemplary linewidth versus frequency curves for (a) sample  $C_{60}$  at 7 K, (b) sample  $C_{60}$  at 6 K, (c) sample  $I_{S-C}$  at 5 K, in the zero-field cooled case (orange circles) and field cooled (0.5 T saturating field applied prior to the measurement) case (blue circles) and (insert) fit of the (ZFC) linewidth to magnon-magnon scattering model. Below the transition temperature (8 K), field cooling increases the measured linewidth substantially at low frequencies, an effect that diminishes as the frequency/resonance field is increased until the two curves are indistinguishable.

In addition to this unusual linewidth dependence, a significant difference between the FMR response of the device when field cooling (FC) versus zero-field cooling (ZFC) below the transition temperature is observed. Figure 4.5 shows the frequency dependence of the linewidth after a saturating magnetic field of 0.5 T had been applied to the sample *prior* to frequency sweep above and below the transition temperature. The sample is then allowed

to relax into its remnant state at zero field before the measurement. The measurement then proceeds as normal by sweeping the magnetic field about each resonance field and measuring the response at fixed frequency for each frequency in ascending frequency order.

Above the transition temperature, the application of a large field prior to measurement has no effect on the frequency dependence of the linewidth. This is consistent with the expected behaviour of permalloy, which has a saturation field ( $\mu_0 H_{sat}$ ) of at most a few mT (see Figure 4.2a), so one would not expect the application of a large field prior to the frequency to have any significant impact when the resonance field of each frequency is already substantially in excess of the expected saturating field. In contrast, below the transition temperature, applying a saturating field prior to the measurement results in a significant change of the measured linewidth, particularly at low frequencies (and hence small resonance fields) and low temperatures.

The origin of this behaviour cannot be either paramagnetic or diamagnetic in origin, as once a large field has been applied below the transition temperature, it is not possible to recover the original zero-field cooled linewidths (orange circles in Figure 4.5) whilst remaining below the transition temperature: the linewidths remain permanently broadened. However, if the sample is heated up to above the transition temperature, then zero-field cooled back down below it, it is possible to recover the ZFC linewidths. Heating/cooling below the transition temperature has minimal effect on the linewidth once the sample has entered its 'remnant' state (i.e. experienced a large field that is then reduced to zero). Consequently, the hysteretic behaviour cannot simply be an effect that emerges in the permalloy natively, but rather can only be caused by a magnetic-field dependent coupling between the ferromagnetic permalloy and the superconducting condensate.

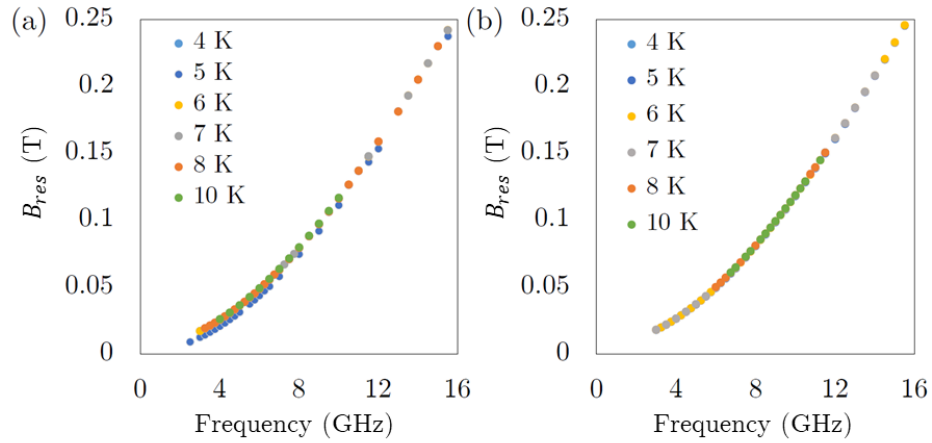


Fig. 4.6 Temperature dependence of the resonance field's ( $B_{res}$ ) frequency dependence above and below the transition temperature ( $\approx 8.5$  K) for sample  $I_{S-C}$  (a) and sample  $C_{60}$  (b). Neither sample shows a particularly strong temperature dependence, nor any signs of a particular dependence on the transition above/below  $T_C$ .

To further emphasize this point, Figure 4.6 shows the temperature dependence of the resonance frequencies of the permalloy ferromagnetic above and below the transition temperature. As there is no significant difference between the, any kind of ferromagnetic phase transition (e.g. to a ferrimagnetic state) in the permalloy can be ruled out as it would be expected to significantly affect the resonance frequencies. Additionally, the change in the linewidth cannot be attributed to the change in the resonance frequency and hence Gilbert damping.

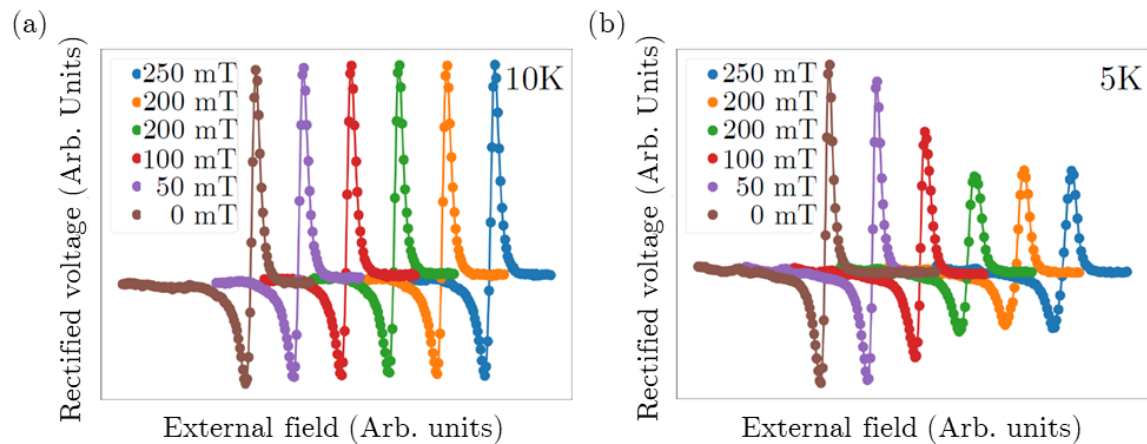
**Evidence of hysteretic behaviour of the FMR response:**

Fig. 4.7 Measured rectified voltages above (a) and below (b) the transition temperature for a range of fields applied prior to the measurement (legend) for sample  $C_{60}$  (Nb/ $C_{60}$ /Py) at a 5 GHz. Above the transition temperature, applying a larger field prior to the measurement has no effect. Below the transition temperature, applying a saturating field has a significant effect on the measured linewidth, up until around 100 mT. Each resonance curve has been offset in the x-axis for clarity.

Figure 4.7 shows the measured resonance curves as a function of the applied static field prior to the measurement at a fixed frequency (5 GHz). Applying progressively larger fields before each repeated measurement always results in a monotonic increase in the measured linewidth up until some sufficiently large field, at which point it settles at its final value. Figure 4.8 shows this enhancement in the linewidth between a ZFC and FC measurement, with the FC sample showing a broadened peak. This behaviour is repeatable across both samples for temperatures below  $T_C$  (particularly below 6 K and lower) (see also Figure 4.5).

Figure 4.9 shows the evolution of the line shape before/after a saturating field has been applied to the device at 6 K for a range of frequencies (sample  $C_{60}$ ), showing an entirely new peak appearing in the resonance spectrum close to the original resonance, and a deviation from the expected Lorentzian shape at larger frequencies, with a broadening of the low-field tail relative to the high field tail.

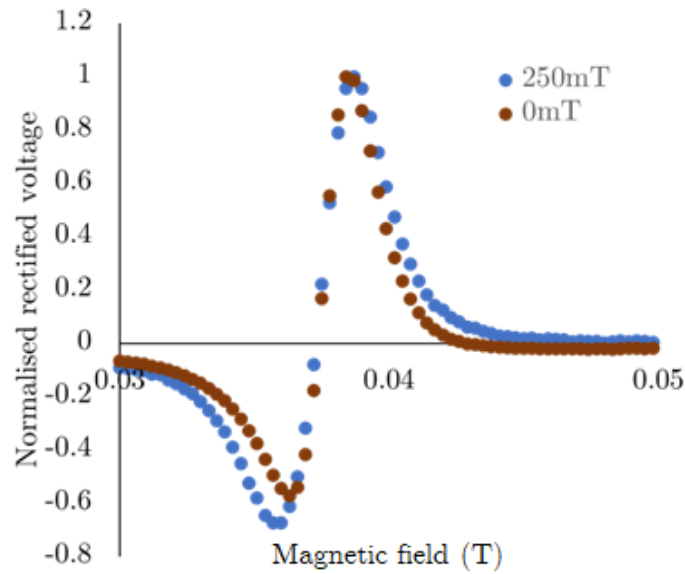


Fig. 4.8 Normalised rectified voltage of the FMR signal at 5 GHz and 5 K for sample  $C_{60}$  (Nb/ $C_{60}$ /Py) before and after a 250 mT external field is applied. After the field is applied, the linewidth of the signal appears to increase, whilst the resonance frequency remains unaltered.

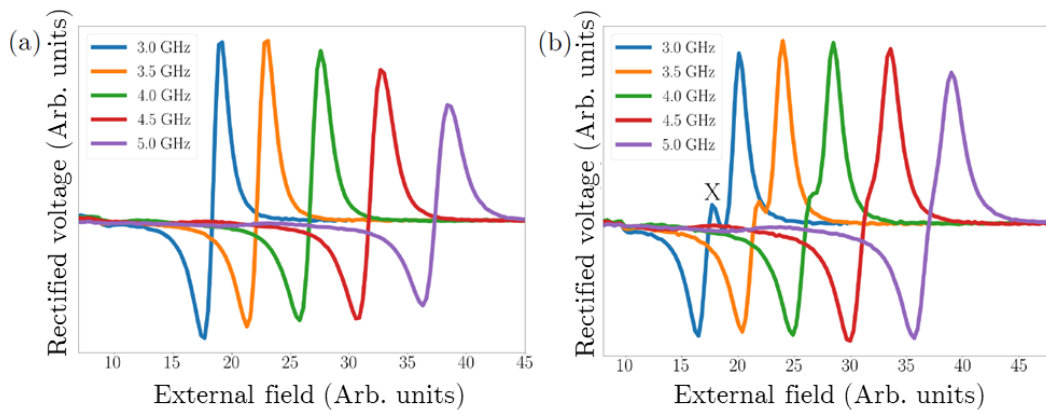


Fig. 4.9 Frequency dependence of the lineshape of sample  $C_{60}$  (without  $I_{S-C}$ ) at 6 K in the ZFC (a) and FC (0.5 T field applied before the measurement) (b) case. Applying a saturating field results in a substantial distortion in the lineshape such that at sufficiently low frequencies, a whole new peak appears in the output voltage (labelled by a cross in (b)).

These observations can be explained by a model of overlapping, but distinct, resonances, whose position relative to one another is somehow shifted due to the interaction of the superconductor and the ferromagnet by the application of a large magnetic field prior to the

measurement. The net output of the device is the superposition of these resonances, and this results in an increase in the measured linewidth as their resonance fields become spread-out and separated, as observed. If they become sufficiently separated, then their superposition would produce a multi-resonance spectrum, as in Figure 4.9b. Distinct resonances of this form can occur in a ferromagnet if the oscillations become localised, where the ferromagnet oscillates not as a single, uniform, mode, but rather as distinct localised modes [101, 108–110], and are typically a result of a sufficiently inhomogeneous effective field acting on the ferromagnet.

What remains to be determined what is mechanism is responsible for this localisation, and why this should cause the resonance peaks to display such strong hysteretic behaviour even at high (relative to  $H_{sat}$ ) magnetic fields at resonance. In the following sections, it is argued that this can be understood as resulting from an interaction between the stray fields of a superconducting vortex population, induced by the saturating field during FC, and the ferromagnetic Py.

### 4.3.3 Physical origin of the magnetic-superconductor interaction

The distortion in the lineshape at low frequencies (Figures 4.7, 4.5, and 4.8), and indeed in some cases additional peaks appearing in the spectrum (Figure 4.9), suggests that the magnetisation, rather than oscillating as a single, uniform, Kittel-like mode, is instead split up into localised oscillations of the magnetic moment, each with their own resonance field and linewidth. Localised precession can occur in FMR experiments if the magnetisation experiences highly inhomogeneous local magnetic fields. In this limit, the effect of inhomogeneities must be treated differently from the more common magnon-magnon scattering picture, where the inhomogeneities are sufficiently small that they can be treated as a perturbation to the single coherent, uniform precessional motion. This localisation causes the local magnetic moment to oscillate in domain-like patterns at its own resonance frequency about the local

magnetic field [101, 108–110]. Consequently, the observed resonance spectrum is not a single peak, but rather a superposition of many local oscillations, all slightly offset from one another and overlapping to produce a single, distorted and broadened resonance peak (Figure 2.2c). If the local magnetic fields are disparate enough, then additional resonances can also appear in the spectrum (Figure 4.9b).

Localised oscillations of this form have not previously been reported in the literature in otherwise homogeneous (as evidenced by the above- $T_C$  behaviour of the samples) SC/FM heterostructures. The closest observation is that of localised oscillations in nuclear magnetic resonance (NMR) measurements in a SC/FM heterostructure, where a similar distortion in the lineshape from the expected single resonance was observed in Ni/V/Ni trilayers in the superconducting (V) state [250] due to a spin-screening effect [251]. Their results are not directly comparable to ours, as in NMR the nuclei oscillate effectively independently whereas, in FMR, one considers the mutual oscillations of strongly coupled oscillators (the electronic spins), making NMR very sensitive to distortions in the lineshape due to local inhomogeneities. Consequently, such a mechanism should not be expected to be able to induce localised oscillations in the ferromagnetic moments, as the strength of the induced inhomogeneity would be far too weak: whatever mechanism is causing the magnetisation oscillations to localise must be of a hitherto unknown nature or strength.

In order to further investigate the properties of the superconducting condensate, and hence what might be capable of inducing such a strong inhomogeneous magnetic field that it could cause the ferromagnetic oscillations to become localised, SQUID magnetometry measurements were performed on both samples  $I_{S-C}$  and  $C_{60}$ .

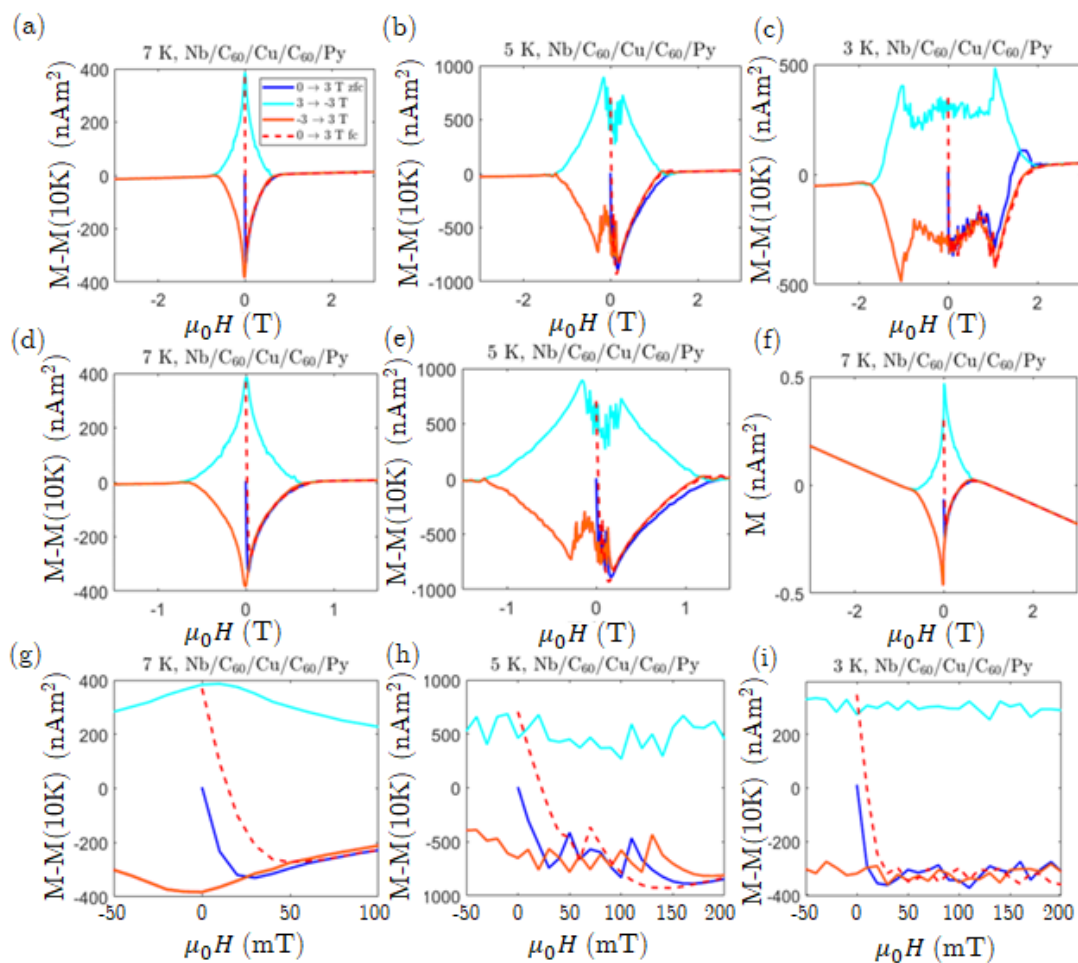


Fig. 4.10 The difference in the magnetic moment of sample  $I_{S-C}$  ( $\text{Nb}/\text{C}_{60}/\text{Cu}/\text{C}_{60}/\text{Py}$ ) at (a) and (d) 7 K, (b) and (e) 5 K, and (c) 3 K, and 10 K. At 7 K, the curve is characteristic of a type-II superconductor with a trapped vortex lattice. The data is left as the magnetic moment as the total volume over the superconducting region is uncertain due to a substantial proximity induced SC state in the  $\text{C}_{60}$ . Below this, the net magnetic moment displays unusual magnetic field dependence. (f) Raw magnetic moment at 7 K. The magnetic moment from the trapped flux dominates over the ferromagnetic contribution from the permalloy. Trapped flux at low fields at (g) 7 K, (h) 5 K, and (i) 3 K. The virgin ZFC and FC curves intersect at similar magnetic field values to where the ZFC and FC linewidth curves intersect. Measurements performed by Guillermo Nava-Antonio from the University of Cambridge.

Figure 4.10 shows a SQUID measurement of the difference in magnetic moment (versus in-plane field) between a measurement performed at 10 K (above  $T_C$ ) and at a range of temperatures below  $T_C$  for sample  $I_{S-C}$  ( $\text{Nb}/\text{C}_{60}/\text{Cu}/\text{C}_{60}/\text{Py}$ ).<sup>1</sup> Subtracting the 10 K mea-

<sup>1</sup>SQUID measurements were performed by Guillermo Nava-Antonio from the University of Cambridge

surement removes the signal from the normal state ferromagnetic Py, leaving behind only the magnetic moment that is a consequence of the superconducting transition.

At 7K (Figure 4.10a), just below the transition temperature, the resulting hysteresis curve is characteristic of a type-II superconductor in the Shubnikov state, where the superconducting order surrounds a lattice of normal state vortices with a net magnetic moment [219]. The field at which the sample transitions from the Meissner phase to the Shubnikov phase ( $H_{C1}$ , see Section 2.5.3) can be estimated from the minima in the magnetic moment, which provides an upper bound of  $\sim 25$  mT. The presence of a significant number of in-plane vortices at such low fields is in direct contrast to the existing literature on in-plane vortex formation in type-II superconductors, which is generally assumed to occur only at large magnetic fields [235, 252–254], especially when the thickness of the SC layer is less than the penetration depth. In Section 4.3.5, it is calculated that for typical Nb SC-parameters and these film thicknesses, a field well in excess of 100 mT should be required to form an in-plane vortex population. Consequently, the presence of the  $C_{60}$  layers must significantly alter the properties of the Nb superconducting condensate for it to be possible for such a state to form.

The presence of a significant vortex population has been shown to have a significant effect on the FMR properties of adjacent ferromagnets due to coupling between the ferromagnet and the flux lines expelled by the vortices [28]. Figures 4.10g-i show a close-up of the ZFC and FC virgin curves (i.e. the magnetic curves recorded at the start of each sweep from 0 T). There is a coincidence of the two curves around 60 mT. This coincides roughly with the coincidence of the ZFC and FC linewidth/frequency graphs, which join close to 6 GHz. A 6 GHz resonances has a corresponding resonance field of around 45 mT (Figure 4.4), and in practice the device will experience a field larger than this during the measurement, as the magnetic field must be swept some way beyond the resonance field to collect data on the whole curve. This coincidence has not been measured precisely, but nevertheless shows that the two measurements can be correlated to the same order of magnitude in the magnetic field.

The above evidence points to an interaction between the superconductivity and ferromagnetism, mediated by the stray field of the vortex population. There is some precedent for such an interaction in the literature, although important differences remain. The effect of vortices on ferromagnetic resonance behaviour was studied by Jeon et al. [28], who observed a significant increase in the zero-field linewidth below  $T_C$  in Nb[ $\geq 100$  nm]/Py heterostructures that they attributed to the inhomogeneous field from pinned magnetic flux vortices in the adjacent Nb. The behaviour of the linewidth they observe, and the influence of the vortices, is similar to ours, except that the inhomogeneities induced in the Py still leave it within the magnon-magnon scattering picture of inhomogeneity-induced damping, and they do not report any hysteresis in their measured values.

Whilst Jeon et al. do not observe any hysteresis in their linewidth, hysteretic effects have been observed in FMR studies of SC/FM heterostructures in which the SC is expected to contain a significant population of vortices in its remnant state. Golovchanskiy et al. [255] performed an FMR study in an out-of-plane magnetic field on a Nb waveguide (150 nm thick) patterned on-top of a YIG (ferromagnetic insulator) substrate. They observed a significant hysteresis in the measured peak intensity below the transition temperature, measuring a factor of 2 decrease in the measured signal when field cooling at small fields compared to the ZFC case. This difference reduce as the applied field was gradually increased. This is similar to the behaviour observed in the FC/ZFC studies of the linewidth/lineshape (see Figures 4.7, 4.5, and 4.9). They do not, however, report any unusual behaviour of the linewidth.

Despite the apparent similarities, the mechanism behind the observations of Golovchanskiy et al. is unlikely to be applicable to the variation in the linewidth observed. They attribute the measured variation in intensity to a variation in the coupling strength between the Nb coplanar waveguide (which carries the microwaves used to excite the YIG) and the YIG itself, rather than to a modification of the field experienced by the YIG in the inhomogeneous field of the superconductor. Whilst for the FMR experimental set-up used in this work

the magnetic properties of the superconducting layer could be expected to expel some of the microwave magnetic fields carried by the waveguide and hence affect the measured signal strength, this would not be expected to effect the linewidth (as Golovchanskiy et al. observed).

Consequently, although the existing literature supports a strong interaction between the magnetisation and vortex population, and one that is capable of displaying hysteric behaviour, there are no reports that show that vortices can induce the kind of behaviour observed in these samples. However, from direct comparison between the work Jeon et al. and this work, and in particular by analysing the difference in the temperature dependence of the measured magnetisation curves, the origin of these effects becomes clear.

In Jeon et al. [214], the shape of the magnetisation of the superconducting film is the same as for these samples at 7 K across the whole temperate range. This is the typical magnetisation curve of superconductors with a significant pinned vortex population and, as they observe, should not vary significantly with temperature. In contrast, as the temperature is decreased the superconductor develops a magnetisation that appears to jump erratically with changes in the magnetic field at lower and lower temperatures, up until some critical magnetic field, denoted as  $H_M$  (Figures 4.10b-c, e), where the curve becomes smooth again. These jumps in the magnetisation, and their temperature dependence, are typical of a superconductor exhibiting a phenomenon known as flux jumping, or thermomagnetic avalanches (TMAs) [252, 256].

Flux jumps occur when a pinned vortex is suddenly freed from its pinning site, allowing it to move throughout the superconductor, dissipating energy as it moves [257]. This results in local heating, transforming some of the adjacent superconducting into the normal state, allowing additional flux into the sample and freeing other vortices from their pinning sites. This results in a cascading, or ‘avalanche,’ effect that causes in a jump in the macroscopic magnetisation of the sample. The first observed mechanism of this form was by Evetts in

1967, who saw jumps in the magnetisation on one side of the hysteresis curve due to the heat dissipated in the annihilation of the pinned negative flux vortices (relative to the external field) with newly nucleated positive flux vortices [258]. However, the motion of vortices itself in many cases is sufficient to induce this effect [252, 257], resulting in a symmetric spectrum about  $H = 0$  [257]. What is notable is that the temperature dependence of the hysteresis correlates not with the absolute value of the vortex-induced magnetic field, which is already considerable at 7 K (Figure 4.10a) and yet results in very little hysteresis (Figure 4.5), but rather with the instability of the sample to flux-jumping/TMA.

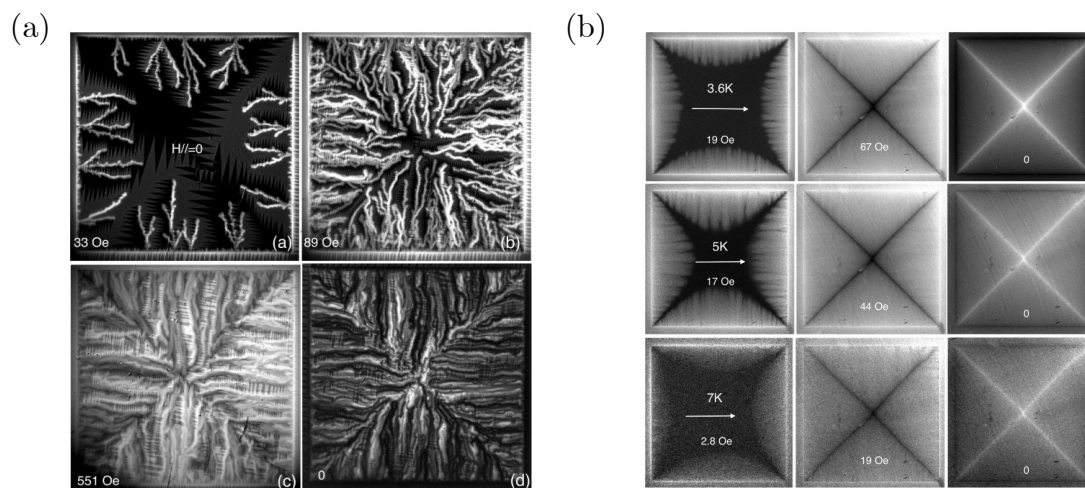


Fig. 4.11 Magneto-optical images of magnetic flux reentry in (a) 200 nm and (b) 100 nm thick Nb thin-films. In the 200 nm thick films, a population of in-plane vortices nucleated at the edge of the sample are unstable to TMAs, causing a highly chaotic dendritic pattern in the magnetic field. In the 100 nm sample, in-plane vortices are energetically forbidden at these fields, and so the magnetic flux reentry is smooth and uniform. Figures reproduced from [252].

Figures 4.11a and 4.11b show magneto-optic images of the magnetic flux in (200 nm and 100 nm thick respectively) thin-film Nb superconductors observed by Vlasko-Vlasov et al. [252]. In the 200 nm film, they observe TMAs, resulting in a highly chaotic dendritic pattern of magnetic flux. In contrast, the 100 nm sample (which contains no in-plane vortices responsible for TMAs) shows a very smooth reentry of the magnetic flux. From this, and the

correlation between the temperature dependence of the unstable region and the hysteretic behaviour, it is proposed that it is the inhomogeneous magnetic field that results from TMAs in the vortex population that causes the hysteretic localisation of the magnetic oscillations. The implications of the instability of the vortex population to the formation of TMAs are discussed in greater depth in Section 4.3.5.

Figure 4.12 shows the equivalent magnetic moment measured on sample C<sub>60</sub>, which does not appear to show the presence of any vortex formation below  $T_C$ . The hysteresis effect is comparable in both samples, and so consequently if the presence of vortices is the underlying physical mechanism and not merely incidental then one would expect to detect them in both samples. However, these structures are known to be vulnerable to degradation due to oxidation and damage from UV light, and subsequent FMR measurements performed after these SQUID measurements no longer showed any hysteresis with magnetic field. This suggests that the absence of vortex formation is likely due to device degradation and, consequently, further measurements on freshly fabricated samples are required to confirm or refute the presence of a vortex state in the Nb/C<sub>60</sub>/Py structures.

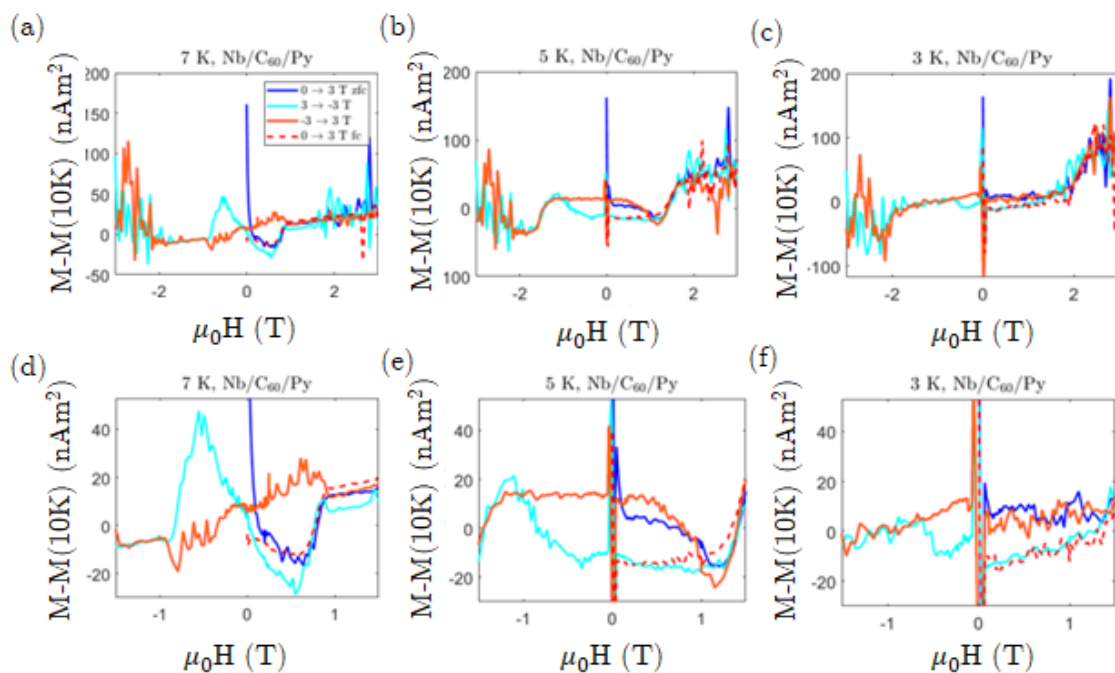


Fig. 4.12 Magnetic moment of the superconductor in sample  $C_{60}$  (relative to 10 K) at: 7 K (a), (d); 5 K (b), (e); 3 K (c), (f). Unlike sample  $I_{S-C}$  (Figure 4.10), this sample shows no sign of a significant vortex population below  $T_C$ . Subsequent FMR measurements showed that the hysteretic effect was no longer present, suggesting the sample had decayed as it is known to be sensitive to atmospheric/UV-light exposure. Measurements performed by Guillermo Nava-Antonio from the University of Cambridge.

#### 4.3.4 Alternative mechanisms of interaction between the superconducting and ferromagnetic order

The Meissner effect is only one of a number of mechanisms via which the superconducting and ferromagnetic orders can interact. More direct interactions, driven by energetic competition between the two antagonistic orders, have been shown to have considerable strength in many cases, and can be directly responsible for inhomogeneous behaviour in ferromagnets coupled to strong superconductors. Such interactions are responsible for spin-triplet formation in SC/FM/SC Josephson junctions [183–187], where competition between the energies of the superconducting and ferromagnetic order results in the breakup of the ferromagnet into a domain-like structure. A detailed explanation of this effect can be found in Section

2.5.1. The breaking up of the Py into domains, even if only locally at the interface, is an attractive explanation for the localisation of the resonances, and should be expected to display significant hysteresis with magnetic field in the same way as demagnetisation field-induced domains in normal ferromagnets. This effect should diminish as the field strength increases and the domain pattern is destroyed. The strength of this effect is also expected to grow as the temperature is reduced and the energy balance tips in favour of the superconducting order, in line with the observed temperature dependence of the hysteresis.

However, whilst spin-triplets have been observed in Nb/Py/Nb Josephson junctions with Py layers many nanometres thick [192, 193], due to the formation of a non-uniform magnetic state at the interface (see Section 2.5.1), the separation of the Nb from the Py should suppress this effect as the superconducting gap will be much weaker in the  $C_{60}$ , which is only superconducting to around 30 nm in thickness via the proximity effect. Additionally, this effect diminishes with increasing Py thickness [193]; an 8 nm layer of Py displaying this effect would be exceptional. The vortex state mechanism is less affected by the width of the intermediate layers as it does not require direct contact between the ferromagnetic and superconducting order, and so the strength of the condensate at the interface is of less relevance.

On the other hand, the surface roughness of the  $C_{60}$ /Py is expected to be substantial, measured at 1 nm in similar structures (the thickness of the Py layer is around 8 nm). Consequently, there may be a significant layer of weakly coupled ferromagnetic moments near the interface, which have been proposed to play a significant role in the formation of such inhomogeneous ferromagnetic states [175, 192]. It should be noted that hysteretic effects have not been observed in similar reports on the FMR characteristics of Nb/Py heterostructures (in which would expect the strength of the condensate to be stronger at the Py interface than in these samples) [28, 51].

The hysteresis in the linewidth is able to persist up to relatively high fields, suggesting there would need to be a significant energy benefit to forming the inhomogeneous magnetic state to counteract the increase in Zeeman energy. Josephson junctions based on SC/FM/SC heterostructures with superconductivity induced non-uniform magnetic textures have been shown to be able to maintain a critical current up to significant magnetic fields [188], well in excess of those employed here. Hence, in principle, it is plausible such an effect could be strong enough to explain these observations. However, in this case the remnant state of the ferromagnet should be more ordered, not less, as expected from standard micromagnetic theory, and as seen in hysteresis measurements of the critical current of ferromagnetic Josephson junctions [188]. This is at odds with the experimental observations presented here that the inhomogeneity is increased in the remnant state. In contrast, FC induces the formation of vortices in the SC layer, consistent with the increased inhomogeneity the experimental results are attributed to.

SC-induced uniaxial anisotropy might be able to induce a non-uniform texture if its strength and direction were not uniform over the whole sample [259]. However, a SC induced uniaxial anisotropy of the strength required to explain these observations should show up in a shift in the resonance frequency of the sample below the transition temperature, which is instead roughly constant for both samples (Figure 4.6).

Consequently, unless a hitherto unknown effect is present in these systems, one can rule out direct interaction between the superconducting condensate and magnetic order as the source of these observations.

### 4.3.5 Flux-jumping/thermomagnetic avalanches

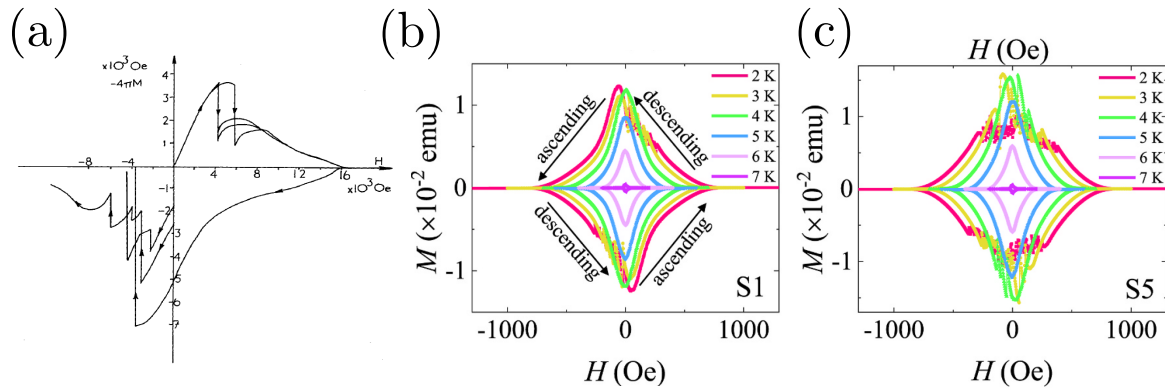


Fig. 4.13 (a)  $-M$  versus  $H$  curves observed by Evetts et al. [258]. Discontinuous jumps in  $M$  are observed due to the mutual annihilation of positive flux vortices with trapped negative flux vortices causing a macroscopic discontinuity in the magnetisation. Figure reproduced from [258].  $M$  versus  $H$  curves observed for Pb (200 nm, out-of-plane magnetic field) superconductors at a range of temperatures for a sample with large (b) and small (c) grain sizes. The sample with large grains exhibits similar behaviour to (a). As the grain size is reduced, the  $M$  versus  $H$  curve becomes symmetric about  $H = 0$ . Figures reproduced from [260].

From the experimental evidence presented above, it has been proposed that both samples are capable of supporting a significant vortex population, nucleated by the application of a large magnetic field, that is unstable to TMAs. In the following section, this vortex population and its behaviour will be analysed in light of theoretically derived free-energy criteria, which provide bounds on the magnetic fields and thin-film thickness required for a superconductor to be able to exhibit these phenomena. It is found that, for a well behaved superconductor with the expected superconducting/physical parameters of the Nb thin films, these experimental conditions should not be conducive to any of the observed phenomena. Consequently, there must be some interaction between or influence of the  $C_{60}$  on the Nb that makes the formation of these states possible.

Type-II superconductors with thicknesses below their penetration depth are believed to only be able to support in-plane vortex formation [235, 252–254] at large magnetic fields because of the repulsive interaction between the unscreened magnetic field at the surface

( $He^{-x/\lambda}$ ) and the vortex supercurrents. This model provides a formula for  $H_{C1}$  in a thin-film in an in-plane magnetic field [222]:

$$H_{C1} = \frac{\Phi_0}{4\pi\lambda^2} \times \frac{\cosh(d/2\lambda)}{\cosh(d/2\lambda) - 1} \times \left( K_0(\lambda/\xi) - 2 \sum_{n=1}^{\infty} (-1)^n K_0(n\lambda/d) \right) \quad (4.3)$$

where  $\Phi_0$  is the magnetic flux quantum,  $K_0$  is the zeroth order second modified Bessel function, and using typical values of  $\lambda = 100$  nm and  $\xi = 10$  nm for Nb (at temperatures well below  $T_C$ ), one obtains  $H_{C1} \sim 120$  mT for a 50 nm film, which is well in excess of the experimentally observed field at which vortices begin to form (less than 25 mT, as determined by the minima in  $M$  in a typical  $M$  versus  $H$  curve of a type-II SC, see Figures 4.10g-i, which gives an upper limit for  $H_{C1}$ . This formula is typically in good agreement with reported experimental results in Nb [214, 252].

It is therefore surprising to see evidence of vortex formation at as low as 25 mT (Figure 4.10g-i), and this suggests that there must be some modification of the superconducting properties of the Nb by the adjacent  $C_{60}$ . Note that this is less than the external field applied during the low-energy muon-spin rotation measurements in Figure 4.1 (30 mT). Such an interaction would have to be distinct from the usual proximity interaction, which should weaken the diluted superconducting condensate via the loss of Cooper pairs in the  $C_{60}$ , reducing its ability to screen the external magnetic field via the usual Meissner screening and hence discourage the formation of magnetic vortices.

Another possibility is that the interaction of the Nb with the stray field from the adjacent Py layer may encourage vortex formation. Over the whole volume, the Py layer is expected to contribute a stray field that opposes the external field, and hence should inhibit vortex formation. However, it is possible that imperfections in the interface could lead to stray fields which contribute large, localised, fields parallel to the external field that may promote vortex formation at the interface, although no reports of this kind of behaviour in the literature were encountered during this project.

It may also be possible that there is a degree of misalignment of the sample inside the magnetic field, such that the field is no longer purely in plane. Such a field could lead the formation of out of plane vortices at relatively low magnetic fields. Figure 4.10 shows that from 5 K and below, the magnetic field changes from flux jumping is a substantial proportion of the overall magnetisation of the device. In order for this to be the case, the magnetic flux trapped in the vortices must also be a significant fraction of the total magnetic moment of the superconductor. As the flux trapped in the vortices is necessarily related to the strength of the field, this would imply a large degree of misalignment of the sample, making this the origin of the vortices unlikely. Additionally, a normal lattice of out of plane vortices would not lead to the re-emergence of the magnetisation at high fields as observed here. Another possibility is that if there are some out of plane vortices that nucleate normally, when they annihilate one another in a TMA this induces a normal region of the superconductor that could allow in-plane vortices to form more easily. It may be possible that the combined presence of a field perpendicular and parallel to the thin film could induce a tilted vortex state; although, in thin Nb films, this angle of tilt is relatively small even at film thickness of 100 nm [252].

Additionally, there is some experimental evidence from high-temperature superconductors that, for certain grain sizes, magnetic flux penetration can occur below  $H_{C1}$  [261]. If the concentration of defects is sufficiently high then this can also result in a net paramagnetic Meissner effect [261]. It may be that a similar mechanism is operative in the superconducting  $C_{60}$ , whose precise microstructure for this sample has not been measured, but that, under similar fabrication conditions, typically consists of small, bordering on amorphous, crystalline grains [262].

The notion that the grain size of the  $C_{60}$  film may be an important mechanistic factor is supported by a recent report from Zang et al. [260], who studied the magnetisation curves of Pb superconductors as a function of grain size. For large grains, and thus less pinning, they observe magnetisation curves similar to those of Evetts et al. (Figure 4.13b). However, for the

samples with the smallest grain size, and thus most pinning, the magnetisation curves become symmetric about  $H = 0$ , displaying qualitatively similar temperature and field dependence to these samples (Figure 4.13c). This suggests that different mechanisms are operative in different regimes of pinning site density. These results, as well as the unusually low magnetic fields at which the formation of vortices is observed, suggest that an understanding of the grain size in the Nb/C<sub>60</sub> layers may be crucial to understanding the underlying physical mechanisms at play.

The unusual behaviour of these vortices is not limited to their existence. A range of criteria have been developed over the years to determine whether or not a superconductor will be unstable to flux jumping. It should be noted that, in terms of stability, the samples follow the trends described by theories for thick (relative to the penetration depth) superconductors, based on the critical state model — whose details are beyond the scope of this work (see for instance [253, 263]). This gives the following stability criteria (i.e. if this inequality is not satisfied, the sample will be unstable to the formation of TMAs) [263]:

$$\frac{\mu_0 d^2 J_C^2}{3S(T_C - T)} = \frac{\mu_0 d^2 \alpha^2 (T_C - T)}{3B^2 S} \leq 1 \quad (4.4)$$

where  $d$  is the thickness of the film,  $J_C$  the critical current of the superconductor (replaced in the equality using Kim's assumption that  $J_C$  varies inversely with the magnetic field,  $B$ , and proportional to  $T_C - T$ , i.e.  $J_C = \alpha(T_C - T)/(B_0 + B) \approx \alpha(T_C - T)/B$ , for  $B \gg B_0$  [264], which is approximately valid for Nb [265]), and  $S$  is the volumetric heat capacity. Clearly, such a criterion qualitatively reproduces the observed magnetic field and temperature dependence in Figure 4.10, which predicts an increased critical magnetic field,  $H_M$ , at which the superconductor becomes stable against flux jumping perturbation, with decreasing  $T$ . Additionally, the critical state theory predicts a minimum magnetic field at

which flux instability can occur [257]:

$$B > B_* = \sqrt{3S(T_C - T)} \quad (4.5)$$

Clearly, if  $d$  is small enough, it is not possible to satisfy (4.4) and (4.5) simultaneously, and so thin films are not generally expected to be unstable to flux jumping. Of course, these samples are not ‘thick,’ in the sense that their thickness is less than the penetration depth, and so one would imagine this analysis is not strictly valid in this regime. There has been some work in recent years on the stability of thin-films in out-of-plane magnetic fields (see [256] and the references therein); however, work on thin-films with in-plane magnetic fields is still lacking. Hence, it may still be possible for TMAs to form in this way in thin-film samples under these experimental conditions. Nevertheless, it is still somewhat surprising that such pronounced flux jumping is observed in such a thin sample. Similar measurements in 100 nm Nb films [214, 252] at similar magnetic field values do not report such behaviour.

Another unusual aspect of the flux jumping behaviour of sample  $I_{S-C}$  is the re-emergence of the absolute magnetic field close to the critical field where flux-jumping becomes suppressed (Figure 4.10c). No reports of this kind of behaviour in the literature were encountered during this project (the curves shown in Figures 4.13a-c are typical of this phenomena), and it does not seem possible for the usual flux jumping mechanism to explain why, for example, in the dark-blue/red-dashed curve in Figure 4.10c, the negative magnetic moment should increase suddenly as the field approaches  $H_M$ . Flux jumping has the tendency to bring magnetic flux in the superconductor closer to the external field (and hence decreases the absolute value of the magnetisation in both increasing and decreasing H sweeps of the hysteresis loop [257], as can be seen clearly in Figure 4.13a), whereas here there is a sudden expulsion of flux. Additionally, in the light blue curve for  $H < 0$ , the superconductor appears to suddenly oppose the field far more strongly as it approaches  $H_M$ . This is presently not well understood mechanistically.

In conclusion, the existence of a vortex population unstable to TMAs is not well understood based on the current theoretical understanding. Neither are some of the observed features of this vortex state, such as the re-emergence of the magnetic moment close to the critical field  $H_M$  where instability to the formation of TMAs is suppressed. It has been suggested that these behaviours might be related to the amorphous grain structure of the  $C_{60}$ , though further work is needed to confirm this.

Having established the existence of this unstable vortex population and elucidated its effect on the ferromagnetic resonance measurements, it is now possible to interpret the linewidth versus frequency data presented in Figure 4.3. In the following section, the temperature dependence of the Gilbert damping is extracted from the FMR data, which suggests that there is minimal contribution from any spin-triplet mediated spin-pumping to the FMR linewidth. This result is discussed, and the low-energy muon spin-rotation measurements that purported to show the presence of a spin-triplet condensate inside the device, in light of the discovery of the significant vortex state inside the superconducting portion of the sample, which may provide an alternative explanation of the observed trends in the muon spin-rotation data.

#### **4.4 Investigating the presence of a spin-triplet population**

The purpose of this study was to confirm the presence of spin-triplets in Nb/ $C_{60}$ /Cu/ $C_{60}$  heterostructures using FMR measurements of the spin-pumping induced magnetic damping. The presence of a significant vortex state significantly complicates the interpretation of the experimental data, as it results in an artificially high gradient of the linewidth with respect to frequency due to the increased contribution of vortices as the magnetic field is swept every layer. This effect diminishes as the frequency is increased, where presumably the inhomogeneous magnetic field due to the vortices becomes increasingly small relative to the large external static magnetic field. Indeed, whether or not the inhomogeneous broadening

contributes to the linewidth is not important, so long as it does not vary with frequency, allowing the Gilbert damping to be determined unambiguously from the gradient of the linewidth.

Within the range of frequencies available experimentally (limited mostly by the detectable signal strength to sub 20 GHz), applying a large field and then relaxing back to a remnant state always has some effect on the linewidth, as can be seen by the fact the Nb is never truly saturated until around 1-2 T (Figure 4.10, well in excess of the resonance fields measurable by the experimental setup (Figure 4.4)). However, above around 10 GHz, this effect is small and furthermore, since any increase in the concentration of vortices always results in an increase in the linewidth, decreasing with increasing resonance field, the measured linewidth in the ZFC case always represents an upper bound on the true Gilbert damping (see the gradient of the linewidth below 6 GHz for the FC and ZFC case in Figure 4.5). Consequently, it is possible to obtain a good estimate of the Gilbert damping from measurements of the linewidth versus frequency if one only include data points collected above 10 GHz, where the resonance field is sufficiently large that the inhomogeneous field from the vortices is small in comparison (the ZFC and FC curves intersect well before this frequency (Figure 4.5), and hence this distinction is not important under these experimental conditions).

Figure 4.14 shows the dependence of the measured Gilbert damping for samples  $I_{S-C}$  (a) and  $C_{60}$  (b) with temperature using the above procedure. Both samples show a significant decrease in the measured Gilbert damping below the transition temperature. This has a number of implications. First, it supports the view that it is indeed possible to inject a spin-current through a  $C_{60}/\text{NM}$  interface, as the reduction in  $\alpha$  can be attributed to the blocking of the spin-pumping induced spin-current by the spin-singlet superconducting condensate. The spin-transparency of  $C_{60}/\text{NM}$  interfaces is important for the interpretation of a number of experimental results [243], and is still a point of some contention within the community

[249]. The second, and principal objective of this study, is that these results imply that no significant spin-triplet condensate is present in either sample.

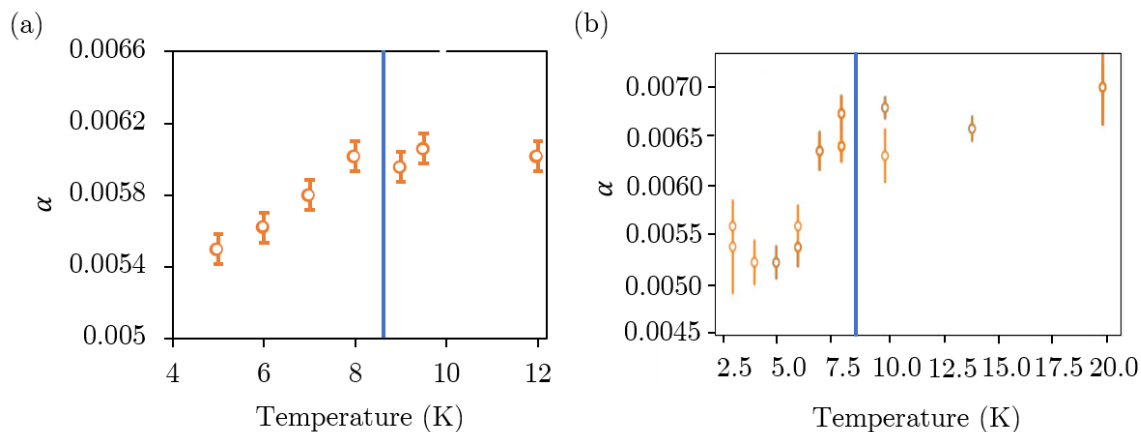


Fig. 4.14 Gilbert damping coefficient,  $\alpha$ , versus temperature for sample  $I_{S-C}$  (a) and sample  $C_{60}$  (b). The transition temperature is indicated by the vertical blue line on each graph. Both samples show a decrease in  $\alpha$  below the transition temperature, indicating that the spin-singlet superconducting condensate is blocking the transmission of spin due to spin-pumping, and there is no evidence of a spin-triplet population in either system.

This is in direct contrast to the proposed interpretation of the low-energy muon spin-rotation measurements. Indeed, it may be possible that the observed paramagnetic signal in the  $C_{60}$  layer is not from a spin-triplet condensate, but rather the result of a vortex state forming inside the Nb/ $C_{60}$  superconductor.

#### 4.4.1 Interpreting muon-rotation results in terms of vortices

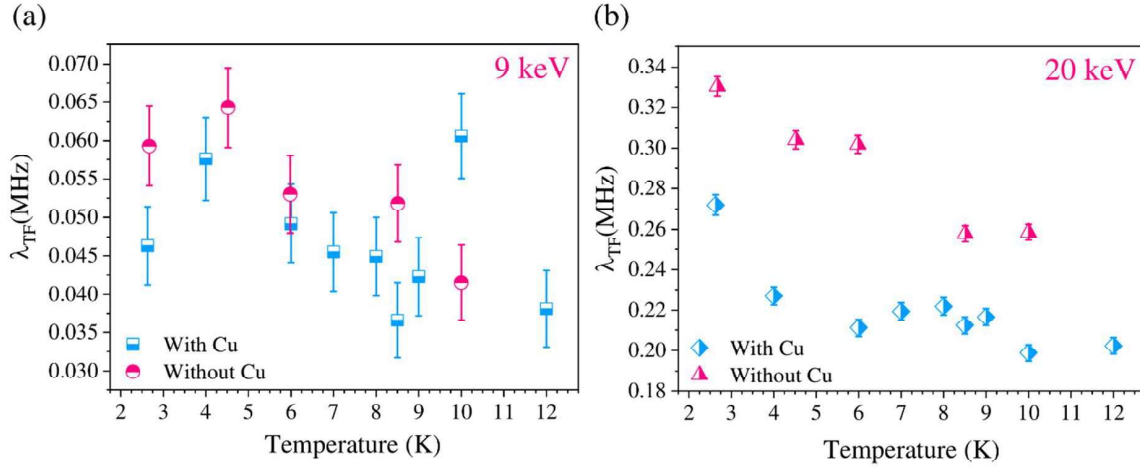


Fig. 4.15 depolarization rate ( $\lambda_{TF}$ ) of 9 keV (a) and 20 keV (b) implanted muons in samples with and without the Cu ( $I_{S-C}$ ) layer. The 20 keV muons show a significant increase in the depolarization rate below  $T_C$ , which may be attributable to the formation of flux-vortices in the superconductor. Figure reproduced from Rogers et al. supplementary information [235].

Pinned vortices have been shown to induce a similar paramagnetic Meissner response in experiments on out of plane-vortices in Nb thin-films [266, 267]. It should be noted that these papers report a *overall* paramagnetic Meissner response. Whereas in this work, they are only claiming a locally paramagnetic response, a much weaker condition. This possibility was discussed in the original work [235], which they discounted for two principal reasons. The first is the thickness of the Nb film itself, which at 50 nm is not expected to be able to support in-plane vortices. Clearly, this is not so (note that the muon rotation experiments were performed in a 30 mT external field, in excess of the experimentally measured upper bound for  $H_{C1}$ ). The second is the effect that the presence of a vortex state ought to have on the depolarization rate of the implanted muons. The argument goes that a vortex state should introduce a significant degree of inhomogeneity into the magnetic field in the sample, resulting in a faster depolarization rate of the net muon-spin as the muons incoherently precess about their local magnetic moments below the transition temperature. Figure 4.15 shows the measured depolarization rates for both samples and beam energies. The 9 keV

shows no statistically significant change in the depolarization rates above and below the transition temperature, which is to be expected as these lower energy muons primarily implant in the Au layer where the superconducting condensate is weak. The 20 keV beam, however, which primarily implants in the Nb layer, shows a significant increase in the depolarization rate below the transition temperature.

This was claimed to show that a vortex state cannot explain the observations of Rogers et al. [235], as the sample without the  $I_{S-C}$  exhibits consistently higher depolarization rates than the sample with the  $I_{S-C}$ . However, these results suggest that a vortex state is present in both samples; the higher depolarization in the sample without the  $I_{S-C}$ , which is also true above  $T_C$ , is therefore irrelevant. The higher depolarization rate is simply the result of this particular sample structure/quality, rather than a superconducting induced property. Both samples show a similar relative increase in the depolarization rate below  $T_C$ , which may be attributable to an inhomogeneous vortex state forming in the Nb. Consequently, these measurements cannot be used to rule out the presence of a vortex state inside the superconductor.

This interpretation of the muon spin-rotation data begs the question, ‘if a vortex state is present in both samples, then why is a paramagnetic susceptibility only measured in the sample with the  $I_{S-C}$ ?’ Whilst it is true that the sample without the  $I_{S-C}$  does not exhibit a paramagnetic signal, the 9 keV muon beam only measures a very slightly diamagnetic susceptibility. Consequently, the variation in the susceptibility between the two samples is actually quite small, and, like the difference in depolarization rate (Figure 4.15), could simply be the result of slight differences in the structure’s properties/fabricational variation or the vortex state that forms inside the sample.

These results do not necessarily prove definitively that a vortex state is inherent to Nb/C<sub>60</sub>/Cu/C<sub>60</sub> heterostructures. The samples measured in the low-energy muon spin-rotation measurements differ from ours in that the Py layer is replaced by non-magnetic

Au. It may be that the Py layer is required for the formation of a vortex state in the SC. Consequently, the only way to confirm/refute the presence of a vortex state would be to perform the SQUID measurements shown in Figure 4.10 on the sample structures used in the low-energy muon spin-rotation measurements. If these measurements were to detect the presence of a significant vortex state below the transition temperature, a significant reinterpretation of the muon spin-rotation data would be required, possibly ruling out the presence of a spin-triplet condensate.

## 4.5 Future work

It will be necessary to repeat the magnetic-moment measurements on sample  $C_{60}$  (Figure 4.12) to confirm the presence of a significant Shubnikov state, as well as similar measurements to determine whether such a state is present in the sample structures used for the low-energy muon rotation measurements. Should such a state be confirmed, then it is likely that a significant reinterpretation of the low-energy muon spin-rotation measurements would be required.

At present, there is no literature on the influence of TMA on FMR studies. Because there is a growing body of literature that employs FMR measurements, and measurements of the Gilbert damping, in order to investigate the presence of spin-triplets, there may be some interest in a more systematic study of this effect. Clearly, should TMAs be present in a sample, this would have a significant impact on the measured frequency dependence of the linewidth that must be accounted for in the analysis, least the induced spurious increase in the linear dependence of the linewidth be reported as a genuine increase in the Gilbert damping (see low-frequency data in Figure 4.3). Hysteretic effects of this form are perhaps interesting, but not tremendously useful.

The existence of vortices, and ones unstable to TMAs, in the Nb/ $C_{60}$  bilayers at such low fields, is surprising given the widely accepted theories. By comparison with samples with

similar behaviour in the literature, it is possible to speculate that this is likely to be due to the grain-morphology of the  $C_{60}$ , which typically has very small grain sizes unless grown under special conditions [262]. Nevertheless, this remains to be determined. It would be interesting to see where this vortex population exists within the bilayer. Low-energy muon spin-rotation measurements could help measure this, although they suffer from a low implantation rate in  $C_{60}$ . Additionally, some degree of out of plane vortex formation is likely even in the present data due to small degrees of misalignment of the sample. A more systematic study of this effect versus the out of plane angle of the magnetic field could more accurately determine the role, if any, any out of plane vortices play in the underlying mechanism.

## 4.6 Conclusion

In conclusion, the temperature dependence of the FMR signal in  $Nb/C_{60}/Py$  and  $Nb/C_{60}/Cu/C_{60}/Py$  heterostructures has been measured. It has been proposed that a  $C_{60}/Cu/C_{60}$  layer, adjacent to the superconducting Nb, may act as a source of spin-triplet Cooper pairs. It is found that, below the transition temperature, the FMR response displayed significant hysteresis with respect to both temperature and magnetic field. This was attributed to the presence of a significant flux-vortex population and to its instability to flux-jumping/thermomagnetic avalanches within the superconducting condensate. This was detected directly by SQUID magnetometry measurements below the Nb transition temperature. The formation of vortices in a Nb film of such thin thickness at low fields goes against previously reported results and theory. This hysteretic behaviour can be correlated with the instability of the superconducting condensate to thermomagnetic avalanches.

It was found that the Gilbert damping decreased below the transition temperature for both samples. This suggests that there is no significant spin-triplet population within either sample. Consequently, it was suggested that the reported evidence of a spin-triplet population could instead be explained by the flux-vortices forming within the superconductor, which has

---

been shown to induce a paramagnetic Meissner screening signal in similar superconducting thin-films.



# Chapter 5

## Symmetry and the dynamics of magnetic oscillators

*Important features in the evolution of the modes of a physical system under some suitable parameter (external field, wavevector etc.) have long been understood in terms of the symmetry of the system and the modes themselves. The mathematical language in which this understanding is described is group theory. Spin-wave modes are the linearised excitations of a ferromagnetic or antiferromagnet. When considering the entirety of the Brillouin zone, it becomes necessary to describe the magnetic vibrations using quantum mechanics, where group theory is commonly employed in understanding the magnonic bands' features and evolution.*

*Spin-waves, in their low-to-zero  $\mathbf{k}$  guise, which are often those probed during ferromagnetic resonance (FMR) experiments and in magnonic devices, are more readily described by the classical Landau-Lifshitz-Gilbert (LLG) equation. In this chapter, it is shown how, with some minor modifications, the usual language of group theory can be applied to the eigenmodes of the LLG equation, and how this can be used to understand their behaviour as being 'enforced' by their symmetry properties, with a particular focus on mode anticrossings and symmetry enforced degeneracies. This behaviour is illustrated via FMR measurements*

*on synthetic antiferromagnets, where the top and bottom layers have similar/mismatched perpendicular magnetic anisotropy, the difference tuned by the sample structure. This offers a new perspective on the use of symmetry to analyse magnetisation dynamics described by the LLG equation.*<sup>1</sup>

## 5.1 Introduction and scientific background

Ferromagnetism is characterised by a long-range ordering of a material's spins below the Curie temperature due to an exchange force of microscopic origin. This long-range order exhibits a spectrum of excitations formed from oscillatory modes with a well-defined frequency ( $\omega$ ) and wave-vector ( $\mathbf{k}$ ) in a ferromagnet of uniform and infinite extent. The relationship between the two is defined by the dispersion relationship:  $\omega(\mathbf{k})$ . Understanding the behaviour of spin-waves/magnons is an area of both physical and technological interest.

In its earliest guise, beginning with the theoretical prediction of Bloch, Holstein and Primakoff [269, 270], spin-waves were principally objects of academic study that enabled the development of useful models for understanding the properties of materials (for a review of the field's early progress, see [271] and the references therein). This includes the magnetic properties of the material: Bloch's laws for the  $T^{3/2}$  temperature dependence of the magnetisation [272]; the considerable body of literature measuring and predicting the magnon dispersion of YIG [273], a still active area of research [274], and other physical properties coupled/influenced by the magnetic order, for instance, the  $T^{3/2}$  dependence of the heat capacity [271]. In recent years, the study of spin-wave physics has moved over into device physics and donned the neologism 'magnonics,' a rather broad church that encompasses both spin-wave (which form the excited modes of the classical LLG equation in the low-wavelength limit) and magnonic (where the excited modes have sufficiently small wavelengths, comparable with the unit cell dimensions, although in practice, both these

---

<sup>1</sup>Part of this chapter is published in J. Patchett et al., *Phys. Rev. B* 105, 104436 [268].

terms are often used interchangeably) that a quantum mechanical description is required [77]) devices that aim to use magnons for wave-based computing, information processing and storage [275–277]. Because of its compatibility with existing CMOS technology and the promise of low-energy, low-footprint, wave-based computing, magnonics has emerged as one of the most active contemporary areas of magnetic research [278, 279].

Early studies into magnonic behaviour often involved the calculation and measurement of the magnon bands' dispersion in reciprocal space [77, 273]. Here, symmetry was used as an important tool to simplify quantum mechanical calculations and offer intuitive insight into the band's evolution and features, such as symmetry-enforced degeneracy and band crossings. This is in exact analogy with its use in the calculation of the electronic band structure, or phonon dispersion.

Close to the centre of the Brillouin zone, where the wavelength of oscillations significantly exceeds the dimensions of the unit cell, a quantum mechanical calculation of their properties is both unnecessary and cumbersome. Consequently, the classical Landau-Lifshitz-Gilbert (LLG) equation is overwhelmingly used to calculate and predict spin-wave behaviour [42, 43, 94, 95, 280–282], a regime that encompasses much of contemporary magnonic/spin-wave research. The influence of symmetry on the behaviour and evolution of spin-waves has not been widely explored. The term 'spin-waves' is used to refer only to the low-wavelength spin-excitations predicted by the classical LLG equation.

The principal reason for this is that the traditional workhorse of spin-wave physics are ferromagnets probed in a frequency/energy regime in which only low- $k$  excitations of the lowest band (if indeed, multiple-bands exist) are accessible. Ferrimagnets, such as YIG, in principle, can exhibit a large and diverse range of low- $k$  modes that permit a classical description. However, the strong exchange interaction typically raises the frequency of these modes into the hundreds of GHz / low THz range, well outside of the range of typical FMR experiments, and well separates them enough that they are unlikely to interact

within the experimental conditions available. Consequently, as the typical features of an excitation spectrum that make symmetry-based analysis worthwhile involve the interaction or confluence of multiple modes, symmetry offers very little insight in these cases.

During the course of this study, two reports were published that discovered that mode crossing/anticrossings could be explained in terms of the symmetry of the magnetic oscillations [42, 43]. In Section 5.4.4, their results will be discussed in depth, showing how the treatment of the LLG equation by group theory comes to the same conclusion from a different perspective. Additionally, it is shown how it is possible to extend the analysis of spin-wave modes in terms of symmetry by examining mode degeneracy.

### **5.1.1 Motivating the use of groups for the LLG equation**

Groups are interesting to physicists because the mathematical representations of real-world objects used in physical models often form a group. Because the objects under study form a group, group theory can say a great deal about their behaviour. In particular, it is able to do so in a strikingly elegant manner, that both aids comprehension and eliminates the need for a great deal of tedious calculation.

Previously, group theory had not been applied to the solutions of the LLG equation, despite its apparent similarity with the eigenvalue equations where it has been used extensively. This work will be exploring the use of groups as applied to the solutions of the LLG equation. It will be established in what sense the solutions to the LLG equation form a group, using a modification of the standard procedure to account for the ‘generalised Hermitian eigenvalue problem’ structure of the LLG equation, and then apply the techniques of group theory to analysing the modes of two SAF structures.

Viewing the dynamics of the LLG equation from a group theory perspective it is hoped will offer another perspective on some of the analyses of the influence of symmetry on magnetic resonance modes in the literature [42, 43], as well as show how another phe-

nomenon, mode degeneracy, can also be understood by symmetry arguments. Previous work into understanding the effect of symmetry on magnetic oscillators worked from the direct output of calculations of the resonance frequencies of the Landua-Lifshitz-Gilbert equation [42, 43] for their specific magnetic system in their investigation. Whilst this is valuable, it can be hard to obtain a sense of how these phenomena generalise to other magnetic systems without repeated calculations, and it is not always clear to what extent the observed change in behaviour with changes in symmetry can be ascribed to symmetry itself, or just different physical parameters producing different outputs from the equations of motion. Additionally, groups offer a much less calculation-intensive way of coming to some of these results once the basic principles are understood.

For example, in the case of the magnetic resonance mode anticrossings reported in the literature [43], they argue that the anticrossing they observe is the result of non-vanishing off-diagonal terms,  $\Delta$ , in their LLG equation:

$$\begin{vmatrix} \omega_a^2(H, \psi) - \omega^2 & \Delta^2(H, \psi) \\ \Delta^2(H, \psi) & \omega_o^2(H, \psi) - \omega^2 \end{vmatrix} = 0 \quad (5.1)$$

where  $\omega_a$  and  $\omega_o$  are the unperturbed resonance frequencies of the LLG equation, and  $\Delta^2$  is a coupling term that has a functional form which they calculate explicitly that only vanishes when the external field is applied in plane (all expressed as a function of the external field,  $H$ , and its angle with respect to the high symmetry plane,  $\psi$ ). Liensberger et al. [42] argue along the same lines with a different LLG equation relevant to their physical system.

Clearly, each equation is specific to each magnetic system, and so any attempt to generalise this result will require a recalculation of the LLG equation for each new model one wishes to consider. In contrast, the analysis using groups presented in Section 5.4.2, requires no knowledge of the precise form of the new, lower symmetry, LLG equation that forms after

the perturbation has been applied. Understanding symmetry effects in the LLG equation from groups therefore offers a valuable different perspective to the working physicist.

As many are not familiar with the underlying mathematics behind group theory, Section 2.6.2 provides a basic explanation of some of the mathematical principles behind group theory. In the following section, a few simple examples of using groups to analyse resonance phenomena are provided with the aim of providing a basic overview of how groups are typically applied to physical problems.

## 5.2 Introduction to using groups to analyse resonance phenomena

The fundamentals of the mathematics of group theory are detailed in Section 2.6.2. The following section is not intended to go into the details of the mathematics, which is left to Section 2.6.2, but rather illustrates the basic uses of groups to analyse resonance phenomena through the use of physical examples.

### Irreducible representations:

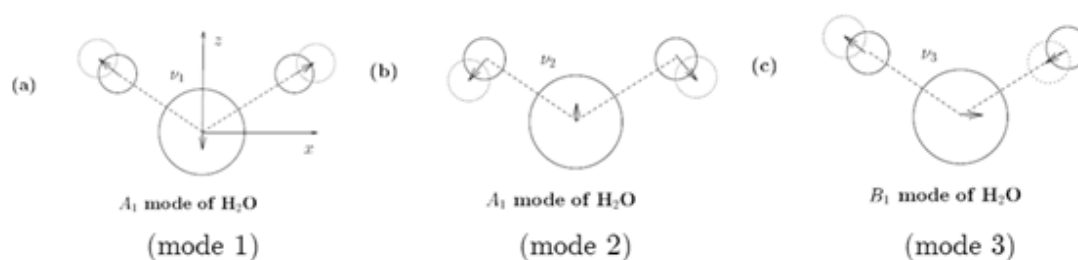


Fig. 5.1 The vibrational modes of  $H_2O$ . Reproduced from [122].

Every symmetry group has a set of irreducible representations, one of which can ascribe to each resonance mode in an eigenvalue equation. Intuitively, the irreducible representation ascribed to a given mode describes how that mode ‘transforms’ under the symmetry operations

of the group. As a simple example, consider the vibrational modes of a  $\text{H}_2\text{O}$  molecule shown in Figure 5.1. Mode 1 is a breathing mode (also referred to as a symmetric stretching mode) that changes the bond lengths only. Modes 2 is a symmetry bending modes that change the angle of the bonds, and mode 3 is an asymmetric stretching mode. By thinking about how each mode transforms under the symmetry operations of the  $\text{H}_2\text{O}$  molecule, it is possible to write down the representation of the symmetry group each mode forms, which is shown in Table 5.1.

Modes	Irrep.	$E$	$C_2$	$\sigma_v$	$\sigma'_v$
Mode 1 & 2	$A_1$	1	1	1	1
	$A_2$	1	1	-1	-1
Mode 3	$B_1$	1	-1	1	-1
	$B_2$	1	-1	-1	1

Table 5.1 The irreducible representations of the symmetry group of  $\text{H}_2\text{O}$  and which of its vibrational modes correspond to which representation. Here  $E$  is the identity,  $C_2$  a 180-degree rotation about the axis down the centre of the molecule, and  $\sigma_v$  and  $\sigma'_v$  are reflections in the plane and perpendicular to the plane of the molecule respectively.

Symmetry operations that leave the mode unchanged are assigned 1, and symmetry operations that transform the mode back into itself with a phase change (in this example always  $\pi$ ) are given the value of -1 ( $e^{i\phi}$  for an arbitrary phase shift). Table 5.1 also shows that there are other possible irreducible representations ( $A_2$  and  $B_2$ ) that no mode transforms as.

Representations need not be one dimensional. Figure 5.2 shows the molecule vibrational modes of a  $\text{CO}_2$  atom. As before, it is possible to construct the representation of the group these modes form by thinking about how they transform under the symmetry operations of the molecule. Two of the modes (modes 3 & 4 in Figure 5.2) form one-dimensional representations as before, which means all the symmetry operations transform them back into themselves, but two of the modes are transformed into one another by the symmetry

operations (Table 5.2). Consequently, they form a 2-dimensional representation, and as described in the next section, this means that they must be degenerate.

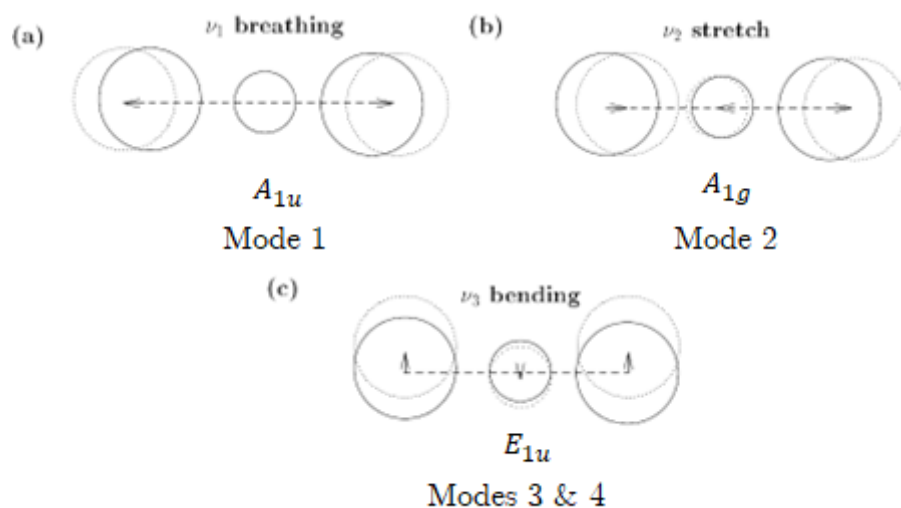


Fig. 5.2 Vibrational modes of  $\text{CO}_2$ . Modes 3 & 4 are both bending modes (where the O-C-O angle changes) with orthogonal displacements and are degenerate by symmetry. Figure reproduced from [122].

Establishing which irreducible representation each mode transforms under is the first step to using group theory in any physical problem. Once this is established, one can begin to it to analyse the effect of symmetry on the mode behaviour. Below, it is shown how an understanding of the irreducible representations of a set of modes can give information about their degeneracy, and avoided crossings, two phenomena that are analysed in depth in this Chapter for the magnetic modes of a SAF.

Modes	Irrep.	$E$	$2C_\infty$	...	$\infty\sigma_v$	$i$	$2S_\infty$	...	$\infty C'_2$
Mode 1	$A_{1g}$	1	1	...	1	1	1	...	1
Mode 2	$A_{1u}$	1	1	...	1	-1	-1	...	-1
Mode 3 & 4	$E_{1u}$	2	$2 \cos(\phi)$	...	0	-2	$2 \cos(\phi)$	...	0

Table 5.2 The irreducible representations of the symmetry group of  $\text{CO}_2$  and which of its vibrational modes correspond to which representation. Here  $E$  is the identity,  $C_\infty$  a set of rotations by an angle  $\phi$  about the axis of the molecule,  $\infty\sigma_v$  are a set of reflections in a plane of the molecule at an angle  $\phi$ ,  $i$  is an inversion,  $2S_\infty$  are improper rotations about an angle  $\phi$  about the molecule axis, and  $\infty C'_2$  are rotations by 180 degrees about axes perpendicular to the molecular axis.

**Degeneracy:**

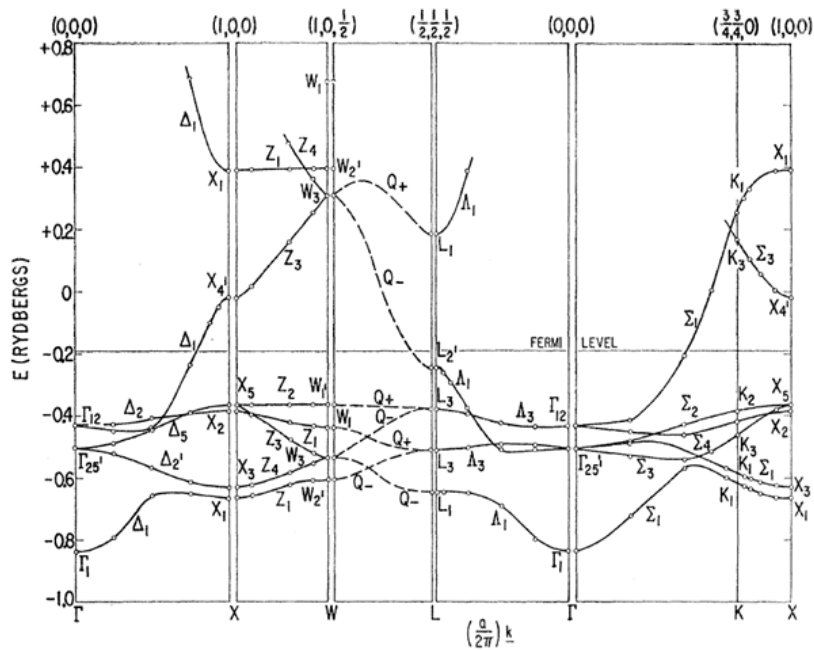


Fig. 5.3 The electronic band structure of Copper. Reproduced from [224].

Figure 5.3 shows the electronic band structure of Copper. Consider the three degenerate modes at the  $\Gamma$  point labeled  $\Gamma_{25}'$ . This label denotes the irreducible representation of these modes transform as at the  $\Gamma$  point. As discussed in Section 2.6.2, the fact that they transform

as the same irreducible representation already shows that they must be degenerate, although in practice the exact modes and their energies are usually calculated first at a high symmetry point like the  $\Gamma$  point (where the calculation is easiest) and then the irreducible representation worked out after the fact. Where groups are useful in this instance is understanding how this symmetry-enforced degeneracy changes as one moves away from the high symmetry point in the bandstructure. This is the same analysis that is performed on the magnetic modes of the antiferromagnetically coupled oscillators in this chapter.

Consider the modes as the energy band moves from  $\Gamma \rightarrow X$ . The three modes on the diagram are split into two sets of modes, labeled by their irreducible representations  $\Delta_5$  and  $\Delta_{2'}$ . This decomposition is the result of the lowering of symmetry of the system as the band moves away from the high symmetry point at the  $\Gamma$  point. The details of how to perform this decomposition calculation using group theory are given in Section 2.6.2. The modes that transform as  $\Delta_5$  transform according to a 2-dimensional irreducible representation, and hence remain degenerate (note how they split apart from  $X \rightarrow W$  as the symmetry is lowered further), whereas the  $\Delta_{2'}$  mode is now a single mode without degeneracy.

Now compare this behaviour with the behaviour as the band moves from  $\Gamma \rightarrow K$ . Here the degenerate set of modes split into 3 modes with 3 different energies, labelled again by their irreducible representations  $\Sigma_2$ ,  $\Sigma_3$  and  $\Sigma_4$ , which are all one-dimensional representations as expected. The difference between these two cases is because the symmetry group of the Hamiltonian is different at the  $K$  and  $X$  points. Group theory allows the computation of these effects without ever solving the Hamiltonian at these points, or taking any experimental data. Knowledge of the symmetries of the equation and the modes at the  $\Gamma$  point alone is sufficient. The procedure to calculate this is as follows:

1. Write down the new, lower symmetry group, at the lower symmetry point in the bandstructure. Compute, or look up in a standard reference table, the irreducible representations of this new group.

2. Using the group decomposition algorithm (see 2.6.2), decompose the old irreducible representation of the modes in the higher symmetry group into the new irreducible representations of the new, lower symmetry group. In this example, the formula will give the decompositions:

$$\Gamma_{25'} \rightarrow \Delta_5 + \Delta_2 \quad (5.2)$$

from  $\Gamma \rightarrow X$ , and:

$$\Gamma_{25'} \rightarrow \Sigma_2 + \Sigma_3 + \Sigma_4 \quad (5.3)$$

from  $\Gamma \rightarrow K$ .

3. The type and number of different irreducible representations in the decompositions tells you how the modes will either retain or lose their degeneracy as the symmetry is lowered. The dimensions of each irreducible representation in the decomposition indicates the degeneracy of the new modes. E.g. if a 3-dimensional irreducible representation splits into a 2-dimensional and 1-dimensional irreducible representation, then you will have a set of doubly degenerate modes and a singularly degenerate mode (as in the example  $\Gamma_{25'} \rightarrow \Delta_5 + \Delta_2$ , where  $\Delta_5$  is a two-dimensional representation and  $\Delta_2$  is a one dimensional one).

The decomposition in step 2 is a simple mathematical procedure that can be done by hand relatively quickly and easily and is shown in detail in Section 2.6.2. In this way, group theory enables one to understand the effect of symmetry on the degeneracy of the modes without extensive calculation or experimentation. What is more, it allows this behaviour to be pinpointed exclusively to the effect of symmetry.

**Avoided crossings:**

When is it possible for two modes to cross, or when must they repel one another? If there is a perturbation,  $\delta H$ , to the eigenvalue problem:

$$(H + \delta H)\boldsymbol{\mu}' = (\omega + \delta\omega)\boldsymbol{\mu}' \quad (5.4)$$

where  $H\boldsymbol{\mu} = \omega\boldsymbol{\mu}$  is the unperturbed equation, and  $\delta\omega$  is the perturbation to the eigenvalue, then for two unperturbed modes,  $\boldsymbol{\mu}, \boldsymbol{\nu}$ , the Wigner Von-Neuman avoided crossing theorem shows that they may only cross if their matrix element

$$\boldsymbol{\mu}^\dagger \delta H \boldsymbol{\nu} \quad (5.5)$$

vanishes, otherwise they will hybridise strongly and repel.

Group theory allows one to calculate straightforwardly if (5.5) vanishes. *If the two modes transform according to the same irreducible representation of their symmetry group, (5.5) is non-zero, and the modes must repel to form an anticrossing. Otherwise, (5.5) is zero, and the modes may cross.*

Why this is the case can be understood simply from the usual perturbation theory formula:

$$\delta\omega \approx \boldsymbol{\mu}^\dagger \delta H \boldsymbol{\nu} + \frac{|\boldsymbol{\mu}^\dagger \delta H \boldsymbol{\nu}|^2}{\omega - \omega_\nu} \quad (5.6)$$

where  $\omega_\nu$  is the unperturbed eigenvalue of the mode  $\boldsymbol{\nu}$ . This shows that as the two modes converge in frequency, the second perturbation term can only remain finite (and zero) if (5.5) is zero. This result can be used to understand the anticrossings that form when a SAF is perturbed from a perfectly symmetrical configuration.

Note that this also enables one to determine when apparent anticrossings truly result in a strong hybridisation of the two modes or is just an incidental feature of the band structure with

no underlying hybridisation of the modes (as (5.5) is zero). This is important for applications where the hybridisation of the modes is the principal physical phenomenon of interest, as is the case in the hybridisation of magnetic modes with lowered symmetry reported in the literature [42, 43].

## 5.3 Methods

### 5.3.1 Computation methods used for the analysis of experimental data:

Throughout this work, computer simulations were employed extensively in order to analyse and understand the experimental data. Where possible, explicit formulae were derived from the LLG equation and the experimental data fit to these models using numerical least squares regression.

For more complex models, involving a large range of terms, solving the LLG equation by hand can become excessively cumbersome – especially when the terms that need to be included are not known *a priori*. In addition, in order to solve the LLG equation, one must first determine the solution to Brown’s equation, which can become likewise unwieldy, and it may also be unclear which of the solutions is the relevant one to the experimental conditions because of hysteresis effects. In these cases, a simple numerical simulation programme was written in order to simulate the predicted positions of the magnetisation, and its response to a driving magnetic field.

#### Solving Brown’s equation numerically:

The solution to Brown’s equation gives a local minima in the energy of the system for a given magnetic configuration. It has the form:

$$\mathbf{M}_i \times \mathbf{H}_i^{eff} = \mathbf{0} \quad (5.7)$$

where  $\mathbf{M}_i$  is the  $i^{\text{th}}$  magnetisation vector with magnitude  $M_S$ ,  $\mathbf{M}_i = M_S \mathbf{m}_i$ , and  $\mathbf{H}_i^{\text{eff}}$  is the effective magnetic field it experience. It must be satisfied for all magnetisation vectors in the system simultaneously. Solving this equation, or equivalently minimising the magnetic energy of the system, gives one of the potentially multiple equilibrium magnetic configurations. However, because the solution of Brown's equation is not unique, it is often easier to work from the LLG equation instead:

$$\partial_t \mathbf{M}_i = -\gamma_0 \mathbf{M}_i \times (\mathbf{H}_i^{\text{eff}} + \mathbf{h}) + \frac{\alpha}{M_S} \mathbf{M}_i \times \partial_t \mathbf{M}_i + \frac{\kappa}{M_S^2} \mathbf{M}_i \times (\mathbf{M}_i \times \mathbf{h}) \quad (5.8)$$

where  $\mathbf{h}$  is a time-varying effective field,  $\alpha$  is the Gilbert damping coefficient,  $\gamma_0 = \gamma \times \mu_0$  — the product of the gyromagnetic ratio and permeability of free space — and  $\kappa$  determines the strength of its associated antidamping torque. Under the conditions  $\mathbf{h} = \mathbf{0}$ , (5.8) shows that (5.7) is equivalent then to the condition that the magnetisations are stationary with respect to time.

This is useful because it provides a simple way of finding the correct solution to Brown's equation by solving the evolution of the magnetisation under the LLG equation until it reaches an equilibrium point. The value of  $\alpha$  has no effect on the final equilibrium point, so is usually chosen to maximise the rate of convergence to the new stationary magnetic configuration. This data can then be used to simulate experiments that directly measure the position of the magnetisation, e.g. VSM, or fed into further simulations of magnetoresistance or FMR experiments.

The LLG equation constitutes an initial value problem where, denoting the two magnetisation vectors by  $\mathbf{y} = (\mathbf{m}_A, \mathbf{m}_B)$ , the first order ordinary differential equation  $\dot{\mathbf{y}} = \mathbf{f}(t, \mathbf{y})$  is solved subject to the boundary conditions  $\mathbf{y}(t_0) = \mathbf{y}_0$  over some time interval  $[t_0, t_f]$ .  $\mathbf{f}(t, \mathbf{y})$  is given by the right hand side of (5.12). This differential equation will be solved via a Runge-Kutta numerical integration scheme.

Runge-Kutta methods are a family of numerical integration schemes of the form:

$$\mathbf{y}_{n+1} = \mathbf{y}_n + h \sum_i^s b_i k_i \quad (5.9)$$

$$k_i = f(x_n + c_i h, y_n + h \sum_{j=1}^s a_{ij} k_j) \quad c_i = \sum_{j=1}^s a_{ij} \quad (5.10)$$

Where  $h$  is the step size, and  $b_i$ , and  $a_{ij}$  are method-specific constants. They compute an estimate to the output vector,  $\mathbf{y}(t_{n+1})$ , or  $\mathbf{y}_{n+1}$ , based on the previous value  $\mathbf{y}_n$  and a weighted average of estimates of the slope of  $\mathbf{f}(t, \mathbf{y})$  at intermediate steps. In these simulations, the Scipy implementation of a Runge-Kutta method known as Dormand-Prince was used.

Dormand-Prince uses two Runge-Kutta methods, one of order 5 and another of order 4 (the order, in this case, referring to the local truncation error), and by comparing their estimates of  $\mathbf{y}_{n+1}$  the local truncation error can be computed. The step size is then adjusted to keep the error below a user-specified tolerance. This allows for as large a step size as possible to be used whilst not compromising on accuracy.

Expressed as in (5.8), the LLG is an implicit equation. The Dormand-Prince method requires an explicit differential equation. It is possible to recast (5.8) into explicit form by taking the cross product of (5.8) with  $\mathbf{M}_i$ . Expanding out the triple cross product in the Gilbert damping term, and noting  $\mathbf{M}_i \cdot \dot{\mathbf{M}}_i = 0$ , one finds:

$$\mathbf{m}_i \times \frac{d\mathbf{m}_i}{dt} = -\gamma_0 \mathbf{m}_i \times (\mathbf{m}_i \times (\mathbf{H}_{eff} + \mathbf{h})) - \alpha \frac{d\mathbf{m}_i}{dt} - \kappa \mathbf{m}_i \times \mathbf{h} \quad (5.11)$$

where  $\mathbf{M}_i = M_{si} \mathbf{m}_i$ . Substituting this into (5.8) for the Gilbert damping term, one obtains the final extrinsic equation:

$$(1+\alpha^2) \frac{d\mathbf{m}_i}{dt} = -\gamma_0 \mathbf{m}_i \times (\mathbf{H}_{eff} + \mathbf{h}) - \gamma_0 \alpha \mathbf{m}_i \times (\mathbf{m}_i \times (\mathbf{H}_{eff} + \mathbf{h})) - \kappa \alpha \mathbf{m}_i \times \mathbf{h} + \kappa \mathbf{m}_i \times (\mathbf{m}_i \times \mathbf{h}) \quad (5.12)$$

which is solved using the `scipy.integrate` implementation of the Runge-Kutta method in (5.10).

### 5.3.2 Simulating the LLG for oscillating magnetic fields

In this limit of small variations in the magnetisation in the presence of an oscillating MW field  $\mathbf{h}(t) = \mathbf{h}(\omega)e^{i\omega t}$ , it is possible to expand out (5.12) by writing the magnetisation as a combination of a static term,  $\mathbf{m}_0$ ,  $\mathbf{m}_i = \mathbf{m}_0 + \mathbf{m}e^{i\omega t}$  and a small oscillating term  $\mathbf{m}(\omega)e^{i\omega t}$ . By linearising this equation, the coupling between different  $\omega$  modes vanishes to first order:

$$\begin{aligned} i\omega(1 + \alpha^2)\mathbf{m} &= -\gamma_0\mathbf{m} \times \mathbf{H}_{eff} - \gamma_0\mathbf{m}_0 \times \mathbf{h} \\ -\gamma_0\alpha\mathbf{m}_0 \times \mathbf{m}_0 \times \mathbf{h} - \kappa\alpha\mathbf{m}_0 \times \mathbf{h} + \kappa\mathbf{m}_0 \times (\mathbf{m}_0 \times \mathbf{h}) \end{aligned} \quad (5.13)$$

(5.13) clearly has a solution of the form  $\boldsymbol{\omega} = \chi(\omega)\mathbf{h}(\omega)$ . Consequently, if the solution for  $\mathbf{m}(t)$  is found in the presence of an oscillating eternal field, one should expect, by Fourier transforming this solution, to find  $\chi(\omega)$ . *It must be stress that it is not the linearised version (5.13) that is solved in the simulation programme, but rather the full version given in (5.12).*

To verify this programme was working as expected, its output is compared against known analytical results. Figure 5.4 shows the predicted resonance frequencies of a single, elliptical bodied, magnet in a magnetic field,  $H$ , along its x-axis. This magnetic configuration has a simple analytical expression for its resonance frequencies:

$$(\omega/\gamma_0)^2 = (H + (N_z - N_x)M_s)(H + (N_y - N_x)M_s) \quad (5.14)$$

where  $N_i$  are the components along the diagonal of the demagnetisation tensor,  $\mathbf{N} = \text{diag}(N_x, N_y, N_z)$  [95].

This data was collected by first determining the equilibrium position of the magnetisation by waiting for the magnetic configuration to converge to a stationary point as detailed above.

To find the resonance frequency, a microwave oscillating magnetic field was then introduced to the effective field of the simulation, whose amplitude was modulated by a sinc function over time:

$$\mathbf{h}(t) = \mathbf{h}(0) \times e^{i\omega_0 t} \text{sinc } 2\Delta\omega t \quad (5.15)$$

The sinc function modulation means that the Fourier transform of the microwave driving field is a top hat, whose width is determined by the width of the modulation sinc function. Consequently, the Fourier transform of the simulated magnetisation dynamics,  $\mathcal{F}\mathbf{m}(t) = \mathbf{m}(\omega)$  is a direct measure of the linear susceptibility,  $\chi(\omega)$ :

$$\mathbf{m}(\omega) = \chi(\omega)\mathbf{h}(\omega) \propto \chi(\omega) \quad (5.16)$$

across a range of frequencies:  $\omega_0 - \Delta\omega < \omega < \omega_0 + \Delta\omega$ . Because of the efficiency of the fast-Fourier transform algorithm, this is more efficient than solving the LLG equation for a range of single-frequency driving fields. The resonance frequency can then be determined by the maxima in  $\mathbf{m}(\omega)$ , as shown in Figure 5.4. Figure 5.4 shows that the simulations are in good agreement with the known result.

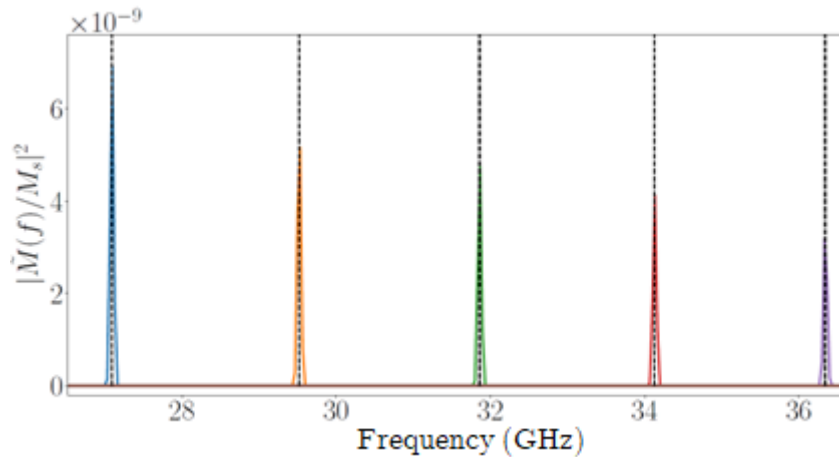


Fig. 5.4 Power spectrum of the simulated magnetic oscillations of an elliptical magnet in response to a microwave driving field at different external field values. Dashed lines indicate the analytical resonance frequency; the two show excellent agreement.

**Simulating the resonance frequency of the LLG equation:**

The above approach can be used to simulate the resonance frequency of a magnetic system. However, when used as part of a fitting routine in which the magnetic parameters of the simulation are constantly being changed and re-simulated to find the best fit to the experimental data, it is often prohibitively slow. Instead, I:

1. Find the equilibrium position of the magnetisation by relaxing the LLG equation as detailed above
2. Solve the resulting linearised LLG matrix eigenvalue equation using the method of Smit and Blejers [96] numerically

This requires an additional analytic step compared to the fully numerical method of finding the resonance frequencies used to validate the Runge-Kutta simulation of the LLG equation used above, as the matrix components of the LLG equation in the Smit and Beljers form must all be found (which is performed in the following section). Solving the resulting eigenvalue equation numerically however is computationally fast and saves the difficulty of solving it fully by hand, allowing the resonance frequencies to be determined sufficiently quickly for a gradient-descent least squares regression method to be practical to use to fit experimental data. The eigenvalue equation was solved numerically using the `numpy.linalg.eig` package in Python.

For each new magnetic configuration under consideration, step 2 will need to be repeated. In the following section, it is shown how the components of the LLG equation were derived for the case of two coupled magnetic oscillators where the equilibrium magnetisations lie entirely in-plane.

### Deriving an analytic form for the LLG equation of coupled ferromagnets:

The magnetisation dynamics of a series of coupled ferromagnetic oscillators can be modeled by the LLG equation:

$$\frac{d\mathbf{m}_i}{dt} = -\gamma\mathbf{m}_i \times \mathbf{H}_{eff}^i + \alpha_i\mathbf{m}_i \times \frac{d\mathbf{m}_i}{dt} \quad (5.17)$$

where  $\mathbf{m}_i$  is the (normalised) magnetisation of the  $i^{th}$  magnetic moment,  $\mathbf{H}_{eff}^i$  is the effective field it experiences, and  $\alpha_i$  is the Gilbert damping. Solutions of the form  $\mathbf{m}_i = \mathbf{m}_{0i} + \boldsymbol{\mu}_i e^{i\omega_\mu t}$  are assumed.  $\mathbf{m}_{0i}$  is the equilibrium magnetisation vector and  $\boldsymbol{\mu}_i$  oscillates in a plane transverse to  $\mathbf{m}_{0i}$  with frequency  $\omega_\mu$ . In spherical coordinates  $\boldsymbol{\mu}_i$  is given by  $\boldsymbol{\mu}_i = \mu_{i\theta}\hat{\mathbf{e}}_\theta + \mu_{i\phi}\hat{\mathbf{e}}_\phi$ , where  $\hat{\mathbf{e}}_\theta$  and  $\hat{\mathbf{e}}_\phi$  are the usual unit vectors in the  $\theta$  and  $\phi$  directions.

To derive a linearised equation for the dynamics of the magnetisation, the procedure of Smit and Beljers [96] is followed, the logic of which is straightforwardly illustrated in the case of a single layer, and can then be extended to the multi-layer case. The effective field is defined as the derivative of the free energy,  $U$ , with respect to the magnetisation directions and volume. Taylor expanding the magnetisation about its equilibrium direction in the usual way (noting that by definition of the equilibrium direction, all first derivatives vanish):

$$U = U_0 + \frac{1}{2}\boldsymbol{\mu}^\dagger H \boldsymbol{\mu} \quad (5.18)$$

where  $\boldsymbol{\mu}$  is a small displacement,  $U_0$  is the energy at equilibrium, and  $H$  is the Hessian of  $U$ . From the definition of  $\mathbf{H}_{eff}$  as the derivative of the energy density with respect to the magnetisation:

$$\mathbf{H}_{eff} = \frac{1}{\mu_0 M_s V} H \boldsymbol{\mu} \quad (5.19)$$

where  $V$  is the volume of the magnet. Substituting this into the LLG equation (5.17) with  $\alpha = 0$  it is found, to first order in  $\boldsymbol{\mu}$ :

$$i\omega_\mu \boldsymbol{\mu} = -\gamma \mathbf{m}_{0i} \times \frac{1}{\mu_0 M_s V} H \boldsymbol{\mu} \quad (5.20)$$

noting that  $\mathbf{m}_{0i}$  is a unit vector in the radial direction, the cross product in (5.20) can be replaced by a matrix of the form  $\begin{bmatrix} 0 & -1 \\ 1 & 0 \end{bmatrix}$ . Taking the resultant matrix onto the other side gives the final form:

$$-\omega_\mu \mathcal{I} \boldsymbol{\mu} = \gamma H \boldsymbol{\mu} \quad (5.21)$$

where:

$$\mathcal{I} = \mu_0 \begin{pmatrix} 0 & iM_s V \\ -iM_s V & 0 \end{pmatrix} \quad (5.22)$$

It is straightforward to extend this to the case of a two-layer (labeled A and B) device with the replacement of  $H$  with the appropriate Hessian and  $\mathcal{I}$  with [280]:

$$\mathcal{I} = \mu_0 \begin{pmatrix} 0 & iM_{sA} V_A & 0 & 0 \\ -iM_{sA} V_A & 0 & 0 & 0 \\ 0 & 0 & 0 & iM_{sB} V_B \\ 0 & 0 & -iM_{sB} V_B & 0 \end{pmatrix} \quad (5.23)$$

where  $\boldsymbol{\mu}$  is the 4-component vector that represents the oscillating part of both layers A and B:  $\boldsymbol{\mu} = (\boldsymbol{\mu}_A, \boldsymbol{\mu}_B) = (\mu_{A\theta}, \mu_{A\phi}, \mu_{B\theta}, \mu_{B\phi})$ , and  $V_i$  and  $M_{si}$  are the volumes and saturation magnetisation of the  $i^{th}$  layer. In this notation, the definition of the oscillating effective field

is given by:

$$\begin{bmatrix} h_{A\theta} \\ h_{A\phi} \\ h_{B\theta} \\ h_{B\phi} \end{bmatrix} = \begin{bmatrix} 1/M_{sA}V_A & 0 & 0 & 0 \\ 0 & 1/M_{sA}V_A & 0 & 0 \\ 0 & 0 & 1/M_{sB}V_B & 0 \\ 0 & 0 & 0 & 1/M_{sB}V_B \end{bmatrix} \begin{bmatrix} H_{AA}^{\theta\theta} & H_{AA}^{\theta\phi} & H_{AB}^{\theta\theta} & H_{AB}^{\theta\phi} \\ H_{AA}^{\phi\theta} & H_{AA}^{\phi\phi} & H_{AB}^{\phi\theta} & H_{AB}^{\phi\phi} \\ H_{BA}^{\theta\theta} & H_{BA}^{\theta\phi} & H_{BB}^{\theta\theta} & H_{BB}^{\theta\phi} \\ H_{BA}^{\phi\theta} & H_{BA}^{\phi\phi} & H_{BB}^{\phi\theta} & H_{BB}^{\phi\phi} \end{bmatrix} \begin{bmatrix} \mu_{A\theta} \\ \mu_{A\phi} \\ \mu_{B\theta} \\ \mu_{B\phi} \end{bmatrix} \quad (5.24)$$

Here, the component  $H_{AB}^{\theta\phi}$  for instance represents the second derivative with respect to  $\theta_A$  and  $\phi_B$  of the energy. The second matrix on the right is the Hessian of the energy density. Strictly, it is the curvature of the free energy density that enters into the LLG equation, but at equilibrium, where first derivatives vanish, this is equivalent to the Hessian and is denoted by  $H$  in (5.21).

In order to reproduce the experimental data, the SAFs are modelled as having an effective field with contributions from an external field, exchange fields, demagnetisation fields, and uni-axial fields. This results in a total energy of the system given by:

$$U = U_e + U_{ex} + U_{demag} + U_{ani}^A + U_{ani}^B \quad (5.25)$$

where  $U_e$  is the energy of the external field,  $U_{ex}$  the exchange field energy,  $U_{demag}$  the energy due to demagnetisation interactions, and  $U_{ani}^i$  the energy from uni-axial anisotropy in layer  $i$ .

These terms can be written explicitly as:

$$U_e = -\mu_0 \mathbf{h}_e \cdot (\mathbf{m}_A M_{sA} V_A + \mathbf{m}_B M_{sB} V_B) \quad (5.26)$$

where  $\mathbf{h}_e$  is the external field, which lies in-plane at an angle  $\phi_H$  to the x-axis, which is defined to be along one edge of the bar parallel to the direction of the current.

$$U_{demag} = \frac{\mu_0 V_A}{2} M_{sA}^2 \mathbf{m}_A \cdot \mathbf{N}^{AA} \mathbf{m}_A + \frac{\mu_0 V_B}{2} M_{sB}^2 \mathbf{m}_B \cdot \mathbf{N}^{BB} \mathbf{m}_B + \frac{\mu_0 V_A}{2} M_{sA} M_{sB} \mathbf{m}_A \cdot \mathbf{N}^{AB} \mathbf{m}_B + \frac{\mu_0 V_B}{2} M_{sA} M_{sB} \mathbf{m}_B \cdot \mathbf{N}^{BA} \mathbf{m}_A \quad (5.27)$$

here  $\mathbf{N}^{ij}$  is the matrix that describes the demagnetisation field in layer  $i$  due to the magnetic moment in layer  $j$ . The demagnetisation tensors are calculated assuming that the magnetic oscillations are contained only within the bar-like constriction that makes up each sample, which oscillates as a single magnetic moment. If the volumes  $V_A$  and  $V_B$  are taken to be equal  $V_A = V_B = V$ , then  $\mathbf{N}^{AB} = \mathbf{N}^{BA} = \text{diag}(\lambda, \lambda, -2\lambda)$  and  $\mathbf{N}^{AA} = \mathbf{N}^{BB} = \text{diag}(\delta, \delta, 1 - 2\delta)$ , where  $\lambda$  and  $\delta$  depend on the precise geometry of the device.

The exchange field between the two layers has an energy:

$$U_{ex} = JA \mathbf{m}_A \cdot \mathbf{m}_B + J_2 A (\mathbf{m}_A \cdot \mathbf{m}_B)^2 \quad (5.28)$$

$J$  and  $J_2$  are the exchange constants for the bilinear and biquadratic exchange fields, while  $A$  is the surface area of the bar. These can be combined into the effective exchange fields:

$$H_{E(i)}^{(1)} = \frac{2J_1}{\mu_0 t_i M_{si}} \quad (5.29)$$

$$H_{E(i)}^{(2)} = \frac{J_2}{\mu_0 t_i M_{si}}$$

where  $t_i$  is the thickness of the layer.

The magnetocrystalline anisotropy is modeled as having two contributions. One from the out-of-plane perpendicular magnetic anisotropy, and one from the in-plane magnetocryst-

talline anisotropy induced by a magnetic field applied during sample growth:

$$U_{ani}^i = -\frac{\mu_0 V_i}{2} M_{si} H_{a(i)}^{(P)} \left( \mathbf{m}_i \cdot \hat{\mathbf{H}}_{a(i)}^{(P)} \right)^2 - \frac{\mu_0 V_i}{2} M_{si} H_{a(i)}^{(N)} \left( \mathbf{m}_i \cdot \hat{\mathbf{H}}_{a(i)}^{(N)} \right)^2 \quad (5.30)$$

$\mathbf{H}_{a(i)}^{(P)} = H_{a(i)}^{(P)} \hat{\mathbf{H}}_{a(i)}^{(P)}$  is the strength and direction of the in-plane anisotropy in layer  $i$  at angle  $\phi_E$  to the x-axis of the bar, and likewise  $\mathbf{H}_{a(i)}^{(N)} = H_{a(i)}^{(N)} \hat{\mathbf{H}}_{a(i)}^{(N)}$  is the strength and direction of the out of plane anisotropy in layer  $i$ .

The matrix elements of the Hessian, defined in (5.24), are calculated from the energy terms given by (5.45)-(5.48). They have the following form:

$$\begin{aligned} \frac{1}{M_{si} V} H_{ii}^{\theta\theta} = & h_e \cos(\phi_i - \phi_H) - M_{sj} \lambda \cos(\phi_i - \phi_j) + M_{si} (1 - \delta) \\ & - H_{a(i)}^{(N)} + H_{a(i)}^{(P)} \cos^2(\phi_i - \phi_E) - H_{E(i)}^{(1)} \cos(\phi_i - \phi_j) - H_{E(i)}^{(2)} \cos^2(\phi_i - \phi_j) \end{aligned} \quad (5.31)$$

$$\begin{aligned} \frac{1}{M_{si} V} H_{ii}^{\phi\phi} = & h_e \cos(\phi_i - \phi_H) - M_{sj} \lambda \cos(\phi_i - \phi_j) + H_{a(i)}^{(P)} \cos(2(\phi_i - \phi_E)) - H_{E(i)}^{(1)} \cos(\phi_i - \phi_j) \\ & - H_{E(i)}^{(2)} \cos^2(\phi_i - \phi_j) \end{aligned} \quad (5.32)$$

$$H_{ii}^{\theta\phi} = H_{ii}^{\phi\theta} = 0 \quad (5.33)$$

$$\frac{1}{M_{si} V} H_{ij}^{\theta\theta} = -2\lambda M_{sj} + H_{E(i)}^{(1)} + H_{E(i)}^{(2)} \cos(\phi_i - \phi_j) \quad (5.34)$$

$$\frac{1}{M_{si} V} H_{ij}^{\phi\phi} = M_{sj} \lambda 2 \cos(\phi_i - \phi_j) + H_{E(i)}^{(1)} \cos(\phi_i - \phi_j) + H_{E(i)}^{(2)} \cos(2(\phi_i - \phi_j)) \quad (5.35)$$

$$H_{ij}^{\theta\phi} = H_{ij}^{\phi\theta} = 0 \quad (5.36)$$

where  $\phi_i$  is the angle between the magnetisation of layer  $i$  and the x-axis. Physically  $\frac{1}{M_{si} V_i} H_{ij}^{kl}$  gives the contribution of the  $l^{th}$  component of the oscillating magnetisation of the  $j^{th}$  layer to the microwave field in the  $k^{th}$  direction in the  $i^{th}$  layer.

To simulate the resonance frequencies at a given external magnetic field, it is necessary to first find the equilibrium directions of the two magnetic moments at that field,  $\phi_A$  and  $\phi_B$ , by numerically solving the LLG equation with  $\alpha \neq 0$  until the two magnetisations relax into a local minimum in energy (5.44) using the Runge-Kutta method described above. This ensures that the correct local minima in the energy distribution is found and hence hysteresis is appropriately accounted for. Then, the eigenvalue equation (5.21) is solved numerically to find the frequencies of the modes.

To verify the validity of this simulation, consider the case of two antiferromagnetically coupled layers with a uniaxial anisotropy in an external field perpendicular to the easy axis. The resonance fields have the magnetic field dependence given in Table 5.3 [283].

Field	Resonance frequency 1	Resonance frequency 2
$0 < h_e < H_{E\perp}$	$\omega_1/\gamma_0 = \sqrt{H_C^2 + (H_{E\parallel}/H_{E\perp})h_e^2}$	$\omega_2/\gamma_0 = \sqrt{H_C^2 - (H_A^{(P)}/H_{E\perp})h_e^2}$
$H_{E\perp} < h_e$	$\omega_1/\gamma_0 = \sqrt{h_e(h_e - H_A^{(P)})}$	$\omega_2/\gamma_0 = \sqrt{(h_e - 2H_E^{(1)})(h_e - H_E^{(1)})}$

Table 5.3 Resonance frequencies of an AF with the external field applied perpendicular to its easy axis.

where  $H_{E\parallel} = 2H_E^{(1)} - H_A^{(P)}$ ,  $H_{E\perp} = 2H_E^{(1)} + H_A^{(P)}$ , and  $H_C = \sqrt{H_A^{(P)}(2H_E^{(1)} - H_A^{(P)})}$ .

Figure 5.5 shows the prediction of the simulation programme versus the analytical formula for a uniaxial antiferromagnet with exchange field  $\mu_0 H_E^{(1)} = 100$  mT, an anisotropy field  $\mu_0 H_A^{(P)} = 10$  mT, and  $\mu_0 M_s = 1$  T. Demagnetisation effects are neglected here (such as for a perfectly spherical sample).

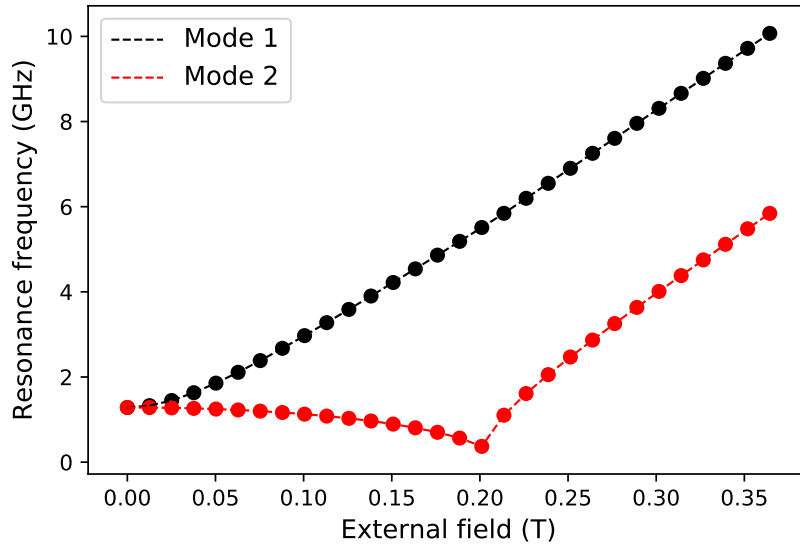


Fig. 5.5 Analytical expression for the two modes of a uniaxial antiferromagnet (dashed line) and the corresponding prediction by the simulation programme (dots).

#### Fitting the simulations to experimental data:

Using the explicit forms for  $H_{ii}$  derived in the previous section, and the Smit and Blejers form of the LLG equation,  $\omega \mathcal{I} \boldsymbol{\mu} = \gamma H \boldsymbol{\mu}$ , it is possible to easily calculate the resonance frequency of a SAF model once the equilibrium position has been determined from simulations of Brown's equations as detailed above. Additionally, from the equilibrium position, the net moment can be determined and this is used to model magnetometry measurements. By comparing a model's output to experimental data, standard chi-square regression can be used to adjust the parameters of the model in order to best reproduce the experimental data.

When fitting the experimental data in this work, both the FMR data and VSM data were simultaneously modeled using the same set of input parameters using the model described

above. The formula for  $\chi^2$  used was then:

$$\chi^2 = \sum_{\text{VSM data points}} \frac{|(M_{VSM} - (\mathbf{M}_A V_A + \mathbf{M}_B V_B) \cdot \hat{\mathbf{h}}_e)|^2}{\sigma_{VSM}^2} + \sum_{\text{FMR data points}} \frac{(\omega_{FMR}^{(1)} - \omega_{sim}^{(1)})^2}{\sigma_{\omega^{(1)}}^2} + \frac{(\omega_{FMR}^{(2)} - \omega_{sim}^{(2)})^2}{\sigma_{\omega^{(2)}}^2} \quad (5.37)$$

where  $\hat{\mathbf{h}}_e$  is a unit vector along the external field direction,  $M_{VSM}$  is the magnetic moment measured by the VSM,  $\sigma_{\omega^i}$  and  $\sigma_{VSM}$  are the errors of each data points,  $\omega_{FMR}^{(i)}$  is the experimentally measured FMR resonance frequency of mode  $i$ , and  $\omega_{sim}^{(i)}$  is the simulations predicted resonance mode under the same experimental conditions. By minimising  $\chi^2$  using a gradient descent algorithm, the best match to the combined experimental data and its uncertainty can be determined.

## 5.4 Results

### 5.4.1 Group theory and the Landau-Lifshitz-Gilbert equation

The symmetry of physical systems provides serious constraints on their behaviour and greatly simplifies any necessary calculation or understanding. The mathematical language of symmetry is group theory, and it is frequently employed in physical problems to great effect [122, 225].

An understanding of how groups could be applied to physical problems was first investigated by Wigner [225]. Group theory has subsequently been widely used in physical problems to simplify otherwise exceedingly complex calculations and offers ‘intuitive’ insight into the outputs of otherwise entirely abstract calculations.

Should one wish to conduct a similar inquiry into the LLG equation in order to understand its symmetry-influenced properties, as seems reasonable, it will be necessary to establish in what sense, if at all, the eigenvector solutions ‘engender’ a representation of the symmetry

group of the magnetic system. Here, there is a slight difference between the LLG and the aforementioned physical systems (quantum mechanical systems, mechanical oscillators etc.). Because of the strong inter-atomic exchange forces that rapidly quench any out-of-equilibrium variations in the magnetisation's magnitude, the LLG dynamical equation of motion contains a cross product that ensures  $\dot{\mathbf{M}}$  is always orthogonal to  $\mathbf{M}$ :

$$\partial_t \mathbf{M} = \gamma_0 \mathbf{H}_{eff} \times \mathbf{M} \quad (5.38)$$

where  $\gamma_0 = \mu_0 \gamma$ ,  $\mathbf{H}_{eff}$  is the effective magnetic field, and  $\mathbf{M}$  the unnormalised magnetisation vector (magnitude  $M_s$ ). As a consequence of this, the resultant linearised equation of motion is typically non-Hermitian. For example, the linearised equation of motion of a thin-film single ferromagnetic layer in an external field  $h_e$  is given by:

$$\begin{pmatrix} i\omega/\gamma_0 & h_e + M_s \\ -h_e & i\omega/\gamma_0 \end{pmatrix} \begin{pmatrix} m_y \\ m_z \end{pmatrix} = \begin{pmatrix} 0 \\ 0 \end{pmatrix} \quad (5.39)$$

$$A(\omega) \tilde{\mathbf{m}} = \mathbf{0}$$

Clearly  $A \neq A^\dagger$ . This is important because the eigenvector solutions to a Hermitian eigenvalue problem: a) form a complete basis and b) are orthogonal under the standard inner product. Condition a) is required for the modes to be able to engender a representation of the group (see Section 2.6), and condition b) allows the formulation of a simple recipe for determining the coefficients of this representation. In order to apply group theory to the LLG equation, it will be necessary to establish these qualities in its solutions.

Intuitively, one should expect to be able to do this as the eigenvalues of the (undamped) LLG equation represent the oscillations of a real physical system, and hence must be real. Consequently, it is expected that underneath there should be some Hermitian structure that

ensures the real nature of the eigenvalues. From this Hermitian structure, completeness and some notion of orthogonality under a suitable inner product should follow.

Consider the case of two coupled magnetic oscillators within the macropsin approximation, whose deviation from their equilibrium position is labelled  $\mathbf{M}_A(t) = M_{sA}\tilde{\mathbf{m}}_A(t) = M_{sA}\tilde{\mathbf{m}}_A e^{i\omega t}$  for layer A, and likewise  $\mathbf{M}_B(t) = M_{sB}\tilde{\mathbf{m}}_B(t) = M_{sB}\tilde{\mathbf{m}}_B e^{i\omega t}$  for layer B.  $M_{si}$  is the saturation magnetisation of layer  $i$ . The case of time-dependent single-frequency solutions is the case that will be relevant to the experimental measurements of synthetic antiferromagnets in Section 5.4.3 and is the simplest system in which one should expect symmetry to have a significant effect on the spin-wave properties. The linearised LLG equation for simple systems is typically calculated via expanding both sides of (5.38) to linear order in  $\tilde{\mathbf{m}}_{A/B}$ . For more complex systems, consisting of many coupled oscillators or many terms in the magnetic free energy, Smit and Beljers [96] showed that the linearised form of (5.38) could be calculated more straightforwardly using the Hessian of the free energy, similar to standard linearised oscillation problems, with some modifications due to the definition of the effective magnetic field and the cross product. A short derivation of this is given in Section 5.3.2. The resulting eigenvalue equation has the form:

$$\omega_\mu \mathcal{I} \boldsymbol{\mu} = \gamma H \boldsymbol{\mu}$$

$$\mathcal{I} = \mu_0 \begin{pmatrix} i\mathcal{A}(M_{sA}V_A) & 0 \\ 0 & i\mathcal{A}(M_{sB}V_B) \end{pmatrix}; \quad \mathcal{A}(x) = \begin{pmatrix} 0 & x \\ -x & 0 \end{pmatrix} \quad (5.40)$$

where  $\boldsymbol{\mu}$  is a 4-component vector consisting of the transverse harmonic oscillations (at frequency  $\omega_\mu$ ) of the two magnetic layers:  $\boldsymbol{\mu} e^{i\omega_\mu t} = (\tilde{\mathbf{m}}_A(t), \tilde{\mathbf{m}}_B(t)) = (\tilde{\mathbf{m}}_A, \tilde{\mathbf{m}}_B) e^{i\omega_\mu t}$ ,  $H$  is the Hessian of the energy in terms of the transverse magnetic coordinates, and  $\mathcal{I}$  is a four by four matrix that originates from the cross product of the magnetisation with the effective field. In Section 5.3.2 these matrices are evaluated explicitly for a uniaxial SAF.

Aside from the benefit of its relative ease of computation, the method of Smit and Beljers reveals explicitly the underlying Hermitian structure of the LLG equation. Unlike the Hermitian eigenvalue problems familiar from other areas of physics, the form of the LLG equation is that of a ‘generalised’ eigenvalue problem: equations of the form  $A\mathbf{x} = \omega B\mathbf{x}$ , where both  $A$  and  $B$  are Hermitian matrices. In (5.40),  $\mathcal{I}$  is evidently Hermitian, as is the Hessian by the definition of its elements and the symmetry of mixed partial derivatives:  $(H)_{ij} = (H)_{ji} = \partial^2 E / \partial \mu_i \partial \mu_j$ . Note that because of the conservation of the norm of  $\mathbf{M}$ , it is usually convenient to work in spherical polars, minus the radial component, which is constant. Should the magnetisation lie in the plane  $\theta = \pi/2$ , as is usual for thin-film magnets without significant PMA, then the components of the Hessian are just  $H_{\theta\phi} = \partial^2 H / \partial \theta \partial \phi$  etc.. Otherwise, additional factors of  $1/\sin \theta$  are required because of the metric in these coordinates. These are straightforwardly calculated from the definition of the Hessian as the Jacobian of the gradient of  $E$ :  $H = \mathbf{J} \nabla E$ . The Hessian is still symmetric in its indices regardless, and so retains its Hermitian nature.

Because the Hessian evaluated at a minimum of an energy landscape (from the definition of an equilibrium magnetic configuration) is positive definite, the eigenvectors of the LLG equation have the following properties:

1. They form a complete set
2. They are orthogonal under the modified inner product: i.e.  $\boldsymbol{\mu}^\dagger \mathcal{I} \boldsymbol{\nu} = \delta_{\mu\nu}$  for eigenvectors  $\boldsymbol{\mu}$  and  $\boldsymbol{\nu}$

Equation (5.40) gives an explicit form for  $\mathcal{I}$  for a uniform  $\mathbf{k} = \mathbf{0}$  mode with two magnetic moments, and this is straightforwardly extended to larger systems with an arbitrary number of moments and to non-zero  $\mathbf{k}$  (so long as a classical treatment is still permitted). For an example of applying the method of Smit and Beljers to non-uniform modes, see [280]. From a group theory perspective, the main difference between non-zero  $\mathbf{k}$  modes and uniform modes is that only the symmetry operations of the  $\mathbf{k} = \mathbf{0}$  mode that leave  $\mathbf{k}$  (a vector, not a

pseudo-vector like the magnetisation) invariant are allowed in the lower symmetry  $\mathbf{k} \neq \mathbf{0}$  group. Hence, for this mode, the symmetry of the system will be lowered compared to the  $\mathbf{k} = \mathbf{0}$  mode.

$$R_{\mu\nu} = (\det\{R\}) \boldsymbol{\mu}^\dagger \mathcal{I} R \boldsymbol{\nu} \quad (5.41)$$

Compare this with the usual component form for a Hermitian eigenvalue problem:  $R_{\mu\nu} = \boldsymbol{\mu}^\dagger R \boldsymbol{\nu}$ . The additional factor of  $\det\{R\}$  in (5.41) accounts for the pseudo-vector nature of the magnetisation, and consequently operations such as reflections induce an additional sign change in its components compared with a regular vector. The factor of  $\mathcal{I}$  originates from the inner product under which the eigenvectors are orthonormal (after appropriate normalisation).

With this slight modification to the usual procedure of generating the representation of the group from the eigenvectors, it is possible to inherit all of the wealth of methods developed for applying group theory to other eigenvalue problems to the linearised LLG equation. This will allow for a complete analysis of the symmetry-induced behaviour of spin-wave modes.

### 5.4.2 Analysing the ferromagnetic resonance modes of antiferromagnetically coupled oscillators using group theory

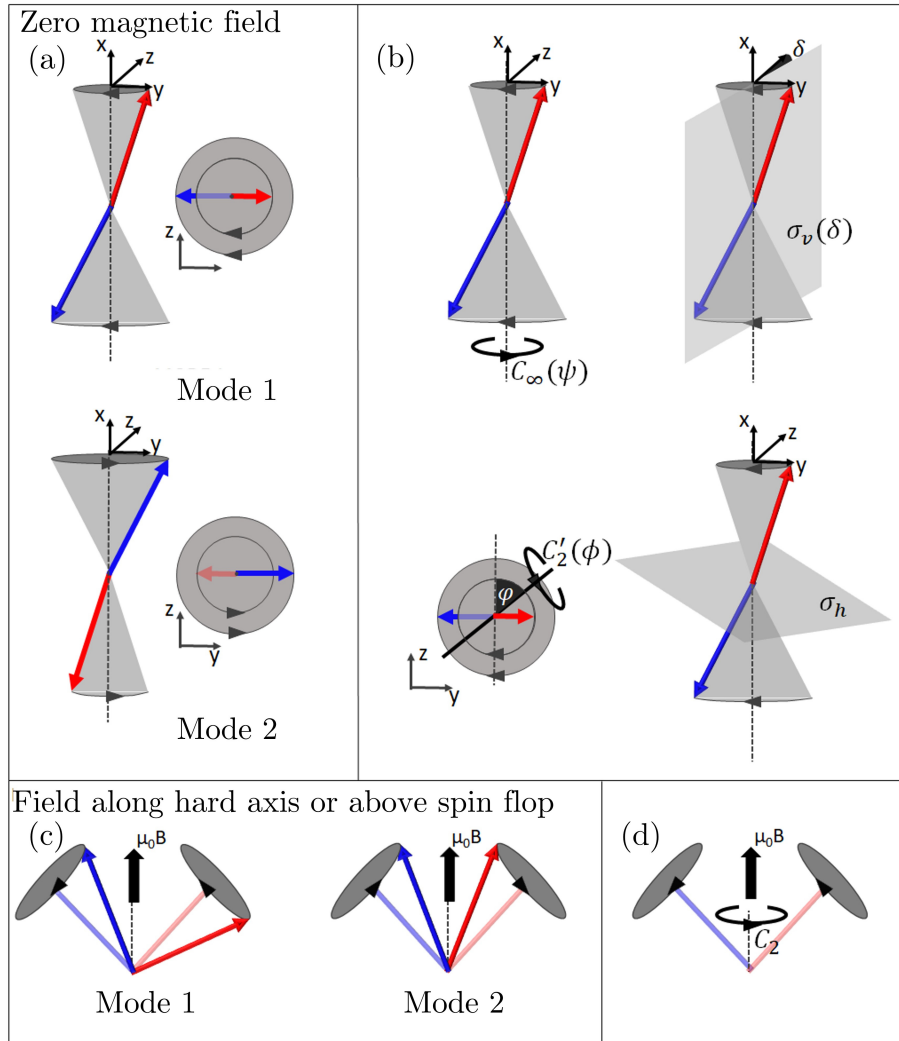


Fig. 5.6 Pictorial representation of the resonance modes (a) and some of the symmetry operations (b) of an antiferromagnet with a uniaxial anisotropy along the x-axis at zero magnetic field. The two arrows represent the magnetisations, and the cones the area they sweep out as they rotate.  $C_\infty(\phi)$  represents a rotation about the x-axis of angle  $\phi$ .  $\sigma_v(\delta)$  represents a reflection in a plane parallel to the x-axis and at angle  $\delta$  with respect to the z-axis.  $C'_2(\phi)$  represents a rotation of 180 degrees about an axis in the y-z plane at an angle  $\phi$  to the z-axis.  $\sigma_h$  represents a reflection in the y-z plane. Resonance modes (c) and symmetry operation  $C_2$ , a rotation of 180 degrees about the field direction, (d) for a system of thin-film antiferromagnetically coupled oscillators when the magnetic field,  $\mu_0 B$ , is applied along the hard-axis or is above the spin flop field. This figure has been reproduced from [268].

Once how to engender a representation of the symmetry group using the eigenmodes of the LLG equation has been established, analysing their symmetry-enforced properties follows in the usual way. In the following section, it is illustrated how it is possible to understand both the degeneracy of modes and avoided crossing phenomena. Understanding the degeneracy of the zero-field modes of an antiferromagnet in terms of symmetry has not been reported before in the literature<sup>2</sup>.

### **Degeneracy:**

*Group theory shows that the degeneracy of a set of resonance modes can be understood as consequence of the symmetry of the system. This understanding can be used to then show how or when this degeneracy is lost as a consequence of symmetry lowering (e.g. due to external magnetic fields, device structure changes).*

Coupled oscillators have two unique modes, referred to as *Mode 1* and *Mode 2* (Figure 5.6a) [284–286]. The terminology ‘optical’ and ‘acoustic’ mode is often employed to describe these modes [43, 281], in analogy with phonon modes, rather than because their frequencies correspond to these regimes. Unique identification of these modes across the whole spectrum is a source of some contention within the community. First consider the case where no external magnetic field is applied. In a uniaxial antiferromagnet the two magnetisations lie along the easy-axis, and the two modes, shown in Figure 5.6a, are degenerate at zero field (Figure 5.7a). In a SAF, the magnetisations still lie along the easy-axis, but now the spectrum looks radically different, with the degeneracy being removed (Figures 5.7b and 5.7c). This difference can be understood in terms of the different symmetries that characterise the two types of antiferromagnetically coupled oscillators.

---

<sup>2</sup>Anticrossings were first understood in terms of symmetry in the literature by MacNeill et al. and Liensberger et al. [42, 43], although this work was performed independently of these studies. An analysis of their methods for understanding symmetry-induced anticrossings and this one is presented in Section 5.4.4

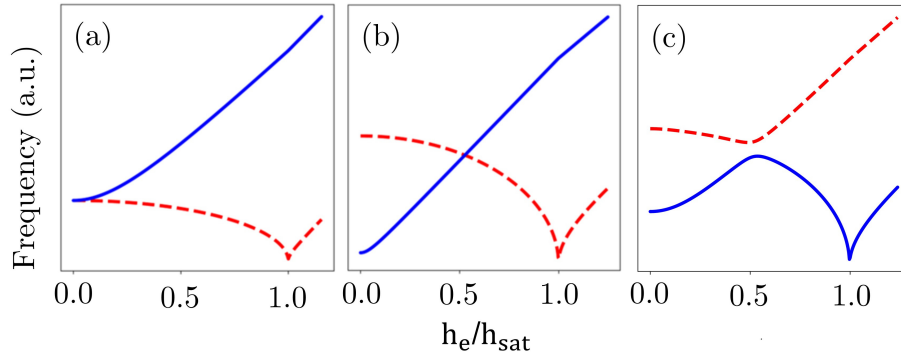


Fig. 5.7 Resonance frequencies versus field of an antiferromagnet with an in-plane magnetocrystalline uniaxial anisotropy (a), and a synthetic antiferromagnetic with an in-plane magnetocrystalline uniaxial anisotropy with symmetric (b) and asymmetric (c) magnetic layers calculated from the LLG equation. The external field,  $h_e$  is normalised relative to the field at which the two magnetisations align,  $h_{sat}$ . The external magnetic field is applied along the in-plane hard-axis.

For a uniaxial antiferromagnet, the symmetry operations, i.e. the operations that leave the static configuration of the system invariant, are the same as those of the familiar homonuclear diatomic molecule and form the symmetry group  $D_{\infty h}$ . This applies so long as it is possible to neglect the shape anisotropy as is typical for an AF due to their net zero moment [283]. A selection of these symmetry operations is shown in Figure 5.6b and their action on the two modes is summarised in table 5.4.

$D_{\infty h}$	$C_{\infty}(\psi)$	$\sigma_v(\delta)$	$C'_2(\phi)$	$\sigma_h$
$E_{1g}$	$\begin{pmatrix} e^{-i\psi} & 0 \\ -0 & e^{i\psi} \end{pmatrix}$	$\begin{pmatrix} 0 & -e^{-i2\delta} \\ -e^{i2\delta} & 0 \end{pmatrix}$	$\begin{pmatrix} 0 & e^{-i2\phi} \\ e^{i2\phi} & 0 \end{pmatrix}$	$\begin{pmatrix} -1 & 0 \\ 0 & -1 \end{pmatrix}$

Table 5.4 Representations of a selection symmetry operations engendered by the degenerate eigenmodes of a uniaxial antiferromagnet at zero fields. Note the effect the pseudo-vector nature of the magnetisation has on the representations of the reflection operator  $\sigma_h$ . Were the magnetisation a vector, its modes would engender the representation  $E_{1u}$ .

These matrices can be derived by explicit calculation using (5.41), or more intuitively by visualising how each operation maps the original modes onto themselves/their counterpart.  $C_{\infty}(\psi)$  describes an anticlockwise rotation about the easy-axis by an angle  $\psi$  and adds a

phase  $e^{-i\psi}$  and  $e^{i\psi}$  to mode 1 and mode 2 respectively.  $\sigma_v(\delta)$  is a reflection in a plane that contains the easy-axis and makes an angle  $\delta$  with the z-axis. Following the usual rules for pseudo-vectors under reflection/inversion, this operation transforms the modes into one another with the additional phase  $e^{-i2\delta}$  and  $e^{i2\delta}$ .  $C'_2(\phi)$  is a 180 degrees rotation about an axis lying in the yz-plane at an angle  $\phi$  with the z-axis and again transforms the modes into each other with the addition of a phase.  $\sigma_h$ , a reflection in the yz-plane perpendicular to the easy-axis, transforms the modes into themselves with the addition of a 180 degrees phase. The additional elements of  $D_{\infty h}$ , consisting of an inversion operator and improper rotations, can be calculated similarly. Together, the matrix representations engendered by the modes form the irreducible representation  $E_{1g}$  of the full symmetry group  $D_{\infty h}$ .

A representation is said to be irreducible when there is no change in basis (that is, it is not possible to find two new modes in which to form a basis from a linear combination of the original ones) in which all the matrices that make the group are reduced in a block-diagonal form (or in the case of a 2-dimensional representation, as in this case, diagonal form). There is a standard procedure for determining if a representation is reducible or irreducible (see [122]). However, to those less familiar with these methods, because in a 2-dimensional representation being reducible is equivalent to being diagonalisable, it may be easier to instead to think of irreducible representations as those which have non-zero commutators for at least one pair of matrices. The matrices in Table 5.4 have non-zero commutators for  $\psi \neq n\pi$  and  $\phi$  and  $\delta \neq n\pi/2$  and this means that they cannot be simultaneously diagonalised by a similarity transformation. Consequently, because group theory shows that modes that transform as an N-dimensional irreducible representation have an N-fold degeneracy, the two modes must be degenerate at zero field, and hence their degeneracy here may be thought of as a consequence of the symmetry of the system.

To lift the degeneracy, group theory shows it is therefore necessary to lower the symmetry of the system such that the 2D irreducible representation of the higher symmetry group

decomposes into two 1D irreducible representations of the new lower symmetry group. Equivalently, the symmetry operations with non-vanishing commutators must be removed from the group.

In a SAF, where the coupled magnets are thin films in the  $xy$ -plane and assumed to be identical, the presence of shape anisotropy leads to  $C_\infty(\psi)$ ,  $\sigma_v(\delta)$  and  $C'_2(\phi)$  being symmetry operations only when  $\psi = n\pi$  and  $\phi$  and  $\delta = n\pi/2$ . This removes the offending commutators and hence the the 2-dimensional irreducible representation of the higher symmetry group splits into two one-dimensional irreducible representations of the new, lower symmetry, group. Hence, from group theory this induces the splitting of the modes at zero field. Therefore, it is possible to understand the presence or absence of degeneracy at zero field as a consequence of symmetry.

### **Avoided crossings**

*Groups allow the analysis of anticrossings straightforwardly as a consequence of the symmetry of the system. This follows from the Wigner Von-Neuman avoided crossing theorem, that states that two modes can cross only when they transform as different irreducible representations of the symmetry group.*

In other disciplines, such as in the study of the vibrational modes of complex molecules or electronic energy levels in crystals, anticrossings are commonly understood via the Wigner-Von Neuman avoided-crossing theorem, which states that only modes that transform according to different irreducible representations of their symmetry group may cross. Because the modes of a coupled magnetic oscillator engender the representation of a group, the Wigner-Von Neuman theorem still holds. Here the case of a magnetic field applied along the hard-axis direction or along the easy-axis above the spin-flop value is considered. The two modes of

a symmetric SAF are shown in Figure 5.6c. The resonance spectra of *mode 1* and *mode 2* correspond respectively to the continuous blue and dashed red lines in Figure 5.7b.

In a symmetric SAF where the two magnetic layers are equal,  $C_2$ , describing 180-degree rotations about the field direction (Figure 5.6d), is the only symmetry operation other than the identity. The same is true for the field applied along the easy-axis above the spin-flop value. By considering the behaviour of the two modes in Figure 5.6c under  $C_2$ , one can see that they transform as the irreducible representations of the group  $A_2$  and  $A_1$ :

$$\begin{array}{c|cc}
 & E & C_2 \\
 \hline
 A_1 & 1 & 1 \\
 A_2 & 1 & -1
 \end{array} \quad (5.42)$$

Here,  $E$  is the identity transformation. Because these two modes transform according to different representations, from the Wigner-Von-Neumann avoided crossing theorem [225], they are predicted to cross at a single external field value. However, when the symmetry of the system is lowered, for example by making the two magnetic layers unequal or by applying the magnetic field in a direction that does not coincide with a high symmetry direction,  $C_2$  is no longer a symmetry operation and the modes must transform according to the same trivial representation, causing them to hybridise strongly and repel (Figure 5.7c). Note that this result clearly applied to *any* symmetry lowering effect that removes  $C_2$  as a symmetry operation. In this way, it has been possible to generalise this phenomenon without the need to consider the details of the LLG equation for each and any symmetry lowering effect one might wish to consider. It is satisfactory only to consider if the new device or experimental configuration will retain  $C_2$  as a symmetry element.

### 5.4.3 Experimental realisation in synthetic antiferromagnets

In the following section, it is demonstrated experimentally the features predicted by symmetry by measuring the resonance spectrum via FMR of two synthetic antiferromagnets: one with identical ferromagnetic layers, and one with disparate ones.

Two structures are measured, Ta[2]/Pt[3]/CoFeB[1.4]/Ru[0.9]/CoFeB[1.4]/Pt[x]/Ta[2] (all thicknesses in nm), where  $x = 1$  nm (referred to as the single-sided structure) or 6 nm (referred to as the double-sided structure). The SAF structures were fabricated according to the procedure detailed in Section 3.2.2 by Dr W. Liao in the group of Prof R. P. Cowburn at the University of Cambridge. The devices were patterned into  $5 \mu\text{m} \times 5 \mu\text{m}$  bars by electron beam lithography and argon ion milling and electrically contacted on two opposite sides. The low aspect ratio for the bars is chosen so as not to further lower the symmetry of the device by introducing additional shape anisotropy terms (the in-plane demagnetisation field for this geometry is estimated to be  $\sim 1$  mT, negligible with respect to the other anisotropy terms). The orientation of the device is such that the in-plane field-induced easy-axis cuts along one diagonal of the square, 135 degrees from the current flow direction.

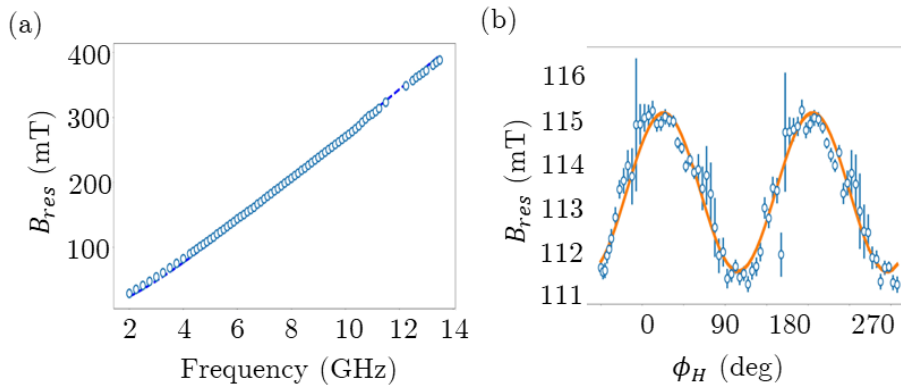


Fig. 5.8 (a) Resonance field ( $B_{res}$ ) versus frequency for the single ferromagnetic layer sample. From a fit to the Kittel mode (dashed blue line), a value of 211 mT is obtained for the effective magnetisation, suggesting that the lower layer in the SAF structures has sizeable out-of-plane anisotropy. (b)  $\phi_H$  dependence of the resonance field of the single layer sample. From a fit of  $B_{res}(\phi)$  from the Kittel formula, an estimate of the uniaxial in-plane anisotropy of 3.17 mT is obtained.

An additional single magnetic layer structure Ta[2]/Pt[3]/CoFeB[1.4]/Ru[0.9]/Ta[2] was also fabricated under the same conditions and used to characterise the anisotropy terms. Figure 5.8a shows a measurement of the resonance field versus frequency for the single layer sample and its associated fit to the Kittel formula:

$$\omega/\gamma = \mu_0 \sqrt{(H_{res} + H_1)(H_{res} + H_2)} \quad (5.43)$$

where  $H_1 = M_s - H_{\perp} + H_a \cos^2(\phi_H - \phi_E)$  and  $H_2 = H_a \cos(2(\phi_H - \phi_E))$ .  $H_a$  is in the in-plane uniaxial anisotropy with an easy-axis at an angle  $\phi_E$  to the x-axis and  $H_{\perp}$  is the perpendicular magnetic anisotropy. From this fit, an effective magnetisation of  $\mu_0 M_s^{eff} = \mu_0(M_s - H_{\perp}) = 211 \pm 2$  mT was found, significantly lower than the bulk magnetisation of CoFeB ( $\approx 1500$  mT). From other measurements on similar structures with 4 nm thick layers of CoFeB, where the PMA is expected to be negligible, the effective magnetisation can be expected to be around 1200 mT. This reduction relative to the bulk is likely attributable to a magnetic dead layer near the interface, owing to the sizeable out-of-plane anisotropy. Consequently, the lower layer in the SAF structures is expected to also have significant out-of-plane anisotropy, whilst still being an in-plane magnetised sample. Figure 5.8b the dependence of the resonance field on the angle of the external field  $\phi_H$ . The fit to the Kittel formula (5.43) determines that the in-plane uniaxial anisotropy is  $\mu_0 H_a = 3.17 \pm 0.12$  mT.

Structure	$\mu_0 \Delta(M_s^{eff})$ (mT)	$\mu_0 \Delta(M_s)$ (%)	$J^{(1)}$ ( $\mu\text{J}/\text{m}^3$ )	$J^{(2)}$ ( $\mu\text{J}/\text{m}^3$ )	$\mu_0 H_a$ (mT)
Single Sided	$610 \pm 40$	$7.5 \pm 0.6$	$50.5 \pm 0.5$	$6.7 \pm 0.6$	$3 \pm 2$
Double Sided	$13 \pm 9$	$15.2 \pm 1.2$	$58.6 \pm 0.6$	$12.2 \pm 1.0$	$2 \pm 2$

Table 5.5 Numerical parameters calculated from FMR and VSM fitting.

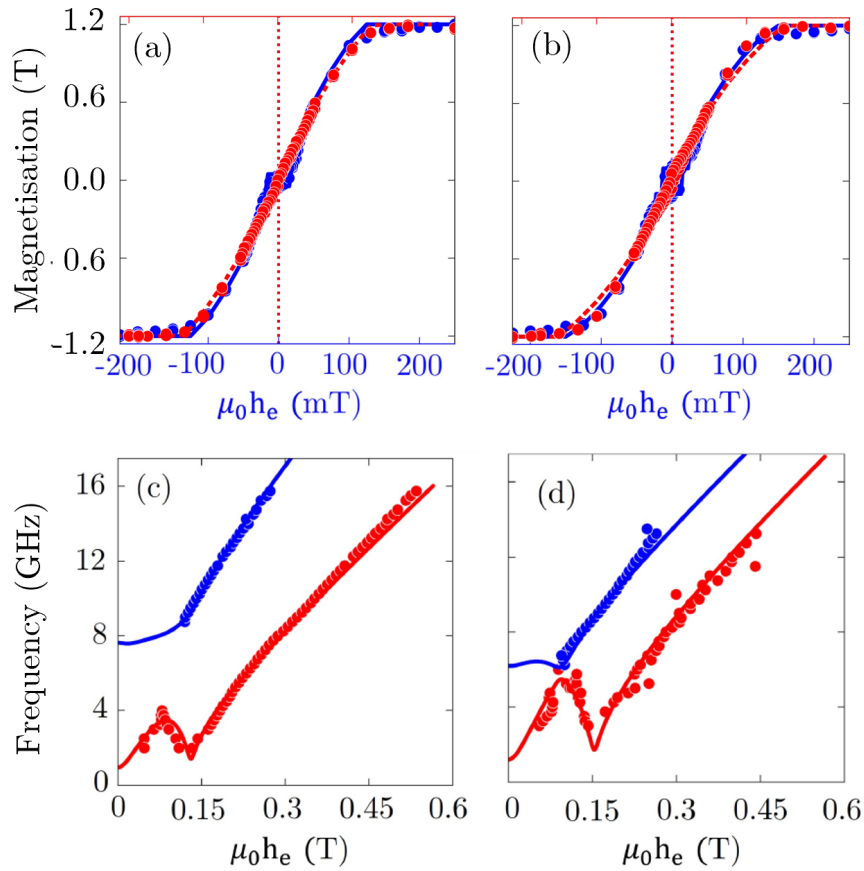


Fig. 5.9 The net magnetic moment measured by VSM and the FMR spectrum for a field applied along the in-plane hard-axis for the single-sided, (a) & (c), and double-sided, (b) & (d), structures. In (a) and (b), the blue (red) data set represents the net magnetic moment when the external field is applied along the easy (hard) axis. Vertical dashed lines correspond to zero external field. VSM measurement was taken by Dr Z. Sorban of the Academy of Science of the Czech Republic.

To investigate the effects of symmetry lowering on the dynamic properties of the synthetic antiferromagnets, the magnetic field dependence of the resonance frequencies was measured by ST-FMR and the net magnetic moment was measured by vibrating sample magnetometry (VSM) by Dr Z. Sorban of the Academy of Science of the Czech Republic, as shown in Figure 5.9. The two plots are fitted simultaneously (continuous line in the figure) via least squares regression using a custom macrospin simulation of the resonance frequencies of the SAF versus the external field. The details of this simulation programme are given in Section 5.3.2. The equilibrium position of the two magnetic moments for a certain value of

the external magnetic field is found by numerically simulating the LLG equation via a finite difference method with  $\alpha \neq 0$  until convergence. Subsequently, the resonance frequencies are determined numerically by solving the eigenvalue equation (5.40) using the free energy density derived in Section 5.3.2. The SAFs are modelled as having both linear and biquadratic exchange, and the magnetisation and PMA are allowed to vary between the layers. The in-plane anisotropy is assumed to be the same in both layers to within the resolution of the experiments. This gives an analytic form for energy of the magnetic system:

$$U = U_e + U_{ex} + U_{demag} + U_{ani}^A + U_{ani}^B \quad (5.44)$$

where  $U_e$  is the energy of the external field,  $U_{ex}$  the exchange field energy,  $U_{demag}$  the energy due to demagnetisation interactions, and  $U_{ani}^i$  the energy from uni-axial anisotropy in layer  $i$ . These terms can be written explicitly as:

$$U_e = -\mu_0 \mathbf{h}_e \cdot (\mathbf{m}_A M_{sA} V_A + \mathbf{m}_B M_{sB} V_B) \quad (5.45)$$

where  $\mathbf{h}_e$  is the external field, which lies in-plane at an angle  $\phi_H$  to the x-axis.

$$\begin{aligned} U_{demag} = & \frac{\mu_0 V_A}{2} M_{sA}^2 \mathbf{m}_A \cdot \mathbf{N}^{AA} \mathbf{m}_A + \frac{\mu_0 V_B}{2} M_{sB}^2 \mathbf{m}_B \cdot \mathbf{N}^{BB} \mathbf{m}_B + \frac{\mu_0 V_A}{2} M_{sA} M_{sB} \mathbf{m}_A \cdot \mathbf{N}^{AB} \mathbf{m}_B \\ & + \frac{\mu_0 V_B}{2} M_{sA} M_{sB} \mathbf{m}_B \cdot \mathbf{N}^{BA} \mathbf{m}_A \end{aligned} \quad (5.46)$$

here  $\mathbf{N}^{ij}$  is the matrix that describes the demagnetisation field in layer  $i$  due to the magnetic moment in layer  $j$ .

$$U_{ex} = J A \mathbf{m}_A \cdot \mathbf{m}_B + J_2 A (\mathbf{m}_A \cdot \mathbf{m}_B)^2 \quad (5.47)$$

$J$  and  $J_2$  are the exchange constants for the bilinear and biquadratic exchange fields, while  $A$  is the surface area of the bar.

$$U_{ani}^i = -\frac{\mu_0 V_i}{2} M_{si} H_{a(i)}^{(P)} \left( \mathbf{m}_i \cdot \hat{\mathbf{H}}_{a(i)}^{(P)} \right)^2 - \frac{\mu_0 V_i}{2} M_{si} H_{a(i)}^{(N)} \left( \mathbf{m}_i \cdot \hat{\mathbf{H}}_{a(i)}^{(N)} \right)^2 \quad (5.48)$$

For the derivation of converting this energy expression into an effective field, and subsequently solving the resultant LLG equation, see Section 5.3.2. The extracted parameters are summarised in Table 5.5.  $\mu_0 \Delta(M_s^{eff})$  and  $\mu_0 \delta(M_s)$  represent the relative difference in effective and saturation magnetisation respectively of the top magnetic layer relative to the bottom one as measured by FMR (effective magnetisation) and the VSM (saturation magnetisation),  $J^{(1)}$  and  $J^{(2)}$  are the bilinear and biquadratic exchange constants, while  $\mu_0 H_a$  is the in-plane uniaxial anisotropy. The double-sided sample behaves in a similar manner to a perfectly symmetric SAF, with no experimentally observable anticrossing. The similar magnetic properties between the layers imply that  $C_2$  remains a symmetry operation, and hence no anticrossing is measured. In the single-sided structure, it is found that the out-of-plane anisotropy of the upper magnetic layer is significantly reduced compared to the lower layer, resulting in a large difference in effective magnetisation that removes  $C_2$  as symmetry operation and results in significant anticrossing.

The strength of this anticrossing is characteristic of the strength of the coupling between the modes. This is an important figure of merit for devices which rely on the strong hybridisation of modes for information technology devices, such as the conversion of microwave photons into optical photons [287, 288], and is quantified by the coupling rate  $g/2\pi$ .  $g/2\pi$  is calculated from half the difference of the largest frequency gap between the two modes [43], which from figure 5.9c gives  $g \approx 2$  GHz. Although from this data alone it cannot be concluded that the system is in the strong-coupling regime, which is defined as when  $g > \kappa_A$  &  $g > \kappa_B$ , where  $\kappa_{A/B}$  are the damping rates of the two modes, the large values of  $g$  are suggestive that tuning the out-of-plane anisotropy of the two layers is a viable means

of generating strong magnon-magnon interactions. PMA can not only be varied by varying the sample composition but can also be controlled electrically by applying a voltage to a gate separated from the sample by an insulating layer [289]. This offers the prospect of an all-electronic means of controlling the magnon-magnon coupling strength. Because the demagnetisation field and PMA are some of the strongest interactions known in thin-film ferromagnets, varying them between the layers even further offers the greatest prospect of boosting the mode coupling.

#### 5.4.4 Comparison with other works

During the course of this study, two works were published that likewise showed that avoided or anticrossings in magnetic systems could be understood as a result of symmetry-lowering perturbations. In this Section, their arguments are reviewed and compare them to the understanding of this phenomenon from a group theory perspective developed here.

MacNeill et al. [43] studied the FMR spectrum of the weak (Néel temperature  $\approx 15$  K [290]) antiferromagnet  $\text{CrCl}_3$  as a function of the out-of-plane angle ( $\theta$  in Figure 2.1) of the external field, showing that an anticrossing develops for  $\theta \neq n\pi/2$  (for integer  $n$ ). They conclude that the out-of-plane external field results in a loss of exchange symmetry between the layers and that this results in an eigenvalue equation of the form:

$$\begin{vmatrix} \omega_a^2(\theta) - \omega^2 & \Delta^2(\theta) \\ \Delta^2(\theta) & \omega_o^2(\theta) - \omega^2 \end{vmatrix} = 0 \quad (5.49)$$

where (5.49) has been written in the basis of the  $\theta = n\pi/2$  eigenvectors of the LLG equation that are simultaneously odd (o) and even (a) eigenvectors of the parity exchange operator, with unperturbed eigenvectors  $\omega_o(n\pi/2)$  and  $\omega_a(n\pi/2)$  respectively (the parity exchange operator swaps the two magnetic sublattices). They show that the off-diagonal terms,  $\Delta^2(\theta)$ , occur because of the loss of exchange symmetry as the matrix in the linearised LLG equation

no longer commutes with the exchange matrix, and hence the basis of eigenvectors of the exchange operator no longer simultaneously diagonalise the linearised LLG equation. They derive an explicit form  $\Delta$ , which vanishes when  $\theta = n\pi/2$ , and show that non-zero  $\Delta$  leads to a mode anticrossing by explicitly calculating the new eigenvalues numerically.

Liensberger et al. [42] study a two-lattice ferrimagnet in the colinear state that develops a weak magnetocrystalline anisotropy non-colinear with a larger uniaxial magnetocrystalline anisotropy that defines the easy-axis direction. This likewise breaks the rotational symmetry about the easy-axis. Their subsequent argument follows along the same lines as MacNeill et al. (i.e. from explicit calculation of the new, lower symmetry eigenvalues).

This approach is advantageous in that the implications of matrix commutation on eigenvalue problems are likely to be familiar to most physicists from other areas such as quantum mechanics. However, like in the quantum mechanics literature, using groups simplifies the required calculation, and in this instance approach allows the anticrossing phenomena to be understood without the need to calculate the dynamic equation of motion or its solutions.

This gives the group theory perspective a certain conceptual elegance, and the requirement of having to explicitly calculate, solve, and then transform (into the unperturbed eigenvector basis) the linearised LLG equation can become very involved for even simple coupled magnetic systems. Consequently, group theory is generally computationally more straightforward than explicit calculation.

As a simple illustration of this point, Section 5.3.2 for the terms in the linearised LLG equation of a uniaxial synthetic antiferromagnet, which already for a relatively simple coupled system becomes quite unwieldy. Compare the effort required to solve this equation, transform the resulting eigenvalue equation in the new basis, and then show explicitly that this results in a sufficiently strong interaction to repel the two modes from each other, with the computational effort of the arguments in Section 5.4.2, which can be completed in a

single line and generalised instantly to all other forms of symmetry lowering in this particular system.

A further benefit of understanding this phenomenon in terms of groups is that it gives a clear picture of why and *when* a loss of symmetry will result in an anticrossing. A lowering of symmetry of the system does not necessitate that two modes may no longer cross: it is only when they now are members of the same irreducible representation that the Wigner-Von Neuman avoided-crossing theorem applies. In the cases so far in the literature, which have all involved antiferromagnetically coupled bimagnetic systems, the arguments in Section 5.4.2 show that the symmetry of the system is sufficiently trivial that any further lowering will result in an anticrossing. However, should more complex multi-oscillator systems be pursued in the future, either by macroscopic design or by microscopic structure, as seems likely given the interest in these strongly coupled magnon-magnon systems, then the effect of symmetry lowering may be more complex.

## 5.5 Future work

One of the most interesting applications of group theory to physical problems is determining the degeneracy of the modes of atoms symmetry alone, i.e. without referencing the equations of motion at all, only symmetry and their associated conservation laws. This is perhaps most familiar when applying group theory of the vibrational modes of atoms (or equivalently systems of masses on springs) [122]. In Section 5.4.2 the degeneracy of the modes of an AF at zero field is analysed using group theory. However, in doing so the argument began from the shape of the modes, which in order to know this one must solve the LLG equation at this point. From there effects like loss of degeneracy can be determined from symmetry breaking alone, anticrossings etc. but it would be more satisfying if there was no need to use the LLG equation at all.

Now that it has been established how to apply group theory to the LLG equation, a similar procedure should be possible as is done when analysing the degeneracy of the vibrational modes of atoms. That is, determining the degeneracy of the modes from group theory, symmetry, and conservation laws alone without ever having to solve the underlying equation of motion, as is done for vibrational modes in molecules which are clearly a very strong analog to magnetic oscillators.

## 5.6 Conclusion

The main result of this chapter is that the classical eigenmodes of the LLG equation may engender a representation of the symmetry group of the magnetic system. From this, the effect symmetry on the resonance spectra of coupled magnetic oscillators was shown, with a particular focus on synthetic antiferromagnets and antiferromagnets. The influence of symmetry on mode degeneracy and avoided crossings was illustrated experimentally by performing FMR measurements on symmetric and asymmetric SAFs. The asymmetry in the structure was tuned by tuning the difference in the PMA between the top and bottom layers, a novel and powerful way for generating strong anticrossings (coupling rate 2 GHz) in synthetic antiferromagnets.

Understanding these phenomena in terms of group theory offers an alternative way of understanding these phenomena from those already presented in the literature. By arguing entirely from symmetry, the conceptual understanding of these phenomena is enhanced, bringing the field in line with the larger body of quantum mechanical avoided-crossing literature. Additionally, it is possible to easily distinguish between true avoided crossing and splittings that result from symmetry-lowering induced losses of degeneracy.



## Chapter 6

# Magnetoresistance effects in synthetic antiferromagnets

*Magnetoresistance, the dependence of a magnetic sample's resistance on the orientation of its magnetic moment, is one of the oldest known couplings between ferromagnetism and a charge current. Magnetoresistive effects remain crucial to spintronics, allowing the state of spintronic devices to be read out electronically. In this chapter, it is shown that the experimentally realised solutions to Brown's equation obey the symmetry of the device. This is used to devise a method for distinguishing between contributions to the magnetoresistance in synthetic antiferromagnets.*

*Additionally, in ferromagnets it has been shown that exchange magnons excited by sufficiently high current densities and their associated antidamping torques can induce an asymmetry in the anisotropic magnetoresistance. The excitation of these exchange magnons is associated with an overcoming of damping in the system, and subsequent coherent self-oscillations in devices with a nanowire geometry. A current dependent anisotropy in the magnetoresistance in a synthetic antiferromagnet nanowire is reported here. This suggests that it may be possible to generate self-oscillating dipolar in these devices. It is proposed that*

*this exchange magnetoresistance could be a useful source of unidirectional magnetoresistance for magnetic device applications.*<sup>1</sup>

## 6.1 Introduction

Anisotropic magnetoresistance (AMR), the  $\cos^2 \phi$  dependence of a magnetic sample's resistance on the angle of its magnetic moment,  $\phi$ , with respect to the current direction, was discovered by Lord Kelvin in 1856 [291], making it the oldest known interaction between magnetic ordering and a charge current. Magnetoresistive effects continue to play a central role in modern spintronics. Giant magnetoresistance (GMR) remains perhaps the field's crowning achievement [3], and virtually all spintronic devices rely on some kind of magnetoresistive effect to read out the resulting state of the magnetisation during operation.

In this chapter, some novel features of the anisotropic magnetoresistance signal in synthetic antiferromagnets (SAFs) are explored. In Chapter 5, it was shown how symmetry, or the lack thereof, had major implications for the dynamic resonance spectrum of a synthetic antiferromagnet. A natural question then to ask is, 'does the symmetry of a synthetic antiferromagnet have any implications for its magnetoresistance signal?' It is found that in the special case when there is a reflection plane at  $135^\circ/45^\circ$  to the current direction, the measured AMR signal has a sign change when the external field is reflected in the symmetry plane, whereas the GMR signal remains unchanged. This provides a simple means to distinguish the two effects in a sample. Additionally, it is shown that the strength of the measured AMR signal along the high-symmetry direction is related to the symmetry of the ferromagnetic layers, vanishing when the two layers are identical.

Measurements of the magnetoresistance at high current densities in narrow bar SAFs are performed. Similar measurements in Permalloy(Py)/Pt bilayers have revealed an asymmetry in the AMR signal at high current densities [148] that is induced by the excitation of exchange

---

<sup>1</sup>Part of this chapter is published in J. Patchett et al., *Phys. Rev. B* 105, 104436 [268].

magnons. These measurements are then repeated, first in Pt/CoFeB bilayers, observing much the same effect as what was reported in Py, and then in a Pt/CoFeB/Ru/CoFeB/Pt SAF, where a current dependent asymmetry in the magnetoresistance of a SAF is reported for the first time. It is proposed that this effect could be a useful source of unidirectional magnetoresistance.

## 6.2 Symmetry and magnetoresistance

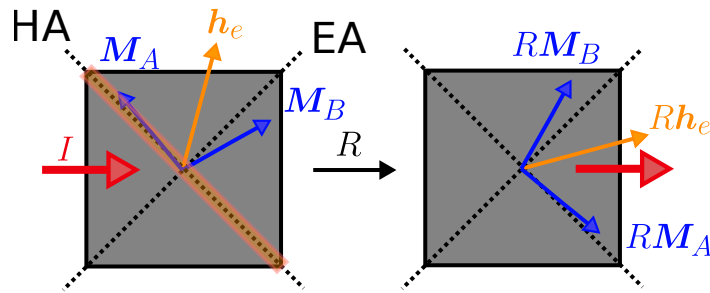


Fig. 6.1 A uniaxial SAF with an easy-axis/hard-axis (EA/HA) at  $45^\circ/135^\circ$  to the current direction.  $R$  is a reflection operator in the plane containing the hard-axis and the out-of-plane direction (translucent orange plane). By applying this reflection operator to the magnetisation and external field, one obtains a new solution to Brown's equation at the transformed external field.

The equilibrium position of a ferromagnet is determined by Brown's equation [60]:

$$\mathbf{M} \times \mathbf{H}_{eff} = \mathbf{0} \quad (6.1)$$

This equation must be satisfied at all points in space. Intuitively, if one knows a solution to Brown's equation for a particular external field, by applying a symmetry operation of the device to the magnetisation and the external field, one should be able to generate a new field/magnetisation configuration that is also a solution to Brown's equation (see Figure 6.1). The solutions to Brown's equation are not unique, and whether or not this solution is realised depends on the history of the magnetisation and the external field. Hence, one can only

expect to realise this new, symmetry-transformed, solution if the entire hysteresis path up to that field value is likewise transformed.

In the macrospin picture, this is straightforward to show explicitly. It is possible to write the effective field in layer  $i$ ,  $\mathbf{H}_{eff}^i$ , in the form  $\mathbf{H}_{eff}^i = \Lambda^{ij} \mathbf{M}_j + \mathbf{h}_e^i$ , where  $\Lambda^{ij}$  is an operator that describes the contribution of the  $j^{th}$  magnetisation to the  $i^{th}$  effective field, and  $\mathbf{h}_e^i$  is the external field in layer  $i$ . For a uniaxial SAF, all terms except the biquadratic exchange are linear in the magnetisation, and so  $\Lambda_{ij}$  is just a matrix. For instance, the uniaxial magnetocrystalline anisotropy effective field can be written as a matrix with components:

$$(\Lambda_{ani}^{ii})_{jk} = \frac{2K^{(i)}}{\mu_0 M_{si}^2} n_j^{(i)} n_k^{(i)} \quad (6.2)$$

where  $n_j^{(i)}$  is the  $j^{th}$  component of the easy-axis direction in the  $i^{th}$  layer, and  $K^{(i)}$  is its anisotropy constant. The biquadratic exchange term has an additional multiplicative factor of  $\mathbf{M}_A \cdot \mathbf{M}_B$  that is invariant under any transformation of the magnetisations, and so for the purposes here can still be treated as a matrix with components:

$$(\Lambda_{ex2}^{ij})_{kl} = \frac{-2J_2}{\mu_0 M_{sA}^2 M_{sB}^2 t_i} \mathbf{M}_A \cdot \mathbf{M}_B \delta_{kl} \quad (6.3)$$

where  $J_2$  is the exchange constant, and  $t_i$  is the thickness of layer  $i$ .  $R$  is a symmetry operation of the static magnetic system if it commutes with all  $\Lambda^{ij}$ , and hence if  $\mathbf{M}_i$  is a solution to Brown's equation at the external field  $\mathbf{h}_e^i$ , then so is  $R\mathbf{M}_i$  at  $R\mathbf{h}_e^i$  as  $(R\mathbf{M}_i) \times (\Lambda^{ij} R\mathbf{M}_j + R\mathbf{h}_e^i) \rightarrow (R\mathbf{M}_i) \times R(\Lambda^{ij} \mathbf{M}_j + \mathbf{h}_e^i) = \mathbf{0}$ , which follows as both  $\mathbf{M}_i$  and  $\mathbf{H}_{eff}^i$  have been transformed by the same operation  $R$ , and hence must still be parallel. In Appendix A, this is shown explicitly for a uniaxial SAF with bilinear and biquadratic exchange fields in the case of uniform and non-uniform magnetisations. In the non-uniform case, some of the operators that describe the effective field become integral linear operators (e.g. the demagnetisation field), but the logic is identical.

For a square uniaxial SAF with the in-plane easy-axis lying at  $45^\circ$  or  $135^\circ$  to the current direction along one of the edges of the square, a symmetry operation,  $R$ , is a reflection in the plane containing the out-of-plane direction and the hard-axis. If the in-plane  $i^{th}$  magnetisation is at an angle  $\phi'_i$  to the easy-axis at field  $\mathbf{h}_{eff}^i$ , then the symmetry transformed configuration will be at an angle  $-\phi'_i$  to the easy-axis at the external field  $R\mathbf{h}_{eff}^i$ . Consequently, the AMR contribution to the resistance,  $r$ , transforms as follows:

$$r = \sum_i \cos(2\phi'_i + 90) \rightarrow \sum_i \cos(-2\phi'_i + 90) = - \sum_i \cos(2\phi'_i + 90) \quad (6.4)$$

i.e. there is a change in sign of the anisotropic magnetoresistance at the same magnetic field strength. Conversely, as the angle between the magnetisations is invariant, contributions such as GMR remain the same. Hence, by looking at the symmetric/antisymmetric component of the magnetoresistance under a suitable reflection, it should be possible to disentangle the contributions of different magnetoresistances to the overall resistance. This should allow for a characterisation of each term's strength in devices with multiple contributions, or indeed to confirm the presence/absence of such terms.

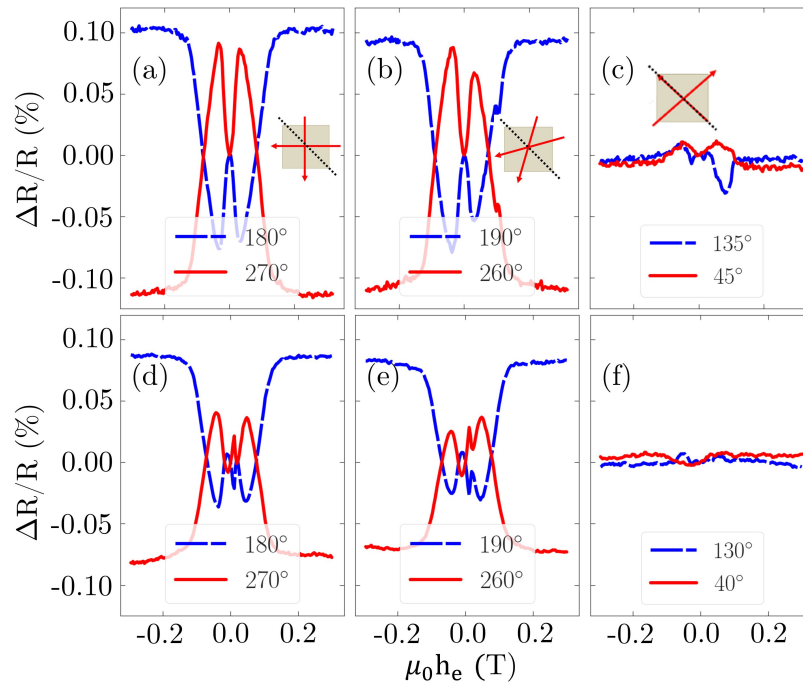


Fig. 6.2 Magnetoresistance data for the single-sided ((a) and (b)) and double-sided ((d) and (e)) structures when the magnetic field is swept from negative to positive values along different directions connected by symmetry (in-plane). The magnetoresistance is measured relative to the resistance at zero external field. Additionally, the magnetoresistance is measured along the hard and easy axes ((c) and (f)). Inserts: cartoons showing the magnetic field sweep directions (red and blue arrows) relative to the easy-axis (dotted line).

In order to confirm that the solutions to Brown's equation predicted by a symmetry transformation of the entire hysteresis path are the experimentally realised ones, magnetoresistance measurements are performed where the external magnetic field is swept at a fixed angle with respect to the current direction. Figure 6.2 shows the magnetoresistance signal for field sweeps from for both the single (Figure 6.2a-b) and double-sided (Figure 6.2d-e) samples from Chapter 5. As shown in Chapter 5, the properties of these two samples differ substantially, and correspondingly, their magnetoresistance signals for the same field strength and orientation show very different features. Despite this, as predicted, they both show a clear antisymmetry in their magnetoresistance signal as expected from an AMR-based magnetoresistance. This confirms that the symmetry-transformed solutions to Brown's equation are the experimentally realised ones and that AMR is the dominant source of magnetoresistance in

these devices. There is no/minimal contribution from GMR as expected for devices with this structure. It is useful to confirm this when analysing the rectified voltages produced as the output of ST-FMR experiments.

The above symmetry considerations apply irrespective of the different properties the two layers might possess. If there exists an additional exchange symmetry between the layers, then in the special case in which the external field is applied along the easy or hard-axis, applying the reflection symmetry operation merely exchanges the magnetisations and leaves the external field invariant. This transformed configuration has the opposite sign magnetoresistance to the original one. However, because the two layers are identical, the transformed configuration is indistinguishable from the original one, and hence the magnetoresistance must be zero for all magnetic field strengths. Figure 6.2c and 6.2f show the magnetoresistance along the easy and hard axes for the single and double-sided samples respectively. The single-sided sample, which has very different layer properties, shows a sizeable magnetoresistance along both axes. In contrast, the double-sided sample has almost no variation in its resistance along the easy or hard axes, confirming that there is a high degree of symmetry between both layers as expected from the FMR measurements in Chapter 5. Note that the dominant difference in the FMR measurements was in the strength of the PMA. So long as this remains below the thin-film demagnetisation field strength, this should have no impact on the in-plane magnetisation of either layer. However, as PMA is related to the spin-orbit coupling strength at the interface, a sizeable difference in PMA should also indicate a significant difference in other transport-related quantities affected by the spin-orbit coupling, or qualities of the device that influence the spin-orbit coupling (e.g. AMR, interface-related scattering etc.).

## 6.3 Current dependent magnetoresistance asymmetry in SAFs

### 6.3.1 Introduction

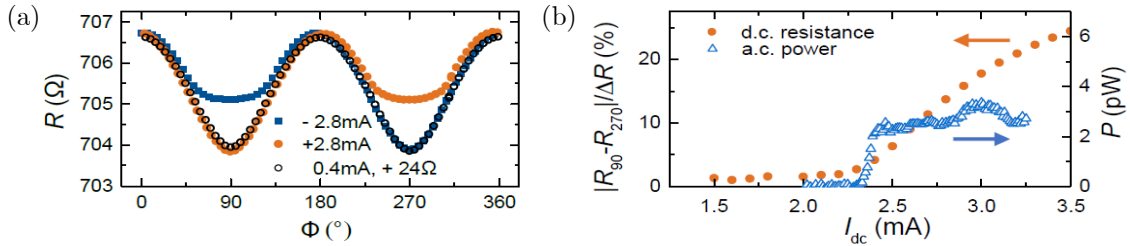


Fig. 6.3 (a) Asymmetry in the AMR of a Py/Pt nanowire at high current densities induced by the self-oscillation of exchange magnons at room temperature. (b) Magnitude of the asymmetry as a function of DC current at cryogenic temperatures (orange dots). Note that the magnitude of the resistance asymmetry is reduced compared to that at room temperature at comparable current densities. Also, the measured microwave power from the dipolar modes (blue triangles). Figures reproduced from [148].

Langenfeld et al. [148] have demonstrated that in a Py[3]/Pt[4] nanowire (dimensions  $500 \text{ nm} \times 6 \text{ } \mu\text{m}$ ) the anisotropic magnetoresistance develops an asymmetry in the resistance between the  $90^\circ$  and  $270^\circ$  (between the current direction and magnetisation:  $\phi_H$ ) directions at sufficiently high current densities (Figure 6.3). They attribute this to an overcoming of damping by the current-induced antidamping torques, which causes a dramatic increase in the population of now self-oscillating exchange magnons (defined as magnons with wavelengths much smaller than the sample dimensions, whose physics is dominated by the exchange force). The phenomenology of this effect has not yet been investigated rigorously, but it is likely to be the results of the magnetic oscillations causing an ‘averaging’ of the AMR effect that diminishes its size. It should be noted that magnon-induced resistive effects, such as magnon-electron scattering [292], cannot be responsible as their contribution to the resistance is both typically too small to explain the size of the observed effects and should be antisymmetric with respect to inversion of  $M/J$ .

This increase in magnon population causes a reduction in the anisotropic magnetoresistance that is strongest close to when the current-induced spin-accumulation and magnetisation are antiparallel. Langenfeld et al. [148] show that the onset of this asymmetry in the magnetoresistance is correlated with the onset of coherent power generation in the nanowire due to the self-oscillation of dipolar magnons as the damping in the system is overcome (whose wavelengths are comparable with the device geometry, and thus capable of producing a non-zero output microwave power), see Figure 6.3b. Consequently, the observation of such an asymmetry is a strong indicator that the antidamping torques are capable of overcoming damping in a magnetic device and sustaining self-oscillations.

In this chapter, a current-induced asymmetry in the AMR of CoFeB/Pt nanowires, and Pt/CoFeB/Ru/CoFeB/Pt SAF nanowires is reported. These results are analysed from the perspective of evaluating the feasibility of inducing coherent auto-oscillations in SAFs. The observation of auto-oscillations in a SAF may be of some physical and technological interest: as a model system for the heavily theoretically investigated [145] but as of yet experimentally unrealised antiferromagnet (AF) auto-oscillators, and to open up possibilities of higher frequency oscillation modes than in single layer ferromagnets and mode multiplexing. In addition, it is proposed that this effect may be a viable alternative to other unidirectional magnetoresistive effects for use in two terminal spintronic-switching devices and AMR-based sensors.

### 6.3.2 Results

In this chapter, the current dependent magnetoresistance in two samples, a Pt/CoFeB bilayer structure, and a Pt/CoFeB/Ru/CoFeB/Pt SAF, is measured. The structures of these two samples are given in Table 6.1 and details of the fabrication procedure can be found in Section 3.2.3. Following sample deposition, each sample is patterned into  $500 \text{ nm} \times 6 \text{ }\mu\text{m}$

nanowires, whose magnetoresistance is measured using a two-probe magnetoresistance measurement, as described in Section 3.4.

Synthetic antiferromagnet	$(\text{Al}_2\text{O}_x)\text{Ta}[2]\text{Pt}[3]\text{CoFeB}[2]\text{Ru}[0.9]\text{CoFeB}[2]\text{Pt}[6]\text{Ta}[2]\text{Al}_2\text{O}_x[50]$
Single-layer	$(\text{Al}_2\text{O}_x)\text{Ta}[2]\text{Pt}[3]\text{CoFeB}[4]\text{Ru}[0.9]\text{Ta}[2]\text{Al}_2\text{O}_x[50]$

Table 6.1 (All thicknesses in nm) Structures of the synthetic antiferromagnet and ferromagnet samples measured in Chapter 6. The thickness of each layer is determined by the sputtering time multiplied by the measured deposition rate of the sputterer under the same deposition conditions.

The variations in the magnetoresistance measured will be a small fraction of the overall resistance of the device, and so it is necessary to ensure that the instrumentation has sufficient resolving power to measure such signals accurately, and in addition the measurements will be performed at high current densities where device degradation may become possible. Both these factor must be accounted for in the experimental procedure.

The accuracy of a Keithley 2400 SMU is quoted by the manufacturer as 0.012% (or 6 and a half significant figures). Using a sourced current value of 3 mA – representative of the higher end of currents used in the magnetoresistive measurements – for a sample with a resistance of 1 k $\Omega$ , one must use the 10 V range on the Keithley’s input. Combined with the Keithley’s measurement accuracy of 0.012%, this gives a minimum resolvable resistance change of 3.6  $\mu\Omega$  — or 1.2 mV. The signal is far in excess of this limit, and so it is not expected that the resolution of the instrumentation is a significant limitation in resolving the desired signal.

When performing measurements at high current densities, the sample will heat up and increase its resistance until it reaches a new stable temperature. This can have a significant effect on the resistance of the sample. For this reason 1) only relative changes in the magnetoresistance are meaningful to report, and 2) the sample must be allowed to come into thermal equilibrium before the measurement can proceed. This second point was achieved

by applying the desired current to the device and waiting for the absolute resistance of the sample to stabilise before proceeding to the full measurement. Each magnetoresistance sweep was then performed three times in secession. If there was any significant change in the sample resistance over time due to temperature changes, this manifests as a gradient in the resistance over time and differences between the different sets of data, then the measurement was discarded and repeated until a repeatable set of data could be obtained.

This final point also enables the detection of changes to the sample's microscopic structure caused by the high current densities and heat produced during the experiment: for example, electromigration. This would appear as an irreversible change in the device's resistance at the same current density. As the current measurements were performed from low to high current density, as a check against this possibility, each sample was measured at a low current density after the final measurement, and the magnetoresistance recorded and compared with its resistance at that same current density before the current sweep to ensure that its behaviour had not changed. If a device was found to have degraded, as it is not possible to when this degradation began to occur, the data must be thrown out and the measurement repeated on an equivalent structure with a lower maximum current density.

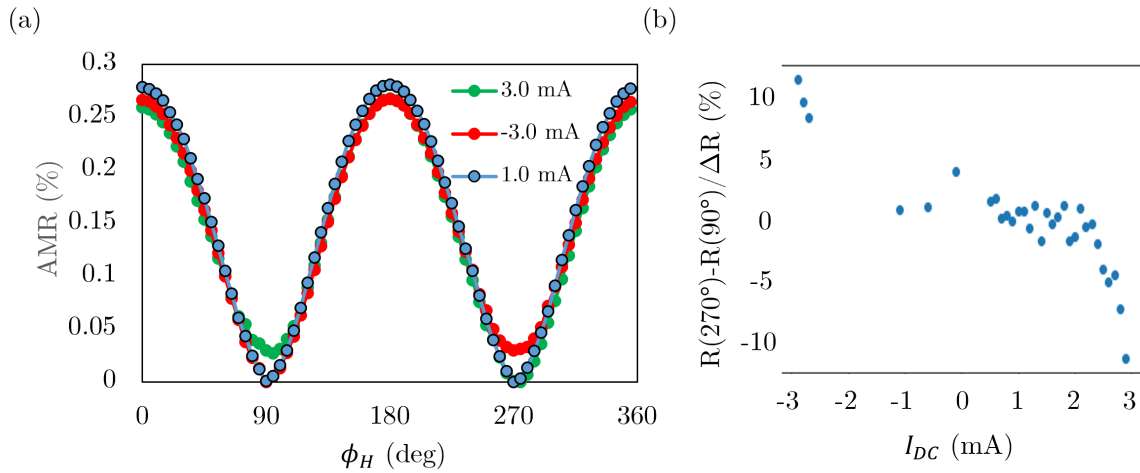


Fig. 6.4 (a) AMR of a single CoFeB layer taken at 3 different current densities (width 500 nm) at 55 mT (in-plane). As the current is increased, beyond a certain threshold the damping in the system is overcome and a burgeoning population of exchange magnons causes an asymmetry to develop in the magnetoresistance. This asymmetry is reversed when the current direction is reversed, confirming that it is related to the current-induced antidamping torque. (b) Size of the asymmetry as a function of DC current. Beyond around 2 mA, the natural damping in the system is overcome and an asymmetry in the magnetoresistance that increases with  $I_{DC}$  develops.

Figure 6.4a shows the magnetoresistance of the single-layer nanowire taken at three different DC currents at a fixed external field of 55 mT. At low current densities, the magnetoresistance follows the familiar  $\cos^2 \phi_H$  dependence. However, at larger current densities, once the damping in the system is overcome by the antidamping torques, an asymmetry between the 90° and 270° directions emerges, reversing with reversed current direction. This indicates that exchange magnons have been successfully excited as self-oscillators within the magnetic layer, as was reported in Py [148]. Figure 6.4b shows the magnitude of this asymmetry as a function of the DC current, showing a sharp onset around 2.5 mA as damping is overcome. Figure 6.5b shows the FMR linewidth as a function of applied current in the same device, showing a predicted onset of auto-oscillations at around 4 mA. This is obviously in excess of the approximately 2.5 mA threshold shown in Figure 6.4b. However, these measurements were taken at 6 K, where the Gilbert damping of thin CoFeB/Pt films is typically 2-3 times that at room temperature [293], and is detecting the

quasi-uniform Kittel mode that is expected to have a larger onset current for self-oscillations than the exchange modes responsible for the magnetoresistance asymmetry. Figure 6.5b shows that an onset of current of 2.5 mA at room temperature is quite reasonable.

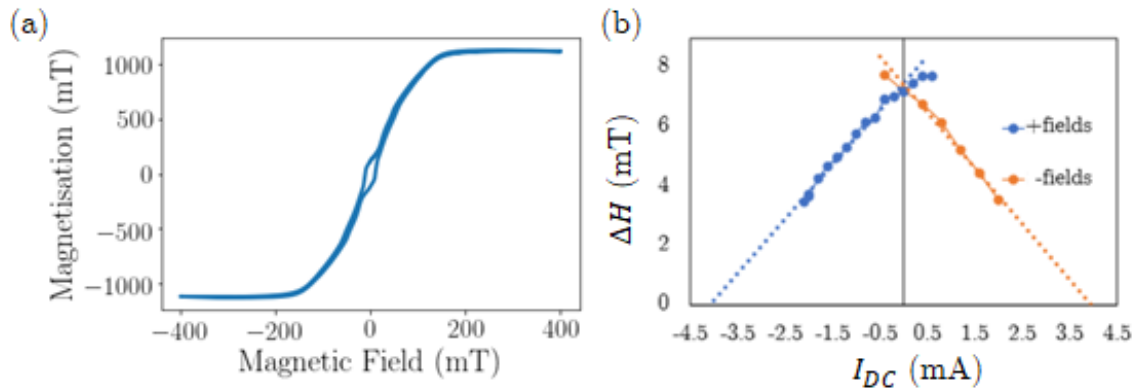


Fig. 6.5 (a) Vibrating sample magnetometry data for the synthetic antiferromagnet nanowire sample before patterning at room temperature with an (in-plane) applied field. The SAF has relatively symmetric layer magnetisations, as shown by the small gap at zero field, and a saturating field of around 180 mT. (b) FMR linewidth versus DC current in the single-layer sample, showing a predicted onset of auto-oscillations at around 4 mA.

It is interesting to compare these results with previously reported results in Pt[3]/Py[4]  $500 \text{ nm} \times 6 \text{ }\mu\text{m}$  nanowires [148] (Figure 6.3). Both samples exhibit a similar onset-current, and hence current density, of around 2.5 mA. The size of the asymmetry in the CoFeB sample is reduced compared with Py — around one-quarter of that in Py at 2.8 mA.

Figure 6.6 shows similar magnetoresistance measurements conducted in the synthetic antiferromagnet nanowires with dimensions of  $500 \text{ nm} \times 6 \text{ }\mu\text{m}$ . These measurements were performed at an external field of 230 mT. This field was chosen as it is beyond the saturation field and so both layers should be aligned parallel to it, like in a ferromagnet. The external field is considerably in excess of the field used in the signal layer case. However, owing to the approximately 180 mT external field required to align the two ferromagnetic layers in the SAF (Figure 6.5a), there should still exist a low-energy band of magnons that are excitable at realisable current densities. This is because their energies are lowered by their favourable interaction with the exchange field, as it acts as if it were an opposing magnetic field.

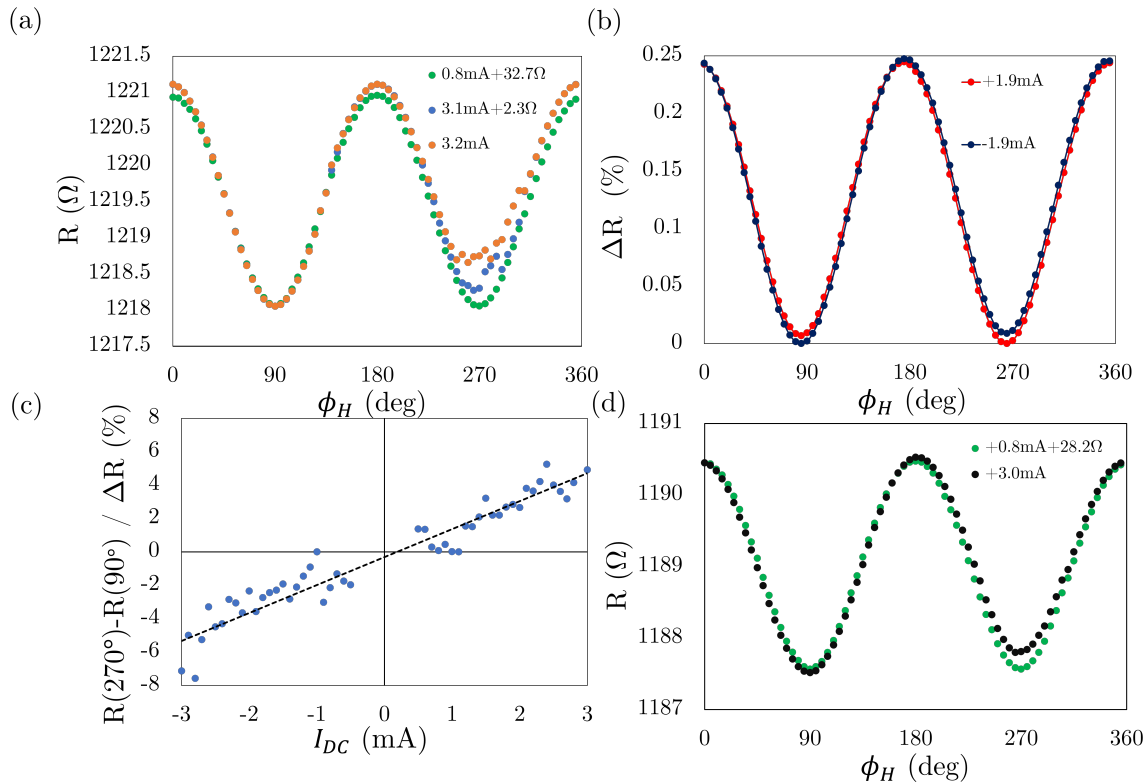


Fig. 6.6 (a) Magnetoresistance as a function of  $\phi_H$  for the low-current regime (0.8 mA) and beyond the threshold current (3.1-3.2 mA). Beyond this current density, a large asymmetry in the magnetoresistance develops (22% of the AMR coefficient at 3.2 mA), indicative of an exchange magnon-induced asymmetry. The curves are offset to account for the change in the sample resistance with Joule heating. (b) At intermediate currents, a small asymmetry that reflects the symmetry of the exchange magnon magnetoresistance develops. (c) Sign and magnitude of the asymmetry as a function of current below the threshold current, showing a linear dependence on current. The origin of this small initial asymmetry is not well understood. (d) Comparison of magnetoresistance dependence at low and high currents, showing that the high current case does not also have a decrease in resistance at  $90^\circ$ , ruling out magnetoresistive effects with a  $\sin \phi_H$  dependence.

Figures 6.6b-d show that a small asymmetry between the  $90^\circ$  and  $270^\circ$  degree directions exists even at low currents, appearing to increase linearly with increasing current up to around 3 mA. One possible explanation for this effect may be an increase in the background thermal magnon population (before the onset of auto-oscillations) as the damping in the system is decreased/compensated for. The energy stored in a given magnetic mode scales as  $k_B T / (\Gamma - \eta J)$  [139], where  $\Gamma$  is a mode-dependent quantity that scales loosely with

the mode frequency (for instance, for a ferromagnetic thin film, the Kittel mode has  $\Gamma = \alpha\mu_0\gamma(H + 0.5M_S)$ ),  $J$  is the current density (and  $\eta$  a constant of proportionality between  $J$  and the antidamping torque), and  $T$  the temperature. The nature and strength of this increase will be device and external condition dependent, as these factors modify the dispersion relationship and hence  $\Gamma$  for each mode. Consequently, at low  $J$  one may see a gradual increase in the asymmetry due to this thermal magnon background population, followed by a sharp increase as  $\eta J$  approaches  $\Gamma$ . This could be straightforwardly tested by repeating the experiment as a function of temperature.

Another possible explanation is the anomalous Nernst effect, which, in the case of an out-of-plane temperature gradient, would produce a voltage perpendicular to the magnetisation and temperature gradient [294]. Reported values for the Nernst coefficient in [294] Pt/CoFeB bilayers mean a resistance change of this magnitude could plausibly be produced if the temperature gradient was large enough. The anomalous Nernst effect, however, should also produce a relative decrease in the resistance at high current densities compared with the low current case (i.e. in Figure 6.4a the 3 mA curve should dip below the 1 mA curve at  $90^\circ$ , rather than track it exactly). In other words, the anomalous Nernst effect is antisymmetric with respect to the magnetisation, whereas the observed magnetoresistance is asymmetric. As this is not observed, it is ruled out as a relevant effect. The same line of reasoning can be used to rule out unidirectional spin-Hall magnetoresistance (USHMR) [14] and the spin-Seebeck effect [295], which likewise exhibit  $R(\mathbf{J}, \mathbf{M}) = -R(\mathbf{J}, -\mathbf{M})$  symmetry, and are typically far too small in NM/FM bilayers to explain the magnitude of the observed effect (studies in Ta/Co bilayers report USHMR coefficients of around 0.002% [14, 296]).

Beyond around 3.1 mA, a sharp increase in the asymmetry is observed (Figure 6.6a). This sharp increase is indicative of the onset of self-oscillation of exchange magnon modes in the device. The largest asymmetry was measured at 3.2 mA, with a 22% difference between the  $90^\circ$  and  $270^\circ$  directions relative to the AMR coefficient. Regrettably, the device is irreversibly

damaged by Joule heating/electromigration at current densities not much in excess of this, and so it was not possible to measure particularly far into this regime. A threshold current density of this magnitude is quite reasonable given the result in the single layer, as although much of the current density will be shunted uselessly through the additional metallic layers in the SAF, the thickness of the CoFeB layer is also reduced by half relative to the single layer — reducing by half the magnitude of the antidamping torque required to overcome the damping.

The field-like and antidamping torques are characterised in a Pt/CoFeB bilayer in Appendix B. For a DC current of 1 mA in a 500 nm wide bar with the single-layer structure, a field-like torque strength of around 1 mT is expected. For a SAF, because some of this current will be shunted into the additional metallic layers, one can generally expect the field-like torque experienced by each layer to be less than this. It is clear that the field-like torque is insufficiently strong to overcome the difference between the external field and the saturating field (around 50 mT), and hence field-torque induced canting of the magnetisations cannot explain the asymmetry in the magnetoresistance.

It should be noted that an antidamping torque-induced asymmetry is only possible if there are asymmetries between the layers themselves. Because the spin-accumulation is opposite in either layer, it should only be expected to excite a significant population of exchange magnons in one layer at a time for a given field orientation. If the two layers, and the current-induced antidamping torques in them, were identical, a symmetrical distortion from the expected  $\cos^2 \phi_H$  dependency would be seen in this configuration of the magnetic layer. As it occurs, one-half of the magnetoresistance signal remains undistorted at the experimentally investigated currents. This indicates that the torques are exciting significant exchange magnons in one layer only, which is not unexpected. The lower layer is expected to have a significantly higher quality of Pt/CoFeB interface, allowing for superior spin-current injection and hence a much lower onset current, if self-oscillations can be induced in the top

layer at all. Consequently, as probing further into the self-oscillating regime, one may see further distortions in the magnetoresistance as this top layer likewise passes its threshold current density.

The existence of this asymmetry shows that it is possible to overcome the damping and induce self-oscillations in SAFs, at least for these short-wavelength exchange modes. Although exchange modes are unable to generate a net power output, dipolar modes should be likewise excited at similar current densities if the deleterious effects of the exchange mode population can likewise be overcome in SAF as in single ferromagnetic layers. It is hoped that this will eventually lead to the realisation of coherent power generation from magnetic self-oscillations in SAFs.

## 6.4 Discussion

The observation of an asymmetry in the magnetoresistance can be considered a form of unidirectional magnetoresistance. Such effects can be induced either intrinsically in the ferromagnetic layer itself through the spin-orbit coupling induced by the crystal structure [297], or extrinsically through the addition of a normal metal layer with strong spin-orbit coupling via spin-Hall-related effects [14].

Unidirectional magnetoresistances have been intensively researched in recent years because they offer a simple mechanism for distinguishing between antiparallel states in ferromagnets using a simple two terminal measurements [14, 298–302]. Additionally, they offer the possibility of  $360^\circ$  sensitivity in AMR-based sensors. The exchange magnon-induced asymmetry observed here is a potential alternative to such mechanisms. The advantage of USHMR and other similar mechanisms [303] is that they do not require large current densities to operate, nor is the timescale for a read operation limited by the speed of the magnetisation dynamics — and perhaps most crucially do not require an external field. However, the current densities required to induce an exchange magnon magnetoresistance

should be no more than those required to flip a memory element via the SOT and should operate on a similar timescale. The requirement for an external field may also be solved by the exchange field in SAF, as they are capable of supporting different stable orientations at zero field at the cost of additional fabrication complexity. In AMR sensors, which are commonly used for the detection of magnetic fields and as current sensors, an external magnetic field is already present by definition during operation.

The main weakness of the USHMR is that it is severely limited by the size of the anisotropy it can generate. Typical USHMR coefficients in NM/FM heterostructures are on the order of 0.002%, minuscule compared to even the relatively weak AMR coefficient in CoFeB. This effect has been enhanced in devices utilising topological insulators and their superior spin-Hall angles, and hence spin accumulation, up to around 1.1% [299], although this limits the range of useable materials. Because the exchange magnon magnetoresistance is not a magnetoresistive effect in and of itself, but rather modifies existing magnetoresistive effects within the device, it may be possible to piggyback on much stronger magnetoresistive effects than AMR (i.e. GMR, tunnelling magnetoresistance (TMR)) to generate a sizeable unidirectional magnetoresistance. In this respect, the observation of this exchange magnon asymmetry in a SAF is an important step, as it opens up the possibility of future work exploiting this effect in conjunction with GMR and TMR to generate a sizeable unidirectional magnetoresistance. Furthermore, this mechanism appears conceptually simple to extend to AF, which the field is looking towards to improve the stability of devices to stray fields and increase the operation speed of magnetic memories [53] and for which evidence of USHMRs have not yet been reported.

## 6.5 Future work

It would be useful to repeat the magnetoresistance measurements at lower temperatures, where the device should survive longer before succumbing to current-induced degradation

into the self-oscillating regime. However, given the similarities between the observed behaviour and that in Py/Pt bilayers [148], and the lack of other mechanisms that produce the manifestly *asymmetric* magnetoresistance signal, the evidence presented here is already fairly conclusive.

It would be interesting to try and observe this effect at zero field. The exchange magnon magnetoresistance in ferromagnets requires the application of an external field, which for some applications is a major limitation. However, in a SAF such an effect should be, in principle, observable at zero field due to the exchange field between the layers and the energetic barrier between the two stable arrangements of the magnetisations. Because AMR depends on the square of the magnetisation, the fact the two layers are oppositely aligned should not result in the effect cancelling out. Note that in the zero-field case, an asymmetric magnetoresistance between  $\pm J$  would occur even in the case of a symmetric SAF, as magnons can only be excited in one layer at a given orientation of the current with respect to the magnetisation. The challenge will be to design a SAF structure that has an equilibrium magnetisation direction at zero field perpendicular to the current direction/parallel to the spin-Hall-induced spin accumulation. In these devices, the shape anisotropy of the bar means that the magnetisation will attempt to align parallel with the current direction at zero field. By varying the device geometry/crystalline anisotropies/fixed magnetic layers, it may be possible to overcome this problem. Here, AFs may prove a natural candidate as they do not experience shape anisotropy due to the compensated local moments. Additionally, as highlighted above, a combination of this effect with strong magnetoresistances such as GMR and TMR may be able to produce a strong uniaxial magnetoresistance.

Reports into unidirectional magnetoresistances typically rely on measurements of the second harmonic component of the resistance, as measured by an AC current, in order to subtract out the large AMR background [14]. These measurements still require detailed analysis in order to rule out a plethora of other effects that can also cause similar signals.

Consequently, methods for additional, independent, measurements of the unidirectional magnetoresistance are likely to be of great interest. In principle, the USHMR and AMR should have different symmetry responses to symmetry transformations of the external field. For instance, in a nanowire structure, when the field is applied perpendicular to the current direction, the AMR signal will be even in the magnetic field and the USHMR odd. It would be interesting to see if it is experimentally feasible to characterise the USHMR from such a measurement. The main limitation might be the accuracy with which one can calibrate the angle of the external field with respect to the current direction. The larger the difference between the two signals that you wish to distinguish, the more precise this would need to be.

## 6.6 Conclusion

In this chapter, reported a number of novel results relating to magnetoresistance in synthetic antiferromagnets have been reported. It has been shown that the symmetry of Brown's equation can be used to differentiate between magnetoresistance effects and that these symmetry-transformed solutions are indeed the ones experimentally realised in synthetic antiferromagnets. It has been shown that current-induced asymmetries can be induced in the magnetoresistance of synthetic antiferromagnets due to the excitation of exchange magnons, indicating the damping in the system has been overcome. It is hoped this may lead to the detection of coherent microwave power output from synthetic antiferromagnets, and as a possible source of unidirectional magnetoresistance for the readout of two terminal SOT induced switching devices and in  $360^\circ$  AMR-based sensors.

# Chapter 7

## Conclusion

In this work, ferromagnetic thin-films coupled strongly to other physical subsystems (magnetic or otherwise) have been studied, and investigated the effect this coupling has on both their static and dynamic properties, to both understand the ferromagnets themselves, and the systems they are coupled to.

In Chapter 4, an attempt was made to detect the presence of spin-triplets, as suggested by recent experimental reports, in Nb/C<sub>60</sub>/Cu/C<sub>60</sub> heterostructures via spin-pumping FMR experiments. Instead of detecting the characteristic increase in the Gilbert damping below the transition temperature, a reduction in the linewidth was found once a substantial hysteresis has been accounted for. This has been shown to occur because of the presence of thermomagnetic avalanches (TMAs) inside the superconducting layers. TMAs should be energetically forbidden at these film thickness and magnetic fields according to conventional theory; their presence still requires some further work to understand from a theoretical perspective. Nevertheless, their experimental signature is clear, and suggests that the low-energy muon spin rotation experiments that purported to show the presence of spin-triplets in these heterostructures, may in fact have been measuring the vortex condensate instead.

In Chapter 5, it was shown how symmetry influences the resonance properties of magnetic oscillators obeying the Landau-Lifshitz-Gilbert (LLG) equation. It is shown how the

eigenmodes of the LLG equation can engender a representation of the symmetry group of the systems with some slight modifications from the usual Hermitian eigenvalue problem case. From there, it is straightforward to inherit all of the mathematical methods developed for analysing resonance problems using group theory, allowing one to examine symmetry-enforced degeneracies and symmetry-protected crossings/avoided crossings. These principles were demonstrated experimentally by measuring the ferromagnetic resonance response of two synthetic antiferromagnets: one with symmetry layers, the other with asymmetric layers, by tuning the PMA in the top layer. This enabled the realisation of a device with strong hybridisation of the two modes.

In Chapter 6, it was shown that the solutions of Brown's equation obey the symmetry of the device, and that these are the experimentally realised solutions, so long as the whole hysteresis path is likewise transformed. From this, it is possible to establish a simple procedure to distinguish between contributions to the magnetoresistance based on their transformation properties under an appropriate symmetry transformation. It was then demonstrated experimentally that an asymmetry in the anisotropic magnetoresistance can be induced at sufficiently high current densities in synthetic antiferromagnets. This is due to the antidamping torques in the device overcoming the damping in the system, allowing for the self-oscillation of exchange magnons. It is hoped that this result may lead to the generation of coherent microwave power from synthetic antiferromagnets in the near future, and to act as a source of unidirectional magnetoresistance to aid in the readout of two-terminal spin-orbit torque induced switching devices and in  $360^\circ$  AMR-based sensors.

# References

- [1] “International energy outlook 2021,” U.S. Energy Information Administration, 2021.
- [2] A. S. G. Andrae and T. Edler, “On Global Electricity Usage of Communication Technology: Trends to 2030,” *Challenges*, vol. 6, no. 1, pp. 117–157, 2015.
- [3] S. M. Thompson, “The discovery, development and future of GMR: The Nobel Prize 2007,” *J. Phys. D. Appl. Phys.*, vol. 41, p. 93001, Mar 2008.
- [4] M. Kateb, E. Jacobsen, and S. Ingvarsson, “Application of an extended van der Pauw method to anisotropic magnetoresistance measurements of ferromagnetic films,” *J. Phys. D. Appl. Phys.*, vol. 52, p. 75002, Dec 2018.
- [5] M. Julliere, “Tunneling between ferromagnetic films,” *Phys. Lett. A*, vol. 54, no. 3, pp. 225–226, 1975.
- [6] J. S. Moodera, L. R. Kinder, T. M. Wong, and R. Meservey, “Large Magnetoresistance at Room Temperature in Ferromagnetic Thin Film Tunnel Junctions,” *Phys. Rev. Lett.*, vol. 74, pp. 3273–3276, Apr 1995.
- [7] T. Miyazaki and N. Tezuka, “Giant magnetic tunneling effect in Fe/Al<sub>2</sub>O<sub>3</sub>/Fe junction,” *J. Magn. Magn. Mater.*, vol. 139, no. 3, pp. L231–L234, 1995.
- [8] P. M. Tedrow and R. Meservey, “Spin-Dependent Tunneling into Ferromagnetic Nickel,” *Phys. Rev. Lett.*, vol. 26, pp. 192–195, Jan 1971.
- [9] P. M. Tedrow and R. Meservey, “Spin Polarization of Electrons Tunneling from Films of Fe, Co, Ni, and Gd,” *Phys. Rev. B*, vol. 7, pp. 318–326, Jan 1973.
- [10] P. A. Grünberg, “Nobel Lecture: From spin waves to giant magnetoresistance and beyond,” *Rev. Mod. Phys.*, vol. 80, pp. 1531–1540, Dec 2008.
- [11] J. Barnaś, A. Fuss, R. E. Camley, P. Grünberg, and W. Zinn, “Novel magnetoresistance effect in layered magnetic structures: Theory and experiment,” *Phys. Rev. B*, vol. 42, pp. 8110–8120, Nov 1990.
- [12] N. F. Mott and H. S. W. Massey, *The theory of atomic collisions*,. Oxford: Clarendon Press, 1965.
- [13] J. E. Hirsch, “Spin Hall Effect,” *Phys. Rev. Lett.*, vol. 83, no. 9, pp. 1834–1837, 1999.

- [14] C. O. Avci, K. Garello, A. Ghosh, M. Gabureac, S. F. Alvarado, and P. Gambardella, “Unidirectional spin Hall magnetoresistance in ferromagnet/normal metal bilayers,” *Nat. Phys.*, vol. 11, no. 7, pp. 570–575, 2015.
- [15] M. N. Baibich, J. Broto, A. Fert, F. Nguyen Van Day, F. Petroff, P. Eitenne, G. Creuzet, A. Frederich, and J. Chazelas, “Giant Magnetoresistance of Fe and Cr Magnetic Superlattices,” *Phys. Rev. Lett.*, vol. 61, no. 001, pp. 2472–2475, 1988.
- [16] J. W. Jung, Y. Sakuraba, T. T. Sasaki, Y. Miura, and K. Hono, “Enhancement of magnetoresistance by inserting thin NiAl layers at the interfaces in  $\text{Co}_2\text{FeGa}_{0.5}\text{Ge}_{0.5}/\text{Ag}/\text{Co}_2\text{FeGa}_{0.5}\text{Ge}_{0.5}$  current-perpendicular-to-plane pseudo spin valves,” *Appl. Phys. Lett.*, vol. 108, no. 10, p. 102408, 2016.
- [17] S. Yuasa, A. Fukushima, T. Nagahama, K. Ando, and Y. Suzuki, “High Tunnel Magnetoresistance at Room Temperature in Fully Epitaxial Fe/MgO/Fe Tunnel Junctions due to Coherent Spin-Polarized Tunneling,” *Jpn. J. Appl. Phys.*, vol. 43, p. L588, Apr 2004.
- [18] A. Hirohata, K. Yamada, Y. Nakatani, I.-L. Prejbeanu, B. Diény, P. Pirro, and B. Hillebrands, “Review on spintronics: Principles and device applications,” *J. Magn. Magn. Mater.*, vol. 509, p. 166711, 2020.
- [19] J. C. Slonczewski, “Current-driven excitation of magnetic multilayers,” *J. Magn. Magn. Mater.*, vol. 159, no. 1, pp. L1 – L7, 1996.
- [20] L. Berger, “Low-field magnetoresistance and domain drag in ferromagnets,” *J. Appl. Phys.*, vol. 49, no. 3, p. 2156–2161, 1978.
- [21] J. Slonczewski, “Conductance and exchange coupling of two ferromagnets separated by a tunneling barrier,” *Phys. Rev. B*, vol. 39, no. 6995, 1989.
- [22] J. Sinova, S. O. Valenzuela, J. Wunderlich, C. H. Back, and T. Jungwirth, “Spin Hall effects,” *Rev. Mod. Phys.*, vol. 87, 2015.
- [23] E. I. Rashba and V. I. Sheka, “Symmetry of Energy Bands in Crystals of Wurtzite Type II . Symmetry of Bands with Spin-Orbit Interaction Included,” *New J. Phys.*, vol. 17, p. 050202, 2015.
- [24] G. Bihlmayer, O. Rader, and R. Winkler, “Focus on the Rashba effect,” *New J. Phys.*, vol. 17, p. 050202, 2015.
- [25] G. Dresselhaus, “Spin-Orbit Coupling Effects in Zinc Blende Structures,” *Phys. Rev.*, vol. 100, no. 2, 1955.
- [26] H. Kurebayashi, J. Sinova, D. Fang, A. C. Irvine, T. D. Skinner, J. Wunderlich, V. Novák, R. P. Campion, B. L. Gallagher, E. K. Vehstedt, L. P. Zârbo, K. Výborný, A. J. Ferguson, and T. Jungwirth, “An antidamping spin-orbit torque originating from the Berry curvature,” *Nat. Nanotechnol.*, vol. 9, no. 3, pp. 211–7, 2014.
- [27] S. Fukami, C. Zhang, S. DuttaGupta, A. Kurenkov, and H. Ohno, “Magnetization switching by spin-orbit torque in an antiferromagnet-ferromagnet bilayer system,” *Nat. Mater.*, vol. 15, no. 5, pp. 535–541, 2016.

- [28] K.-r. Jeon, C. Ciccarelli, H. Kurebayashi, L. F. Cohen, X. Montiel, M. Eschrig, S. Komori, J. W. A. Robinson, and M. G. Blamire, “Exchange-field enhancement of superconducting spin pumping,” *Phys. Rev. Appl.*, vol. 99, 2019.
- [29] B. Koopmans, “Pumping spins through polymers,” *Nat. Phys.*, vol. 10, no. 4, pp. 249–250, 2014.
- [30] N. Tombros, C. Jozsa, M. Popinciuc, H. T. Jonkman, and B. J. van Wees, “Electronic spin transport and spin precession in single graphene layers at room temperature,” *Nature*, vol. 448, no. 7153, pp. 571–574, 2007.
- [31] K. Tsukagoshi, B. W. Alphenaar, and H. Ago, “Coherent transport of electron spin in a ferromagnetically contacted carbon nanotube,” *Nature*, vol. 401, no. 6753, pp. 572–574, 1999.
- [32] S. Datta and B. Das, “Electronic analog of the electro-optic modulator,” *Appl. Phys. Lett.*, vol. 56, no. 7, pp. 665–667, 1990.
- [33] S. Datta, “How we proposed the spin transistor,” *Nat. Electron.*, vol. 1, no. 11, p. 604, 2018.
- [34] A. T. Hanbicki, B. T. Jonker, G. Itskos, G. Kioseoglou, and A. Petrou, “Efficient electrical spin injection from a magnetic metal/tunnel barrier contact into a semiconductor,” *Appl. Phys. Lett.*, vol. 80, no. 7, pp. 1240–1242, 2002.
- [35] J. Grollier, D. Querlioz, K. Y. Camsari, K. Everschor-Sitte, S. Fukami, and M. D. Stiles, “Neuromorphic spintronics,” *Nat. Electron.*, vol. 3, no. 7, pp. 360–370, 2020.
- [36] M. Hayashi, L. Thomas, R. Moriya, C. Rettner, and S. S. P. Parkin, “Current-Controlled Magnetic Domain-Wall Nanowire Shift Register,” *Science*, vol. 320, no. 5873, pp. 209–211, 2008.
- [37] M. Ranjbar, P. Drrenfeld, M. Haidar, E. Iacocca, M. Balinskiy, T. Q. Le, M. Fazlali, A. Houshang, A. A. Awad, R. K. Dumas, and J. Kerman, “CoFeB-Based Spin Hall Nano-Oscillators,” *IEEE Magn. Lett.*, vol. 5, pp. 1–4, 2014.
- [38] A. Giordano, M. Carpentieri, A. Laudani, G. Gubbiotti, B. Azzerboni, and G. Finocchio, “Spin-Hall nano-oscillator: A micromagnetic study,” *Appl. Phys. Lett.*, vol. 105, no. 4, p. 42412, 2014.
- [39] H. Fulara, M. Zahedinejad, R. Khymyn, M. Dvornik, S. Fukami, S. Kanai, H. Ohno, and J. Åkerman, “Giant voltage-controlled modulation of spin Hall nano-oscillator damping,” *Nat. Commun.*, vol. 11, no. 1, p. 4006, 2020.
- [40] X. Zhang, N. Zhu, C.-L. Zou, and H. X. Tang, “Optomagnonic Whispering Gallery Microresonators,” *Phys. Rev. Lett.*, vol. 117, p. 123605, Sep 2016.
- [41] Z. Shen, G.-T. Xu, M. Zhang, Y.-L. Zhang, Y. Wang, C.-Z. Chai, C.-L. Zou, G.-C. Guo, and C.-H. Dong, “Coherent Coupling between Phonons, Magnons, and Photons,” *Phys. Rev. Lett.*, vol. 129, p. 243601, Dec 2022.

- [42] L. Liensberger, A. Kamra, H. Maier-flaig, S. Geprägs, A. Erb, S. T. B. Goennenwein, R. Gross, W. Belzig, H. Huebl, and M. Weiler, “Exchange-Enhanced Ultrastrong Magnon-Magnon Coupling in a Compensated Ferrimagnet,” *Phys. Rev. Lett.*, vol. 123, no. 11, p. 117204, 2019.
- [43] D. MacNeill, J. T. Hou, D. R. Klein, P. Zhang, P. Jarillo-herrero, and L. Liu, “Gigahertz Frequency Antiferromagnetic Resonance and Strong Magnon-Magnon Coupling in the Layered Crystal CrCl<sub>3</sub>,” *Phys. Rev. Lett.*, vol. 123, no. 4, p. 47204, 2019.
- [44] M. Ishikawa and Ø. Fischer, “Magnetic ordering in the superconducting state of rare earth molybdenum sulphides, (RE)<sub>1.2</sub>Mo<sub>6</sub>S<sub>8</sub> (RE = Tb, Dy and Er),” *Solid State Commun.*, vol. 24, no. 11, pp. 747–751, 1977.
- [45] A. I. Buzdin, L. N. Bulaevskii, M. L. Kulich, and P. SV, “Magnetic superconductors,” *Sov. Physics Uspekhi*, vol. 27, p. 927, 1984.
- [46] W. A. Fertig, D. C. Johnston, L. E. DeLong, R. W. McCallum, M. B. Maple, and B. T. Matthias, “Destruction of Superconductivity at the Onset of Long-Range Magnetic Order in the Compound ErRh<sub>4</sub>B<sub>4</sub>,” *Phys. Rev. Lett.*, vol. 38, pp. 987–990, Apr 1977.
- [47] M. Eschrig and T. Löfwander, “Triplet supercurrents in clean and disordered half-metallic ferromagnets,” *Nat. Phys.*, vol. 4, no. 2, pp. 138–143, 2008.
- [48] M. Eschrig, J. Kopu, J. C. Cuevas, and G. Schön, “Theory of Half-Metal/Superconductor Heterostructures,” *Phys. Rev. Lett.*, vol. 90, p. 137003, Apr 2003.
- [49] P. W. Anderson and H. Suhl, “Spin Alignment in the Superconducting State,” *Phys. Rev.*, vol. 116, pp. 898–900, Nov 1959.
- [50] A. I. Buzdin and L. N. Bulaevskii, “Ferromagnetic film on the surface of a superconductor: possible onset of inhomogeneous magnetic ordering,” *Sov. Physics JETP*, vol. 94, no. March, pp. 256–261, 1988.
- [51] K.-r. Jeon, C. Ciccarelli, A. J. Ferguson, H. Kurebayashi, L. F. Cohen, X. Montiel, M. Eschrig, J. W. A. Robinson, and M. G. Blamire, “Enhanced spin pumping into superconductors provides evidence for superconducting pure spin currents,” *Nat. Mater.*, vol. 17, no. June, pp. 499–504, 2018.
- [52] P. Wadley, B. Howells, J. Železný, C. Andrews, V. Hills, R. P. Campion, V. Novák, K. Olejnik, F. Maccherozzi, S. S. Dhesi, S. Y. Martin, T. Wagner, J. Wunderlich, F. Freimuth, Y. Mokrousov, J. Kuneš, J. S. Chauhan, M. J. Grzybowski, A. W. Rushforth, K. W. Edmonds, B. L. Gallagher, and T. Jungwirth, “Electrical switching of an antiferromagnet,” *Science*, vol. 351, no. 6273, pp. 587–590, 2016.
- [53] T. Jungwirth, X. Marti, P. Wadley, and J. Wunderlich, “Antiferromagnetic spintronics,” *Nat. Nanotechnol.*, vol. 11, pp. 231—241, 2016.
- [54] R. Cheng, D. Xiao, and A. Brataas, “Terahertz Antiferromagnetic Spin Hall Nano-Oscillator,” *Phys. Rev. Lett.*, vol. 116, p. 207603, May 2016.

- [55] R. A. Duine, K.-J. Lee, S. S. P. Parkin, and M. D. Stiles, “Synthetic antiferromagnetic spintronics,” *Nat. Phys.*, vol. 14, no. 3, pp. 217–219, 2018.
- [56] I. Fina, X. Marti, D. Yi, J. Liu, J. H. Chu, C. Rayan-Serrao, S. Suresha, A. B. Shick, J. Železný, T. Jungwirth, J. Fontcuberta, and R. Ramesh, “Anisotropic magnetoresistance in an antiferromagnetic semiconductor,” *Nat. Commun.*, vol. 5, no. 1, p. 4671, 2014.
- [57] W. Lin and C. L. Chien, “Electrical Detection of Spin Backflow from an Antiferromagnetic Insulator/ $\text{Y}_3\text{Fe}_5\text{O}_{12}$  Interface,” *Phys. Rev. Lett.*, vol. 118, p. 67202, Feb 2017.
- [58] H. Chen, Q. Niu, and A. H. MacDonald, “Anomalous Hall Effect Arising from Noncollinear Antiferromagnetism,” *Phys. Rev. Lett.*, vol. 112, p. 17205, Jan 2014.
- [59] W. Heisenberg, “Zur Theorie des Ferromagnetismus,” *Zeitschrift für Phys.*, vol. 49, pp. 619–636, 1928.
- [60] W. F. Brown, *Micromagnetics*. Interscience tracts on physics and astronomy, New York: J. Wiley, 1963.
- [61] P. W. Anderson, “Local moments and localized states,” in *Nobel Lect. Phys. 1971-1980* (S. Lundqvist, ed.), Singapore: World Scientific Publishing Co., 1992.
- [62] K. H. J. Buschow, R. W. Cahn, M. C. Flemings, B. Ilschner, E. J. Kramer, and S. Mahajan, eds., *Encyclopedia of Materials: Science and Technology*. Oxford: Elsevier, 2001.
- [63] L. Landau and E. Lifshitz, “On the theory of the dispersion of ferromagnetic bodies,” *Phys. Zeitsch. der Sow.*, vol. 8, no. 14, pp. 153–169, 1935.
- [64] R. Becker and W. Döring, *Ferromagnetismus*. Berlin: Julius Springer, 1939.
- [65] W. F. Brown, “Micromagnetics, Domains, and Resonance,” *J. Appl. Phys.*, vol. 30, no. 4, pp. S62–S69, 1959.
- [66] L. D. Landau, L. P. Pitaevskii, and E. M. Lifshitz, *Electrodynamics of Continuous Media*. Amsterdam: Elsevier, 2nd ed., 1984.
- [67] T. L. Gilbert, “A Lagrangian formulation of the gyromagnetic equation of the magnetisation field,” *Phys. Rev.*, vol. 100, p. 1243, 1955.
- [68] A. Manchon and A. Belabbes, “Chapter One - Spin-Orbitronics at Transition Metal Interfaces,” in *Solid State Phys.* (R. E. Camley and R. L. Stamps, eds.), vol. 68 of *Solid State Physics*, pp. 1–89, Academic Press, 2017.
- [69] M. C. Hickey and J. S. Moodera, “Origin of Intrinsic Gilbert Damping,” *Phys. Rev. Lett.*, vol. 102, p. 137601, Mar 2009.
- [70] D. Steiauf and M. Fähnle, “Damping of spin dynamics in nanostructures: An ab initio study,” *Phys. Rev. B*, vol. 72, p. 64450, Aug 2005.

- [71] O. Steinsvoll and T. Riste, "Spin dynamics above the curie temperature studied by neutron scattering," *Hyperfine Interact.*, vol. 31, no. 1, pp. 267–286, 1986.
- [72] J. Osterwalder, "Correlation effects and magnetism in 3d transition metals," *J. Electron Spectros. Relat. Phenomena*, vol. 117–118, pp. 71–88, 2001.
- [73] S. Eich, M. Plötzing, M. Rollinger, S. Emmerich, R. Adam, C. Chen, H. C. Kapteyn, M. M. Murnane, L. Plucinski, D. Steil, B. Stadtmüller, M. Cinchetti, M. Aeschlimann, C. M. Schneider, and S. Mathias, "Band structure evolution during the ultrafast ferromagnetic-paramagnetic phase transition in cobalt," *Sci. Adv.*, vol. 3, no. 3, p. e1602094, 2017.
- [74] P. Zeeman, "XXXII. On the influence of magnetism on the nature of the light emitted by a substance," *London, Edinburgh, Dublin Philos. Mag. J. Sci.*, vol. 43, no. 262, pp. 226–239, 1897.
- [75] A. J. Cox, "The discovery of the electron: II. The Zeeman effect," *Eur. J. Phys.*, vol. 18, pp. 139–144, May 1997.
- [76] J. Jackson, *Classical Electrodynamics*. New York: Wiley, third ed., 1999.
- [77] A. I. Akhiezer, V. G. Bar' Yakhtar, and S. V. Peletminskii, *Spin waves*. Amsterdam: North-Holland Publishing Company, 1968.
- [78] D. J. Dunlop, A. J. Newell, and W. Williams, "A generalization of the demagnetizing tensor for nonuniform magnetization," *J. Geophys. Res.*, vol. 98, no. B6, p. 9551, 1993.
- [79] J. Frenkel and J. Doefman, "Spontaneous and Induced Magnetisation in Ferromagnetic Bodies," *Nature*, vol. 126, no. 3173, pp. 274–275, 1930.
- [80] G. E. Uhlenbeck and S. Goudsmit, "Spinning Electrons and the Structure of Spectra," *Nature*, vol. 117, no. 2938, pp. 264–265, 1926.
- [81] M. T. Johnson, R. Jungblut, P. J. Kelly, and F. J. A. den Broeder, "Perpendicular magnetic anisotropy of multilayers: recent insights," *J. Magn. Magn. Mater.*, vol. 148, no. 1, pp. 118–124, 1995.
- [82] B. Dieny and M. Chshiev, "Perpendicular magnetic anisotropy at transition metal/oxide interfaces and applications," *Rev. Mod. Phys.*, vol. 89, p. 25008, Jun 2017.
- [83] S. Monso, B. Rodmacq, S. Auffret, G. Casali, F. Fettar, B. Gilles, B. Dieny, and P. Boyer, "Crossover from in-plane to perpendicular anisotropy in Pt/CoFe/AlO<sub>x</sub> sandwiches as a function of Al oxidation: A very accurate control of the oxidation of tunnel barriers," *Appl. Phys. Lett.*, vol. 80, no. 22, pp. 4157–4159, 2002.
- [84] M. T. Johnson, P. J. H. Bloemen, F. J. A. den Broeder, and J. J. de Vries, "Magnetic anisotropy in metallic multilayers," *Reports Prog. Phys.*, vol. 59, pp. 1409–1458, Nov 1996.
- [85] U. Gradmann and J. Müller, "Flat Ferromagnetic, Epitaxial 48Ni/52Fe(111) Films of few Atomic Layers," *Phys. status solidi*, vol. 27, no. 1, pp. 313–324, 1968.

- [86] M. A. Rurderman and C. Kittel, "Indirect Exchange Coupling of Nuclear Magnetic Moments by Conduction Electrons," *Phys. Rev.*, vol. 96, no. 1, pp. 72–75, 1954.
- [87] T. Kasuya, "A Theory of Metallic Ferro- and Antiferromagnetism on Zener's Model," *Prog. Theor. Phys.*, vol. 16, no. 1, pp. 45–57, 1956.
- [88] K. Yosida, "Magnetic Properties of Cu-Mn Alloys," *Phys. Rev.*, vol. 106, pp. 893–898, Jun 1957.
- [89] M. Rühlig, R. Schäfer, A. Hubert, R. Mosler, J. A. Wolf, S. Demokritov, and P. Grünberg, "Domain Observations on Fe-Cr-Fe Layered Structures Evidence for a Biquadratic Coupling Effect," *Phys. status solidi*, vol. 125, no. 2, pp. 635–656, 1991.
- [90] J. Slonczewski, "Origin of biquadratic exchange in magnetic multilayers," *J. Appl. Phys.*, vol. 73, no. 5957, 1993.
- [91] G. J. Strijkers, J. T. Kohlhepp, H. J. M. Swagten, and W. J. M. de Jonge, "Origin of Biquadratic Exchange in Fe/Si/Fe," *Phys. Rev. Lett.*, vol. 84, pp. 1812–1815, Feb 2000.
- [92] M. Kowalewski, Z. Celinski, B. Heinrich, J. F. Cochran, M. Kowalewski, J. Kirschner, Z. Celinski, A. S. Arrott, and K. Myrtle, "Magnetic anisotropies and exchange coupling in ultrathin fcc Co(001) structures," *Phys. Rev. B*, vol. 44, pp. 9348–9361, Nov 1991.
- [93] J. Griffiths, "Anomalous High-frequency resistance of ferromagnetic metals," *Nature*, vol. 158, pp. 670–671, 1946.
- [94] C. Kittel, "Interpretation of Anomalous Larmor Frequencies in Ferromagnetic Resonance Experiment," *Phys. Rev.*, vol. 71, pp. 270–271, Feb 1947.
- [95] C. Kittel, "On the Theory of Ferromagnetic Resonance Absorption," *Phys. Rev.*, vol. 73, pp. 155–161, Jan 1948.
- [96] J. Smit and H. G. Beljers, "Ferromagnetic Resonance absorption in BaFe<sub>12</sub>O<sub>19</sub> a highly anisotropic crystal," *Philips Res. Rep.*, vol. 10, no. 113, 1955.
- [97] F. J. A. den Broeder, W. Hoving, and P. J. H. Bloemen, "Magnetic anisotropy of multilayers," *J. Magn. Magn. Mater.*, vol. 93, pp. 562–570, 1991.
- [98] H. J. G. Draaisma, W. J. M. de Jonge, and F. J. A. den Broeder, "Magnetic interface anisotropy in Pd/Co and Pd/Fe multilayers," *J. Magn. Magn. Mater.*, vol. 66, no. 3, pp. 351–355, 1987.
- [99] P. F. Carcia, "Perpendicular magnetic anisotropy in Pd/Co and Pt/Co thin-film layered structures," *J. Appl. Phys.*, vol. 63, no. 10, pp. 5066–5073, 1988.
- [100] F. J. A. den Broeder, D. Kuiper, A. P. van de Mosselaer, and W. Hoving, "Perpendicular Magnetic Anisotropy of Co-Au Multilayers Induced by Interface Sharpening," *Phys. Rev. Lett.*, vol. 60, pp. 2769–2772, Jun 1988.

- [101] K. Zakeri, J. Lindner, I. Barsukov, R. Meckenstock, M. Farle, U. von Hörsten, H. Wende, W. Keune, J. Rucker, S. S. Kalarickal, K. Lenz, W. Kuch, K. Baberschke, and Z. Frait, “Spin dynamics in ferromagnets: Gilbert damping and two-magnon scattering,” *Phys. Rev. B*, vol. 76, p. 104416, Sep 2007.
- [102] R. Arias and D. L. Mills, “Extrinsic contributions to the ferromagnetic resonance response of ultrathin films,” *J. Appl. Phys.*, vol. 87, no. 9, pp. 5455–5456, 2000.
- [103] J. Lindner, K. Lenz, E. Kosubek, K. Baberschke, D. Spoddig, R. Meckenstock, J. Pelzl, Z. Frait, and D. L. Mills, “Non-Gilbert-type damping of the magnetic relaxation in ultrathin ferromagnets: Importance of magnon-magnon scattering,” *Phys. Rev. B*, vol. 68, p. 60102, Aug 2003.
- [104] P. W. Anderson and H. Suhl, “Instability in the Motion of Ferromagnets at High Microwave Power Levels,” *Phys. Rev.*, vol. 100, pp. 1788–1789, Dec 1955.
- [105] J. Lourembam, A. Ghosh, M. Zeng, S. K. Wong, Q. J. Yap, and S. Ter Lim, “Thickness-Dependent Perpendicular Magnetic Anisotropy and Gilbert Damping in Hf/Co<sub>20</sub>Fe<sub>60</sub>B<sub>20</sub>/MgO Heterostructures,” *Phys. Rev. Appl.*, vol. 10, p. 44057, Oct 2018.
- [106] M. Sparks, R. Loudon, and C. Kittel, “Ferromagnetic Relaxation. I. Theory of the Relaxation of the Uniform Precession and the Degenerate Spectrum in Insulators at Low Temperatures,” *Phys. Rev.*, vol. 122, pp. 791–803, May 1961.
- [107] R. C. LeCraw, E. G. Spencer, and C. S. Porter, “Ferromagnetic Resonance Line Width in Yttrium Iron Garnet Single Crystals,” *Phys. Rev.*, vol. 110, pp. 1311–1313, Jun 1958.
- [108] R. D. McMichael, D. J. Twisselmann, and A. Kunz, “Localized Ferromagnetic Resonance in Inhomogeneous Thin Films,” *Phys. Rev. Lett.*, vol. 90, p. 227601, Jun 2003.
- [109] R. D. McMichael and P. Krivosik, “Classical model of extrinsic ferromagnetic resonance linewidth in ultrathin films,” *IEEE Trans. Magn.*, vol. 40, no. 1, pp. 2–11, 2004.
- [110] R. D. McMichael, D. J. Twisselmann, J. E. Bonevich, A. P. Chen, W. F. Egelhoff, and S. E. Russek, “Ferromagnetic resonance mode interactions in periodically perturbed films,” *J. Appl. Phys.*, vol. 91, no. 10, pp. 8647–8649, 2002.
- [111] L. Berger, “Emission of spin waves by a magnetic multilayer traversed by a current,” *Phys. Rev. B*, vol. 54, no. 13, 1996.
- [112] Y. Tserkovnyak, A. Brataas, and G. E. W. Bauer, “Enhanced Gilbert Damping in Thin Ferromagnetic Films,” *Phys. Rev. Lett.*, vol. 88, p. 117601, Feb 2002.
- [113] Y. Tserkovnyak, A. Brataas, and G. E. W. Bauer, “Spin pumping and magnetization dynamics in metallic multilayers,” *Phys. Rev. B*, vol. 66, p. 224403, Dec 2002.

- [114] S. Mizukami, Y. Ando, and T. Miyazaki, "Effect of spin diffusion on Gilbert damping for a very thin permalloy layer in Cu/permalloy/Cu/Pt films," *Phys. Rev. B*, vol. 66, p. 104413, Sep 2002.
- [115] S. Mizukami, Y. Ando, and T. Miyazaki, "Ferromagnetic resonance linewidth for NM/80NiFe/NM films (NM=Cu, Ta, Pd and Pt)," *J. Magn. Magn. Mater.*, vol. 226-230, pp. 1640–1642, 2001.
- [116] R. D. McMichael and A. Kunz, "Calculation of damping rates in thin inhomogeneous ferromagnetic films due to coupling to lattice vibrations," *J. Appl. Phys.*, vol. 91, no. 10, pp. 8650–8652, 2002.
- [117] P. Pincus, M. Sparks, and R. C. LeCraw, "Ferromagnetic Relaxation. II. The Role of Four-Magnon Processes in Relaxing the Magnetization in Ferromagnetic Insulators," *Phys. Rev.*, vol. 124, pp. 1015–1018, Nov 1961.
- [118] A. A. Mikhailov and R. M. Farzetdinova, "Quantum theory of spin-wave relaxation by two level impurities," *Zh. Eksp. Teor. Fiz.*, vol. 80, pp. 1524–1538, 1981.
- [119] H. Suhl, "Theory of the magnetic damping constant," *IEEE Trans. Magn.*, vol. 34, no. 4, pp. 1834–1838, 1998.
- [120] S. Azzawi, A. T. Hindmarch, and D. Atkinson, "Magnetic damping phenomena in ferromagnetic thin-films and multilayers," *J. Phys. D. Appl. Phys.*, vol. 50, p. 473001, Oct 2017.
- [121] J. A. Katine, F. J. Albert, R. A. Buhrman, E. B. Myers, and D. C. Ralph, "Current-Driven Magnetization Reversal and Spin-Wave Excitations in Co /Cu /Co Pillars," *Phys. Rev. Lett.*, vol. 84, pp. 3149–3152, Apr 2000.
- [122] M. Dresselhaus, G. Dresselhaus, and A. Jorio, *Group Theory: Application to the Physics of Condensed Matter*. Heidelberg: Springer, 1 ed., 2008.
- [123] A. Manchon and S. Zhang, "Theory of nonequilibrium intrinsic spin torque in a single nanomagnet," *Phys. Rev. B*, vol. 78, p. 212405, Dec 2008.
- [124] D. A. Pesin and A. H. MacDonald, "Quantum kinetic theory of current-induced torques in Rashba ferromagnets," *Phys. Rev. B*, vol. 86, p. 14416, Jul 2012.
- [125] A. A. Tulapurkar, Y. Suzuki, A. Fukushima, H. Kubota, H. Maehara, K. Tsunekawa, D. D. Djayaprawira, N. Watanabe, and S. Yuasa, "Spin-torque diode effect in magnetic tunnel junctions," *Nature*, vol. 438, no. 7066, pp. 339–342, 2005.
- [126] C. Ciccarelli, L. Anderson, V. Tshitoyan, A. J. Ferguson, F. Gerhard, C. Gould, L. W. Molenkamp, J. Gayles, J. Železný, L. Šmejkal, Z. Yuan, J. Sinova, F. Freimuth, and T. Jungwirth, "Room-temperature spin-orbit torque in NiMnSb," *Nat. Phys.*, vol. 12, no. 9, pp. 855–860, 2016.
- [127] H. C. Koo, S. B. Kim, H. Kim, T.-E. Park, J. W. Choi, K.-W. Kim, G. Go, J. H. Oh, D.-K. Lee, E.-S. Park, I.-S. Hong, and K.-J. Lee, "Rashba Effect in Functional Spintronic Devices," *Adv. Mater.*, vol. 32, no. 51, p. 2002117, 2020.

- [128] X. Wang and A. Manchon, “Diffusive Spin Dynamics in Ferromagnetic Thin Films with a Rashba Interaction,” *Phys. Rev. Lett.*, vol. 108, p. 117201, Mar 2012.
- [129] M. I. Dyakonov and V. I. Perelm, “Possibility of orienting electron spins with current,” *Zh. Eksp. Teor. Fiz. Pis'ma*, vol. 13, no. 11, pp. 657–660, 1971.
- [130] M. I. Dyakonov and V. I. Perel, “Current-induced spin orientation of electrons in semiconductors,” *Phys. Lett. A*, vol. 35, no. 6, pp. 459–460, 1971.
- [131] A. A. Bakun, B. P. Zakharchenya, A. A. Rogachev, M. N. Tkachuk, and V. G. Fleisher, “Observation of a surface photocurrent caused by optical orientation of electrons in a semiconductor,” *Zh. Eksp. Teor. Fiz. Pis'ma*, vol. 40, no. 11, 1984.
- [132] S. Murakami, N. Nagaosa, and S.-C. Zhang, “Dissipationless Quantum Spin Current at Room Temperature,” *Science*, vol. 301, no. 5638, pp. 1348–1351, 2003.
- [133] J. Sinova, D. Culcer, Q. Niu, N. A. Sinitsyn, T. Jungwirth, and A. H. MacDonald, “Universal Intrinsic Spin Hall Effect,” *Phys. Rev. Lett.*, vol. 92, p. 126603, Mar 2004.
- [134] Kato, Myers, Gossard, and Awschalom, “Observation of the spin hall effect in semiconductors,” *Science*, vol. 306, 2004.
- [135] J. Wunderlich, B. Kaestner, J. Sinova, and T. Jungwirth, “Experimental observation of the spin-hall effect in a two-dimensional spin-orbit coupled semiconductor system,” *Phys. Rev. Lett.*, vol. 94, no. 4, 2005.
- [136] R. J. Elliott, “Theory of the Effect of Spin-Orbit Coupling on Magnetic Resonance in Some Semiconductors,” *Phys. Rev.*, vol. 96, pp. 266–279, Oct 1954.
- [137] G. B. Airy, “On certain Conditions under which a Perpetual Motion is possible,” *Trans. Cambridge Philos. Soc.*, vol. 3, pp. 369–372, 1830.
- [138] A. Jenkins, “Self-oscillation,” *Phys. Rep.*, vol. 525, no. 2, pp. 167–222, 2013.
- [139] V. E. Demidov, S. Urazhdin, E. R. J. Edwards, M. D. Stiles, R. D. McMichael, and S. O. Demokritov, “Control of Magnetic Fluctuations by Spin Current,” *Phys. Rev. Lett.*, vol. 107, no. 10, p. 107204, 2011.
- [140] K. Ando, S. Takahashi, K. Harii, K. Sasage, J. Ieda, S. Maekawa, and E. Saitoh, “Electric Manipulation of Spin Relaxation Using the Spin Hall Effect,” *Phys. Rev. Lett.*, vol. 101, p. 36601, Jul 2008.
- [141] Z. Wang, Y. Sun, M. Wu, V. Tiberkevich, and A. Slavin, “Control of Spin Waves in a Thin Film Ferromagnetic Insulator through Interfacial Spin Scattering,” *Phys. Rev. Lett.*, vol. 107, p. 146602, Sep 2011.
- [142] S. M. Rezende, F. M. de Aguiar, and A. Azevedo, “Magnon excitation by spin-polarized direct currents in magnetic nanostructures,” *Phys. Rev. B*, vol. 73, p. 94402, Mar 2006.
- [143] V. E. Demidov, S. Urazhdin, G. de Loubens, O. Klein, V. Cros, A. Anane, and S. O. Demokritov, “Magnetization oscillations and waves driven by pure spin currents,” *Phys. Rep.*, vol. 673, pp. 1–31, 2017.

- [144] T. Kizuka and H. Aoki, "The Dynamics of Electromigration in Copper Nanocontacts," *Appl. Phys. Express*, vol. 2, p. 75003, Jun 2009.
- [145] A. Shukla and S. Rakheja, "Spin-Torque-Driven Terahertz Auto-Oscillations in Non-collinear Coplanar Antiferromagnets," *Phys. Rev. Appl.*, vol. 17, p. 34037, Mar 2022.
- [146] V. E. Demidov, S. Urazhdin, H. Ulrichs, V. Tiberkevich, A. Slavin, D. Baither, G. Schmitz, and S. O. Demokritov, "Magnetic nano-oscillator driven by pure spin current," *Nat. Mater.*, vol. 11, p. 1028, Oct 2012.
- [147] Z. Duan, A. Smith, L. Yang, B. Youngblood, J. Lindner, V. E. Demidov, S. O. Demokritov, and I. N. Krivorotov, "Nanowire spin torque oscillator driven by spin orbit torques," *Nat. Commun.*, vol. 5, no. 1, p. 5616, 2014.
- [148] S. Langenfeld, V. Tshitoyan, Z. Fang, A. Wells, T. A. Moore, and A. J. Ferguson, "Exchange magnon induced resistance asymmetry in permalloy spin-Hall oscillators," *Appl. Phys. Lett.*, vol. 108, no. 19, p. 192402, 2016.
- [149] R. H. Liu, W. L. Lim, and S. Urazhdin, "Spectral Characteristics of the Microwave Emission by the Spin Hall Nano-Oscillator," *Phys. Rev. Lett.*, vol. 110, p. 147601, Apr 2013.
- [150] S. Kaka, M. R. Pufall, W. H. Rippard, T. J. Silva, S. E. Russek, and J. A. Katine, "Mutual phase-locking of microwave spin torque nano-oscillators," *Nature*, vol. 437, no. 7057, pp. 389–392, 2005.
- [151] M. Zahedinejad, A. A. Awad, S. Muralidhar, R. Khymyn, H. Fulara, H. Mazraati, M. Dvornik, and J. Åkerman, "Two-dimensional mutually synchronized spin Hall nano-oscillator arrays for neuromorphic computing," *Nat. Nanotechnol.*, vol. 15, no. 1, pp. 47–52, 2020.
- [152] M. Fiebig, N. P. Duong, T. Satoh, B. B. V. Aken, K. Miyano, Y. Tomioka, and Y. Tokura, "Ultrafast magnetization dynamics of antiferromagnetic compounds," *J. Phys. D: Appl. Phys.*, vol. 41, p. 164005, Aug 2008.
- [153] J. Walowski and M. Münzenberg, "Perspective: Ultrafast magnetism and THz spintronics," *J. Appl. Phys.*, vol. 120, no. 14, p. 140901, 2016.
- [154] D. M. Mittleman, "Perspective: Terahertz science and technology," *J. Appl. Phys.*, vol. 122, no. 23, p. 230901, 2017.
- [155] J.-H. Son, S. J. Oh, and H. Cheon, "Potential clinical applications of terahertz radiation," *J. Appl. Phys.*, vol. 125, no. 19, p. 190901, 2019.
- [156] H. Tsai, T. Higo, K. Kondou, A. Kobayashi, T. Nakano, K. Yakushiji, S. Miwa, Y. Otani, and S. Nakatsuji, "Spin-orbit torque switching of the antiferromagnetic state in polycrystalline Mn<sub>3</sub>Sn/Cu/heavy metal heterostructures," *AIP Adv.*, vol. 11, no. 4, p. 45110, 2021.
- [157] M. Meinert, D. Graulich, and T. Matalla-Wagner, "Electrical Switching of Antiferromagnetic Mn<sub>2</sub>Au and the Role of Thermal Activation," *Phys. Rev. Appl.*, vol. 9, p. 64040, Jun 2018.

- [158] S. Y. Bodnar, L. Šmejkal, I. Turek, T. Jungwirth, O. Gomonay, J. Sinova, A. A. Sapozhnik, H.-J. Elmers, M. Kläui, and M. Jourdan, “Writing and reading antiferromagnetic Mn<sub>2</sub>Au by Néel spin-orbit torques and large anisotropic magnetoresistance,” *Nat. Commun.*, vol. 9, no. 1, p. 348, 2018.
- [159] B. T. Matthias, H. Suhl, and E. Corenzwit, “Spin Exchange in Superconductors,” *Phys. Rev. Lett.*, vol. 1, pp. 92–94, Aug 1958.
- [160] P. A. M. Dirac and R. H. Fowler, “On the theory of quantum mechanics,” *Proc. R. Soc. London. Ser. A, Contain. Pap. a Math. Phys. Character*, vol. 112, no. 762, pp. 661–677, 1926.
- [161] H. Kamerlingh-Onnes, “Further experiments with liquid helium. D. On the change of electric resistance of pure metals at very low temperatures, etc V. The disappearance of the resistance of mercury,” *Commun. from Lab. Phys. Univ. Leiden*, no. 1226, 1911.
- [162] D. van Delft and P. Kes, “The discovery of superconductivity,” *Phys. Today*, vol. 63, no. 9, pp. 38–43, 2010.
- [163] W. Meissner and R. Ochsenfeld, “Ein neuer Effekt bei Eintritt der Supraleitfähigkeit,” *Naturwissenschaften*, vol. 21, no. 44, pp. 787–788, 1933.
- [164] J. Bardeen, L. N. Cooper, and J. R. Schrieffer, “Theory of Superconductivity,” *Phys. Rev.*, vol. 108, pp. 1175–1204, Dec 1957.
- [165] L. P. Gorkov, “On the energy spectrum of superconductors,” *Sov. Phys. JETP*, vol. 7, pp. 505–508, 1958.
- [166] N. N. Bogoliubov, “A new method in theory of superconductivity,” *Sov. Phys. JETP*, vol. 7, p. 41, 1958.
- [167] V. L. Ginzburg, “Ferromagnetic Superconductors,” *Sov. Physics JETP*, vol. 4, p. 153, 1957.
- [168] H. Suhl and B. T. Matthias, “Impurity Scattering in Superconductors,” *Phys. Rev.*, vol. 114, pp. 977–988, May 1959.
- [169] C. Herring, “151. Spin exchange in superconductors,” *Physica*, vol. 24, p. S184, 1958.
- [170] T. Mühge, K. Theis-Bröhl, K. Westerholt, H. Zabel, N. N. Garif’yanov, Y. V. Goryunov, I. A. Garifullin, and G. G. Khaliullin, “Influence of magnetism on superconductivity in epitaxial Fe/Nb bilayer systems,” *Phys. Rev. B*, vol. 57, pp. 5071–5074, Mar 1998.
- [171] V. T. Petrashov, V. N. Antonov, and S. Maksimov, “Conductivity of mesoscopic structures with ferromagnetic and superconducting regions,” *JETP Lett.*, vol. 59, no. 8, pp. 551–555, 1994.
- [172] M. D. Lawrence and N. Giordano, “Weak-localization-like effects in superconductor - ferromagnet - superconductor structures,” *J. Phys. Condens. Matter*, vol. 8, pp. L563–L568, Sep 1996.

- [173] M. Giroud, H. Courtois, K. Hasselbach, D. Mailly, and B. Pannetier, “Superconducting proximity effect in a mesoscopic ferromagnetic wire,” *Phys. Rev. B*, vol. 58, pp. R11872—R11875, Nov 1998.
- [174] V. T. Petrashov, I. A. Sosnin, I. Cox, A. Parsons, and C. Troadec, “Giant Mutual Proximity Effects in Ferromagnetic/Superconducting Nanostructures,” *Phys. Rev. Lett.*, vol. 83, pp. 3281–3284, Oct 1999.
- [175] F. S. Bergeret, K. B. Efetov, and A. I. Larkin, “Nonhomogeneous magnetic order in superconductor-ferromagnet multilayers,” *Phys. Rev. B*, vol. 62, pp. 11872–11878, Nov 2000.
- [176] M. Eschrig, “Spin-polarized supercurrents for spintronics : a review of current progress,” *Reports Prog. Phys.*, vol. 78, 2015.
- [177] G. Yang, C. Ciccarelli, and J. W. A. Robinson, “Boosting spintronics with superconductivity,” *APL Mater.*, vol. 9, no. 5, p. 50703, 2021.
- [178] J. A. Glick, V. Aguilar, A. B. Gougam, B. M. Niedzielski, E. C. Gingrich, R. Loloee, W. P. Pratt, and N. O. Birge, “Phase control in a spin-triplet SQUID,” *Sci. Adv.*, vol. 4, no. 7, 2018.
- [179] K. Y. Camsari, B. M. Sutton, and S. Datta, “p-bits for probabilistic spin logic,” *Appl. Phys. Rev.*, vol. 6, no. 1, p. 11305, 2019.
- [180] F. Hübler, M. J. Wolf, D. Beckmann, and H. v. Löhneysen, “Long-Range Spin-Polarized Quasiparticle Transport in Mesoscopic Al Superconductors with a Zeeman Splitting,” *Phys. Rev. Lett.*, vol. 109, p. 207001, Nov 2012.
- [181] C. H. L. Quay, D. Chevallier, C. Bena, and M. Aprili, “Spin imbalance and spin-charge separation in a mesoscopic superconductor,” *Nat. Phys.*, vol. 9, no. 2, pp. 84–88, 2013.
- [182] M. D. Lawrence and N. Giordano, “Proximity effects in superconductor-ferromagnet junctions,” *J. Phys. Condens. Matter*, vol. 11, pp. 1089–1094, Jan 1999.
- [183] A. I. Buzdin and M. Y. Kupriyanov, “Transition temperature of a superconductor-ferromagnet superlattice,” *JETP Lett.*, vol. 52, p. 487, 1990.
- [184] Z. Radović, M. Ledvij, D.-G. Ljiljana, A. I. Buzdin, and J. R. Clem, “Transition temperatures of superconductor-ferromagnet superlattices,” *Phys. Rev. B*, vol. 44, pp. 759–764, Jul 1991.
- [185] J. S. Jiang, D. Davidović, D. H. Reich, and C. L. Chien, “Oscillatory Superconducting Transition Temperature in Nb/Gd Multilayers,” *Phys. Rev. Lett.*, vol. 74, pp. 314–317, Jan 1995.
- [186] L. N. Bulaevskii, V. V. Kuzii, and A. A. Sobyanin, “Superconducting system with weak coupling to the current in the ground state,” *JETP Lett.*, vol. 25, pp. 314–318, 1977.
- [187] T. Kontos, M. Aprili, J. Lesueur, and X. Grison, “Inhomogeneous Superconductivity Induced in a Ferromagnet by Proximity Effect,” *Phys. Rev. Lett.*, vol. 86, pp. 304–307, Jan 2001.

- [188] R. S. Keizer, S. T. B. Goennenwein, T. M. Klapwijk, G. Miao, G. Xiao, and A. Gupta, “A spin triplet supercurrent through the half-metallic ferromagnet CrO<sub>2</sub>,” *Nature*, vol. 439, no. 7078, pp. 825–827, 2006.
- [189] L. N. Bulaevskii, A. I. Rusinov, and M. Kulić, “Helical ordering of spins in a superconductor,” *J. Low Temp. Phys.*, vol. 39, no. 3, pp. 255–272, 1980.
- [190] D. M. Badiane, M. Houzet, and J. S. Meyer, “Nonequilibrium Josephson Effect through Helical Edge States,” *Phys. Rev. Lett.*, vol. 107, p. 177002, Oct 2011.
- [191] Y. A. Izyumov, Y. N. Proshin, and M. G. Khusainov, “Competition between superconductivity and magnetism in ferromagnet/superconductor heterostructures,” *Physics-Usp ekhi*, vol. 45, pp. 109–148, Feb 2002.
- [192] J. W. A. Robinson, S. Piano, G. Burnell, C. Bell, and M. G. Blamire, “Critical Current Oscillations in Strong Ferromagnetic  $\pi$  Junctions,” *Phys. Rev. Lett.*, vol. 97, p. 177003, Oct 2006.
- [193] C. Cirillo, S. Voltan, E. A. Ilyina, J. M. Hernández, A. García-Santiago, J. Aarts, and C. Attanasio, “Long-range proximity effect in Nb-based heterostructures induced by a magnetically inhomogeneous permalloy layer,” *New J. Phys.*, vol. 19, p. 23037, Feb 2017.
- [194] F. S. Bergeret, “Odd triplet superconductivity and related phenomena in superconductor-ferromagnet structures,” *Rev. Mod. Phys.*, vol. 77, no. October, pp. 1321–1373, 2005.
- [195] K.-r. Jeon, B. K. Hazra, K. Cho, A. Chakraborty, J.-c. Jeon, H. Han, H. L. Meyerheim, T. Kontos, and S. S. P. Parkin, “Long-range supercurrents through a chiral non-collinear antiferromagnet in lateral Josephson junctions,” *Nat. Mater.*, vol. 20, no. October, 2021.
- [196] S. H. Jacobsen, J. A. Ouassou, and J. Linder, “Critical temperature and tunneling spectroscopy of superconductor-ferromagnet hybrids with intrinsic Rashba-Dresselhaus spin-orbit coupling,” *Phys. Rev. B*, vol. 92, p. 24510, Jul 2015.
- [197] F. S. Bergeret and I. V. Tokatly, “Spin-orbit coupling as a source of long-range triplet proximity effect in superconductor-ferromagnet hybrid structures,” *Phys. Rev. B*, vol. 89, p. 134517, Apr 2014.
- [198] A. F. Volkov, F. S. Bergeret, and K. B. Efetov, “Odd Triplet Superconductivity in Superconductor-Ferromagnet Multilayered Structures,” *Phys. Rev. Lett.*, vol. 90, no. 11, p. 117006, 2003.
- [199] M. Houzet and A. I. Buzdin, “Long range triplet Josephson effect through a ferromagnetic trilayer,” *Phys. Rev. B*, vol. 76, p. 60504, Aug 2007.
- [200] T. S. Khaire, M. A. Khasawneh, W. P. Pratt, and N. O. Birge, “Observation of Spin-Triplet Superconductivity in Co-Based Josephson Junctions,” *Phys. Rev. Lett.*, vol. 104, p. 137002, Mar 2010.

- [201] M. Inoue, M. Ichioka, and H. Adachi, “Spin pumping into superconductors: A new probe of spin dynamics in a superconducting thin film,” *Phys. Rev. B*, vol. 96, p. 24414, Jul 2017.
- [202] Morten, J. P., Brataas, A., Bauer, G. E. W., Belzig, W., and Tserkovnyak, Y., “Proximity-effect-assisted decay of spin currents in superconductors,” *EPL*, vol. 84, no. 5, p. 57008, 2008.
- [203] S. Mizukami, Y. Ando, and T. Miyazaki, “Magnetic relaxation of normal-metal (NM)/80NiFe/NM films,” *J. Magn. Magn. Mater.*, vol. 239, no. 1, pp. 42–44, 2002.
- [204] C. Bell, S. Milikisyants, M. Huber, and J. Aarts, “Spin Dynamics in a Superconductor-Ferromagnet Proximity System,” *Phys. Rev. Lett.*, vol. 100, p. 47002, Feb 2008.
- [205] A. F. Andreev, “Thermal conductivity of the intermediate state of superconductors,” *Sov. Physics JETP*, vol. 19, pp. 1228–1230, 1964.
- [206] P. G. de Gennes and D. Saint-James, “Elementary excitations in the vicinity of a normal metal-superconducting metal contact,” *Phys. Lett.*, vol. 4, no. 2, pp. 151–152, 1963.
- [207] D. Saint-James, “Excitations élémentaires au voisinage de la surface de séparation d’un métal normal et d’un métal supraconducteur,” *J. Phys. Fr.*, vol. 25, no. 10, pp. 899–905, 1964.
- [208] J. P. Morten, A. Brataas, G. E. W. Bauer, W. Belzig, and Y. Tserkovnyak, “Proximity-effect-assisted decay of spin currents in superconductors,” *EPL (Europhysics Lett.)*, vol. 84, p. 57008, Dec 2008.
- [209] Y. Yao, Q. Song, Y. Takamura, J. P. Cascales, W. Yuan, Y. Ma, Y. Yun, X. C. Xie, J. S. Moodera, and W. Han, “Probe of spin dynamics in superconducting NbN thin films via spin pumping,” *Phys. Rev. B*, vol. 97, p. 224414, Jun 2018.
- [210] M. A. Silaev, “Large enhancement of spin pumping due to the surface bound states in normal metal – superconductor structures,” *Phys. Rev. B*, vol. 102, no. 18, p. 180502, 2020.
- [211] A. A. Golubov and M. Y. Kupriyanov, “Theoretical investigation of Josephson tunnel junctions with spatially inhomogeneous superconducting electrodes,” *J. Low Temp. Phys.*, vol. 70, no. 1, pp. 83–130, 1988.
- [212] A. A. Golubov, E. P. Houwman, J. G. Gijsbertsen, V. M. Krasnov, J. Flokstra, H. Rogalla, and M. Y. Kupriyanov, “Proximity effect in superconductor-insulator-superconductor Josephson tunnel junctions: Theory and experiment,” *Phys. Rev. B*, vol. 51, pp. 1073–1089, Jan 1995.
- [213] A. Gurevich and T. Kubo, “Surface impedance and optimum surface resistance of a superconductor with an imperfect surface,” *Phys. Rev. B*, vol. 96, p. 184515, Nov 2017.

- [214] K.-R. Jeon, C. Ciccarelli, H. Kurebayashi, L. F. Cohen, X. Montiel, M. Eschrig, T. Wagner, S. Komori, A. Srivastava, J. W. A. Robinson, and M. G. Blamire, “Effect of Meissner Screening and Trapped Magnetic Flux on Magnetization Dynamics in Thick Nb/Ni<sub>80</sub>Fe<sub>20</sub>/Nb Trilayers,” *Phys. Rev. Appl.*, vol. 11, p. 14061, Jan 2019.
- [215] L.-L. Li, Y.-L. Zhao, X.-X. Zhang, and Y. Sun, “Possible Evidence for Spin-Transfer Torque Induced by Spin-Triplet Supercurrents,” *Chinese Phys. Lett.*, vol. 35, p. 77401, Jul 2018.
- [216] I. A. Golovchanskiy, N. N. Abramov, V. S. Stolyarov, V. I. Chichkov, M. Silaev, I. V. Shchetinin, A. A. Golubov, V. V. Ryazanov, A. V. Ustinov, and M. Kupriyanov, “Magnetization Dynamics in Proximity-Coupled Superconductor-Ferromagnet-Superconductor Multilayers,” *Phys. Rev. Appl.*, vol. 14, p. 24086, Aug 2020.
- [217] S. V. Mironov and A. I. Buzdin, “Giant demagnetization effects induced by superconducting films,” *Appl. Phys. Lett.*, vol. 119, no. 10, p. 102601, 2021.
- [218] S. Aull, O. Kugeler, and J. Knobloch, “Trapped magnetic flux in superconducting niobium samples,” *Phys. Rev. ST Accel. Beams*, vol. 15, p. 62001, Jun 2012.
- [219] L. V. Shubnikov, V. I. Khotkevich, Y. D. Shepelev, and Y. N. Ryabinin, “Magnetic Properties of Superconducting Metals and Alloys,” *Zh. Eksp. Teor. Fiz.*, vol. 7, pp. 221–237, 1937.
- [220] V. L. Ginzburg, “Nobel Lecture: On superconductivity and superfluidity (what I have and have not managed to do) as well as on the “physical minimum” at the beginning of the XXI century,” *Rev. Mod. Phys.*, vol. 76, pp. 981–998, Dec 2004.
- [221] L. D. Landau, “73 - On the theory of superconductivity,” in *Collect. Pap. L.D. Landau* (D. Ter Haar, ed.), pp. 546–568, Pergamon, 1965.
- [222] A. A. Abrikosov, *Fundamentals of the Theory of Metals*. Amsterdam: Elsevier Science Publishers, 1 ed., 1988.
- [223] A. V. Narlikar, *Superconductors*. Oxford: Oxford university press, first ed., 2014.
- [224] B. Segall, “Fermi Surface and Energy Bands of Copper,” *Phys. Rev.*, vol. 125, pp. 109–122, Jan 1962.
- [225] P. Wigner, *The Collected Works of Eugene Paul Wigner*. Berlin: Springer-Verlag Berlin Heidelberg, 1 ed., 1993.
- [226] A. Behera, S. Aich, and T. Theivasanthi, “Chapter 8 - Magnetron sputtering for development of nanostructured materials,” in *Des. Fabr. Charact. Multifunct. Nanomater.* (S. Thomas, N. Kalarikkal, and A. R. Abraham, eds.), Micro and Nano Technologies, pp. 177–199, Elsevier, 2022.
- [227] L.-C. Xu and C. A. Siedlecki, “4.18 Surface Texturing and Control of Bacterial Adhesion,” in *Compr. Biomater. II* (P. Ducheyne, ed.), pp. 303–320, Oxford: Elsevier, 2017.

- [228] V. R. Manfrinato, L. Zhang, D. Su, H. Duan, R. G. Hobbs, E. A. Stach, and K. K. Berggren, “Resolution Limits of Electron-Beam Lithography toward the Atomic Scale,” *Nano Lett.*, vol. 13, pp. 1555–1558, Apr 2013.
- [229] F. A. Ma’Mari, T. Moorsom, G. Teobaldi, W. Deacon, T. Prokscha, H. Luetkens, S. Lee, G. E. Sterbinsky, D. A. Arena, D. A. MacLaren, M. Flokstra, M. Ali, M. C. Wheeler, G. Burnell, B. J. Hickey, and O. Cespedes, “Beating the Stoner criterion using molecular interfaces,” *Nature*, vol. 524, no. 7563, pp. 69–73, 2015.
- [230] T. Vemulkar, Personal communication, 2022.
- [231] R. Mansell, R. Lavrijsen, A. Fernández-Pacheco, D. C. M. C. Petit, J. H. Lee, B. Koopmans, H. J. M. Swagten, and R. P. Cowburn, “A robust soliton ratchet using combined antiferromagnetic and ferromagnetic interlayer couplings,” *Appl. Phys. Lett.*, vol. 106, no. 9, p. 92404, 2015.
- [232] T. Vemulkar, R. Mansell, A. Fernández-Pacheco, and R. P. Cowburn, “Toward Flexible Spintronics: Perpendicularly Magnetized Synthetic Antiferromagnetic Thin Films and Nanowires on Polyimide Substrates,” *Adv. Funct. Mater.*, vol. 26, no. 26, pp. 4704–4711, 2016.
- [233] I. S. Maksymov and M. Kostylev, “Broadband stripline ferromagnetic resonance spectroscopy of ferromagnetic films, multilayers and nanostructures,” *Phys. E Low-dimensional Syst. Nanostructures*, vol. 69, pp. 253–293, 2015.
- [234] Z. Fang, *Current-induced torque in ferromagnets at room temperature*. PhD thesis, University of Cambridge, 2017.
- [235] M. Rogers, A. Walton, M. G. Flokstra, F. Al, M. Mari, R. Stewart, S. L. Lee, T. Prokscha, A. J. Caruana, C. J. Kinane, S. Langridge, H. Bradshaw, T. Moorsom, M. Ali, G. Burnell, B. J. Hickey, and O. Cespedes, “Spin-singlet to triplet Cooper pair converter interface,” *Commun. Phys.*, vol. 4, pp. 1–9, 2021.
- [236] A. D. Hillier, S. J. Blundell, I. McKenzie, I. Umegaki, L. Shu, J. A. Wright, T. Prokscha, F. Bert, K. Shimomura, A. Berlie, H. Alberto, and I. Watanabe, “Muon spin spectroscopy,” *Nat. Rev. Methods Prim.*, vol. 2, no. 1, p. 4, 2022.
- [237] J. Woerle, T. Prokscha, A. Hallén, and U. Grossner, “Interaction of low-energy muons with defect profiles in proton-irradiated Si and 4H-SiC,” *Phys. Rev. B*, vol. 100, p. 115202, Sep 2019.
- [238] C. Barraud, P. Seneor, R. Mattana, S. Fusil, K. Bouzehouane, C. Deranlot, P. Graziosi, L. Hueso, I. Bergenti, V. Dediu, F. Petroff, and A. Fert, “Unravelling the role of the interface for spin injection into organic semiconductors,” *Nat. Phys.*, vol. 6, no. 8, pp. 615–620, 2010.
- [239] S. Sanvito, “The rise of spinterface science,” *Nat. Phys.*, vol. 6, no. 8, pp. 562–564, 2010.
- [240] I. Bergenti and V. Dediu, “Spinterface: A new platform for spintronics,” *Nano Mater. Sci.*, vol. 1, no. 3, pp. 149–155, 2019.

- [241] K. Bairagi, A. Bellec, V. Repain, C. Fourmental, C. Chacon, Y. Girard, J. Lagoute, S. Rousset, L. Le Laurent, A. Smogunov, and C. Barreateau, “Experimental and theoretical investigations of magnetic anisotropy and magnetic hardening at molecule/ferromagnet interfaces,” *Phys. Rev. B*, vol. 98, no. 8, 2018.
- [242] K. V. Raman, A. M. Kamerbeek, A. Mukherjee, N. Atodiresei, T. K. Sen, P. Lazić, V. Caciuc, R. Michel, D. Stalke, S. K. Mandal, S. Blügel, M. Münzenberg, and J. S. Moodera, “Interface-engineered templates for molecular spin memory devices,” *Nature*, vol. 493, no. 7433, pp. 509–513, 2013.
- [243] S. Alotibi, B. J. Hickey, G. Teobaldi, M. Ali, J. Barker, E. Poli, D. D. O’Regan, Q. Ramasse, G. Burnell, J. Patchett, C. Ciccarelli, M. Alyami, T. Moorsom, and O. Cespedes, “Enhanced Spin–Orbit Coupling in Heavy Metals via Molecular Coupling,” *ACS Appl. Mater. Interfaces*, vol. 13, pp. 5228–5234, Feb 2021.
- [244] J. E. Shoup, D. A. Arena, J. A. Borchers, B. J. Kirby, A. J. Caruana, C. J. Kinane, S. Langridge, M. Rogers, and O. Cespedes, “Structural studies of magnetic  $C_{60}/Cu$  multilayers,” *AIP Adv.*, vol. 10, no. 2, p. 025312, 2020.
- [245] A. Di Bernardo, Z. Salman, X. L. Wang, M. Amado, M. Egilmez, M. G. Flokstra, A. Suter, S. L. Lee, J. H. Zhao, T. Prokscha, E. Morenzoni, M. G. Blamire, J. Linder, and J. W. A. Robinson, “Intrinsic Paramagnetic Meissner Effect Due to  $s$ -Wave Odd-Frequency Superconductivity,” *Phys. Rev. X*, vol. 5, p. 41021, Nov 2015.
- [246] M. Alidoust, K. Halterman, and J. Linder, “Meissner effect probing of odd-frequency triplet pairing in superconducting spin valves,” *Phys. Rev. B*, vol. 89, p. 54508, Feb 2014.
- [247] T. Yokoyama, Y. Tanaka, and N. Nagaosa, “Anomalous Meissner Effect in a Normal-Metal–Superconductor Junction with a Spin-Active Interface,” *Phys. Rev. Lett.*, vol. 106, p. 246601, Jun 2011.
- [248] R. Arias and D. L. Mills, “Extrinsic contributions to the ferromagnetic resonance response of ultrathin films,” *Phys. Rev. B*, vol. 60, no. 10, pp. 7395–7409, 1999.
- [249] O. Cespedes, Personal communication, Jun 2022.
- [250] R. I. Salikhov, I. A. Garifullin, N. N. Garif’yanov, L. R. Tagirov, K. Theis-Bröhl, K. Westerholt, and H. Zabel, “Experimental Observation of the Spin Screening Effect in Superconductor/Ferromagnet Thin Film Heterostructures,” *Phys. Rev. Lett.*, vol. 102, p. 87003, Feb 2009.
- [251] M. Y. Kharitonov, A. F. Volkov, and K. B. Efetov, “Oscillations of induced magnetization in superconductor-ferromagnet heterostructures,” *Phys. Rev. B*, vol. 73, p. 54511, Feb 2006.
- [252] V. K. Vlasko-Vlasov, F. Colauto, A. A. Buzdin, D. Carmo, A. M. H. Andrade, A. A. M. Oliveira, W. A. Ortiz, D. Rosenmann, and W.-K. Kwok, “Crossing fields in thin films of isotropic superconductors,” *Phys. Rev. B*, vol. 94, p. 184502, Nov 2016.
- [253] R. P. Huebener, *Magnetic Flux Structures in Superconductors*. Berlin, Heidelberg: Springer-Verlag, 1 ed., 1979.

- [254] K.-R. Jeon, C. Ciccarelli, H. Kurebayashi, L. F. Cohen, S. Komori, J. W. A. Robinson, and M. G. Blamire, “Abrikosov vortex nucleation and its detrimental effect on superconducting spin pumping in Pt/Nb/Ni<sub>80</sub>Fe<sub>20</sub>/Nb/Pt proximity structures,” *Phys. Rev. B*, vol. 99, p. 144503, Apr 2019.
- [255] I. A. Golovchanskiy, N. N. Abramov, M. Pfirrmann, T. Piskor, J. N. Voss, D. S. Baranov, R. A. Hovhannisyan, V. S. Stolyarov, C. Dubs, A. A. Golubov, V. V. Ryazanov, A. V. Ustinov, and M. Weides, “Interplay of Magnetization Dynamics with a Microwave Waveguide at Cryogenic Temperatures,” *Phys. Rev. Appl.*, vol. 11, p. 44076, Apr 2019.
- [256] J. I. Vestgård, T. H. Johansen, and Y. M. Galperin, “Nucleation and propagation of thermomagnetic avalanches in thin-film superconductors (Review Article),” *Low Temp. Phys.*, vol. 44, no. 6, pp. 460–476, 2018.
- [257] S. L. Wipf, “Review of stability in high temperature superconductors with emphasis on flux jumping,” *Cryogenics (Guildf.)*, vol. 31, no. 11, pp. 936–948, 1991.
- [258] J. E. Evetts, A. M. Campbell, and D. Dew-hughes, “Flux instabilities in hard superconductors,” *Philos. Mag. A J. Theor. Exp. Appl. Phys.*, vol. 10, no. 104, pp. 339–343, 1964.
- [259] C. González-Ruano, L. G. Johnsen, D. Caso, C. Tiusan, M. Hehn, N. Banerjee, J. Linder, and F. G. Aliev, “Superconductivity-induced change in magnetic anisotropy in epitaxial ferromagnet-superconductor hybrids with spin-orbit interaction,” *Phys. Rev. B*, vol. 102, p. 20405, Jul 2020.
- [260] A.-L. Zhang, W.-Y. Jiang, X.-H. Chen, X.-K. Zhang, W.-L. Lu, F. Chen, Z.-J. Feng, S.-X. Cao, J.-C. Zhang, and J.-Y. Ge, “Anomalous magnetization jumps in granular Pb superconducting films,” *Curr. Appl. Phys.*, vol. 35, pp. 32–37, 2022.
- [261] W. Braunisch, N. Knauf, V. Kataev, S. Neuhausen, A. Grütz, A. Kock, B. Roden, D. Khomskii, and D. Wohlleben, “Paramagnetic Meissner effect in Bi high-temperature superconductors,” *Phys. Rev. Lett.*, vol. 68, pp. 1908–1911, Mar 1992.
- [262] W. Xu, “Preparing (111)-oriented C60 crystalline films on NaCl substrate,” *J. Cryst. Growth*, vol. 220, no. 1, pp. 96–99, 2000.
- [263] L. Dresner, *Stability of superconductors*. New York, Boston, Dordrecht, London, Moscow: Kluwer Academic Publishers, 1 ed., 2002.
- [264] Y. B. Kim, C. F. Hempstead, and A. R. Strnad, “Magnetization and Critical Supercurrents,” *Phys. Rev.*, vol. 129, pp. 528–535, Jan 1963.
- [265] R. Huebener, R. Kampwirth, R. Martin, T. Barbee, and R. Zubeck, “Critical current density in superconducting niobium films,” *IEEE Trans. Magn.*, vol. 11, no. 2, pp. 344–346, 1975.
- [266] D. J. Thompson, M. S. M. Minhaj, L. E. Wenger, and J. T. Chen, “Observation of Paramagnetic Meissner Effect in Niobium Disks,” *Phys. Rev. Lett.*, vol. 75, pp. 529–532, Jul 1995.

- [267] A. K. Gelm, S. V. Dubonos, J. G. S. Lok, M. Henl, and J. C. Maan, “Paramagnetic Meissner effect in small superconductors,” *Nature*, vol. 396, pp. 144–146, 1998.
- [268] J. P. Patchett, M. Drouhin, J. W. Liao, Z. Soban, D. Petit, J. Haigh, P. Roy, J. Wunderlich, R. P. Cowburn, and C. Ciccarelli, “Symmetry effects on the static and dynamic properties of coupled magnetic oscillators,” *Phys. Rev. B*, vol. 105, p. 104436, Mar 2022.
- [269] F. Bloch, *Zur Theorie des Austauschproblems und der Remanenzerscheinung der Ferromagnetika*, pp. 295–335. Berlin, Heidelberg: Springer Berlin Heidelberg, 1932.
- [270] T. Holstein and H. Primakoff, “Field Dependence of the Intrinsic Domain Magnetization of a Ferromagnet,” *Phys. Rev.*, vol. 58, pp. 1098–1113, Dec 1940.
- [271] J. Van Kranendonk and J. H. Van Vleck, “Spin Waves,” *Rev. Mod. Phys.*, vol. 30, pp. 1–23, Jan 1958.
- [272] F. Bloch, “Zur Theorie des Ferromagnetismus,” *Zeitschrift für Phys.*, vol. 61, no. 3, pp. 206–219, 1930.
- [273] V. Cherepanov, I. Kolokolov, and V. L’vov, “The saga of YIG: Spectra, thermodynamics, interaction and relaxation of magnons in a complex magnet,” *Phys. Rep.*, vol. 229, no. 3, pp. 81–144, 1993.
- [274] A. J. Princep, R. A. Ewings, S. Ward, S. Tóth, C. Dubs, D. Prabhakaran, and A. T. Boothroyd, “The full magnon spectrum of yttrium iron garnet,” *npj Quantum Mater.*, vol. 2, no. 1, p. 63, 2017.
- [275] V. V. Kruglyak, S. O. Demokritov, and D. Grundler, “Magnonics,” *J. Phys. D: Appl. Phys.*, vol. 43, p. 264001, Jun 2010.
- [276] A. V. Chumak, A. A. Serga, and B. Hillebrands, “Magnon transistor for all-magnon data processing,” *Nat. Commun.*, vol. 5, no. 1, p. 4700, 2014.
- [277] P. Pirro, V. I. Vasyuchka, A. A. Serga, and B. Hillebrands, “Advances in coherent magnonics,” *Nat. Rev. Mater.*, vol. 6, no. 12, pp. 1114–1135, 2021.
- [278] A. V. Chumak, V. I. Vasyuchka, A. A. Serga, and B. Hillebrands, “Magnon spintronics,” *Nat. Phys.*, vol. 11, no. 6, pp. 453–461, 2015.
- [279] A. Barman, G. Gubbiotti, S. Ladak, A. O. Adeyeye, M. Krawczyk, J. Gräfe, C. Adelman, S. Cotofana, A. Naeemi, V. I. Vasyuchka, B. Hillebrands, S. A. Nikitov, H. Yu, D. Grundler, A. V. Sadovnikov, A. A. Grachev, S. E. Sheshukova, J.-Y. Duquesne, M. Marangolo, G. Csaba, W. Porod, V. E. Demidov, S. Urazhdin, S. O. Demokritov, E. Albisetti, D. Petti, R. Bertacco, H. Schultheiss, V. V. Kruglyak, V. D. Poimanov, S. Sahoo, J. Sinha, H. Yang, M. Münzenberg, T. Moriyama, S. Mizukami, P. Landeros, R. A. Gallardo, G. Carlotti, J.-V. Kim, R. L. Stamps, R. E. Camley, B. Rana, Y. Otani, W. Yu, T. Yu, G. E. W. Bauer, C. Back, G. S. Uhrig, O. V. Dobrovolskiy, B. Budinska, H. Qin, S. van Dijken, A. V. Chumak, A. Khitun, D. E. Nikonov, I. A. Young, B. W. Zingsem, and M. Winklhofer, “The 2021 Magnonics Roadmap,” *J. Phys. Condens. Matter*, vol. 33, p. 413001, Aug 2021.

- [280] M. Grimsditch, L. Giovannini, F. Montoncello, F. Nizzoli, G. K. Leaf, and H. G. Kaper, "Magnetic normal modes in ferromagnetic nanoparticles: A dynamical matrix approach," *Phys. Rev. B*, vol. 70, no. 054409, pp. 1–7, 2004.
- [281] H. J. Waring, N. A. B. Johansson, I. J. Vera-Marun, and T. Thomson, "Zero-field Optic Mode Beyond 20 GHz in a Synthetic Antiferromagnet," *Phys. Rev. Appl.*, vol. 13, p. 34035, Mar 2020.
- [282] Y. Shiota, T. Taniguchi, M. Ishibashi, T. Moriyama, and T. Ono, "Tunable Magnon-Magnon Coupling Mediated by Dynamic Dipolar Interaction in Synthetic Antiferromagnets," *Phys. Rev. Lett.*, vol. 125, p. 17203, Jul 2020.
- [283] A. G. Gurevich and G. A. Melkov, *Magnetization Oscillations and Waves*. Boca Raton: CRC Press, 1st ed. ed., 1996.
- [284] Y. Gong, Z. Cevher, M. Ebrahim, J. Lou, C. Pettiford, N. X. Sun, and Y. H. Ren, "Determination of magnetic anisotropies, interlayer coupling, and magnetization relaxation in FeCoB/Cr/FeCoB," *J. Appl. Phys.*, vol. 106, no. 6, p. 63916, 2009.
- [285] X. Xing, M. Liu, S. Li, O. Obi, J. Lou, Z. Zhou, B. Chen, and N. X. Sun, "RF Magnetic Properties of FeCoB/Al<sub>2</sub>O<sub>3</sub>/FeCoB Structure With Varied Al<sub>2</sub>O<sub>3</sub> Thickness," *IEEE Trans. Magn.*, vol. 47, no. 10, pp. 3104–3107, 2011.
- [286] S. Li, G.-X. Miao, D. Cao, Q. Li, J. Xu, Z. Wen, Y. Dai, S. Yan, and Y. Lü, "Stress-Enhanced Interlayer Exchange Coupling and Optical-Mode FMR Frequency in Self-Bias FeCoB/Ru/FeCoB Trilayers," *ACS Appl. Mater. Interfaces*, vol. 10, pp. 8853–8859, Mar 2018.
- [287] R. Hisatomi, A. Osada, Y. Tabuchi, T. Ishikawa, A. Noguchi, R. Yamazaki, K. Usami, and Y. Nakamura, "Bidirectional conversion between microwave and light via ferromagnetic magnons," *Phys. Rev. B*, vol. 93, p. 174427, May 2016.
- [288] A. Rueda, F. Sedlmeir, M. C. Collodo, U. Vogl, B. Stiller, G. Schunk, D. V. Strelakov, C. Marquardt, J. M. Fink, O. Painter, G. Leuchs, and H. G. L. Schwefel, "Efficient microwave to optical photon conversion: an electro-optical realization," *Optica*, vol. 3, pp. 597–604, Jun 2016.
- [289] Q. Huang, Y. Dong, X. Zhao, J. Wang, Y. Chen, L. Bai, Y. Dai, Y. Dai, S. Yan, and Y. Tian, "Electrical Control of Perpendicular Magnetic Anisotropy and Spin-Orbit Torque-Induced Magnetization Switching," *Adv. Electron. Mater.*, vol. 6, no. 3, p. 1900782, 2020.
- [290] M. A. McGuire, G. Clark, S. KC, W. M. Chance, G. E. Jellison, V. R. Cooper, X. Xu, and B. C. Sales, "Magnetic behavior and spin-lattice coupling in cleavable van der Waals layered CrCl<sub>3</sub> crystals," *Phys. Rev. Mater.*, vol. 1, p. 14001, Jun 2017.
- [291] W. Thomson, "XIX. On the electro-dynamic qualities of metals:-Effects of magnetization on the electric conductivity of nickel and of iron," *Proc. R. Soc. London*, vol. 8, pp. 546–550, 1857.

- [292] B. Raquet, M. Viret, E. Sondergard, O. Cespedes, and R. Mamy, “Electron-magnon scattering and magnetic resistivity in  $3d$  ferromagnets,” *Phys. Rev. B*, vol. 66, p. 24433, Jul 2002.
- [293] G. Lu, X. Huang, S. Fan, W. Ling, M. Liu, J. Li, L. Jin, and L. Pan, “Temperature-and thickness -dependent dynamic magnetic properties of sputtered CoFeB/Ta bilayer films,” *J. Alloys Compd.*, vol. 753, pp. 475–482, 2018.
- [294] J. Wells, E. Selezneva, P. Krzysteczko, X. Hu, H. W. Schumacher, R. Mansell, R. Cowburn, A. Cuenat, and O. Kazakova, “Combined anomalous Nernst effect and thermography studies of ultrathin CoFeB/Pt nanowires,” *AIP Adv.*, vol. 7, no. 5, p. 55904, 2017.
- [295] K. Uchida, S. Takahashi, K. Harii, J. Ieda, W. Koshibae, K. Ando, S. Maekawa, and E. Saitoh, “Observation of the spin Seebeck effect,” *Nature*, vol. 455, no. 7214, pp. 778–781, 2008.
- [296] C. O. Avci, K. Garello, J. Mendil, A. Ghosh, N. Blasakis, M. Gabureac, M. Trassin, M. Fiebig, and P. Gambardella, “Magnetoresistance of heavy and light metal/ferromagnet bilayers,” *Appl. Phys. Lett.*, vol. 107, no. 19, p. 192405, 2015.
- [297] J. Železný, Z. Fang, K. Olejnik, J. Patchett, F. Gerhard, C. Gould, L. W. Molenkamp, C. Gomez-Olivella, J. Zemen, T. Tichý, T. Jungwirth, and C. Ciccarelli, “Unidirectional magnetoresistance and spin-orbit torque in NiMnSb,” *Phys. Rev. B*, vol. 104, p. 54429, Aug 2021.
- [298] C. O. Avci, J. Mendil, G. S. D. Beach, and P. Gambardella, “Origins of the Unidirectional Spin Hall Magnetoresistance in Metallic Bilayers,” *Phys. Rev. Lett.*, vol. 121, p. 87207, Aug 2018.
- [299] N. H. Duy Khang and P. N. Hai, “Giant unidirectional spin Hall magnetoresistance in topological insulator – ferromagnetic semiconductor heterostructures,” *J. Appl. Phys.*, vol. 126, no. 23, p. 233903, 2019.
- [300] C. Lidig, J. Cramer, L. Weisshoff, T. R. Thomas, T. Kessler, M. Kläui, and M. Jourdan, “Unidirectional Spin Hall Magnetoresistance as a Tool for Probing the Interfacial Spin Polarization of  $\text{Co}_2\text{MnSi}$ ,” *Phys. Rev. Appl.*, vol. 11, p. 44039, Apr 2019.
- [301] S. S.-L. Zhang and G. Vignale, “Theory of unidirectional spin Hall magnetoresistance in heavy-metal/ferromagnetic-metal bilayers,” *Phys. Rev. B*, vol. 94, p. 140411, Oct 2016.
- [302] S. Ding, P. Noël, G. K. Krishnaswamy, and P. Gambardella, “Unidirectional orbital magnetoresistance in light-metal–ferromagnet bilayers,” *Phys. Rev. Res.*, vol. 4, p. L032041, Sep 2022.
- [303] H. Nakayama, Y. Kanno, H. An, T. Tashiro, S. Haku, A. Nomura, and K. Ando, “Rashba-Edelstein Magnetoresistance in Metallic Heterostructures,” *Phys. Rev. Lett.*, vol. 117, p. 116602, Sep 2016.

- 
- [304] A. J. Newell, D. J. Dunlop, and W. Williams, "A generalization of the demagnetizing tensor for nonuniform magnetization," *J. Geophys. Res.*, vol. 98, no. B6, p. 9551, 1993.
- [305] M. Hayashi, J. Kim, M. Yamanouchi, and H. Ohno, "Quantitative characterization of the spin-orbit torque using harmonic Hall voltage measurements," *Phys. Rev. B*, vol. 89, p. 144425, Apr 2014.



# Appendix A

## Symmetry of Brown's equation for a uniaxial SAF

In Chapter 6, it was shown that if a symmetry operation commutes with the set of operators  $\Lambda^{ij}$  describing the effective field in layer  $i$  due to the magnetisation of layer  $j$ ,  $\mathbf{H}_{eff}^i = \Lambda^{ij} \mathbf{M}_j$ , then new symmetry-transformed solutions can be constructed from previously known solutions. Here these operators are listed explicitly. Most of these operators are linear, and hence will be described by matrices. The only exception of the terms considered is the biquadratic exchange field, which has an additional  $\mathbf{m}_A \cdot \mathbf{m}_B$  factor, where  $\mathbf{m}_A$  and  $\mathbf{m}_B$  are the (normalised) magnetisations of the two coupled magnets of the SAF. However, as this term is invariant under any orthogonal transformation  $\mathbf{m}_i \rightarrow R\mathbf{m}_i$ , the commutation relation can still be treated as a matrix commutation relation.

A uniaxial magnetocrystalline anisotropy field in layer  $i$  can be expressed by the matrix with components:

$$(\Lambda_{ani}^{ii})_{jk} = \frac{2K^{(i)}}{\mu_0 M_{si}^2} n_j^{(i)} n_k^{(i)} \quad (\text{A.1})$$

where  $n_j^{(i)}$  is the  $j^{th}$  component of the unit vector in the direction of the easy axis in layer  $i$ , and  $K^{(i)}$  is the anisotropy constant that parameterised the strength of the anisotropy ( $H_a^{(i)} = 2K^{(i)}/\mu_0 M_s$ ). Included are contributions from the in-plane anisotropy  $\Lambda_{ani(p)}^{ii}$  and out of plane anisotropy  $\Lambda_{ani(n)}^{ii}$ , where  $\mathbf{n} = (1, 1, 0)$  and  $\mathbf{n} = (0, 0, 1)$  respectively (the current direction between taken as the x-axis, and the z-axis being out of plane as usual).

The demagnetisation fields are expressed using the demagnetisation tensor of Newell et al. [304],  $\mathbf{N}^{ij}$ , as  $\mathbf{H}_{demag}^i = \mathbf{N}^{ij} \mathbf{M}_j$ .  $\mathbf{N}^{ij}$  represents the demagnetisation field in layer  $i$  due to layer  $j$ , and  $\mathbf{M}_i$  is the (un-normalised, magnitude  $M_s$ ) magnetisation of layer  $i$ . The demagnetisation tensor of a square bar is defined by:

$$\mathbf{N}^{ii} = \begin{bmatrix} \delta^{(i)} & 0 & 0 \\ 0 & \delta^{(i)} & 0 \\ 0 & 0 & 1 - 2\delta^{(i)} \end{bmatrix} \quad (\text{A.2})$$

$$\mathbf{N}^{ij} = \begin{bmatrix} \lambda^{(ij)} & 0 & 0 \\ 0 & \lambda^{(ij)} & 0 \\ 0 & 0 & -2\lambda^{(ij)} \end{bmatrix} \quad i \neq j \quad (\text{A.3})$$

in the thin-film limit  $\delta \ll 1$ . The bilinear exchange field takes the form:

$$(\Lambda_{ex1}^{ij})_{kl} = \frac{-JA}{\mu_0 M_{sA} M_{sB} t_i} \delta_{kl} \quad (\text{A.4})$$

where  $J$  is the exchange constant, and  $t_i$  the thickness of layer  $i$ . A positive  $J$  corresponds to antiferromagnetic ordering. The biquadratic term is identical except for an additional factor of  $\mathbf{M}_A \cdot \mathbf{M}_B$ . As suggested above, when considering the commutation relations it can be treat it as a matrix with components:

$$(\Lambda_{ex2}^{ij})_{kl} = \frac{-2J_2}{\mu_0 M_{sA}^2 M_{sB}^2 t_i} \mathbf{M}_A \cdot \mathbf{M}_B \delta_{kl} \quad (\text{A.5})$$

Positive  $J_2$  favours a perpendicular orientation between  $M_A$  and  $M_B$ . It is possible therefore to construct the operators  $\Lambda^{ij}$  as follows:

$$\Lambda^{ii} = \Lambda_{ani(p)}^{ii} + \Lambda_{ani(n)}^{ii} - \mathbf{N}^{ii} \quad (\text{A.6})$$

$$\Lambda^{ij} = \Lambda_{ex1}^{ij} + \Lambda_{ex2}^{ij} - \mathbf{N}^{ij} \quad (\text{A.7})$$

It is straightforward to see that the matrix representing a reflection in the plane containing the easy/hard axis commutes with all of these operators.

## A.1 Non-uniform magnetisation:

Now the considerations made in the previous paragraph are generalised to the case in which the magnetisation has a spatial dependence. In this case Brown's equation must be satisfied at all points in space, i.e.  $\mathbf{H}_{eff}^i(\mathbf{x}) \times \mathbf{M}_i(\mathbf{x}) = \mathbf{0}$ . It will be shown that if  $R$  is a symmetry operation of the device and  $\mathbf{M}_i(\mathbf{x})$  is a solution of Brown's equation for an external field  $\mathbf{h}_e^i(\mathbf{x})$ , then so too must be  $\mathbf{M}'_i(\mathbf{x}) = R\mathbf{M}_i(R^{-1}\mathbf{x})$  for  $\mathbf{h}'_e(\mathbf{x}) = R\mathbf{h}_e^i(R^{-1}\mathbf{x})$ . Fields that depend only on the local magnetisation then transform as:

$$\mathbf{H}'_{local}(R\mathbf{x}) = R\mathbf{H}_{local}^i(\mathbf{x}) \quad (\text{A.8})$$

The same transformation law for non-local effective fields is also required. The only non-local field considered is the demagnetisation field, which in layer  $i$  at the position  $\mathbf{x}$  is given by the operator equation:

$$\mathbf{H}_{demag}^i(\mathbf{x}) = \Lambda_{demag}^{ij}(\mathbf{x})[\mathbf{M}_j(\mathbf{x})] = \int_{V_j} d\mathbf{x}' \mathbf{N}^{ij}(\mathbf{x} - \mathbf{x}') \cdot \mathbf{M}_j(\mathbf{x}') \quad (\text{A.9})$$

where the integral runs over the volume of magnetic layer  $j$ . Using the proposed ansatz

$\mathbf{M}'_j(\mathbf{x}) = R\mathbf{M}_j(R^{-1}\mathbf{x})$ , the effect field transforms as:

$$\mathbf{H}'_{demag}(R\mathbf{x}) = \int_{V_j} d\mathbf{x}' \mathbf{N}^{ij}(R\mathbf{x}-\mathbf{x}') \cdot R\mathbf{M}_j(R^{-1}\mathbf{x}') = \det R \int_{R(V_j)} d\mathbf{x}' \mathbf{N}^{ij}(R(\mathbf{x}-\mathbf{x}')) \cdot R\mathbf{M}(\mathbf{x}') \quad (\text{A.10})$$

In the case considered in this report of reflection symmetry along the diagonal of a square bar, the -1 from  $\det R$  cancels with the sign change from the change in limits, and, using the transformation properties of the demagnetisation tensor [304], in particular by considering which components are even/odd under reflection in the spatial arguments, one obtains  $\mathbf{N}^{ij}(R(\mathbf{x}-\mathbf{x}'))R = R\mathbf{N}^{ij}(\mathbf{x}-\mathbf{x}')$ . Hence  $\mathbf{H}'_{demag}(R\mathbf{x}) = R\mathbf{H}^i_{demag}(\mathbf{x})$ . Consequently:

$$\mathbf{H}'_{eff}(R\mathbf{x}) \times \mathbf{M}'_i(R\mathbf{x}) = (R\mathbf{H}^i_{eff}(\mathbf{x})) \times (R\mathbf{M}_i(\mathbf{x})) = \mathbf{0} \quad (\text{A.11})$$

For all  $\mathbf{x}$  as required.

# Appendix B

## Characterising spin-orbit torques

In order to understand the current-induced dynamics in any ferromagnetic system, it is necessary to characterise the nature of the torques induced in the heterostructure. A current passing through a ferromagnetic heterostructure can generate both field-like and antidamping torques. In order to induce an auto-oscillatory state in the ferromagnet, antidamping torques that are capable of overcoming the native damping in the device will be generated. However, the field-like torques, although they cannot modify the effective damping, may still have a non-negligible effect on the resultant magnetisation dynamics. Consequently, in the following chapter the spin-orbit torques in a Si/SiO<sub>2</sub>[500]/Ta[2]/Pt[3]/CoFeB[2]/Ru[0.9]/Ta[2] heterostructure (thickness of the layers in brackets is in nanometres), patterned into 5  $\mu\text{m}$   $\times$  10  $\mu\text{m}$  bars, will be characterised. These devices were fabricated by Dr W. Liao in the group of Prof. R. P. Cowburn at the University of Cambridge.

The sample is a single-ferromagnetic layer, as characterising the spin-orbit torques in a single layer avoids the complications of the multiple modes and complicated static behaviour of synthetic antiferromagnets. The sample structure has been chosen to replicate the lower layer of the synthetic antiferromagnet samples, with 2 nm of CoFeB next to a 3 nm layer of Pt and a 0.9 nm layer of Ru on top to replicate the interfacial conditions of the lower layer in the SAF. Naturally, the spin-orbit torques measured in such a structure will be representative of

the lower FM layer in the SAFs. The top layer, however, will generally experience different torques due to the degradation in interfacial quality higher up the stack, which is expected to limit the transparency of the interface to spin currents.

A detailed account of how to characterise the spin-orbit torques is given in Sections 2.2.3 and 3.3.3. To summarise, the rectified voltage due to the spin-diode effect,  $V_{SD}$ , has the following angular dependence:

$$\begin{aligned}
 V_{SD} &= V_{sym} \frac{\Delta H^2}{(H - H_{res})^2 + \Delta H^2} + V_{asym} \frac{(H - H_{res})\Delta H}{(H - H_{res})^2 + \Delta H^2} \\
 V_{sym} &= \frac{I\Delta R}{2} \frac{\omega}{\gamma_0 \Delta H (2H_{res} + H_1 + H_2)} h_z \sin 2\phi \\
 &= \frac{I\Delta R}{2} A_{sym} h_z \sin 2\phi \\
 V_{asym} &= \frac{I\Delta R}{2} \frac{H_{res} + H_1}{\Delta H (2H_{res} + H_1 + H_2)} (-h_x \sin \phi + h_y \cos \phi) \sin 2\phi \\
 &= \frac{I\Delta R}{2} A_{asym} (-h_x \sin \phi + h_y \cos \phi) \sin 2\phi
 \end{aligned} \tag{B.1}$$

Consequently, by measuring  $V_{SD}$  via FMR experiments as a function of the angle of the magnetisation,  $\phi$ , the angle of the magnetisation with respect to the current direction (assuming that  $\phi = \phi_H$ , the angle of the external field with respect to the current direction), and fitting it to a combination of symmetric and antisymmetric Lorentzians, the strength of the MW current-induced torques,  $\mathbf{h}e^{i\omega t} = (h_x, h_y, h_z)e^{i\omega t}$  may be determined.

## B.1 Rectified voltage as a function of external field angle

By fitting the rectified voltages to (B.1) it is possible to extract  $V_{sym}$  and  $V_{asym}$  as a function of  $\phi$ , the angle with respect to the x-axis, shown in Figure B.1. These extracted voltages agree well with the theoretically predicted curves from (B.1), with the exception of the need

for an additional  $\sin \phi$  term in both the symmetric and antisymmetric voltages. That is:

$$\begin{aligned} V_{sym} &= \frac{I\Delta R}{2} A_{sym} h_z \sin 2\phi + \xi_{sym} \sin \phi \\ V_{asym} &= \frac{I\Delta R}{2} A_{asym} (-h_x \sin \phi + h_y \cos \phi) \sin 2\phi + \xi_{asym} \sin \phi \end{aligned} \quad (\text{B.2})$$

where  $\xi_{sym}$  and  $\xi_{asym}$  are the magnitude of the  $\sin \phi$  component of the rectified symmetric and antisymmetric voltage components respectively. The existence of a  $\sin \phi$  term in the rectified voltage is not presently well understood. The  $\sin 2\phi$  dependence in the regular terms comes from the derivative of the AMR angle dependence,  $\propto \cos 2\phi$ , and so in order to generate a  $\sin \phi$  term, it is necessary to have a magnetoresistance term with a  $\cos \phi$  angular dependence.

Such a magnetoresistance would be uncommon, as most magnetoresistance effects preserve time-reversal symmetry, and hence are even in the magnetisation (which changes sign upon time-reversal): e.g. AMR, GMR, and SHM [14]. The most common form of unidirectional magnetoresistance in a ferromagnetic thin film is the anomalous Nernst effect, which has a  $\sin \phi$  dependence in its resistance [294] in the presence of an out of plane thermal gradient. Likewise, other effects such as the unidirectional spin-Hall magnetoresistance also exhibit a  $\sin \phi$  dependence [14, 297]. Because the rectified voltage depends on the rate of change of the magnetoresistance with angle, this would give a  $\cos \phi$ , not  $\sin \phi$ , dependence to  $V_{sym}$  and  $V_{asym}$ .

Whatever its origin, the term is likely to be small, as measurements of the device's resistance as a function of  $\phi$ , Figure 6.4 from the main text is consistent with an AMR-like  $\cos 2\phi$  dependence on the magnetic orientation with respect to the current. Consequently, at present, this term is not well understood. However, so long as the  $\sin 2\phi$  dependent terms can be wholly attributed to AMR and the magnetic oscillations, its presence shall not prevent computing the strength of the spin-orbit torques as required.

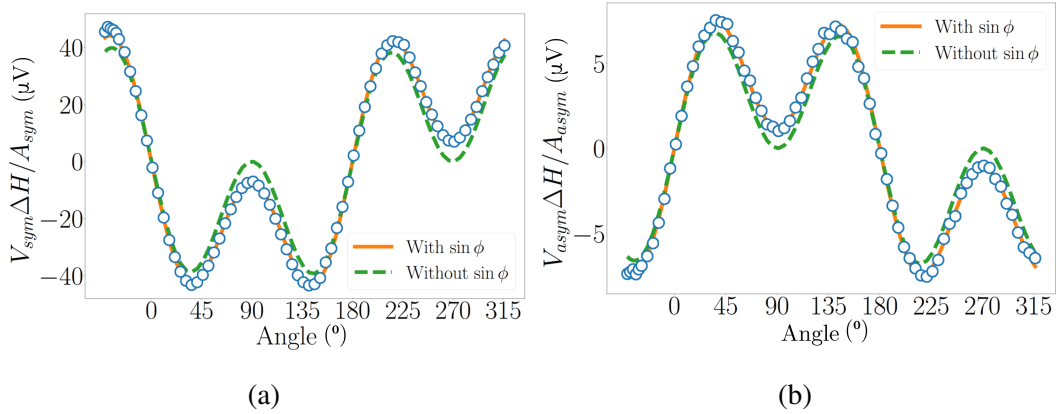


Fig. B.1 Fit of the symmetric (a) and antisymmetric (b) components of the rectified voltage to the theoretically predicted curves (green dashed line) and the predicted curves plus a  $\sin \phi$  term (orange solid line). The expected curve plus a sin term produce good fits to the data. The sin term is attributed to the anomalous Nernst effect. From these plots, the strength of the SOT-induced effective fields can be determined.

From the extracted values of  $V_{asym}$  and  $V_{sym}$  from Figures B.1b and B.1a, it is possible to determine  $h_x$  and  $h_y$  if the microwave current is known. At GHz frequencies, one needs to worry about the wavelike nature of the electric and magnetic field, and so determining the exact microwave current passing through the device is more complicated than at quasi-DC frequencies. A detailed explanation of a bolometric technique for determining the MW current in the device is given in Section 3.3.3. Figure B.2 shows the dependence of the device resistance on the DC current for a range of microwave powers, exhibiting the expected linear dependence on  $I_{DC}^2$ , with an  $I$  dependent offset given by:

$$R = \left( R_0 + \alpha \frac{I^2}{2} \right) + \alpha I_{DC}^2 \quad (\text{B.3})$$

where  $\alpha$  is the constant of proportionality that describes the change in resistance due to the heating caused by current-induced dissipation in the bars. By determining  $\alpha$  from the straight-line fit, one can measure  $I$  from the change in the DC offset when the MW power is turned on/off (Figure B.3). This measurement needs to be repeated for every frequency and microwave power used.

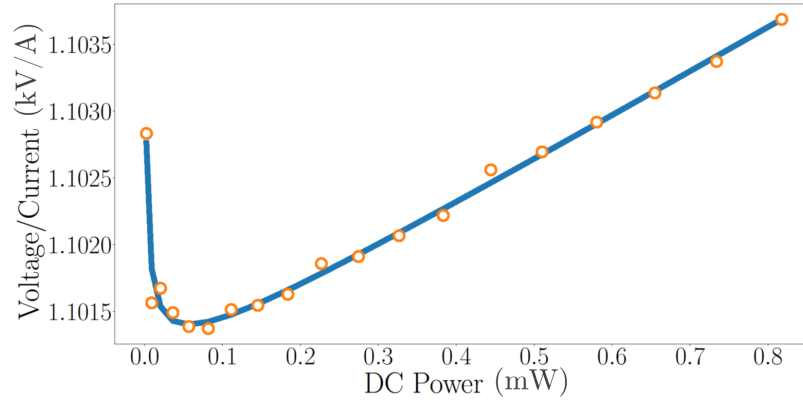


Fig. B.2 Device resistance versus microwave power at the source. The resistance depends linearly on the applied DC power except for a diverging term at low current that occurs because the instrument measures a non-zero voltage at zero current,  $V_{off}$ . Orange points are the raw data, and the blue line is a fit to B.3 with an additional  $V_{off}/I_{DC}$  term to account for the low current divergence.

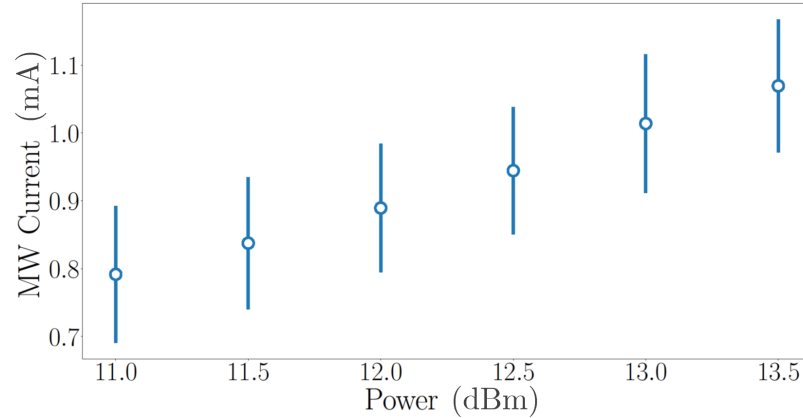


Fig. B.3 Microwave (MW) current in the device  $5\mu\text{m} \times 10\mu\text{m}$ ) as a function of microwave power applied by the source at 5GHz. MW current is calculated by looking at the increase in DC resistance compared to a reference data set with no applied MW power.

With knowledge of  $I$  for a given frequency and microwave power,  $h$  can be determined, see Table B.1. The antidamping torque, which contributes almost entirely to  $h_z$ , is around five times larger than the field-like torque, which is itself dominated by  $h_y$ ; i.e. the field like-torque is mostly of Rashba origins, rather than Dresselhaus (see Section 2.2.3), as expected for a heavy-metal ferromagnet bilayer. These torques are in line with similar values reported in the literature [305].

$\mu_0 h_y / wI$ (T/mA m)	$\mu_0 h_x / wI$ (T/mA m)	$\mu_0 h_z / wI$ (T/mA m)
$129 \pm 12$	$-2.34 \pm 0.22$	$-626 \pm 58$

Table B.1 Summary of the MW torques divided by the bar width,  $w = 5 \mu\text{m}$ , per unit MW current. For a 1 mA current passing through a 5  $\mu\text{m}$  bar, this corresponds to an antidamping torque of about 3 mT.